The MOLLER Experiment

Measurement **O**f a **L**epton **L**epton **E**lectroweak **R**eaction

An Ultra-precise Measurement of the Weak Mixing Angle using Møller Scattering

Submitted by
Thomas Jefferson National Accelerator Facility

on behalf of the MOLLER Collaboration

September 1, 2014

The MOLLER Collaboration

J. Benesch, P. Brindza, R.D. Carlini, J-P. Chen, E. Chudakov, S. Covrig, M.M. Dalton, A. Deur, D. Gaskell, J. Gomez, D.W. Higinbotham, C. Keppel, D. Meekins, R. Michaels, B. Moffit, Y. Roblin, R. Suleiman, R. Wines, B. Wojtsekhowski
Jefferson Lab

G. Cates, D. Crabb, D. Day, K. Gnanvo, D. Keller, N. Liyanage, V.V. Nelyubin, H. Nguyen, B. Norum, K. Paschke, V. Sulkosky, J. Zhang, X. Zheng
University of Virginia

J. Birchall, P. Blunden, M.T.W. Gericke, W.R. Falk, L. Lee, J. Mammei, S.A. Page, W.T.H. van Oers,
University of Manitoba

K. Dehmelt, A. Deshpande, N. Feege, T.K. Hemmick, K.S. Kumar [Contact*]
Stony Brook University, SUNY

T. Kutz, R. Miskimen, M.J. Ramsey-Musolf, S. Riordan, N. Hirlinger Saylor
University of Massachusetts, Amherst

J. Bessuille, E. Ihloff, J. Kelsey, S. Kowalski, R. Silwal
Massachusetts Institute of Technology

G. De Cataldo, R. De Leo, D. Di Bari, L. Lagamba, E. Nappi
INFN, Sezione di Bari and Universita' di Bari

V. Bellini, F. Mammoliti, F. Noto, M.L. Sperduto, C.M. Sutera
INFN Sezione di Catania and Universita' di Catania

P. Cole, T.A. Forest, M. Khandekar, D. McNulty
Idaho State University

K. Aulenbacher, S. Baunack, F. Maas, V. Tioukine
Johannes Gutenberg Universitaet Mainz

R. Gilman, K. Myers, R. Ransome, A. Tadepalli
Rutgers University

R. Beniniwattha, R. Holmes, P. Souder
Syracuse University

D.S. Armstrong, T.D. Averett, W. Deconinck
College of William & Mary

W. Duvall, A. Lee, M. L. Pitt
Virginia Polytechnic Institute and State University

J.A. Dunne, D. Dutta, L. El Fassi
Mississippi State University

F. De Persio, F. Meddi, G.M. Urciuoli
Dipartimento di Fisica dell'Universita' la Sapienza and INFN Sezione di Roma

E. Cisbani, C. Fanelli, F. Garibaldi
INFN Gruppo Collegato Sanita' and Istituto Superiore di Sanita'

K. Johnston, N. Simicevic, S. Wells
Louisiana Tech University

P.M. King, J. Roche
Ohio University

J. Arrington, P.E. Reimer
Argonne National Lab

G. Franklin, B. Quinn

Carnegie Mellon University

A. Ahmidouch, S. Danagoulian
North Carolina A&T State University

O. Glamazdin, R. Pomatsalyuk
NSC Kharkov Institute of Physics and Technology

R. Mammei, J.W. Martin
University of Winnipeg

T. Holmstrom
Longwood University

J. Erler
Universidad Autónoma de México

Yu.G. Kolomensky
University of California, Berkeley

J. Napolitano
Temple University

K. A. Aniol
California State U.(Los Angeles)

W.D. Ramsay
TRIUMF

E. Korkmaz
University of Northern British Columbia

D.T. Spayde
Hendrix College

F. Benmokhtar
Duquesne University

A. Del Dotto
INFN Sezione di Roma3

R. Perrino
INFN Sezione di Lecce

S. Barkanova
Acadia University

A. Aleksejevs
Memorial University, Grenfell

J. Singh
NSCL and Michigan State University

*kkumar@physics.umass.edu

Executive Summary

We present the physics case and a conceptual overview of the MOLLER experiment, in which we propose to measure the parity-violating asymmetry A_{PV} in polarized electron-electron (Møller) scattering. In the Standard Model, A_{PV} is due to the interference between the electromagnetic amplitude and the weak neutral current amplitude, the latter being mediated by the Z^0 boson. A_{PV} is predicted to be ≈ 33 parts per billion (ppb) at our kinematics. Our goal is to measure A_{PV} to a precision of 0.7 ppb. The result would yield a measurement of the weak charge of the electron Q_W^e to a fractional accuracy of 2.4% at an average Q^2 of 0.0056 GeV^2.

The measurement is sensitive to the interference of the electromagnetic amplitude with new neutral current amplitudes as weak as $\sim 10^{-3} \cdot G_F$ from as yet undiscovered dynamics beyond the Standard Model. Such discovery reach is unmatched by any proposed experiment measuring a flavor- and CP-conserving process over the next decade, and results in a unique window to new physics at MeV and multi-TeV scales, complementary to direct searches at high energy colliders. Some examples of physics beyond the Standard Model, where our measurement reaches into new regions of discovery space, include new MeV-scale and multi-TeV-scale vector bosons, electron compositeness, supersymmetry and doubly charged scalars.

In the Standard Model, the Q_W^e measurement yields a determination of the weak mixing angle $\sin^2\theta_W$ with an uncertainty of $\pm 0.00024(\mathrm{stat}) \pm 0.00013(\mathrm{syst})$. Such precision and accuracy are unmatched by any conceivable method at $Q^2 \ll M_Z^2$ in the foreseeable future, and matches the uncertainty from the single best such determination from high energy colliders. Indeed, our result could potentially influence the central value of this fundamental electroweak parameter, a critical input to deciphering many of the signals of physics beyond the Standard Model that might be discovered in higher luminosity and higher center of mass energy running at the Large Hadron Collider (LHC).

The measurement would be carried out in Hall A at Jefferson Laboratory, where a 11 GeV longitudinally polarized electron beam would be incident on a 1.5 m liquid hydrogen target. Møller electrons (beam electrons scattering off target electrons) in the full range of the azimuth and spanning the polar angular range 5 mrad $< \theta_{lab} <$ 19 mrad, would be separated from background and brought to a ring focus ~ 30 m downstream of the target by a spectrometer system consisting of a pair of toroidal magnet assemblies and precision collimators. The Møller ring would be intercepted by a system of fused silica detectors; the resulting Cherenkov light would provide a relative measure of the scattered flux.

Longitudinally polarized electrons are generated via photoemission on a GaAs photocathode by circularly polarized laser light, enabling rapid polarization (helicity) reversal and suppression of spurious systematic effects. A_{PV} would be extracted from the fractional difference in the integrated Cherenkov light response between helicity reversals. Additional systematic suppression to the sub-ppb level would be accomplished by periodically reversing the sign of the physics asymmetry by three independent methods.

Simultaneously with data collection, the fluctuations in the electron beam energy and trajectory and its potential systematic effects on A_{PV} would be precisely monitored, active feedback loops would minimize beam helicity correlations, and detector response to beam fluctuations would be continuously calibrated. Background fractions and their helicity-correlated asymmetries would be measured by dedicated auxiliary detectors. The absolute value of Q^2 would be calibrated periodically using tracking detectors. The longitudinal electron beam polarization would be measured continuously by two independent polarimeter systems.

A strong collaboration with extensive experience in similar experiments is committed to the design, construction and deployment of the apparatus and to data collection and analysis. It is envisioned that construction and assembly will take three years, to be followed by three data collection periods with progressively improved statistical errors and systematic control over a subsequent three to four year period.

Contents

List of Figures

List of Tables

1 Introduction

1.1 Physics Context

The $SU(2)_L \times U(1)_Y$ gauge structure within the Standard Model (SM), which gives rise to electroweak interactions, has been subject to stringent tests over more than three decades of precision measurements. Consistency has been achieved at $\sim 0.1\%$, a level of accuracy where "hard" electroweak radiative corrections involving the top quark, the massive vector bosons, and their scalar interactions, become manifest. Recently, a scalar resonance with a mass of 126 GeV has been discovered at CERN's LHC, consistent with precision electroweak measurements, and with branching ratios consistent (within available statistics) with that predicted for a SM Higgs boson. The detailed exploration of the multi-TeV scale to find direct clues to new phenomena beyond the Standard Model will continue with renewed intensity when LHC restarts in 2015 at higher energy and higher luminosity.

Compelling theoretical arguments, input from cosmological observations, and the discovery of neutrino mass strongly motivate the continued exploration of SM-allowed and SM-suppressed processes over a range of energy scales to discover clues to address some of the outstanding questions for which the SM has incomplete answers. Direct searches at colliders are an essential component of this endeavor. However, the answers to some of the most important outstanding questions might be manifest at much lower energy scales. Therefore, an equally important part of a comprehensive strategy to discover failures to the full extent of SM validity involves indirect probes, where one seeks signals of new dynamics in subtle violations of symmetry at lower center of mass energies. One focuses on judiciously chosen processes where the SM expectations are known to high accuracy or are predicted to be zero.

Classic examples of discoveries that played central roles using indirect probes are the observation of parity-violation in nuclear beta decay, the observation of weak-electromagnetic interference in lepton-quark deep inelastic scattering, and the agreement between the direct mass measurements and the average of the indirect mass determinations of the top quark and the Higgs boson. The next generation of viable projects focused on discoveries of breakdowns of SM predictions has been facilitated by input from nuclear theorists as well as measurement techniques pioneered by nuclear experimentalists. These latter activities constitute an important component of the burgeoning Nuclear Physics subfield of Fundamental Symmetries and Neutrinos, and also includes initiatives in the "Intensity Frontier" program in High Energy Physics,

In this document, we present the MOLLER experiment, a new measurement that would build on the concept of indirect probes. We propose to measure the parity-violating asymmetry in the scattering of longitudinally polarized electrons off unpolarized electrons, using the upgraded 11 GeV beam in Hall A at Jefferson Laboratory, to an overall accuracy of 0.7 ppb, a fractional accuracy of 2.4%. Such a measurement would constitute more than a factor of five improvement in fractional precision over the only other measurement of the same quantity by the E158 experiment at SLAC [1]. The upgraded electron beam energy, luminosity and stability at Jefferson Laboratory creates a unique opportunity to carry out such a measurement, making it feasible to achieve a new benchmark in sensitivity to discover deviations from SM predictions due to multi-TeV scale dynamics as well as MeV-scale mediators with tiny parity admixtures.

The compelling nature of the measurement, which cannot be done elsewhere in the world, can be summarized in two primary bullets:

- Under the assumption of a SM Higgs boson mass of 126 GeV, the theoretical prediction for MOLLER A_{PV} is known to better than 0.2 ppb accuracy. The proposed measurement error is 0.6 ppb; any deviation at this level is a signature of new dynamics beyond the Standard Model (BSM). MOLLER impacts three broad classes of BSM physics as enumerated in the following sub-bullets:

    1. New neutral current interactions are best parameterized model-independently at low energies by effective four-fermion interactions via the quantity Λ/g, where g characterizes the strength and

Λ is the scale of the new dynamics. MOLLER A_{PV} is sensitive to new interaction amplitudes as small as $10^{-3} \cdot G_F$, corresponding to $\Lambda/g = 7.5$ TeV. This would be *the* most sensitive probe of new flavor and CP-conserving neutral current interactions in the leptonic sector until the advent of a new lepton collider or a neutrino factory. A deviation from the Standard Model prediction (or lack thereof at the proposed level of sensitivity) will inform searches for TeV-scale parity-violating observables at a next generation lepton collider or neutrino factory.

2. Notwithstanding the lack of a hint of BSM physics in the 7 and 8 TeV LHC data, BSM theories such as Supersymmetry (SUSY), that have been invoked to address some of the Standard Model's shortcomings, might still be awaiting discovery in regions of parameter space where the masses of new super-particles are nearly degenerate. Direct searches in such scenarios are more challenging; MOLLER is sensitive enough to observe a deviation if the compressed spectrum is lower than 1 TeV.
3. An important feature of the proposed measurement is that it would be carried out at $Q^2 \ll M_Z^2$, with equivalent precision to the best measurements from colliders. MOLLER has by far the most sensitive reach among similar potential measurements under discussion and probes a very interesting region of discovery space of new low energy flavor-conserving effective amplitudes that might be induced for example by "dark" photons with a tiny admixture of the Standard Model Z^0 boson.

- The weak mixing angle $\sin^2\theta_W$ is a fundamental parameter of the electroweak theory. While its value is determined within the Standard Model when more precisely measured quantities are used as input, precision measurements of weak neutral current amplitudes provide direct measurements of $\sin^2\theta_W$. The proposed A_{PV} measurement, which aims to achieve $\delta(\sin^2\theta_W) = \pm 0.00028$, maybe the only robust way to match the level of precision and interpretability of the single best such measurement, the left-right Z^0 boson cross-section asymmetry from the SLD experiment [2], in accelerator facilities worldwide that are operational over the next decade, particularly a purely leptonic process at $Q^2 \sim 0$.

The 2007 NSAC long range planning exercise and its associated report [3] comprehensively described the opportunities presented by new sensitive indirect probes such as MOLLER, and how they fit into the subfield of Fundamental Symmetries. The SLAC E158 A_{PV} result was highlighted as one of the important accomplishments of the subfield in the previous 7 years. As also highlighted in the report, one of the overarching questions that serves to define this subfield is: "What are the unseen forces that were present at the dawn of the universe but disappeared from view as the universe evolved?". To address this question and as part of the third principal recommendation, significant new investments were advocated.

The list included investment for equipment and infrastructure for two new parity-violating electron scattering projects that would use the upgraded 11 GeV beam at Jefferson Laboratory. These two projects, named MOLLER and SOLID, have since been formally proposed and reviewed by JLab's Program Advisory Committee (PAC). In 2009, the PAC determined that "the proposed physics reach [of MOLLER] is outstanding and capable of making this effort a flagship experiment at JLAB", leading to the conclusion that "the PAC believes the mission of this experiment to determine the electron's couplings to new precision is so important that the Laboratory should make effort to support the securing of the resources required." In January 2010, a Director's review of the MOLLER project was carried out, chaired by C. Prescott [4]. The review committee strongly endorsed the physics goals of the project and urged JLab to begin preparations to support the development of the experiment. In January 2011, the PAC was assigned the task of grading all approved JLab upgrade experiments in the Fundamental Symmetries category. The MOLLER project received the highest rating and was allocated its full beamtime request of 344 PAC days, with the statement that "the PAC enthusiastically endorses the experiment and considers it one of the flagship experiments for the Jefferson Lab 12 GeV program."

Most recently, the 2012 NSAC subpanel on the implementation of the Long Range Panel (the Tribble Subcommittee) [5] strongly endorsed the MOLLER project as part of the suite of investments advocated for the subfield of Fundamental Symmetries. The listed experiments were nEDM, tonne-scale neutrinoless double-beta decay, MOLLER, SOLID, Muon g-2, KATRIN and Nab. This document presents the case to receive primary funding for MOLLER from the Department of Energy.

1.2 Definitions and Precision Goal

Polarized electron scattering off unpolarized targets provides a clean window to study weak neutral current interactions. These experiments measure an asymmetry defined by

$$A_{PV} = \frac{\sigma_R - \sigma_L}{\sigma_R + \sigma_L} \quad , \tag{1}$$

where σ_R (σ_L) is the scattering cross-section using incident right (left) handed electrons. A non-zero asymmetry constitutes parity nonconservation, dominated at $Q^2 \ll M_Z^2$ by the interference between the weak and electromagnetic amplitudes [6].

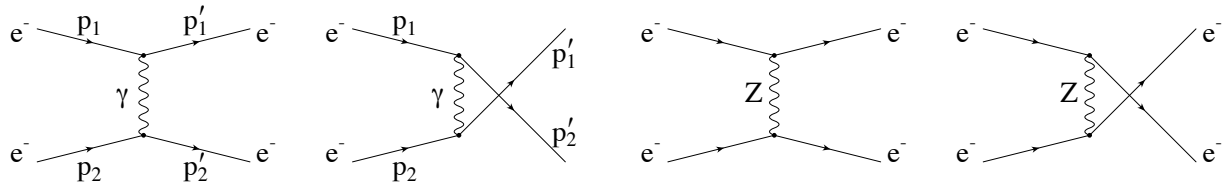

Figure 1: *Feynman diagrams for Møller scattering at tree level (reproduced from Ref. [9])*

The leading order Feynman diagrams relevant for Møller scattering, involving both direct and exchange diagrams that interfere with each other, are shown in Fig. 1. The total unpolarized cross section, dominated by 1-photon exchange, is given by

$$\frac{d\sigma}{d\Omega} = \frac{\alpha^2}{2mE}\frac{(3+\cos^2\theta)^2}{\sin^4\theta} = \frac{\alpha^2}{4mE}\frac{1+y^4+(1-y)^4}{y^2(1-y)^2}, \tag{2}$$

where α is the fine structure constant, E is the incident beam energy, m is the electron mass, θ is the scattering angle in the center of mass frame, $y \equiv 1 - E'/E$ and E' is the energy of one of the scattered electrons. The parity-violating asymmetry A_{PV}, due to the interference between the photon and Z^0 boson exchange diagrams in Fig. 1, is given by [7]

$$A_{PV} = mE\frac{G_F}{\sqrt{2}\pi\alpha}\frac{4\sin^2\theta}{(3+\cos^2\theta)^2}Q_W^e = mE\frac{G_F}{\sqrt{2}\pi\alpha}\frac{2y(1-y)}{1+y^4+(1-y)^4}Q_W^e \tag{3}$$

where Q_W^e (proportional to the product of the electron's vector and axial-vector couplings to the Z^0 boson) is the weak charge of the electron. The electroweak theory prediction at tree level in terms of the weak mixing angle is $Q_W^e = 1 - 4\sin^2\theta_W$; this is modified at the 1-loop level [8, 9, 10] and becomes dependent on the energy scale at which the measurement is carried out, *i.e.* $\sin^2\theta_W$ "runs". It increases by approximately 3% compared to its value at the scale of the Z^0 boson mass, M_Z; this and other radiative corrections reduce Q_W^e to 0.0435, a $\sim 42\%$ change of its tree level value of ~ 0.075 (when evaluated at M_Z).

The prediction for A_{PV} for the proposed experimental design is ≈ 33 parts per billion (ppb) and our goal is to measure this quantity with a statistical precision of 0.7 ppb and thus achieve a 2.4% measurement

of Q_W^e. The reduction in the numerical value of Q_W^e due to radiative corrections leads to increased fractional accuracy in the determination of the weak mixing angle, $\sim 0.1\%$, matching the precision of the single best such determination from measurements of asymmetries in Z^0 decays in the e^+e^- colliders LEP and SLC.

2 Physics Motivation

In this section we elaborate on the primary motivation bullets itemized in the introduction, with examples derived from the literature, especially recent reviews [11, 12, 13]. An important point to note is that, at the proposed level of measurement accuracy of A_{PV}, the Standard Model (SM) prediction must be carried out with full treatment of one-loop radiative corrections and leading two-loop corrections. The "hard" radiative corrections, involving the massive vector bosons at the loop level, modify the tree-level prediction quite significantly and have been extensively studied [8, 9, 10, 14, 15]. The dominant effect comes from the "$\gamma - Z$ mixing" diagrams depicted in Fig. 2 [9].

An important development for MOLLER was the reduction in the theoretical error from extrapolation to the low Q^2 [10]; it is now a factor of five smaller than the proposed MOLLER A_{PV} statistical error, and has been recently verified specifically for MOLLER kinematics [14]. There is an ongoing effort to investigate several classes of diagrams beyond one-loop [16, 17, 18], and a plan has been formulated to evaluate the complete set of two-loop corrections at MOLLER kinematics by 2016; such corrections are estimated to be already smaller than the MOLLER statistical error. A Monte Carlo generator based on the most current work on one- and two-loop effects will be developed in a collaborative effort involving both experimentalists and theorists, taking into account detailed kinematic acceptance of the final apparatus including other Q^2 and $y-$dependent terms [14].

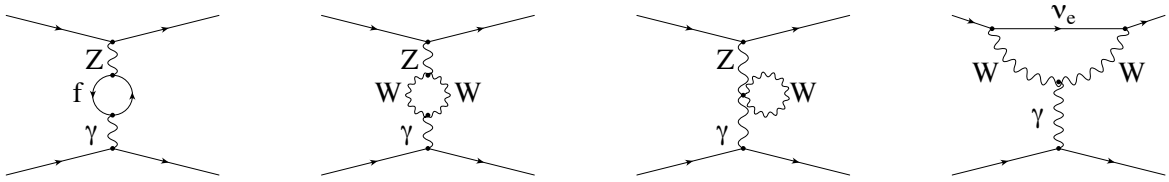

Figure 2: *$\gamma-Z$ mixing diagrams and W-loop contribution to the anapole moment (reproduced from Ref. [9])*

The fact that the proposed measurement provides such a sensitive probe of TeV-scale dynamics beyond the SM (BSM) is a consequence of a very precise experimental goal ($\sim 10^{-3} \bullet G_F$), the energy scale of the reaction ($Q^2 \ll M_Z^2$), and the ability within the electroweak theory to provide quantitative predictions with negligible theoretical uncertainty. The proposed measurement is likely the only practical way, using a purely leptonic scattering amplitude at $Q^2 \ll M_Z^2$, to make discoveries in important regions of BSM space in the foreseeable future at any existing or planned facility worldwide.

2.1 The Weak Mixing Angle $\sin^2\theta_W$ at $Q^2 \ll M_Z^2$

The weak mixing angle $\sin^2\theta_W$ has played a central role in the development and validation of the electroweak theory, especially testing it at the quantum loop level, which has been the central focus of precision electroweak physics over the past couple of decades. To develop the framework, one starts with three fundamental experimental inputs characterizing, respectively, the strength of electroweak interactions, the scale of the weak interactions, and the level of photon-Z^0 boson mixing. The three fundamental inputs are chosen to be α (from the Rydberg constant), G_F (from the muon lifetime) and M_Z (from the LEP Z^0 line-shape).

Precise theoretical predictions for other experimental observables at the quantum-loop level can be made if experimental constraints on the strong coupling constant and heavy particle masses, such as m_H and the top quark mass, m_t, are also included.

Precision measurements of the derived parameters such as the W boson mass M_W, and the weak mixing angle $\sin^2\theta_W$ are then used to test the theory at the level of electroweak radiative corrections. Consistency (or lack thereof) of various precision measurements can then be used to search for indications of BSM physics. One important new development is the discovery of the scalar resonance at LHC with mass of about 126 GeV. Each individual observable used to extract values for M_W and $\sin^2\theta_W$ can now be precisely predicted within the SM context.

A crucially important additional feature of MOLLER A_{PV} is that the measurement will be carried out at $Q^2 \ll M_Z^2$. The two best measurements of the weak mixing angle at lower energies are those extracted from the aforementioned SLAC E158 measurement [1], and the measurement of the weak charge of ^{133}Cs [19] via studies of table-top atomic parity violation. The interpretation of the latter measurement in terms of an extraction of the weak mixing angle has been recently updated [20]. A precise measurement of the weak charge of the proton is expected from the JLab Qweak experiment via the measurement of A_{PV} in elastic electron proton scattering; the first result from the commissioning run was recently published [21].

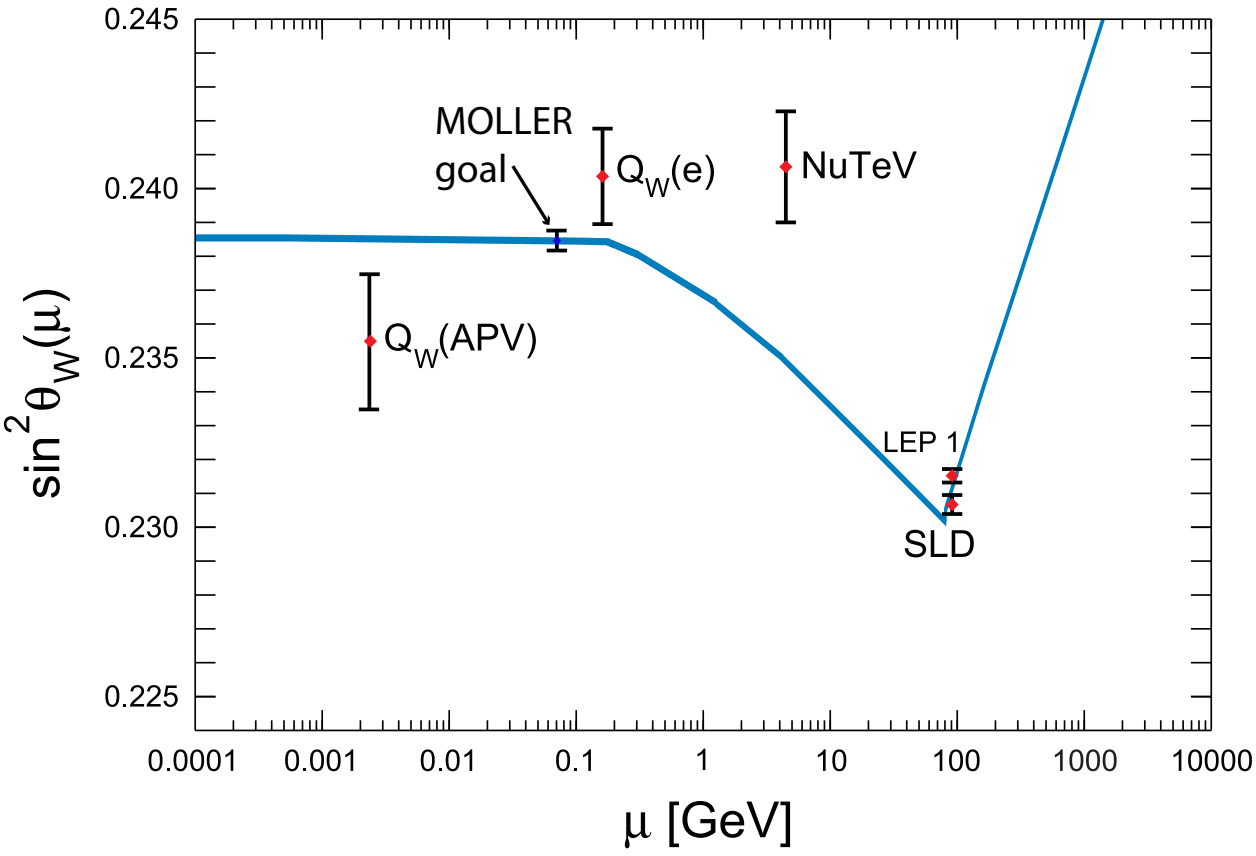

Figure 3: *The three most precise measurements of the weak mixing angle measurements vs. the energy scale μ are shown as red diamonds with error bars; the curve is reproduced from the PDG [22]. The APV result reflects the reanalysis in Ref. [20]. The $Q_W(e)$ point is the E158 result [1]. The NuTeV point is the extracted value from the original publication result [23]. The proposed MOLLER measurement is shown at the appropriate μ value and the proposed error bar but with the nominal SM prediction as the central value.*

Since $\sin^2\theta_W$ "runs" as a function of Q^2 due to electroweak radiative corrections, one can use $\sin^2\theta_W$ as a bookkeeping parameter to compare the consistency of the full Q^2 range of weak neutral current measurements, as shown in Fig. 3. The theory error in the low energy extrapolation is comparable to the width of the line in the figure [10]. MOLLER A_{PV} would be the first low Q^2 measurement to match the precision of the single best high energy measurement at the Z^0 resonance. As discussed previously and also further elaborated in the following with additional examples, low energy measurements have enhanced sensitivity to new physics. MOLLER will build on the pioneering low Q^2 measurements shown in the figure to extend the discovery reach for new physics not only to the multi-TeV scale but also, as we show in the following, to light new degrees of freedom.

Figure 4 shows the dependence of $\sin^2\theta_W$ to m_H and the two best published low energy measurements (evolved to $Q \sim M_Z$) discussed above, as well as the projected A_{PV} error. Remarkably, a variety of BSM dynamics, such as those discussed in previous sections, can have a significant impact on low Q^2 observables while having much reduced impact on corresponding measurements made at colliders. This is because interference effects are highly suppressed on top of the Z^0 resonance; those measurements account for the bulk of the statistical weight in high energy grand averages. Since the low energy measurements at the moment span the entire y-axis range in Fig. 4, there is still plenty of room for new physics effects to be discovered at low energy given the proposed MOLLER A_{PV} uncertainty.

Figure 5 shows the four best measurements of $\sin^2\theta_W$ from studies of Z^0 decays [24] and the projected uncertainty from MOLLER A_{PV}. Also shown is the Standard Model prediction for $m_H = 126$ GeV. The bottom two point are the constraints from the most precise single determinations of $\sin^2\theta_W$: the left-right asymmetry in Z production at SLC (A_l(SLD)) and the forward-backward asymmetry in Z decays to b-quarks ($A_{fb}^{0,b}$). Each of the two measurements taken independently implies very different BSM dynamics [25].

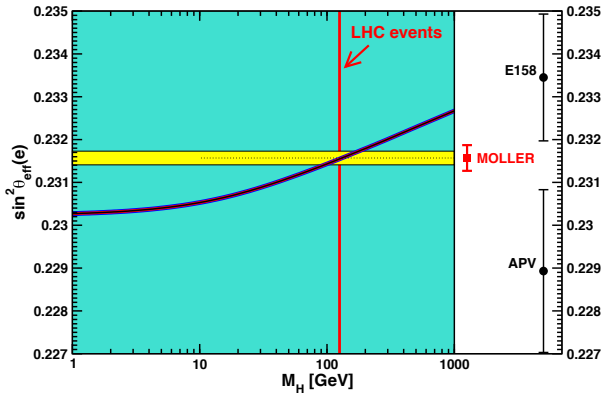

Figure 4: $\sin^2\theta_W$ *vs* m_H. *The yellow band is the world average. The black points are the two most precise measurements at* $Q^2 \ll M_Z^2$. *The projected MOLLER error is shown in red.*

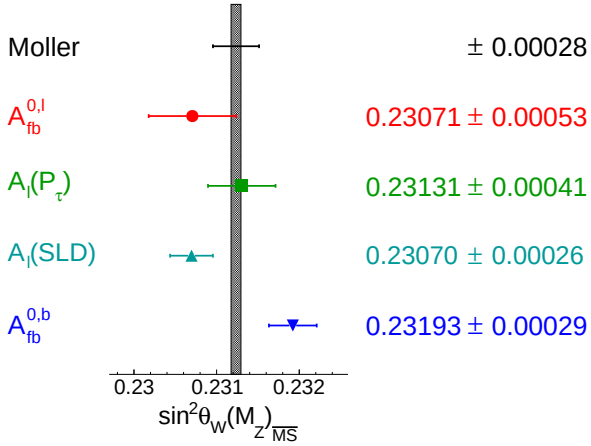

Figure 5: *The four best* $\sin^2\theta_W$ *measurements and the projected error of the MOLLER proposal. The black band represents the theoretical prediction for* $m_H = 126$ *GeV.*

2.2 The Weak Charge of the Electron and BSM Physics

Employing the very precisely measured values of α, G_F, and m_Z along with m_t and $m_H = 126$ GeV in the one-loop corrected SM, but allowing for very heavy new particle loop effects via the electroweak precision

S and T parameters [26, 27], the precision measurements of m_W and $\sin^2\theta_W$ yield $S = 0.07 \pm 0.09$ and $T = 0.10 \pm 0.09$ [11], which can be used to significantly constrain models such as Technicolor or the properties of 4th generation fermions. Similarly, the weak charges of particles and nuclei (defined at the static limit, E and $Q^2 \to 0$) are precisely predicted at the loop level [28].

However, as we have seen in previous discussions about low Q^2 observables, in addition to S and T, deviations in weak charge values can be induced by BSM physics in other ways. To illustrate relative sensitivities, we consider the Z_χ model of $SO(10)$ that violates parity in a well-specified manner [27, 29]. Other effects can be parametrized by $X(Q^2) \equiv \alpha^{-1}(\sin^2\theta_W(Q^2) - \sin^2\theta_W(M_Z^2)$ to account for differences induced by BSM physics between low Q^2 and high energy $\sin^2\theta_W$ measurements beyond SM running effects. $X(Q^2)$ is similar to S, but is allowed to vary with Q^2 [30, 8]. For heavy particle loops (eg. SUSY or heavy fermions [31]) with a generic mass scale M where $X(Q^2) \sim \mathcal{O}(\alpha Q^2/M^2)$, X is already well constrained by the bounds on S from W and Z measurements. However, for very light new physics like the MeV-scale "dark" boson with mass m_{Z_d} that we will discuss in the next subsection [32, 33], $X(Q^2)$ terms can occur that are only visible in low $Q^2 \lesssim m_{Z_d}^2$ experiments.

Given these new physics scenarios, one finds the following shifts in the weak charges [27, 8, 34]

$$\begin{aligned}
Q_W^e &= -0.0435(9)[1 + 0.25\,T - 0.34\,S + 0.7\,X(Q^2) + 7m_Z^2/m_{Z_\chi}^2], \\
Q_W^p &= 0.0707(9)[1 + 0.15\,T - 0.21\,S + 0.43\,X(Q^2) + 4.3m_Z^2/m_{Z_\chi}^2], \\
Q_W(^{12}C) &= -5.510(5)[1 - 0.003\,T + 0.016\,S - 0.033\,X(Q^2) - m_Z^2/m_{Z_\chi}^2], \\
Q_W(^{133}Cs) &= -73.24(5)[1 + 0.011\,S - 0.023\,X(Q^2) - 0.9m_Z^2/m_{Z_\chi}^2],
\end{aligned} \tag{4}$$

(reproduced from Ref. [11]) where the uncertainties have been somewhat expanded to account for as yet uncalculated higher order effects. It is apparent that the large $\sim 40\%$ radiative corrections to Q_W^e improve its fractional sensitivity to new physics relative to Q_W^p. That makes MOLLER A_{PV} better from a systematic (such as polarization) perspective, but statistically similar in difficulty to A_{PV} in elastic electron-proton scattering: many BSM models tend to predict equal contributions to electron and proton weak charges, and in such cases $\delta(Q_W^e) \sim \pm 2\%$ is roughly equivalent to $\delta(Q_W^p) \sim \pm 1\%$. One must measure the nuclear weak charges to 0.3% or better to compete at the same level. Assuming such sensitivity can be reached (MOLLER would be the first to reach the required level), such measurements probe S and T well below ± 0.1. They are about twice as sensitive to $X(Q^2)$ as S, and probe $m_{Z_\chi} \sim 2$ TeV.

2.3 The Dark Z

Some recent BSM models have relatively light new degrees of freedom which cannot be incorporated into the contact interaction formalism. Absence of such BSM-induced deviations in high energy measurements implies that such light particles must couple very weakly. In certain regions of parameter space, low Q^2 measurements can have unique or enhanced sensitivity. In this context, the possibility of a "dark" Z boson [32, 33], denoted as Z_d and of mass m_{Z_d}, stemming from a spontaneously broken $U(1)_d$ gauge symmetry associated with a secluded "dark" particle sector was recently investigated. The Z_d boson can couple to SM particles through a combination of kinetic and mass mixing with the photon and the Z^0-boson, with couplings ε and $\varepsilon_Z = \frac{m_{Z_d}}{m_Z}\delta$ respectively.

This kinetic mixing scenario was conjectured [35, 36, 37, 38] to explain astrophysical observables as well as to account for the long standing deviation of the muon's anomalous magnetic moment, $(g-2)_\mu$, from SM expectations [39]. Taking into account various experimental constraints, the a_μ discrepancy is naturally accommodated by kinetic mixing in the range (assuming the branching ratio for $Z_d \to e^+e^- \sim 1$):

$$|\varepsilon| \simeq 2 \times 10^{-3} \qquad 20\ \text{MeV} \lesssim m_{Z_d} \lesssim 50\ \text{MeV}. \tag{5}$$

In the presence of mass mixing ($\delta \neq 0$), a new source of "dark" parity violation arises [32] such that it has negligible effect on other precision electroweak observables at high energy, but is quite discernable at low Q^2 through a shift in the weak mixing angle [33]:

$$\Delta \sin^2\theta_W(Q^2) \simeq -0.42\varepsilon\delta\frac{m_Z}{m_{Z_d}}\left(\frac{m_{Z_d}^2}{Q^2+m_{Z_d}^2}\right). \tag{6}$$

In this scenario, the small (1.5σ) APV deviation, $\Delta \sin^2\theta_W(0) \simeq -0.003(2)$ suggests $\delta \simeq \pm 1 - 4\times 10^{-3}$ as a potentially interesting region that can be explored by future APV or A_{PV} measurements.

One can relate this to the discussion in the previous section by inspecting the sensitivity of $X(Q^2)$ ($\Delta(X) \sim \Delta(\sin^2\theta_W)/\alpha$) to $m_{Z_d} \sim 20-50$ MeV. APV measurements where Q^2 is naturally small ($Q^2 \ll m_{Z_d}^2$) are excellent probes because they do not have the $m_{Z_d}^2/(Q^2+m_{Z_d}^2)$ suppression. However, because the coupling values are small to begin with, Q_W^e and Q_W^p are far more sensitive to a non-zero $X(Q^2)$ value. For example, the $-0.9\pm 0.6\%$ shift in the APV Cs result would lead to a 27% shift in Q_W^e if measured at the same Q. For $m_{Z_d} \sim 50$ MeV, the MOLLER A_{PV} with $Q \sim 75$ MeV, would see an 8.4% shift ($\sim 3.7\sigma$).

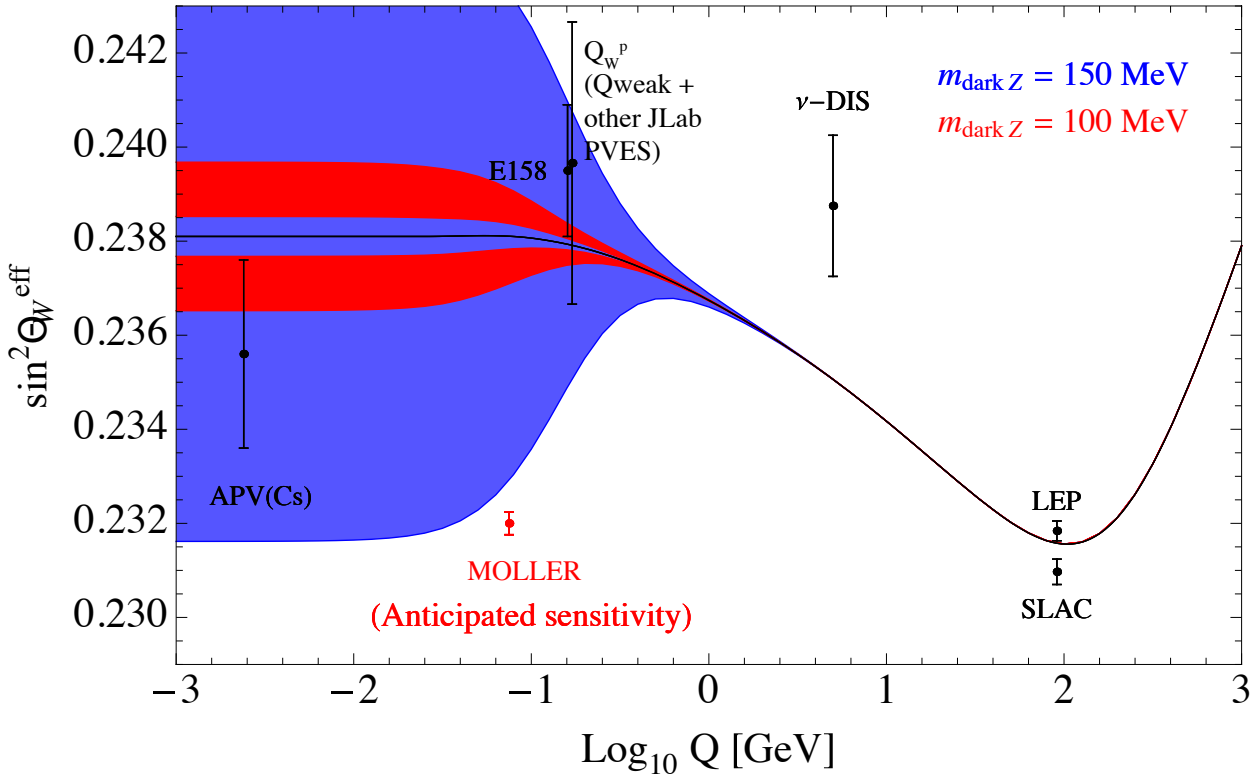

Figure 6: *The potential deviations of* $\sin^2\theta_W(Q)$ *under the scenario of small parity-violating admixture of a light* Z_d *to explain the* $(g-2)_\mu$ *anomaly is shown for two different masses, taking into account rare kaon decay constraints. Also shown is the extracted* $\sin^2\theta_W$ *from the value of the weak charge of the proton* Q_W^p *quoted in the recently published Qweak result from the commissioning run [21]. The proposed MOLLER measurement is shown at the appropriate* Q *value and the proposed error bar but with an arbitrary central value. Note: the sign of the deviation is model-dependent.*

Recently, it has been pointed out [40] that the constraints in Eqn. 5 are considerably weakened if the "dark" Z decays to other dark matter particles, rendering the branching ratio $Z_d \to e^+e^- \ll 1$. In such a

scenario, the only constraints on Z_d masses in the range between 50 and 200 MeV would come from neutral current parity-violation measurements (sensitive to $X(Q^2)$) and rare kaon decay experiments ($K \to \pi + Z_d$, $Z_d \to$ missing energy). Figure 6 shows the range of possible deviations to $\sin^2\theta_W(Q)$ for Z_d mass of 100 and 150 MeV, under the scenario that the "dark" Z explains the $(g-2)_\mu$ anomaly, but taking into account constraints from the K decay measurements. It can be seen that the proposed MOLLER A_{PV} measurement has significant discovery potential under this scenario.

2.4 Contact Interactions from BSM High Energy Dynamics

A fairly general and model-independent way to quantify the effects of large classes of BSM high-energy dynamics in low-energy processes is to express the resulting new amplitudes at low energies in terms of contact interactions (6-D non-renormalizable operators) among leptons and quarks. Specializing here to vector and axial-vector interactions between electrons and/or positrons, such an interaction Lagrangian takes the form [41]:

$$\mathcal{L}_{\mathrm{e_1e_2}} = \sum_{i,j=L,R} \frac{g_{ij}^2}{2\Lambda^2} \bar{e}_i \gamma_\mu e_i \bar{e}_j \gamma^\mu e_j, \tag{7}$$

where $e_{L/R} = \frac{1}{2}(1 \mp \gamma_5)\psi_e$ are the usual chirality projections of the electron spinor, Λ is the mass scale of the contact interaction, $g_{ij} = g_{ij}^*$ are coupling constants, and $g_{RL} = g_{LR}$.

For the MOLLER A_{PV} measurement with 2.4% total uncertainty (and no additional theoretical uncertainty) the resulting sensitivity to new 4-electron contact interaction amplitudes can be expressed as:

$$\frac{\Lambda}{\sqrt{|g_{RR}^2 - g_{LL}^2|}} = \frac{1}{\sqrt{\sqrt{2}G_F|\Delta Q_W^e|}} \simeq \frac{246.22\ \mathrm{GeV}}{\sqrt{0.023 Q_W^e}} = 7.5\ \mathrm{TeV}. \tag{8}$$

For example, models of lepton compositeness are characterized by strong coupling dynamics. Taking $\sqrt{|g_{RR}^2 - g_{LL}^2|} = 2\pi$ shows that mass scales as large as $\Lambda = 47$ TeV can be probed, far beyond the center of mass energies of any current or planned high energy accelerator. This allows electron substructure to be studied down to the level of 4×10^{-21} m.

The best current limits on contact interaction scales come from the high-energy collider data of LEP 2, Tevatron and the LHC, where the latter is sensitive to new interactions involving quarks. The strongest constraints on the coefficients in Eqn. (7) come from LEP 2. We emphasize, however, that the parity-conserving cross-sections and forward-backward asymmetries studied at LEP 2 are only sensitive to g_{RL}^2 and the combination $g_{RR}^2 + g_{LL}^2$. Making the additional assumption that the former (latter) is vanishing, the combination of all four LEP 2 experiments corresponds to sensitivities of $\Lambda/\sqrt{g_{RR}^2 + g_{LL}^2} = 4.4$ TeV ($\Lambda/g_{RL} = 5.2$ TeV), while LEP 2 is blind to the parity-violating combination $g_{RR}^2 - g_{LL}^2$ probed by A_{PV}.

Thus, the proposed measurement would greatly extend the current sensitivity of 4-electron contact interactions[1]. If a deviation is established, there would be new urgency for targeted searches, especially of parity-violating observables, at a future lepton collider. On the other hand, if agreement with the theoretical prediction is established at this new level of sensitivity, it would help establish a new benchmark for future collider searches as well as for low-Q^2 leptonic and semi-leptonic observables. Using Eqn. (8), it is also straightforward to examine the reach in specific models, and compare the sensitivity to other low-energy precision electroweak observables [42, 43]. We discuss a few examples in the following.

[1] Our proposed measurement is also complementary to new physics searches via the Electric Dipole Moment (EDM) of the electron which is modified only if the new interactions violate CP symmetry.

2.4.1 Doubly-Charged Scalars

With the discovery at LHC of a new resonance that exhibits all the characteristics of an elementary scalar, it is now important to search for additional scalars in Nature. The proposed measurement is one of the rare low Q^2 observables with sensitivity to doubly charged scalars, that naturally arise in extended Higgs sector models containing complex triplet representations of SU(2). The left-right symmetric model, for example, contains two such triplets – Δ_L and Δ_R – that transform under $\mathrm{SU}(2)_L$ and $\mathrm{SU}(2)_R$ respectively. The doubly-charged components of both triplets, $\delta^{++}_{L,R}$ can couple to two charged leptons:

$$\mathcal{L}^{\delta^{++}}_{\mathrm{matter}} \sim h^{ij}_L \, \delta^{++}_L \bar{\ell}^C_i P_L \ell_j + h^{ij}_R \, \delta^{++}_R \bar{\ell}^C_i P_R \ell_j + \mathrm{h.c.} \tag{9}$$

where ℓ_i denotes a charged lepton of generation i. The Møller scattering process is unique among lepton scattering observables to be sensitive to the $s-$channel exchange 4-electron amplitude that violates lepton number by 2 units (two analogous expressions LL and RR):

$$\mathcal{M}^{\mathrm{PV}} \sim \frac{|h^{ee}_L|^2}{2M^2_{\delta_L}} \bar{e_L} \gamma_\mu e_L \bar{e_L} \gamma^\mu e_L \ . \tag{10}$$

Gauge and matter interactions involving the $\delta^{++}_{L,R}$'s can also lead to contributions to neutrinoless double-beta decay processes and charged lepton flavor violating processes such as $\mu \to e$ conversion [44]. In general, these processes can put severe limits on these possible new amplitudes, but in the latter case only in models predicting unsuppressed off-diagonal charged lepton couplings $h^{\mu e}_{L,R}$. Neutrinoless double-beta decay gives much weaker constraints for the Δ_L triplet because its vacuum expectation value is constrained to be smaller than a few GeV from electroweak precision data (the ρ parameter).

The amplitude in Eqn. (10) shows that the Δ_L model is equivalent to a contact interaction with $\Lambda = M_{\delta_L}$, $|g^2_{LL}| = |h^{ee}_L|^2/2$, and $g_{RR} = g_{LR} = 0$. The proposed A_{PV} measurement would therefore lead to the most stringent probe of the left-handed charged scalar and its coupling to electrons, with a reach of

$$\frac{M_{\delta_L}}{|h^{ee}_L|} \sim 5.3 \text{ TeV},$$

significantly above the LEP 2 constraint of about 3 TeV.

2.4.2 Heavy Z′ Bosons

Many BSM theories predict the existence of new, super-massive Z' bosons with masses in the multi-TeV range. The absence of new dilepton resonances in the recent LHC 8 TeV data has been used to improve model-dependent 95% C.L. limits for Z' masses up to 2–2.5 TeV. The anticipated 13 and 14 TeV runs in 2015 and beyond are expected to have a mass reach up to 5 TeV, which is currently unexplored by any direct or indirect measurement. However, extracting the detailed properties of the Z' such as its width, chiral couplings to SM fermions etc. will be difficult for $M_{Z'} \gtrsim 3$ TeV. Should a new Z' in the 1-3 TeV range be discovered soon after the onset of 13 TeV running, good discrimination between various models will becomes possible with a large integrated luminosity sample ($\gtrsim 100 \text{ fb}^{-1}$, see for example [45]).

The MOLLER A_{PV} measurement would see a a statistically significant deviation in many models that predict Z' bosons in the 1–3 TeV mass range. The sensitivity can be analyzed in the context of the contact interaction discussion in Sec. 2.4. One can identify the chiral Z' couplings times $U(1)'$ charges to right-handed and left-handed electrons with g^2_{RR} and g^2_{LL}, and one also identify Λ with the Z' mass, $M_{Z'}$. In the future, as new LHC running at high energies increases sensitivity to larger $M_{Z'}$'s and weaker couplings, the proposed A_{PV} measurement will continue to be an important complementary input to a comprehensive search, as we demonstrate with the following example.

We consider a specific case derived from a recent comprehensive analysis of the sensitivity both low and high energy measurements to TeV-scale Z's [46] for a fairly large class of family-universal models contained in the E_6 gauge group. The Z' associated with the remnant $U(1)'$ contains two free parameters that can be tuned to maximize the effect on A_{PV} for Møller scattering, with the sign compatible with the observed 1.3σ deviation of the E158 result i.e. a numerically smaller Q_W^e than that predicted by the Standard Model. In this scenario, we obtain

$$g_{RR}^2 - g_{LL}^2 = -\frac{10\pi\alpha}{3\cos^2\theta_W} \approx -(0.33)^2.$$

This can be compared to a common point in the parameter space like the Z_χ boson, where the corresponding number is about $+(0.2)^2$. For the special case in the equation above, A_{PV} probes $M_{Z'} = 0.33 \times 7.5 \approx 2.5$ TeV, comparable to the anticipated reach of early LHC running after the energy ramp-up to 13 TeV. Additionally, it should be noted that indirect deviations scale linearly with coupling strength whereas dilepton production at colliders is relatively insensitive to this parameter. Thus, the reach of A_{PV} would be further enhanced in comparison to direct searches if one relaxes the model-dependent assumption of GUT coupling strength.

Should a new resonance in the 1–3 TeV range be found relatively quickly after the resumption of LHC running, the importance of off-peak LHC data as well as low-energy precision EW data to completely disentangle all of the chiral Z' couplings to SM particles has been emphasized [47]. The impact of new constraints from the proposed A_{PV} measurement and a very large integrated luminosity LHC data sample ($1\ \mathrm{ab}^{-1}$) was demonstrated explicitly for the Z_χ and Z_{LR} models. It was found that MOLLER would provide an important constraint such that a combined analysis with LHC data would allow for an independent determination of the left- and right-handed leptonic Z' couplings and make it thus possible to distinguish between models.

2.5 Supersymmetry

At the level of sensitivity probed, the MOLLER A_{PV} could be influenced by radiative loop effects of new particles predicted by the Minimal Supersymmetric Standard Model (MSSM). The impact on the weak charges of the electron and the proton $Q_W^{e,p}$ have been analyzed in detail [31]. A combined analysis of precision low energy measurements of both charged and neutral current processes can be found in a comprehensive review [48], which has been recently updated to include LHC data [13]. Inspecting a random scan over a set of MSSM parameters whose values are consistent with current precision measurements as well as the most recent LHC search limits from 7 and 8 TeV running, A_{PV} would see deviations in the range of 2σ and 3σ at larger values of the MSSM parameter $\tan\beta$ (the ratio of vacuum expectation values of the model's two Higgs scalars) or if one of the superpartner masses is relatively light, as would be the case if the super-partner masses were nearly degenerate. This scenario is still quite plausible since LHC signatures in such a situation are very challenging to disentangle from QCD backgrounds.

Alternatively, if the assumption of R-parity conservation (RPC) is relaxed, tree-level interactions could generate deviations in A_{PV} of opposite sign and similar magnitude. It should be emphasized that if Nature is indeed supersymmetric, the sign of the relative shift in the extracted Q_W^e would, if large enough, distinguish between RPC and R-parity violating (RPV) versions of SUSY. The difference is not academic, since RPC would imply that the lightest supersymmetric particle is stable and therefore an obvious candidate for the non-baryonic dark matter which is needed to understand galactic-scale dynamics. On the other hand, RPV would imply that neutrinos are Majorana particles.

3 Experimental Design

A CAD-generated rendition of the layout of the MOLLER apparatus to be placed in Hall A at JLab is shown in Fig. 7. In this section, we provide an overview of the experimental design and discuss the main

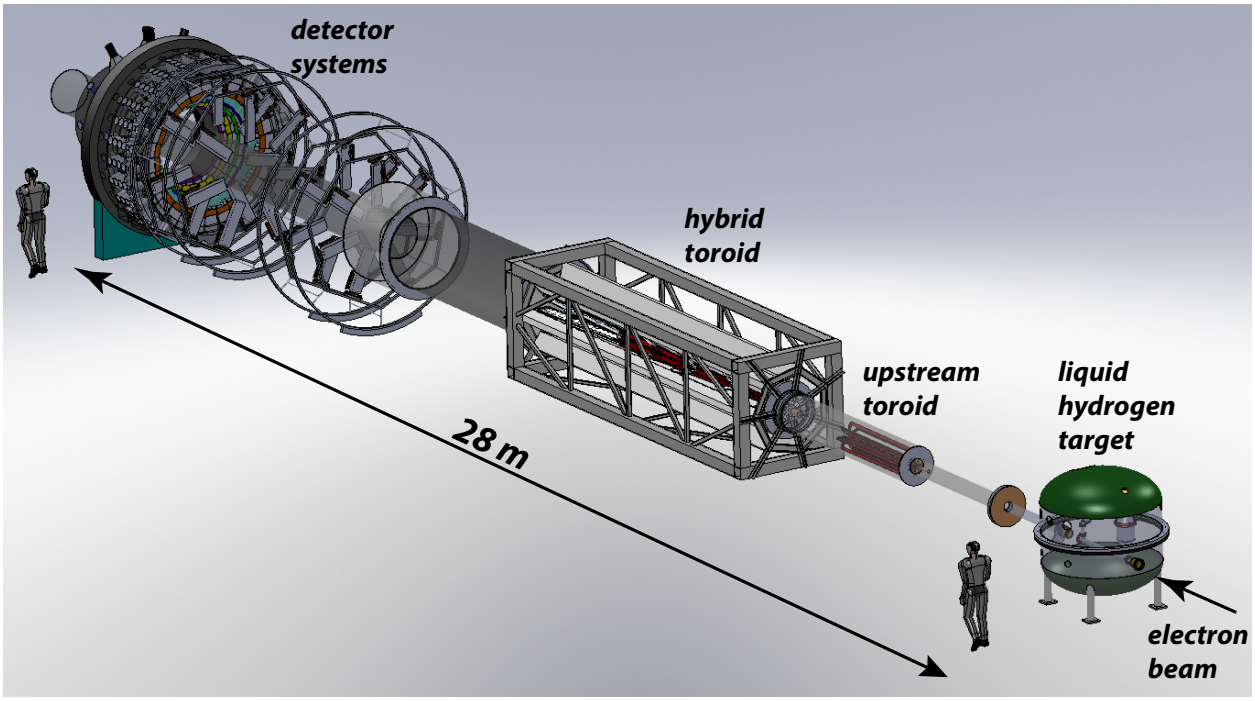

Figure 7: *Layout of the target, spectrometer and detectors.*

subsystems. We start by listing the main experimental parameters in Table 1. Many of the technical choices are driven by the requirement to measure a very small parity-violating asymmetry, and consequently the need to measure the scattered electron flux at an unprecedentedly high rate. The MOLLER design is grounded on the extensive experience gained by the collaboration from completed high flux integrating (as opposed to counting individual particles) parity-violation measurements such as MIT-Bates ^{12}C [49], SAMPLE [50], HAPPEX [51] and SLAC E158 [1] as well as ongoing projects such as PREX [52] and Qweak [53].

3.1 Polarized Beam

MOLLER will use the 11 GeV beam that becomes available in Hall A after completion of the energy upgrade. Fixed target Møller scattering is rather special because the QED cross-section is proportional to $1/E_{\rm beam}$, and the figure of merit for A_{PV} rises linearly with beam energy. The projections for MOLLER are made assuming a 11 GeV, 75 μA electron beam with the anticipated stable beam conditions extrapolated from the extensive experience on "parity quality" beams from the 6 GeV experiments. The upgraded JLab beam is thus a unique opportunity to carry out the proposed MOLLER measurement; indeed these conditions are unavailable in any other currently running or planned accelerator facility worldwide.

The polarized electron beam is created using a technology first developed at SLAC to enable the original parity-violating electron scattering experiment [54]: laser-induced photoemission from a GaAs wafer. The circular polarization of the laser light, controlled by the polarity of the voltage across a Pockels cell [2], determines the sign of the longitudinal polarization of the emitted electron bunch, thus facilitating rapid helicity reversal of the electron beam. Time "windows" are generated in the electron bunch train at a frequency of 1.92 kHz, with the sign of the beam's longitudinal polarization in each window assigned on a

[2]The Pockels cell is a birefringent crystal whose phase retardation is directly proportional to the applied potential difference; $\sim \pm 2.5$ kV is required to produce $\pm\pi/4$ retardation for a wavelength of ~ 800 nm.

Table 1: *Nominal design parameters for the proposed A_{PV} measurement. Note that some of the design parameters will change at the few percent level as the design is further optimized.*

Parameter	Value
E [GeV]	≈ 11.0
E' [GeV]	1.7 - 8.5
θ_{cm}	46°-127°
θ_{lab}	0.23°-1.1°
$< Q^2 >$ [GeV^2]	0.0058
Maximum Current [μA]	85
Target Length (cm)	150
ρ_{tgt} [g/cm^3] (T= 20K, P = 35 psia)	0.0715
Max. Luminosity [cm^{-2} sec^{-1}]	3.4·10^{39}
σ [μBarn]	≈ 40
Møller Rate [GHz]	≈ 140
Statistical Width(2 kHz flip) [ppm/pair]	≈ 83
Target Raster Size [mm]	5 x 5
ΔA_{raw} [ppb]	≈ 0.6
Background Fraction	≈ 0.09
P_{beam}	$\approx 85\%$
$< A_{pv} >$ [ppb]	≈ 35
$\Delta A_{stat} / < A_{expt} >$	2.0%
$\delta(\sin^2\theta_W)_{stat}$	0.00023

pseudo-random basis (with a set pattern of 32 windows optimized to eliminate 60 Hz noise). The design of the apparatus is based on a maximum beam intensity of 85 μA.

Nearby time windows of opposite helicity form window-pairs. The time-averaged responses of beam position monitors characterize the beam trajectory and energy for each window. The monitoring instrumentation has to be precise enough so that the relative cross section (except for statistical fluctuations) is stable over nearby time windows at the level one part in 10^5, after beam fluctuations are regressed out. Therefore, beam properties must be measured window by window with high precision and further, the variance of window pair differences must be small. Specifically, the beam centroid fluctuations must be tracked with precision at the level of a few microns, and should be stable to $\sim$10's of microns, at 1 kHz[3].

Averaged over the entire data collection period, the beam trajectory must remain unchanged with respect to the sign of the electron beam polarization at the sub-nanometer level in order to keep beam-related false asymmetry corrections at the 1 ppb level. It will be necessary to use a "slow reversal" of beam helicity to further cancel systematic errors to the 0.1 ppb level, from sources such as residual electronics cross-talk and higher-order effects such as potential helicity-dependent variations in the beam spot size. These considerations are discussed in Sec. 4.1 and in App. A.

3.2 Liquid Hydrogen Target

After acceleration to 11 GeV, the electron beam will impinge on a liquid hydrogen (LH_2) target. Hydrogen is the ideal source of target electrons for two reasons. First, it provides the greatest electron target thickness for

[3]This does not include 60 Hz noise, since data will be collected in time-slots phased to 60 Hz.

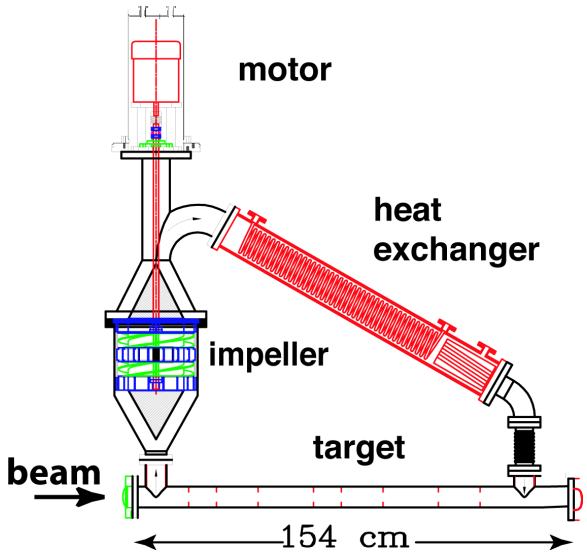

Figure 8: *The SLAC E158 target loop is shown; MOLLER proposes to use the same concept. Liquid flows clock-wise in the picture (downstream to upstream). The liquid-gas interface is just below the motor.*

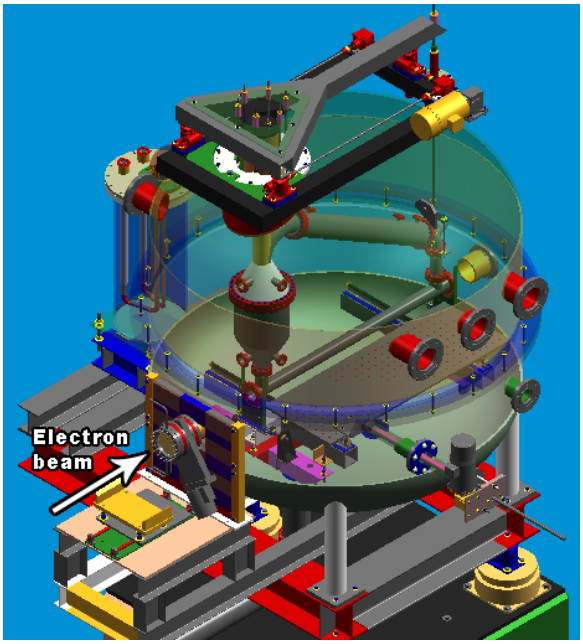

Figure 9: *A CAD drawing of the SLAC E158 target chamber. The target loop is remotely movable 6 in in the vertical direction. A table containing optics targets can be moved in and out horizontally.*

the least radiation length. Secondly, the irreducible backgrounds are confined to radiative electron-proton elastic and inelastic scattering, which are relatively well-understood. Scattering off other nuclei would include radiative elastic scattering ($\propto Z^2$), breakup channels and scattering off neutrons, which would introduce significant systematic errors due to unknown and potentially large electroweak couplings.

In order to achieve the necessary rate, more than 10 g/cm^2 of LH_2 is needed, making the target about 150 cm long, which in turn requires a cryogenic target system capable of handling a heat load of $\sim$ 5 kW from the beam. This is far larger than the typical $\sim$ 1 kW targets that are routinely in use and about twice as large as the recently commissioned target for the Qweak experiment.

The preliminary assessment is that the E158 target cell is a good starting point for the design of the high power target required for MOLLER. Figure 8 shows the E158 target loop containing the main target cell, impeller, hydrogen motor and heat exchanger. The hydrogen flowed against the beam direction. The target loop was housed in a scattering chamber (Fig. 9) which also contained a table with auxiliary targets, with the capability to move both remotely, the main target loop in the vertical and the table in the horizontal direction. The target chamber also serves as a secondary containment vessel for hydrogen, which satisfied a major safety concern for E158. The final design of the MOLLER target will make use of computational fluid dynamics (CFD), a key recent development which has been validated by the successful operation of the Qweak target.

Table 2 shows the main parameters of the target. From the physics point of view, the most important design consideration is suppression of density fluctuations at the timescale of the helicity flip rate, which can ruin the statistical reach of the flux integration technique. Preliminary estimates based on operational experience with the Qweak target suggest that density variation can be maintained at $\lesssim$ 26 ppm at 1.92 kHz, corresponding to 5% excess noise. A plan for adequate target cooling at the JLab site has been formulated. All the considerations raised in this subsection are discussed in detail in App. B.

Table 2: *Design parameters of the MOLLER Liquid Hydrogen Target*

Parameter	Value
nominal cell length [cm]	150
target thickness [gm/cm^2]	10.72
radiation length [%]	17.5
p [psia]	35
T [K]	20
target power [kW]	5

3.3 Toroidal Spectrometer

The experimental configuration downstream of the target is quite novel due to some remarkable features of the Møller scattering process. The topology of interest in the 2-electron system is in the vicinity of $\Theta_{COM} = 90^\circ$. However, the acceptance in the highly boosted laboratory frame is at extremely forward angles (θ_{lab} between 5 and 20 mrad) because the COM energy for a 11 GeV electron scattering from a target electron is 106 MeV. This implies that scattered electrons in the laboratory frame in the range $3 \lesssim E' \lesssim 8$ GeV must be selected, a very large fractional momentum bite.

In addition, the measurement needs as much rate as possible in the range of desired scattering angles (θ) and we must therefore accept scattered electrons over the full range of the azimuthal angle ϕ, which would make the rate of more than 140 GHz available. At this high rate, the only practical solution is to integrate the detector response of each window, eliminating dangerous dead-time systematics. This so-called flux-integration technique requires that Møller-scattered electrons be focused into a region otherwise free of background. All of the above considerations have led us to a unique solution involving two back-to-back sets of coils, one of them of conventional geometry (albeit long and quite skinny) while the other of quite novel geometry. Collimation is a very important issue in such a system.

3.3.1 Kinematical Considerations

In the COM frame, the maximum asymmetry, the minimum differential cross-section and the maximum figure of merit occurs at $\Theta_{COM} = 90^\circ$. A driving principle in the spectrometer design is to maximize acceptance for Møller scattering events in the full ϕ range and a large Θ range centered around $\Theta_{COM} = 90^\circ$. This implies accepting a significant fraction of forward ($\Theta_{COM} < 90^\circ$) and backward ($\Theta_{COM} > 90^\circ$) Møller-scattered electrons. A nice feature of Møller scattering is the energy-angle correlation: there is a one-to-one correspondence between Θ_{COM} and the laboratory frame scattered electron energy E'_{lab}. The energy-angle correlation also implies that there is a one-to-one correspondence between E'_{lab} and θ_{lab}. These features are depicted in the two plots on the left of Fig. 10.

The proposed design aims to accept *all* (forward and backward) Møller-scattered electrons in the range $60^\circ \lesssim \Theta_{COM} \lesssim 120^\circ$, which implies that one must accept scattered electrons over a wide range of momenta. Thus, θ_{lab} and E'_{lab} ranges for forward Møllers are roughly 5.5 to 9.5 mrad and 5.5 to 8.25 GeV respectively, and the corresponding ranges for backward Møllers are roughly 9.5 to 17 mrad and 2.75 to 5.5 GeV. This is depicted by the colored regions in the two plots on the left of Fig. 10.

We have found a way to get 100% azimuthal acceptance with a toroidal geometry which is specific to identical particle scattering. This is depicted in Fig. 10 on the right, which shows the primary acceptance collimator concept (situated 6 m downstream of the target along the beam axis). The idea is to accept both forward and backward Møllers in each ϕ bite, by accepting particles between $5.5 \lesssim \theta_{lab} \lesssim 19$ mrad.

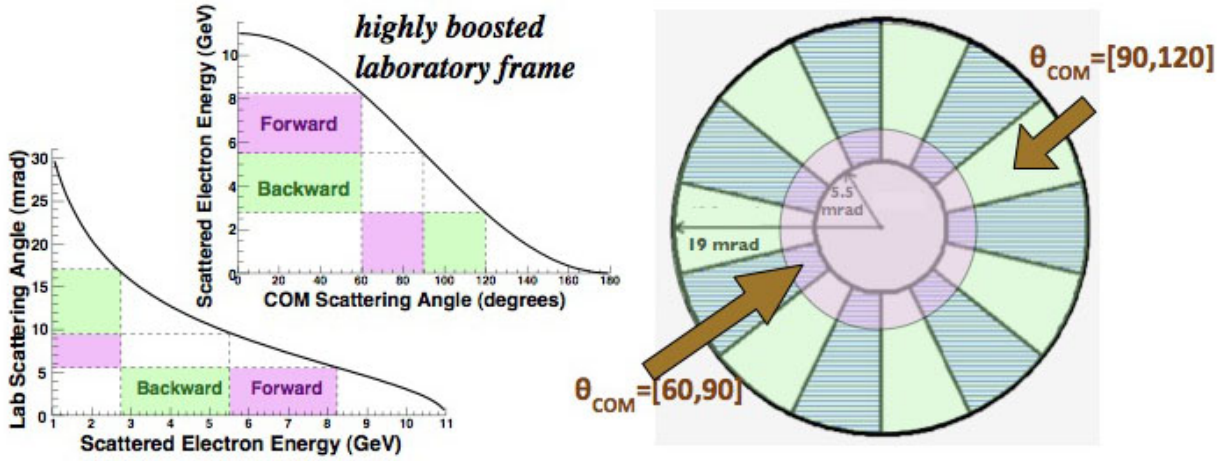

Figure 10: Θ_{COM} *vs* E'_{lab} *for* $E_{beam} = 11$ *GeV, and* E'_{lab} *vs* θ_{lab} *are depicted by the two plots on the left. On the right is shown the proposed concept for the primary acceptance collimator, which is able to achieve 100% acceptance with judiciously chosen* ϕ*-sectors.*

Since we are dealing with identical particles, those that are accepted in one ϕ bite also represent all the statistics available in the ϕ bite that is diametrically opposed ($180^\circ + \phi$). In the figure, each clear ϕ sector is diametrically opposed by a hatched region, which would be shielded from the target and can be used to house magnet coils without any loss of acceptance. The arrows point to regions that contain the two Møller electrons from the same events. In principle, any odd number of coils configured uniformly in ϕ would work; in the following, we describe our current design which contains 7 coils.

3.3.2 Conceptual Design

We itemize the principal requirements of the spectrometer/collimator system:

- Full azimuthal acceptance for Møller electrons in the momentum range between 3 and 8 GeV.
- Clean separation from the primary background of elastic and inelastic electron-proton scattering.
- Placement of detectors out of the line-of-sight of the target.
- Clean channel for the degraded beam and the bremsstrahlung photons to the beam dump.
- Minimization of soft photon backgrounds by designing a "two-bounce" system via judiciously placed collimators.

As discussed earlier, the selected Møller electrons represent a significant range in lab angle and energy and emerge from a very long (1.5 m) target. Minimizing background rates to an acceptable level requires bringing these very different trajectories, from a large region of phase space, into a tight radial focus separated from the majority of the principal backgrounds. The solution is a combination of two toroidal magnets which together act in a non-linear way on the charged particle trajectories. The first is a conventional toroid placed 6 m downstream of the target and the second, a novel hybrid toroid placed between 10 and 16 m downstream of the target. Each of the two toroidal fields is constructed out of seven identical coils uniformly spaced in the azimuth.

The action of the spectrometer can conceptually be divided into a radial and an azimuthal part. In the radial dimension, the successful interaction of the two magnets is key. The total $B \cdot d\ell$ of the first magnet is small and thus the effect on the high-energy, low-angle Mollers is small. More importantly, the lowest energy, highest angle Møller electrons are bent even further away from the beamline, allowing these particles to skirt the strongest field in the second magnet.

The hybrid toroid is in some sense the heart of the spectrometer concept. It is designed so that particles at different radial distances from the beam feel *very* different integral $Bd\ell$. This allows the hard, low angle Mollers to be bent strongly to the radial focal position while the soft, high angle particles are merely 'tickled' into place. This concept can best be seen in Fig. 11.

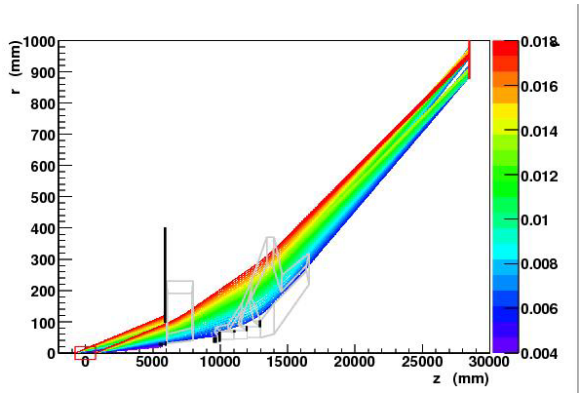

Figure 11: *Projected radial coordinate of scattered Møller electron trajectories. Colors represent θ_{lab} (rad). The spectrometer coils (grey) and collimators (black) are overlaid.*

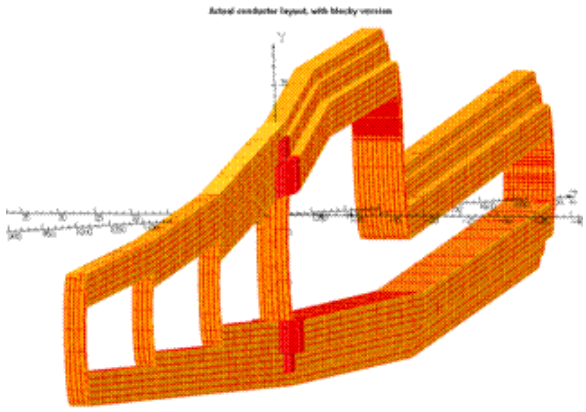

Figure 12: *Single hybrid coil with actual conductor layout, with 1/10 scale in the z direction.*

In the azimuthal dimension, the lower energy electrons are strongly defocussed by radial fields in the hybrid toroid and bend around into the regions behind the blocked portions of the primary acceptance collimator. By the time the electrons reach the detector plane 28.5 m from the target, the full range of azimuthal angles is populated by Møller electrons. The effect of this behavior is that the energy distribution of detected electrons changes along the azimuth. This azimuthal segmentation provides a variety of additional ways to understand the detector response, the modeling of the spectrometer optics and the estimates of the background fraction.

3.3.3 Hybrid Coil Design

In order to achieve the field configuration needed to focus the large range of electron scattering angles and momenta, each coil in the hybrid toroid has four current return paths, as shown in Fig. 12. The upstream parts of the magnet have lower currents because they have fewer turns, with the fourth, most downstream part of the magnet having the full amount of the current (see Table 3). This optimizes the field seen by the lowest angle scattered electron tracks to ensure that the Møller and elastic e-p electrons have sufficient radial separation so that only the Møller electrons (which have a lower momentum) see the full field in the most downstream part of the magnet. The current return paths are also optimized to focus the largest angle (lowest momentum) Møller tracks so that they only experience field for a short distance in the magnet, which results in a negative curvature in the downstream part of the coil. The details of the conceptual design, Monte Carlo studies and preliminary studies of the mechanical design are presented in App. D

Table 3: *Summary of the hybrid coil parameters. The size of the conductor is 0.2362" (square) with a water-cooling hole of 0.177" (ID, round) and 0.08 mm of insulation (0.04 mm half-lapped).*

Mechanical Properties			Electrical Properties	
L_{turn} (m)		15, 13, 11, 9	R_{coil}	0.747 Ω
# turns		20, 8, 12, 36	V_{coil}	287 V
$weight_{coil}$ (lbs)		555	I_{wire}	384 A
Magnetic forces (lbs)	F_r	-3000	P_{magnet}	773 kW
	F_ϕ	0	$\vec{J}$	1996 A/cm^2
	F_z	-50	Field Integral	1.1 T·m

3.4 Detectors

The MOLLER apparatus consists of a number of detector systems: integrating (current mode) detectors, for the asymmetry measurements of both signal and background, and beam and target monitoring, as well as tracking (counting mode) detectors for spectrometer calibration, electron momentum distribution and background measurements. An overview of the main detector systems is shown in Fig. 13. The toroidal spectrometer will focus the Møller electrons $\approx$ 28 m downstream of the target center onto a ring with a central radius of $\approx$ 100 cm and a radial spread of $\approx$ 10 cm.

The region between a radius of 60 to 110 cm will be populated by a series of detectors with radial and azimuthal segmentation. These detectors will measure A_{PV} for Møller scattering and, equally important, will also measure A_{PV} for the irreducible background processes of elastic and inelastic electron proton scattering. Detectors at very forward angle will monitor window to window fluctuations in the scattered flux for diagnostic purposes. Lead-glass detectors placed behind the main Møller ring detectors and shielding, combined with two planes of gas electron multipliers (GEMs) will measure hadronic background dilutions and asymmetries. Finally, four planes of GEM tracking detectors will be inserted periodically just upstream of the integrating detectors, at very low current, to track individual particles during calibration runs.

The following subsections provide a brief overview of the various detector systems, including basic criteria and design choices. Additional details about the design and prototype testing status of the various detectors can be found in the appendices (E, F and H).

3.4.1 Main Integrating Detectors

For the primary A_{PV} measurement, the detector response will be integrated over the duration of each helicity window. Integration of the signal, rather than event counting mode, is required, due to the high flux of scattered electrons. The ideal detector material is artificial fused silica (henceforth "quartz"), since it is radiation-hard, and has negligible scintillation response. Further details of various design considerations are described in App. E

The primary acceptance collimator is divided into seven sectors, evenly distributed around the azimuth, covering exactly one-half the azimuth as described in Sec. 3.3 above. Figure 14 shows a Monte Carlo simulation of the transverse distribution of the scattered electrons after they have travelled through the spectrometer to a distance of 28.5 m from the target. Møller electrons are shown in black and the electrons

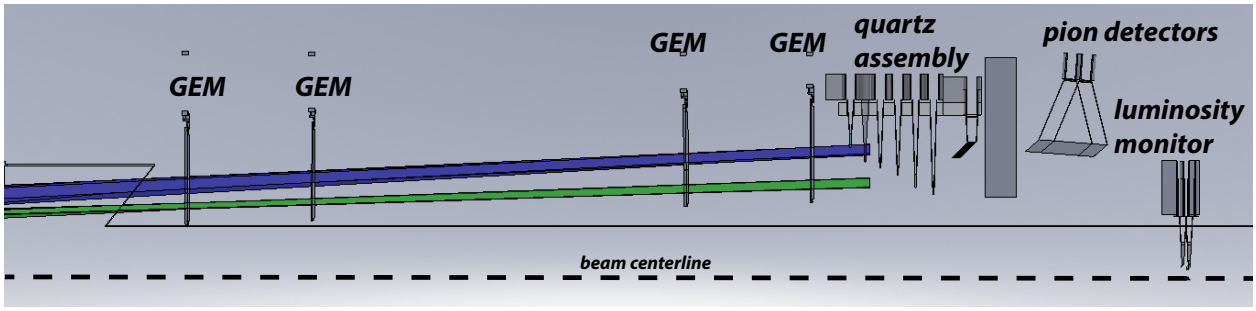

Figure 13: *Layout of the main integrating and tracking detectors. Predicted trajectories from elastically scattered electrons from target protons (green) and target electrons (blue) are also shown.*

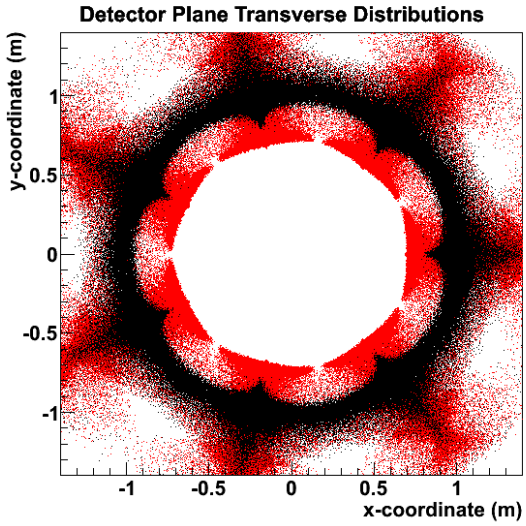

Figure 14: *Transverse distribution of Møller (black) and ep (red) electrons 28.5 m downstream of target*

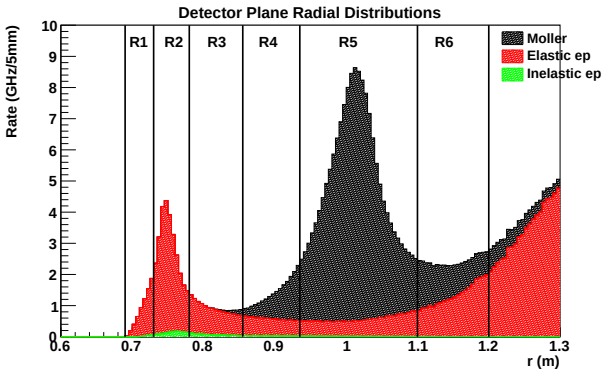

Figure 15: *Radial distribution of Møller (black), ep elastic (red), and ep inelastic electrons 28.5 m downstream of target. The vertical black lines delineate the proposed radial segmentation into 6 rings (R1 thru R6). The principal A_{PV} measurement will be carried out in ring R5.*

from elastic electron-proton scattering ("ep") are shown in red. Figure 15 shows that the "ep" peak flux is concentrated primarily at a smaller radius of $\approx$ 75 cm and at radii larger than $\approx$ 110 cm.

Due to azimuthal defocusing in the magnets the Møller electrons populate the full range of the azimuth at the detector plane. However, as can be seen in Fig. 16, the electron rate is highly non-uniform within a ring and mostly still focused on the individual seven sectors. The figures demonstrate that a detailed understanding of the signal, background fraction, and spectrometer optics requires high detector segmentation, both in the radial and azimuthal dimensions. In addition, azimuthal segmentation is also needed, since defocusing results in a correlation between azimuthal angle and E'.

To address the criteria discussed above, the detector will be segmented, both in the radial and the azimuthal direction. Currently there are six planned radial bins that are being optimized for measuring the main Møller scattering asymmetry as well as the background asymmetries that result from elastic and inelastic scattering of electrons from the target protons, as shown in Fig. 15. A discussion of this optimization can be found in Sec. 4.5. Each azimuthal sector defined by one of the toroids is further divided into 4 sub-sectors, so that there are 28 total azimuthal channels at each radial bin. The exception to this is the Møller radial bin, which is further divided into 3 additional bins, resulting in a total of 84 channels. This

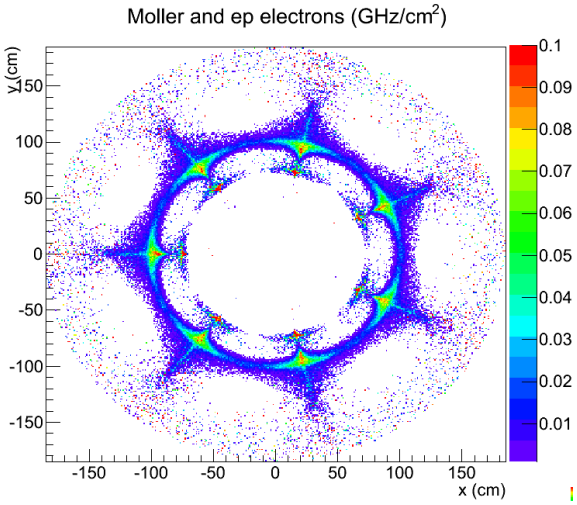

Figure 16: *Simulated, cross-section weighted, Møller and ep electron rates.*

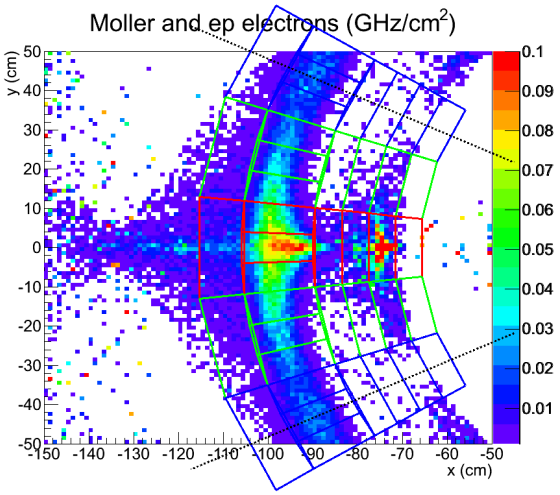

Figure 17: *Superimposed azimuthal and radial bins (detector locations) in one toriodal sector (indicated by the dotted black line).*

arrangement is illustrated in Fig. 17. Additionally, a "shower-max" quartz/tungsten sandwich detector will provide a second independent measurement of the flux in the main Møller "peak". This detector will be less sensitive to soft photon and charged hadron backgrounds.

In the current design, the quartz active volume of each detector is connected to a PMT by an air-core light guide. This is done to remove all PMTs from the envelope of scattered electrons and backgrounds as much as possible while, at the same time, reducing sensitivity to background (the latter resulting in the choice for the air-core, rather than a solid material). The integrated response of the PMT to the collected light yield is then the experiment's measure of the scattered electron flux [55].

Figure 18 is a schematic, cutaway view of the current plan for the integrating detector arrangement. The orientation of the quartz tiles and the angled cuts at end attached to the light guide must be optimized, such that the collection of the Ĉerenkov photons (the light yield) from each quartz piece is maximized, while the detection of light *created by events in the light guide itself* (accidentals) should be minimized. Previous studies [56] show that the quartz thickness along the beam direction is optimized around 1 cm, for the electron energies relevant for this measurement. A thinner detector does not produce enough light while a thicker detector would have unacceptably large Landau tails, increasing the average RMS width. Simulations and prototype tests are currently under way to answer this question. The specific orientation shown in Fig. 18 is arbitrary and the actual orientation and geometry of the quartz pieces and light guides as well as the light guide materials is currently under study (see Appendix E). Figure 19 shows how radial and azimuthal segmentation is achieved with a compact mechanical construction.

3.4.2 Auxiliary Detectors

In the vicinity of the Møller "peak", there is a possibility of a small ($\sim 0.1\%$) contamination from pions and other charged hadrons. The background could result from processes with a very tiny cross-section with a potentially large analyzing power, as discussed in Sec. 4.5.3. It is therefore important to be able to directly measure both the dilution fraction as well as the parity-violating asymmetry of this background.

We propose to accomplish the dilution fraction and asymmetry measurements with a set of auxiliary detectors that will be placed along the primary Møller "peak" trajectory behind shielding. The idea is

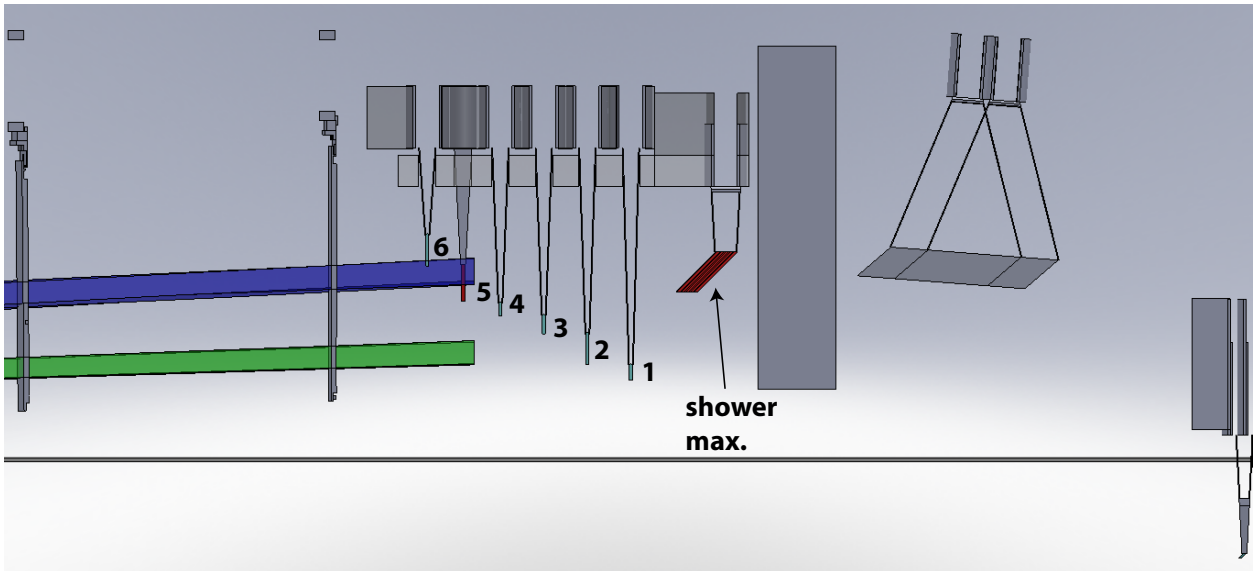

Figure 18: *Plan cutaway view, along with the main elastic Møller (green) and ep (blue) trajectories. The quartz detector rings are numbered. The main Møller events predominantly hit #5, while the elastic ep trajectories hit #2. Rings #3 and #4 in between will be important to estimate the inelastic ep background correction; see Sec. 4.5.2. Note the two back-to-back detector rings that will simultaneously measure the flux of the Møller peak.*

to identify minimum ionizing particles (MIPs) that penetrate the shielding using a Pb-glass calorimeter, followed by two GEM planes to positively identify charged particles (see Fig. 18).

The dilution measurement will be carried out in an auxiliary calibration run at very low current, where pions will be identified by looking for MIP signals in both the Møller "peak" sandwich detector as well as the Pb-glass detector, both in time coincidence with a track from the two downstream GEM detectors. The asymmetry measurement would be carried out during production running. Two methods are being investigated: either integrating the Pb-glass signal or designing a fast-counting electronics chain that establishes a coincidence between a Pb-glass MIP signal and a GEM track.

The final detector at the right edge of Fig. 13 is the so-called "luminosity monitor", which consists of quartz detectors that will detect the charged particle flux at extreme forward angles. Such monitors have two purposes. Since they have higher statistics (by a factor of 5 to 10) than the primary Møller flux, they serve as a sensitive diagnostic of target density fluctuations, beam fluctuations and electronics noise. The small scattering angle also implies that they should have a much smaller parity-violating asymmetry, so that they can also serve as a "null asymmetry monitor".

In the current spectrometer design, we have determined that the forward angle charged particle flux in the $\theta_{\rm lab}$ range between 2 and 2.5 mrad should not feel any fields. We therefore plan to instrument the region between 6.0 and 7.5 cm thirty meters downstream of the target with eight luminosity detectors; the detection technique will be similar in concept to the main integrating detectors i.e. a thin quartz plate with an associated air light guide and photomultiplier tube. The placement of these detectors can be discerned from Figs. 18 and 19.

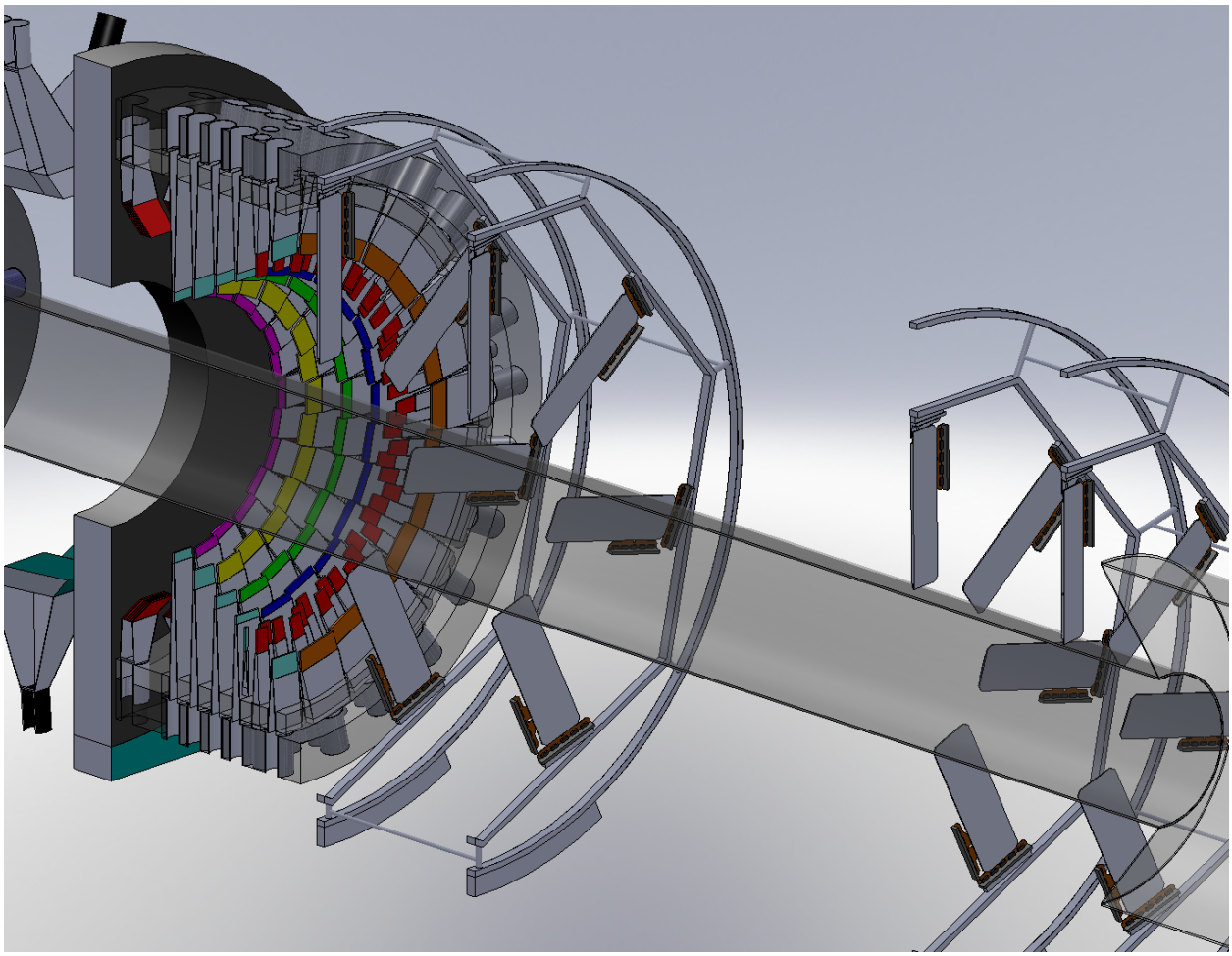

Figure 19: *A perspective view of the integrating detector assembly and the upstream GEM trackers.*

3.4.3 Tracking Detectors and Scanner

In order to verify the spectrometer optics, to measure the absolute scale and the appropriately weighted mean of the kinematic factor multiplying A_{PV}, and to evaluate our understanding of backgrounds, a tracking system is proposed to be used at very low current ($\sim$ 100 pA). The basic concept is to measure particle tracks using 4 GEM planes downstream of the two spectrometer toroids but before the particles arrive at the main integrating quartz detectors.

It is proposed to have GEM planes placed in pairs of two placed in rotatable wheel assemblies, as shown in Fig. 19. The GEM planes must be insertable to intercept the charge particle flux after they exit the vacuum window, but must be out of the way during the collection of production data. In order to reduce costs, we propose to cover four septants with a GEM stack of 4 planes and have them attached to a remotely controlled "wheel" with the ability to rotate up to one septant in either direction.

We expect that a resolution of ~ 500 μm for a flux of $\lesssim 200$ Hz/cm^2 will be required at the proposed operating beam current of 100 pA, which should not be too taxing for established readout techniques for GEMs. The ability to stably deliver such a low-current calibration beam for similar tracking measurements has been demonstrated in the Qweak experiment, which similarly relied on using a tracking system for background and kinematics measurements, at a beam current 6 orders of magnitude lower than that used for the primary asymmetry data-taking.

Another useful diagnostic will be a simple, small, movable detector that can operate at both the full

beam flux and at the low beam currents needed for the tracking measurements. This "focal plane scanner" would consist of a small single Cerenkov detector made of fused silica, read out by PMTs, mounted on an x, y motion stage covering one sector of the acceptance, and located just upstream of the main detectors. Such scanners have been used in E158, HAPPEx-II, and one is now being used by Qweak.

This device can be used to confirm that the rate distribution as measured at low beam currents by the full tracking system is not significantly different than that seen at full luminosity. It also would allow periodic rapid monitoring of the distribution during production data-taking, to ensure stability of the effective kinematics and to any changes in backgrounds.

3.5 Electronics and Data Acquisition

The integrated response of the Cherenkov light from electrons that traverse the detector is linearly proportional to the scattered flux. The parity-violating asymmetry is measured by averaging the fractional difference in the response of the detectors F over many window-pairs:

$$A_i \equiv \left(\frac{F_R - F_L}{F_R + F_L}\right)_i \simeq \left(\frac{\Delta F}{2F}\right)_i ; \quad A_{raw} = \langle A_i \rangle ; \quad \delta(A_{\rm raw}) = \sigma(A_i)/\sqrt{N}. \tag{11}$$

Here, A_i is the asymmetry in the ith window-pair, made from nearby (in the time domain) windows of opposite helicity. There are several aspects of the electronics and data acquisition (DAQ) specific to parity-violation experiments that are worth emphasizing, and we discuss them in the subsequent sections. The collaboration has extensive experience in these aspects of the experimental technique.

3.5.1 Rapid Helicity Flip

Second generation parity violation experiments at JLab such as HAPPEX-II used a helicity reversal frequency of 30 Hz, which had the benefit of largely canceling beam jitter and electronics noise related to 60 Hz line. PREX ran successfully with 240 Hz helicity-reversal, while Qweak used 960 Hz reversal. It will be necessary for MOLLER to flip the helicity even more quickly. One reason as mentioned above in the discussion of the target, is that target density fluctuations are only expected to contribute at frequencies below a few hundred Hz.

More importantly, at the MOLLER event rate of ~ 150 GHz, electronics noise is a very severe challenge. At a helicity flip rate of 60 Hz, the variance $\sigma(A_i)$ would be 28 ppm. A pedestal noise level below 3×10^{-6} would be required in order to ensure negligible contribution to $\sigma(A_i)$. We are designing around a flip rate of 1.92 kHz, such that $\sigma(A_i)$ would be 80 ppm. This requires a pedestal noise floor of 1×10^{-5}, which appears feasible. It also implies that each helicity state is held for $\sim 500\mu$s. In order to avoid excess noise from 60 Hz line variations, a scheme for selecting helicity states will be required which will force complementary pairs at corresponding points in the 60 Hz cycle.

The goal is to flip the Pockels cell within 10 μs, which implies a dead time of 2%. At present, a settling time of 60 μs is achievable for reversal rates of 960 Hz. However, it has proven difficult to push the transition of the Pockels cell to be shorter than 60 μs while keeping the cell optical properties stable after the shock of the fast transitions. The collaboration is exploring modifications to the switching or damping of oscillations, the use of a different Pockels materials such as RTP (which are not piezoelectric and therefore do not experience mechanical shock on transition), and the use of Kerr cells in place of Pockels cells.

3.5.2 Integrating Electronics

At the high helicity flip rate of 2 kHz, the low noise electronics developed for the Qweak experiment by TRIUMF should be suitable for MOLLER with little or no modification. The Cherenkov light from the

quartz travels down a light guide and is then converted to a current by a photodetector. This would be converted to a voltage signal by a transimpedence preamplifier located close to the detectors. The voltage signals from all the quartz detectors would go to electronics outside the Hall where it would be sampled at a 500 kHz rate by an 18-bit analog-to-digital converter (ADC). These digitized samples would be integrated over each helicity window by an internal field-programmable gate array (FPGA). These considerations are described in more detail in App. H.

The main scattered electronic flux detectors are not the only parameters that must be integrated over each helicity window. Even with perfect electronics, $\sigma(A_i)$ in Eqn. 11 would be dominated by fluctuations in electron beam parameters due to window-to-window fluctuations in intensity, position, angle and energy. To exploit the full available statistics one must remove the correlations of F to beam intensity, position, angle and energy, thus extracting the measured raw asymmetry as follows:

$$A_i = \left(\frac{\Delta F}{2F} - \frac{\Delta I}{2I} \right)_i - \sum \left(\alpha_j (\Delta X_j)_i \right). \tag{12}$$

Here, I is the time-averaged beam intensity over the duration of a helicity window, X_j are corresponding average beam trajectory parameters derived from judiciously placed beam position monitors and $\alpha_j \equiv \partial F / \partial X_j$ are coefficients that depend on the kinematics of Møller scattering as well as the detailed spectrometer and detector geometry of the given experiment. The parameters I and X_j will be derived from monitor signals in much the same way as the relative flux F, by feeding voltage outputs that are proportional to beam parameters into the same ADCs. It is critical to maintain close synchronization between the integration cycles of all the ADCs.

3.5.3 Online Calibrations and Feedbacks

The coefficients α_j must be continuously calibrated *simultaneously* with the collection of production data, since the numerical values depend on the details not only of the apparatus but also the accelerator beam tune and the sensitivity and location of beam monitoring devices. Various ways of accomplishing this at Jefferson Laboratory have already been implemented during HAPPEX and G0 measurements, including extensive collaboration with personnel from Accelerator Operations and careful consideration of impact on other Halls.

While α_j can be extracted from a correlation analysis of the response of the detectors and beam monitoring devices to beam fluctuations in window-pairs, proper calibration requires deliberately dithering the beam trajectory concurrent with data-taking in a quasi-continuous fashion by an amount large enough to observe all the correlations while avoiding to add a non-statistical component to $\sigma(A_i)$. More generally, the study of the detailed noise and beam response characteristics of the monitors is a critical component of understanding the systematics.

The success of the experimental technique will also depend on careful preparation of the initial polarization states of the electron beam, which begins with a careful setup of the laser transport electronics of the polarized source. During data collection, there will be extensive electronic communication with optical and magnetic devices at the low energy end of the machine as various automated feedback loops of varying time frequencies will have to be incorporated. These systems will have to be implemented while paying careful attention to potential electronic cross-talk problems for which the proposed measurement will have sensitivity at an unprecedented level. Again, the collaboration has extensive experience on this aspect of the measurement. Details on the considerations in this subsection can be found in App. A.

Error Source	Fractional Error (%)
Statistical	**2.1**
Absolute Normalization of the Kinematic Factor	0.5
Beam (second order)	0.4
Beam polarization	0.4
$e + p(+\gamma) \rightarrow e + X(+\gamma)$	0.4
Beam (position, angle, energy)	0.4
Beam (intensity)	0.3
$e + p(+\gamma) \rightarrow e + p(+\gamma)$	0.3
$\gamma^{(*)} + p \rightarrow (\pi, \mu, K) + X$	0.3
Transverse polarization	0.2
Neutral background (soft photons, neutrons)	0.1
Total systematic	**1.1**

Table 4: *Summary of projected fractional statistical and systematic errors.*

3.6 Hall A Infrastructure

The apparatus depicted in Fig. 7 and related shielding will be designed so that MOLLER runs can be interleaved with other experimental programs in Hall A. A first-order check of the experiment layout in Hall A has been done and no major obstructions have been found. A layout with both Hall A High Resolution Spectrometers (HRSs) parked at 90° to the beam line has been considered. An alternate layout with both spectrometers located beam left is also being evaluated. Such a layout would facilitate installation (open access to the hall truck ramp) but requires more effort to move one spectrometer to the opposite side of the beam line. Moving from the beam entrance along the beam line towards the dump, one would encounter the cryogenic target approximately 6 m upstream of the nominal pivot, the first spectrometer toroid at the HRS nominal target pivot, followed shortly thereafter by the hybrid toroid and, with the detectors approximately 20 m downstream of the pivot. Møller events and the degraded beam travel under vacuum all the way to the detectors and beam dump, respectively.

Cooling of the collimators and room temperature spectrometer toroids will be done using a closed low conductivity water (LCW) circuit to contain the beam activated water in the hall. The LCW distribution system in the hall is being upgraded to handle the additional volume required by this and other experiments. A heat exchanger will transfer the heat from the closed system to the JLab wide LCW system. An additional 2 MVA electrical transformer would be added to handle the load brought by the spectrometer toroids.

For the purpose of estimating the experiment cost, we have assumed a one meter thick concrete wall covering the spectrometer length to minimize radiation in the Hall. As the details of the experimental apparatus improve, simulations are being carried out to optimize the shielding configuration and specific locations. Once simulations and conceptual engineering designs are completed, the best strategies will be devised to handle the disassembly and storage of activated parts for multiple years (with other experiments taking place in between MOLLER runs) in consultation with JLab's Radiation Control group.

With the target significantly upstream of the HRS pivot, the incoming hall beam line also needs to be rearranged. A detailed plan for configuring the upstream magnetic and beam diagnostic elements has been formulated, but final implementation awaits the final design of the spectrometer/collimator configuration.

Beam Property	Assumed Sensitivity	Accuracy of Correction	Required 1 kHz random fluctuations	Required cumulative helicity-correlation	Systematic contribution
Intensity	1 ppb / ppb	$\sim$1%	< 1000 ppm	< 10 ppb	~ 0.1 ppb
Energy	-1.4 ppb / ppb	$\sim$10%	< 286 ppm	< 0.7 ppb	~ 0.05 ppb
Position	0.85 ppb / nm	$\sim$10%	< 47 μm	< 1.2 nm	~ 0.05 ppb
Angle	8.5 ppb / nrad	$\sim$10%	< 4.7 μrad	< 0.12 nrad	~ 0.05 ppb

Table 5: *Goals for first order corrections from electron beam helicity correlations*

4 Systematic Control

The proposed A_{PV} measurement in some sense constitutes a fourth generation parity-violation experiment at Jefferson Laboratory. Apart from the obvious challenge of measuring a raw asymmetry with a statistical error less than 1 ppb, an equally challenging task is to calibrate and monitor the absolute normalization A_{PV} at the sub-1% level. The collaboration continues to gain extensive experience on all aspects of such measurements as work continues on executing and analyzing the third generation experiments PREX [52] and Qweak [53].

We tabulate our estimates of the most important systematic errors in decreasing order of importance in Table 4. It is instructive to recall that the raw asymmetry is about 32 ppb and that the raw statistical error is 0.6 ppb or about 2%. In the following subsections, we describe some of the principal challenges of controlling systematic errors in the proposed measurement and provide justification for the projected errors in the table.

4.1 Beam Fluctuations

As described in Secs. 3.1 and 3.5, the scattered flux would be integrated over the duration ($\sim$ 500 μs) of each helicity window. Equation 12 shows how one then extracts a signal proportional to the raw cross-section asymmetry by removing beam correlations. In this section, we summarize the upper limits for the random and helicity-correlated fluctuations in order to achieve the systematic error goals in Table 4. Apart from active techniques to control helicity correlations in the laser beam as well as in the low energy electron beam, one also gains additional suppression due to so-called "adiabatic damping" and with the use of several methods of "slow helicity reversal". Many more details on these issues based on experience from past experiments can be found in App. A.

Numerical estimates for α_j were made using Monte Carlo simulation, with results which are similar to expectations based on scaling the beam-motion sensitivities measured in HAPPEX-II. They are listed in Table 5. Using these numbers, the required monitoring resolution to achieve counting statistics for 1 kHz window pairs is $\lesssim$ 3 μm in position, and 10 ppm in intensity. The position monitor resolution will be straightforward to achieve based on previous experience in HAPPEX-II, PREX and Qweak. On the other hand, achieving 10 ppm resolution in beam intensity will require significant R&D, which the collaboration has flagged for further study and effort.

4.1.1 Helicity-Correlated Beam Fluctuations

If one averages over the instantaneous pulse-pair asymmetry A_i (see Eqn. 12 in Sec. 3.5.2) and considers the cumulative experimental asymmetry A_{raw} over many window pairs i, one can write

$$\begin{aligned} A_{\rm raw} \equiv \langle A_i \rangle &= \left\langle \left(\frac{\Delta F}{2F} \right)_i \right\rangle - \left\langle \left(\frac{\Delta I}{2I} \right)_i \right\rangle - \sum \alpha_j \left\langle (\Delta X_j)_i \right\rangle \\ &= A_F - A_I - \sum_j A_{Mj}. \end{aligned} \tag{13}$$

In a well-designed and well-executed high flux parity experiment, the helicity-correlated beam asymmetries (HCBAs) A_I and ΔX_i will be small enough so that $\langle A_{raw} \rangle \simeq \langle A_F \rangle$, even though $\sigma(A_F)_i$ will be significantly larger than $\sigma(A_{raw})_i$ for window-pairs.

The first goal is to ensure that each correction A_{Mj} is of the order of, or smaller than the projected raw statistical error of about 0.6 ppb, and that the slopes α_j are known to better than 10%, so that the systematic error contributions from these corrections are small. This can in turn be transformed under reasonable assumptions to goals for the grand average ΔX_j. These considerations are summarized in Table 5. These are realistic goals, as we elaborate briefly in the following. During the relatively short HAPPEX-II experiment, position differences were kept to less than 2 nm and angle differences to less than 0.2 nrad; only a modest improvement over these goals is required. The more recent experience with the PREXI experiment has been similarly good, and further results and experience will come from the full Qweak dataset currently being analyzed and the future PREXII data-taking. Table 6 summarizes the experience of recent, ongoing and future parity experiments on the measured HCBAs.

Selected parity experiments and their measured or projected demands on suppression of helicity-correlated beam-parameter differences						
Experiment (*) actual (†) projected	physics asymmetry	stat. error	sys. error due to beam	limits on position differences	limits on angle differences	limits on diameter differences
*HAPPEX I	-15,050 ppb	980 ppb	± 20 ppb	< 12 nm		
*SLAC E158	-131 ppb	14 ppb	± 3 ppb	< 12 nm	0.4 nrad	$< 10^{-5}$
*HAPPEX II-p	-1,580 ppb	120 ppb	± 17 ppb	< 1.7 nm	0.2 nrad	
*HAPPEX III	-22,100 ppb	550	± 66 ppb	< 40 nm		
*PREX-I	657 ppb	60 ppb	± 7.2 ppb	< 4.0 nm		$< 10^{-4}$
Upcoming or ongoing parity experiments						
†PREX-II	500 ppb	15 ppb	± 3.0 ppb	< 1.0 nm		$< 10^{-4}$
†Qweak	-288 ppb	5 ppb	± 1.4 ppb	< 2 nm	30 nrad	$< 7 \times 10^{-3}$
† 12 GeV Møller	36 ppb	0.6 ppb	± 0.05 ppb	~ 0.5 nm	0.05 nrad	$< 10^{-5}$

Table 6: *Shown are various parameters for several parity experiments, including HAPPEX I, E158, and HAPPEX II-p, that are published, HAPPEX III and PREx, the results of which are available, and QWeak, currently being analyzed. Also shown are PREx-II, recently approved, and MOLLER. The second and third columns show the actual measured or projected asymmetries and statistical errors. The fourth column shows the actual or projected error associated with corrections for helicity-correlated beam-parameters. The remaining columns indicate actual or projected limits on helicity-correlated beam parameter differences.*

Extensive tools for tightly controlling A_I have been developed in previous experiments. The nonlinearity between the detectors and beam current monitors is typically controlled at the 0.5% level. Given the goal of 0.1 ppb contributed error from intensity corrections, this implies that the grand average A_I must be smaller than 10 ppb. Intensity feedback will be employed to assure convergence within that bound.

A large degree of cancellation for the slopes α_j is expected when considering the full azimuthal symmetry of the detector. A conservative estimate of a factor 10 reduction in sensitivity is taken to account for detector alignment tolerances. After applying corrections for small position and angle differences, an uncertainty of approximately 10% is likely to remain. This leads to the specifications for the run-averaged ΔX_j in order to keep the contributed uncertainty to less than 0.05 ppb each, as listed in Table 5.

4.1.2 Beam Spot Size Differences

In all the discussion above on beam-related systematic effects, it has been assumed that the dominant component in the scattered flux response to fluctuating parameters is linear. In practice, it is possible that certain second-order effects might be helicity-correlated and thus lead to systematic shifts. The stability of the CEBAF beam makes it highly unlikely that there are large effects, and none have been seen in experiments to date. Typically, second-order effects tend to scale as a fraction of the first-order effects, providing additional incentive to control the first-order effects as tightly as possible. Furthermore, the $g-2$ and "double-wien" slow reversals (discussed in Sec. A.4) will be powerful cross-checks of this assumption.

One common manifestation of a second-order effect is a helicity-correlated difference in the beam spot-size σ. We have simulated the effect for the proposed spectrometer/collimator geometry, finding it to be at the level of (12 ppm)$\times\Delta\sigma/\sigma$. Work on the laser table should be able to bound the laser spot size asymmetry to be less than 10^{-4}, in which case the potential effect would be as large as 1 ppb. We assume a factor of 10 suppression from cancellation due to the proposed periodic slow helicity reversals, so that the net contribution will be limited to 0.1 ppb.

4.2 Longitudinal Beam Polarization

The experiment requires a relative accuracy of the electron beam polarization measurement at the level of 0.4%. The electron beam polarization is expected to be between 80 and 90%, with the exact value depending on specific photocathode materials and a variety of other factors. The beam polarization might vary at the 0.5 to 1% level over the duration of a specific photocathode's lifetime. Thus, achieving 0.4% systematic control will require redundant, continuous monitoring during data collection.

JLab has accumulated extensive experience with polarimetry at or below 6 GeV. Recently completed and ongoing experiments in the JLab "6 GeV" parity-violation program, in both Halls A and C (PREX, HAPPEXIII, PVDIS and Qweak), have developed polarimeters with precisions on the order of 1%. However, these polarimeters have never been cross-checked with each other at the level of 0.4%, nor has any experiment at Jefferson Lab yet required this level of precision. It is worth noting that a comparable level of accuracy was achieved by the SLD collaboration [2] using a Compton polarimeter with a ~ 46 GeV pulsed beam at SLAC.

In order to reach a robust 0.4% precision, we propose the use of a Compton polarimeter for a continuous measure of beam polarization. Independent analysis of scattered photons and electrons provides a pair of continuous measurements with a high degree of independence in systematic errors. This polarimeter will be cross checked against periodic measurements with a Møller polarimeter using ferromagnetic foil targets. An upgrade to the Hall A Møller polarimeter, presently underway, will support improvements and studies that should ultimately lead to a systematic accuracy near 0.4%.

An alternative second-stage upgrade would incorporate a polarized atomic hydrogen gas target in the Møller polarimeter, which would provide for continuous operation of a polarimeter with systematic uncertainties completely independent of the Compton-scattered photon or electron measurements. Each of these three polarimeters (the Compton polarimeter, and Møller polarimeters using foil and hydrogen targets) are described briefly in the following sections, with more details in the appendices.

Relative error (%)	electron	photon
Position asymmetries*	-	-
E_{Beam} and λ_{Laser}*	0.03	0.03
Radiative Corrections*	0.05	0.05
Laser polarization*	0.20	0.20
Background / Deadtime / Pileup	0.20	0.20
Analyzing power Calibration / Detector Linearity	0.25	0.35
Total:	0.38	0.45

Table 7: *Goals for systematic errors for the Hall A Compton polarimeter at 11 GeV. Topics marked * are a common systematic error between the photon and electron analyses, while the other are largely independent between the detector systems.*

4.2.1 Compton Polarimetry

Compton polarimetry is a very attractive technique for high precision polarimetry with high energy electron beams. When electrons scatter off circularly polarized laser photons, the associated Compton cross-section depends on both the electron and photon polarizations. Beam interactions with a photon target are non-disruptive, so Compton polarimetry can be employed at high currents as a continuous polarization monitor. The photon target polarization can be measured and monitored with a very high precision, and the scattering between a real photon and free electron has negligible theoretical uncertainty, without atomic or nuclear effects which can complicate other measurements. Radiative corrections to the scattering process are at the level of 0.1% and are very precisely known. The SLD result of 0.5% polarimetry demonstrates the feasibility of very high accuracy Compton polarimetry.

JLab Compton polarimeters employ a 4-dipole vertical chicane, just below the primary beamline. The interaction point is between the second and third dipoles, where the electron beam is parallel to the primary beamline but at a lower height. A Fabry-Perot cavity serves as the photon target. The scattered electrons lose energy and are separated by the third and fourth dipoles from the primary beam and are intercepted by position-sensitive detectors such as silicon microstrips. The scattered photons are detected by a calorimeter downstream of the third dipole. The electron polarization can be extracted independently by measuring the helicity-dependent rate of the electrons or the photons, and important systematics studies can be carried out by studying electron-photon coincidences. The existing Hall A Compton polarimeter will be upgraded for 11 GeV operation as part of the baseline energy upgrade project.

Based on the collaboration's experience with Compton polarimetry from the third generation experiments PREX and Qweak, we have estimated the systematic uncertainties that are feasible for continuous monitoring at 11 GeV. These ambitious goals are summarized in Table 7. The goal is to have an internal cross-check at the 0.4% level by comparing the extracted beam polarization from the scattered photons to that from the scattered electrons. Detailed considerations leading to the projected systematic errors can be found in App. I, and plans for improving the capabilities of the polarimeter are described in Sec. 7.6.1.

4.2.2 Møller Polarimetry

Møller polarimeters exploit the helicity dependence of polarized Møller scattering $\vec{e^-} + \vec{e^-} \rightarrow e^- + e^-$ to extract the beam polarization by using a polarized electron target of known polarization. Møller scattering has a very high analyzing power, equal to 7/9 for 90° scattering in the center of mass, a very large cross section, and the two electrons with high energies in the final state make it easy to detect their coincidence

and reduce background to negligible values. Such polarimeters have been in use for more than three decades and many potential systematic effects are now controlled at a level below 1%.

The most common polarized electron targets are "large μ" ferromagnetic alloy foils which saturate at relatively small applied magnetic fields. The electron polarization for a foil in saturation is about 8%. That is, roughly two electrons in the d-shell of each iron atom are polarized. The exact value cannot be calculated from first principles but must be inferred from calibration measurements of foil magnetization, with corrections for the expected contribution of orbital angular momentum. The magnetization may vary as a function of position on the foil, varying with thickness and perhaps also with thermal or mechanical annealing history. The accuracy of this determination is the fundamental limitation to precision polarimetry with this type of target. The best techniques have produced relative target polarization accuracy approaching 2%.

A significant improvement has been achieved by using pure iron foils in a strong longitudinal field approaching 4T to achieve full saturation of the magnetization. Experimental determination of the spontaneous magnetization of bulk iron at zero applied field and temperature, along with data constraining the evolution of magnetization with temperature and applied field, are used to determine the magnetization in operating conditions. An additional correction of $\approx 4\%$, based on measurements of the magneto-mechanical factor, is needed to subtract the contribution from orbital angular momentum. Accounting for these corrections, an accuracy of 0.25% in the determination of the electron spin polarization in a "saturated" iron foil is claimed [57].

Inserting foils into the beam is a "destructive" measurement requiring periodic measurements at a beam current of a few to tens of μA, thus precluding continuous polarization monitoring at high beam current. Consequently, Møller polarimetry with foil targets will be used as a cross check on measurements with the Compton polarimeter, verifying that there is no common systematic error in the measurement of Compton-scattered electron and photons that leads to a beam polarization error of larger than 0.4%.

An alternative strategy to avoid the limitations of conventional Møller polarimetry is to use polarized atomic hydrogen gas, stored in an ultra-cold magnetic trap, as the electron target. Such a target has an electron polarization of practically 100%, removing the target polarization uncertainty associated with the ferromagnetic targets. Other errors can be strongly suppressed. Furthermore, such a target is thin enough to be used continuously with the experiment, providing a continuous polarization measurement which is entirely independent of the Compton polarimeter. With this system, a 1% statistical accuracy can be achieved in less than 30 minutes of running [58, 59].

Table 8 shows the current and projected list of systematic errors for Møller polarimeters at Jefferson Lab. More details on Møller polarimetry are described in App. J, and near-term plans for the development of the polarized hydrogen target alternative are described in Sec. 7.6.2.

4.3 Transverse Beam Polarization

If there is any transverse polarization component to the beam on target, the apparent A_{PV} as a function of the azimuthal angle would show a modulation due to the vector analyzing power A_T in Møller scattering, a QED effect involving the interference between the tree-level amplitudes and the two-photon exchange amplitudes. The relevant parameter for A_T is the energy of each electron in COM frame, which is 53 MeV; the electron's boost factor is therefore rather modest. The magnitude of A_T is such that even a few percent transverse polarization can result in an azimuthal modulation of the measured polarization asymmetry that is an order of magnitude larger than A_{PV}. While this effect should cancel if one averages data over the full range of the azimuth, imperfect cancellation could lead to a significant systematic error.

Some interesting features of A_T facilitate a strategy that would allow us to keep this potential systematic error under control. If one looks at A_T as a function of the COM scattering angle, or equivalently $y \equiv 1 - E'/E$, one finds that A_T must vanish at $y = 1/2$, which corresponds to 90° scattering in the COM

Variable	Hall C	Hall A: Foil		Alternate:
		Tilted	High Field	Hydrogen
Target polarization	0.25%	1.50%	0.25%	0.01%
Target angle	‡	0.50%	‡	⋆
Analyzing power	0.24%	0.30%	0.20%	0.10%
Levchuk effect	0.30%	0.20%	0.20%	⋆
Target temperature	0.05%	‡	0.05%	⋆
Dead time	‡	0.30%	0.10%	0.10%
Background	‡	0.30%	0.10%	0.10%
Others	0.10%	0.50%	0.10%	0.30%
Total	0.47%	1.8%	0.42%	0.35%

⋆: Not applicable ‡: Not Estimated

Table 8: *Systematic error summary for Møller polarimeters at JLab, including anticipated uncertainties for future prospects. The Hall C polarimeter [60] uses a high field pure iron target [57, 61] with a simple two-quadrupole spectrometer. The existing Hall A device [62] uses a tilted ferromagnetic alloy target, and a spectrometer with a dipole magnet following three quadrupoles. A high-field pure iron target upgrade is underway, with an additional quadrupole in the spectrometer for high energy operation. Research and development for a hydrogen gas target [58, 59] provides the basis for a second continuously-running high precision polarimeter to complement the Compton apparatus.*

frame, due to CP symmetry. Thus, the maximum A_T is around 15 ppm, and occurs at $|y - 0.5| \approx 0.2$, at the very edges of the momentum acceptance and more importantly, A_T is of opposite sign at these two extremes. This leads to an order of magnitude suppression in the effective A_T averaged over all detectors.

It is possible by passive setup procedures to limit the transverse component of the beam polarization at the target to be less than 1°. One can measure the ϕ modulation to very high precision during production data collection within the first few hours, by studying the azimuthal dependence of the raw detector asymmetry, since different azimuthal detectors have very different acceptances as a function of y. Thus, it should be possible to devise a "manual" feedback loop that would make small tweaks to the launch angle of the electron beam polarization at the low energy end of the machine based on the measured A_T's. This technique is designed to converge to zero transverse polarization. In practice, the suppression should go like $1/N$, where N is the number of adjustments. In principle, we should gain a factor of about 25 below the setup accuracy of 1° in a week. We will assume this factor for the duration of the entire data collection period for the estimate of the systematic error.

If one now further conservatively assumes only a factor of 10 suppression in the grand average of A_{PV} over the full range of detectors, then the total systematic error from the correction to A_{PV} is less than 0.07 ppb. If this level of suppression is difficult to achieve in practice, some of it can be recovered by a slightly different reweighting of the data from the various different azimuthal detectors with only a small loss in the statistical error in the extracted A_{PV}.

4.4 Absolute Normalization of the Kinematic Factor

For momentum transfers $Q^2 \ll M_Z^2$, A_{PV} at tree level is directly proportional to Q^2. For Møller scattering, there is an additional kinematic dependence on the accepted energy range of scattered electrons i.e. the average value of the kinematic factor in Eqn. 3 in Sec. 1.2. The uncertainty in the overall kinematic factor therefore contributes directly to the ultimate uncertainty on Q_W^e. Our goal is to determine the overall kinematic factor for our apparatus to a fractional accuracy of 0.5%. We will rely on the extensive experience

that was developed to measure Q^2 for Qweak. Also, sub-1% accuracy has been achieved in the HAPPEx measurements.

The average kinematic factor can be determined from data using comparisons to a detailed Monte Carlo. By taking measurements at fixed angle and energy points and the known $e + e \rightarrow e + e$ cross section (including radiative effects), the acceptance function can be accurately reconstructed. In the approximation where radiation in the target is neglected, the kinematic factor can be largely determined from survey measurements of collimator apertures and the absolute beam energy calibration tools in the Hall A beam line. Additionally, the use of a moveable sieve is planned, allowing fixed angles to be calibrated with a set of carbon target foils (to suppress radiative effects and fix vertex position) at several beam energies, as discussed in App. F.

With the beam going through a 10.5 gm/cm^2 target however, the distribution of trajectories and energies are significantly modified. This requires not only a detailed Monte Carlo simulation but also validation by direct measurement of individual tracks in calibration runs at low current. This is one of the primary motivations for the tracking system presented in Sec. 3.4.3. The large amount of multiple scattering, dE/dx and radiative losses due to the thick target, coupled with the large kinematic acceptance, and the rapid variation of the asymmetry with scattering angle, means that the Monte Carlo simulation of the effective kinematic factor seen by each detector segment needs to be validated carefully.

If the integrating quartz detectors cover the full acceptance of the events passing through the collimators, a precise survey of the collimators would in principle provide an accurate measurement of the kinematic factor. The general requirements and the quantitive analysis of cross-checks are discussed in App. G. Another consideration is that a variation in the analog response of the integrating detectors would reweight the effective kinematic factor associated with the integrated response. The aforementioned tracking system can evaluate this effect by measuring the variation in response as a function of position in the quartz using single Møller electron tracks at low beam currents.

4.5 Backgrounds

4.5.1 Elastic ep Scattering

The principal irreducible background under the Møller "peak" (see Fig. 20) is radiative elastic electron-proton (ep) scattering, which constitutes 8.9% of the signal. The background can be easily modeled and then verified explicitly with auxiliary tracking measurements of the radial profile of the scattered flux. The theoretical prediction for the parity-violating asymmetry is also well known for this process. Recently, the $\gamma - Z$ box radiative correction was calculated at 11 GeV [63]; this significantly impacts the value of effective value of Q_W but does not add significantly to the projected error in the correction. In addition, the Qweak measurement of the weak charge of the proton Q_W^p can be used directly cross-check the predicted background asymmetry.

After the modeling has been fine-tuned with calibration data, the Q^2 distribution of the background under the Møller peak can be estimated from the Monte Carlo simulation. The average Q^2 is 0.004 GeV^2. Assuming an uncertainty of 4% on the knowledge of Q_W^p, this leads to a 0.3% systematic error

4.5.2 Inelastic ep Scattering

A more challenging background correction is due to the smaller dilution from inelastic ep scattering. Even though the contribution from the background is expected to be small, $\lesssim 0.5\%$, the asymmetry correction can be significantly larger due to the fact that the estimated coupling to the Z boson is more than an order of magnitude larger than Q_W^e. Indeed, this background was studied in E158 and the parity-violating asymmetry from inelastic electron-proton scattering was consistent with the formula $A_{PV}^{\text{inel.}} \sim 0.8 \times 10^{-4} \cdot Q^2[\text{GeV}^{-2}]$. This is to be contrasted with $A_{PV}^{\text{el.}} \sim 1.0 \times 10^{-5} \cdot Q^2[\text{GeV}^{-2}]$, while $A_{PV}^{\text{Møll.}}$ is another 40% smaller.

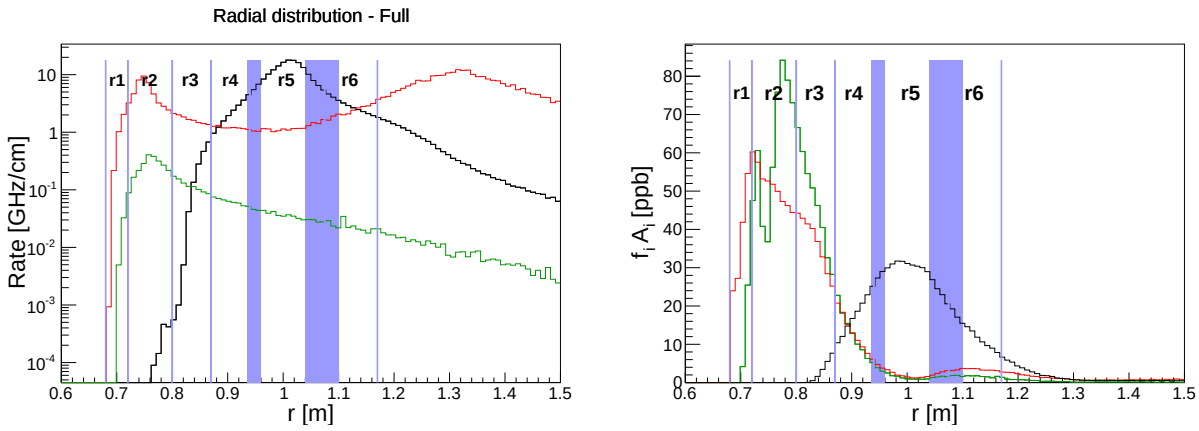

Figure 20: *The black, red and green curves are radial rate distributions from Møller, elastic e-p and inelastic e-p scattering at the detector plane 28.5 m downstream of the target. The left plot is the rate distribution in log scale whereas the right plot shows individual A_{PV} contributions in linear scale in units of ppb. The proposed radial segmentation of the scattered electron flux is superimposed. The six rings r1 thru r6 correspond to the numbered quartz detectors as shown in Fig. 18*

We have done a preliminary optimization of the radial segmentation of the integrating detectors that will allow us to measure the relevant combination of vector couplings and make a reliable background correction to the raw Møller asymmetry. The six radial extents of the numbered quartz tiles shown in Fig. 18 correspond to the six radial bins shown in Fig. 20, where the segmentation is overlaid on the Monte Carlo radial distributions for scattered Møller, elastic ep and inelastic ep electrons. The left plot is the rate distribution of the three components whereas the right plot are the individual estimated contributions to A_{PV} in each radial bin. The Møller electrons primarily hit the red quartz (r5) and the radial extent of this ring will be varied somewhat as a function of the azimuthal position with respect to the mid-plane of each toroidal sector to optimize the figure of merit; this variation is reflected by the thicker lines in the figure.

It is remarkable that the A_{PV} contributions to rings 2 and 3 are dominated by the contribution from inelastic ep scattering (the right plot of Fig. 20) whereas the rates in these bins are dominated by elastic ep scattering. This is because the inelastic ep coupling is expected to be 20 times bigger than the elastic ep coupling, whereas the inelastic ep flux (green) is only 5 to 10 times smaller than the elastic (red) flux (left plot Fig. 20). Those measurements can be used to estimate the correction due to the inelastic ep background in the "red" (r5) detectors that contain the raw Møller asymmetry of interest.

We use an ansatz for $A_{PV}^{\text{inel.}}$ such that the inelastic e-Z vector coupling can be different in three different regimes of the recoiling hadron mass W (but constant within each regime): the Delta resonance, other resonances below 2 GeV, and the continuum above 2 GeV. A Monte Carlo study has demonstrated that we can reliably estimate the correction for the Møller detectors by studying the variation of the radial detectors as a function of the azimuth. We have concluded that we can make the estimated 4% correction to 10% of itself, leading to a 0.4% systematic error.

4.5.3 Hadrons and Muons

There is the possibility of negatively charged pions, heavier mesons and muons to contribute at a small level to the signal in the Møller detectors. The dilution from such a background is likely to be negligibly small, but the parity-violating asymmetry of this background will depend on the processes that create them. The dominant source is from pions produced by real and virtual photoproduction off protons in the target.

This background was studied for the E158 configuration and the dilution factor was explicitly measured to be 0.12% in the Møller detector. The parity-violating asymmetry, measured in dedicated pion detectors sensitive to the hadronic leakage behind the Møller detector and shielding, was found to be ~ 0.5 ppm.

For the configuration of this proposal, a reasonable extrapolation from the E158 kinematics implies that the background fraction will be about the same: the Møller cross section has gone up by a factor of 4, but the solid angle bite has also gone up by about a factor of 4. This has been verified explicitly using a Monte Carlo generator that combines pions from photo- and electro-production. Parametrized photoproduction rates from SLAC [64] are related to electoproduction through the equivalent-photon approximation, in addition to real photoproduction from bremsstrahlung. The resulting spectrum of inclusive pions are sent through the spectrometer to determine the fraction that would fall within the detector acceptance. The ratio of the pion rate to the electron rate was found to be 0.13%.

If one conservatively assumes that the asymmetry is of the same magnitude as that measured in E158, it would lead to a significant ($\sim$ 0.7 ppb) but manageable correction. However, it is possible to have a contribution from a fractionally tiny flux of pions or muons from weak decays of heavy baryons produced by electro- or photo-production in the target. If there is sufficient polarization transfer, the potentially large analyzing power in weak decays might lead to a significantly larger correction.

It is therefore desirable to directly evaluate the asymmetry correction due to pions, kaons and muons that fall in the detector acceptance. We have a preliminary concept to accomplish this with dedicated "pion" detectors described in Sec. 3.4.2. Using realistic assumptions for the efficiency of measuring the parity-violating asymmetry by integrating the detector response over the full duration of data-taking, the projected statistical error is ~ 105 ppb. This projects to a systematic error of the order of 0.14 ppb on the correction to the Møller A_{PV} in the thin quartz detectors or about 0.5%. The correction and thus the systematic error will be smaller by a factor of 3 for the "shower-max" quartz/tungsten sandwich detectors. Given the redundancy and the different weights to the corrections in the two kinds of detectors, we assign a systematic error of 0.3%. Additional Monte Carlo studies of the kinematic acceptances of pions from weak decays are being planned as input to further refine the conceptual design of the "pion" detectors.

4.5.4 Photons and Neutrons

In a forward spectrometer of the type being discussed, it is very challenging to suppress neutral background from soft photons and neutrons. We will follow a strategy similar to E158, where neutron background was heavily suppressed by burying the photodetectors in a lead shield and we will follow a similar strategy here. We have taken a preliminary look at the collimation system and we believe that we can greatly suppress photon background, designing a near-perfect "two-bounce" collimation system. There will be at most one or two edges from which photons could reach one of the primary detectors after undergoing only one bounce from the target. The flux at these edges will be rather modest compared to the signal flux.

Further suppression will be achieved for the auxiliary Møller detector made of alternating plates of quartz and tungsten i.e. a "shower max" detector. Based on previous experience and simulation, we anticipate suppressing this background at the level of a fraction of a percent and expect to make the correction with an error less than 0.1%. These backgrounds can be measured with special runs, such as by "blinding" the Cherenkov photodetectors and looking for the residual beam-correlated response, as well as runs with the spectrometer magnets turned off. Such backgrounds are not expected to have any polarization asymmetry.

5 Beam Time Request and Run Goals

While the MOLLER apparatus is being designed for a beam current of 85 μA at 11 GeV, we have assumed a beam current of 75 μA and a beam polarization of 80% to formulate the beam time request. If higher beam

Run Period	1kHz Width (ppm)	% Stat. Error	Stat. Error (ppb)	PAC Days (Prod.)	Eff. %	Calendar Weeks (Prod.)	Comm. Weeks	Total Weeks
I	100	11.0	2.94	14	40	5	6	11
II	95	4.00	1.07	95	50	27	3	30
III	90	2.41	0.65	235	60	56	4	60
		2.03	0.54	**344**			**13**	101

Table 9: *Summary of the Estimated Beam Time (75 μA, $P_e = 80\%$).*

current and/or higher beam polarization are considered routine, the request can correspondingly be reduced using the appropriate P^2I factor. In order to ensure the technical success of this challenging measurement, we are proposing to take data in three separate run periods. These run periods have been optimized so that not only important technical milestones are met, but also that each run will provide publishable results and will significantly add to our knowledge of electroweak physics to date.

One important criterion for gauging the amount of running time required is to estimate how close one can approach counting statistics in the instantaneous raw asymmetry measurement (see the discussion in Sec. 3.5.1). From our Monte Carlo simulation, we estimate that $\sigma(A_i)$ for a 0.96 kHz pulse-pair is 83 ppm. Considering the various sources of additional fluctuations such as target density and electronics noise, an aggressive but realistic goal for final production running is $\sigma(A_i) = 90$ ppm. However, it will be challenging to achieve the final goal for $\sigma(A_i)$ in early running, so we will assume 100, 95 and 90 ppm respectively for the three running periods.

Another important criterion is overall efficiency. Generally, once parity experiments have been properly commissioned, the up-time should be 90% for the experimental apparatus, since stable run conditions are required over extended periods of time. Coupled with an accelerator efficiency of 70%, the final running should yield an effective efficiency greater than 60%. Again however, we are unlikely to achieve this in early on. So, we have assumed total efficiencies of 40, 50 and 60% respectively for the three running periods.

We summarize our estimated beam time in Table 9. The total request is for 344 PAC days for production running and 13 commissioning weeks over the three running periods. In the following, we summarize the goals of each run and then discuss special considerations that must be part of the discussion with both the scheduling committee and accelerator operations before final beam time allocation.

5.1 The Three Runs

5.1.1 Run I

The primary goal of the first run will be to commission the principal subsystems of the apparatus. The focus will be on validating the target design, the spectrometer optics, rejection of background and the demonstration that detector fluctuations are dominated by statistics. Once this is established, a reasonable goal would be to achieve a statistical error better than or equal to the E158 result, which we conservatively estimate can be done in 5 calendar weeks. The duration of production running also allows enough sensitivity to demonstrate that there are no anomalously large background asymmetries from charged current processes.

5.1.2 Run II

The primary goal of the second run is to get more than 25% of the proposed statistics so that one is able to achieve $\delta(\sin^2\theta_W) \sim 0.0005$. This would be the single-best such measurement at $Q^2 \ll M_Z^2$, which

could already potentially have a major impact on TeV-scale physics depending on the status of LHC data anomalies. The control of beam helicity correlations must be fully commissioned to achieve $\delta(A_{raw}) \sim 1$ ppb. The fractional statistical error of 4% will require modest but not the ultimate systematic control of absolute normalization errors such as the beam polarization. We have assigned 3 weeks for recommissioning of the apparatus. We will also strive to achieve better than 50% overall efficiency for data collection.

5.1.3 Run III

This run must have all aspects of the apparatus to be working to their full scope. We must also have enough diagnostics in place and sufficient trained personnel within the collaboration so that high quality data can be collected with the best possible efficiency. We are targeting 60% total efficiency. The full control of normalization errors such as the absolute value of Q^2 and the beam polarization at the level of 0.4-0.5% must be achievable. The long duration of this run likely means that it must be split between two fiscal running cycles, and we have assigned 2 weeks of commissioning for each period.

5.2 Special Beam Considerations

Systematic control is one of the most important considerations that must govern various decisions on the design as well as running conditions for the experiment. Two important aspects of this are the methods of "slow helicity reversals" (passive sign flips of the raw asymmetry), and controlled changes to the degree of transverse beam polarization.

5.2.1 Transverse Polarization Running

The large vector analyzing power A_T for Møller scattering (ranging from 5 to 15 ppm at our kinematics) presents a unique opportunity to test the complete apparatus and its capability for absolute normalization at the fraction of a percent level, including detector acceptance, background corrections, azimuthal imperfections, radiative corrections, absolute value of Q^2 and the longitudinal beam polarization. This is because A_T is known theoretically at the 0.1% level. The Møller apparatus is capable of measuring A_T with a fractional statistical error of $\sim 0.2\%$ in a matter of 8 hours at full luminosity. We are therefore planning to request several periods, each lasting 2 to 3 shifts, of 100% transverse polarization in Hall A for a sensitive test of systematics. The periods can likely be synchronized with a change of beam energy that we also plan to request (see Sec. 5.2.4 below).

5.2.2 Wien Angle "Tweaks"

The large A_T value also represents a challenge in terms of systematic control. As discussed in Sec 4.3, in order to ensure a negligible systematic error at the fraction of a ppb level due to a coupling between residual transverse components of the electron beam polarization with azimuthal imperfections in the apparatus, it will be required to make periodic corrections to the polarization launch angle at the polarized source. We estimate that changes at the level of 1° to the launch angle might be requested once a day during production running. Assuming the launch angle was set correctly given the sensitivity of the available diagnostics, over many days the total change to the launch angle should average out to zero to high precision. We expect that these changes will be small enough to have no impact on the average longitudinal polarization that will be seen in any of the Halls that happen to be running at the same time.

5.2.3 The Double-Wien

The "Double-Wien" filter at the front end of CEBAF was commissioned during the PREX run. The system accomplishes a full flip of the beam polarization direction with a aid of two Wien filters and a solenoid lens. The method is very effective because the flip is achieved with a relatively minor change to the beam optics at the front end of the machine. This is a very powerful and crucial way to cancel subtle systematic errors. It would be good to get 50 to 100 flips by this method over the duration of the full set of runs. This might require a configuration change once every 5 to 7 days during production running.

5.2.4 Beam Energy

Over the next two years, as the detailed design of the MOLLER apparatus evolves and depending on discussions with the Accelerator Division, the exact beam energy for MOLLER (somewhere in the range of 10.5 to 11 GeV) will be chosen and used to fix the geometry of the spectrometer and the associate collimation. Once this energy is chosen, we will immediately investigate what minimum configuration change would accomplish a beam polarization sign flip either by slightly reducing the total energy of the machine or moving from symmetric to slightly asymmetric energies in each of the two linacs.

For a symmetric linac configuration change, the beam energy change needed is $\sim$ 93 MeV. This is a small enough fractional change in the total beam energy that the MOLLER apparatus can be designed to accommodate both energies for production running with no other changes. Of course, if an asymmetric linac configuration can be found that will maintain the total energy to be the same while accomplishing a polarization sign flip, that would be desirable. However, we do not believe this is a necessary constraint, especially if it complicates other aspects of beam quality.

Over the duration of all the production running, a total of 10 energy flips would be desirable, with at least one such flip during run I, 3 to 4 flips in run II and 6 to 8 flips in run III, or effectively a configuration change every 6 to 10 weeks during production running. The exact frequency and the nature of the configuration change would be chosen after detailed consultation with the Accelerator and Physics Divisions. Since the requested frequency for the configuration change is similar to that required for transverse running, it might well be optimal to schedule the required 100% transverse running in the period in which an energy configuration change is being made.

6 Collaboration

Our collaboration has extensive experience in the measurement of small, parity-violating asymmetries with proton and electron beams. In particular, we have brought together participants in the ongoing 3rd generation Jefferson Laboratory parity-violation program (Qweak [53] and PREx [52]), plus senior members of the completed E158 [1] program at SLAC. The experimental collaboration is still growing, and we continue to expand international involvement. Theoretical support is provided by A. Aleksejevs, S. Barkanova, J. Erler and M. Ramsey-Musolf.

6.1 Subsystems

In the following paragraph, we list key subsystems and institutions who are interested in design, construction and implementation of them. Note that these are not firm or binding responsibilities and not meant to be comprehensive, but indicate the current thinking of the larger groups in the collaboration given each institution's current interests and previous experience. We have listed all the Canadian institutions (University of Northern British Columbia, University of Manitoba, University of Winnipeg and TRIUMF) as a group in this list and the detailed distribution of responsibilities among them will be determined later.

- Polarized source: UVa, JLab, Miss.St.
- Hydrogen Target: JLab, CalState LA, Miss.St.
- Spectrometer Magnets: Canada, ANL, MIT, SBU, UVa
- Focal Plane Detectors: Syracuse, Canada, JLab, UNC A&T, VaTech, SBU
- Luminosity Monitors: VaTech, Ohio
- Pion Detectors: SBU, LATech, UNC A&T
- Tracking Detectors: William & Mary, Canada, SBU, UVa, INFN Roma, MIT
- Electronics: Canada, JLab, UMass
- Beamline Instrumentation: SBU, JLab, VaTech
- Polarimetry: UVa, Syracuse, JLab, CMU, ANL, Miss.St., Clermont-Ferrand, Mainz, William & Mary, Temple
- Data Acquisition: Ohio, Rutgers, JLab
- Simulations: SBU, UMass, Canada, Berkeley, Idaho State, UVa, LaTech

6.2 Governance

The MOLLER collaboration consists of a little over 100 collaborators from about 30 institutions. At the moment, oversight of the development of the experimental design is being carried out by the spokesperson (K. Kumar) and the Executive Board (EB) whose members are D. Armstrong, J. Gomez, T. Keppel, F. Maas, J. Mammei, K. Paschke, M. Pitt and P. Souder. M. Pitt is the Chair of the EB and the Deputy Spokesperson. We have also formed working groups to organize the development of various subsystems, with coordinators to oversees various developments. The groups and conveners are:

- Polarized Source: G. Cates
- Polarized Beam and Beam Instrumentation: M. Pitt
- Hydrogen Target: S. Covrig
- Spectrometer: J. Mammei
- Integrating Detectors: M. Gericke
- Tracking Detector: D. Armstrong
- Polarimetry: K. Paschke
- Electronics/DAQ: R. Michaels, P. King
- Simulations: S. Riordan, D. McNulty

The collaboration also has an Institutional Board consisting of one principal investigator from each collaborating institution. The IB controls the overall framework of the collaboration and ultimately will establish a speakers bureau, authorship policies etc. If/when MOLLER moves forward as a project funded by DoE and NSF, we anticipate putting a more formalized collaboration structure similar to other projects of comparable size. The spokesperson and the EB Chair are responsible for the day-to-day running of the experiment as a whole. The spokesperson is the principal point of contact with the physics community, the funding agencies and JLab management. Once the project is launched, a project manager (PM) will be appointed and a Technical Board will be formed under the PM consisting of all the group conveners and few additional technical experts. This group would develop the MOLLER project, with oversight from the spokesperson and the EB.

7 Pre-R&D and Evolutionary Design Topics

It is hoped that the MOLLER project can obtain funding approval in FY 15 and that proper planning would allow assembly of the apparatus in the Hall to commence by the end of FY18 or the beginning of FY19. In anticipation of this schedule, the collaboration has developed pre-R&D activities that are being carried out since 2011 and will continue into 2014-15 as we await project funding. We discuss these activities in this section. While some of the topics are being carried out in collaborating institutions with partial graduate student and postdoc efforts from ongoing user grant funds, a significant portion of the activities require technical manpower from national laboratories. There has been a small amount of seed funding provided for these activities by the JLab Physics Division. Based on further discussions within the collaboration and with JLab management, the prioritization of the various activities will be continuously updated given the amount of available funding.

7.1 Polarized Beam

7.1.1 Polarized Laser Light

In collaboration with the Polarized Electron Gun Group at JLab, research has started on methods for achieving the fast helicity flip goal of stable polarization in 10μs. A prototype Kerr cell is being developed. A liquid Kerr material may not experience mechanical shock from a fast high voltage transition and is expected to allow for very fast transition times. As an alternative, studies are continuing on shaping the high voltage transition to speed transition and reduce piezo-optical ringing in a Pockels cell. More generally, the ongoing program of study to optimize alignment and characterization techniques for polarized source optics is continuing.

7.1.2 Beamline Instrumentation

As noted in Sec. 4.1, the experiment requires that the beam charge be measured with a precision of 10 ppm for 1 kHz window pairs. Achieving this goal will require further developments, but they can largely be merged with the lab's continuing efforts to improve the beamline instrumentation electronics. Ongoing investigations have relied on tests carried out during the Qweak experiment (which includes many MOLLER collaborators). As part of its systematic studies, the Qweak collaboration has studied the behavior of its BCM (beam charge monitor) device measurement resolution. These results are helping the MOLLER experiment plan further investigations on this topic. The charge monitoring system used by Qweak consists of two stainless steel microwave cavity charge monitors with a primarily analog electronic read-out system. This system provided adequate resolution ($\sim$ 60 ppm for 240 Hz window "quartets") for the physics production running of the experiment.

For redundancy in this critical measurement, an alternate system was also used during the run. It consisted of two cavity monitors of the same design with a digital electronic read-out system designed by the JLab RF electronics group. This system showed great promise, but it was limited by common mode noise. An improved version of this electronics with better isolation was implemented for the second production run of Qweak in Nov. 2011 - May 2012. Also, two additional cavity charge monitors (equipped with the digital electronics readout system) were added to the Qweak beamline for this run. Routine production running of the Qweak experiment provided data on the stability of the BCM resolution and the valuable comparison of the charge normalization with the two different systems.

Systematic studies will also be performed to measure the charge monitor resolution as a function of beam current and window pair rate for both systems once similar systems are installed in the Hall A beam line and the first beams arrive in the Hall in 2014 after the upgrade, which will facilitate parasitic studies. These studies will help determine most important contributing factors to the charge monitor resolution, which will allow the MOLLER experiment to plan the optimal upgrade path to meet our resolution goal.

7.1.3 Beam Transport

Compared to 6 GeV, at 11 GeV the CEBAF beam will have a much larger emittance due to synchrotron radiation in the recirculation arcs. The effect of this emittance growth will be complicated by skew focusing fields in the RF accelerating cavities and in other optical elements. Accelerator Division has initiated simulation studies of beam properties to predict the increase in beam halo associated with this effect and known non-linearities in machine optics. These studies will also be used to refine procedures for maximizing the benefits of adiabatic damping of helicity-correlated beam asymmetries. The collaboration will encourage and assist this program of studies, including supplementing these studies with beam-based measurements after the energy upgrade.

7.2 Target Design

Work must begin soon on the issue of achieving a reliable conceptual design for the liquid hydrogen target system. The first activities will be more sophisticated simulations with the CFD program by physicists, a review of the appropriateness of the E158 target cell and the loop pump by designers and engineers associated with the JLab target group, and a collaborative effort for calculations related to cryogenic supply and return. A software license has been purchased for the CFD calculations as part of the Early Career award to Silviu Covrig at JLab; the MOLLER target design is now part of a a multi-purpose CFD facility at JLab. Among other things, the possibility of designing and testing a prototype target using liquid nitrogen is being investigated.

7.3 Simulations and Software

The collaboration has chosen to use GEANT4 to develop an application for designing the acceptance and studying the backgrounds for the experiment. Field maps are produced using the "coils only" capability of TOSCA (which was used to design the actual conductor layout for the coils of the magnets) and then read into the GEANT4 simulation. The basic framework of the simulation package for MOLLER is described in App. C.

The geometry used in the simulation will continue to grow in complexity. The simulation group is in the process of designing and verifying a "2-bounce" collimation system for photon background. Additional physics generators are being added for backgrounds from pion production, electrons which scatter from the aluminum in the target cell, and weak decays with large analyzing power, to test the conceptual design of auxiliary detectors, and to gauge the radiation levels in the Hall from neutron production. The simulation will

also be used to determine the expected energy deposited in the collimators and the coils of the spectrometer, and to optimize the dimensions of the radial and azimuthal segmentations of the primary quartz detectors, and design the air light-guides.

The analysis software and software tools needed for MOLLER will be related to those used by previous parity violation measurements at JLab, such as Qweak and PREX. The higher event rate and larger number of detector channels lead to a data rate that would be a challenge for the software to provide rapid diagnostic and analysis results. The development of the analysis software and online tools can progress in parallel with the continuing development of simulation, allowing exploration of different software choices before the electronics and data acquisition designs are fully developed.

7.4 Spectrometer Design

In summer 2010, a Magnet Advisory Group was formed to provide advice to the MOLLER project regarding the design of the spectrometer magnets. The group consists of engineers and physicists who have extensive experience with high power warm magnet designs. The group members are: George Clark (TRIUMF), Vladimir Kashikhin (Fermilab), Dieter Walz (SLAC) and Steve Williamson (UIUC). Their initial input was used to prioritize the design efforts over the past couple of years and also used to optimize the design to avoid potential technical problems.

The conceptual design for the spectrometer has been improved to take into account the actual layout of the conductor within the available space between the beamline and the acceptance electron envelope. Although the current optics with the actual conductor layout are acceptable, efforts are ongoing to improve the focus of the Møller electrons at the detector plane to reduce the size of the peak in order to minimize the contribution from backgrounds. The collimation system also has to be adjusted to work optimally with the new fields, and to reduce the amount of photon backgrounds seen from the edges of the collimators. Conceptual designs of the support structure of the magnets and collimators are being developed, as well as the water-cooling systems for both the toroids and the collimators and the electrical connections for the toroids.

In October 2013, the Magnet Advisory Group was consulted again to update them on the progress made. The feedback has been uniformly positive. We elaborate on a few details in the following.

7.4.1 Toroid Design

The optics of the spectrometer with the actual conductor layouts changed slightly from that of the idealized fields used in the proposal, and further optimization was done in order to minimize both the neutral backgrounds and those from electron-proton scattering, and to improve the radial focus of the Møller peak as well as the radial separation of the Møller and e-p peaks. Studies of the manufacturing tolerances for coil mis-alignments or rotations, as well as for the straightness of the conductor along the length of the coils are now being performed. Preliminary studies of the magnetic forces on the coils need to be expanded to study the effect of coil mis-alignments as well.

Conceptual designs of the support structure and electrical and water-cooling connections are being carefully considered so as not to interfere with the scattered electron envelope, or to cause stray fields which could affect the focus. The support structure must support the weight of the collimators, coils, water and water and electrical connections, and be able to withstand the magnetic forces on the coils as well as the mechanical stresses of the water flowing through the conductor. Initially, TOSCA will be used to check for interferences with the conceptual designs of the coil supports and the various connections. Ultimately, the GEANT4 Monte Carlo package will be used to verify the geometry of the support structure.

7.4.2 Collimation and Shielding

The collimation system is needed to define the acceptance of the Møller electrons, block line-of-sight to the target and shield the coils. A first-pass at such a collimation system has been completed and seems to satisfy the requirement of a "two-bounce" system. The collimators will be neutron sources in the hall, and the shielding for the electronics needs to take this into account. Simulations will also be used to estimate the power deposited in the collimators, some of which will need to be water-cooled.

The next steps will be to develop mechanical designs for the collimators and associated water cooling. The support structure of the toroids will have to support the collimators and allow for the water-cooling connections for them as well. Additionally, once the mechanical structure is defined, appropriate sections of the beamline must be housed in custom concrete structures to limit radiation; these structures must be designed to be easily removable and must be optimized for quick assembly so that multiple runs and interleaving with other projects can be done efficiently.

7.5 Detector Design

Figures 18 and 19 in Sec. 3 show the layout of the main detector elements. The conceptual design is a natural evolution of the experience gained from the performance of the Qweak and PREX detector designs. Ongoing efforts are focused on fleshing out the detector concept and reaffirming the technology choices that were made based on this experience.

7.5.1 Quartz and Light Guide

Thin quartz detectors were the technology of choice for the PREX and Qweak experiments. The shape, dimensions and surface quality of the quartz all play critical roles in determining how many photo-electrons will reach the detector. An equally important issue is the shape and material of the air light guide. We have begun the process of optimization by detailed Monte Carlo studies, which were used to build the first prototypes. In October 2013, the first prototypes were tested in an electron beam at Mainz. The results are now being used to benchmark the Monte Carlo simulation and further optimization will be carried out and verified via cosmic ray studies. More details are provided in App. E.

An important issue that needs further investigation is the amount of potential background in the PMT's from scintillation of charged particles that traverse the light guides after exiting the quartz detectors. Once the quartz geometry is optimized, dedicated test beam studies will be carried out to measure and suppress this scintillation background. An optimized mixture of quenching gases might have to be added to the air in the light guides, and this will be explicitly verified in beam tests.

7.5.2 Mechanical Assembly

We have developed a proof-of-principle concept using a CAD program for a compact assembly of the full complement of quartz detectors and light guides. Once the light guides have been optimized with Monte Carlo simulations and benchmarked with cosmic and beam tests, the next step would be to have an engineering design of the detector assembly, which is complicated not only by the compact and dense detector array, but also the necessity to have a significant lead housing for the light detectors. This significantly increases the weight of the detector assembly and careful thought must be put into designing an assembly that can be properly aligned with respect to the rest of the apparatus. In addition, the entire assembly must be easily transportable in order to facilitate placement slightly beyond crane coverage in the Hall, and to reduce the turnaround time between interleaved projects.

7.5.3 Pion Background

As discussed in Secs. 3.4.2 and 4.5.3, we plan to design auxiliary detectors that will measure the relative flux of pions as well as the resultant parity-violating asymmetry directly during data collection. We have a preliminary conceptual design for these measurements. A full Monte Carlo generator for pion production including those from weak hyperon decays is being developed, and will be used to carry out more accurate simulations of pion background, which will in turn be used to optimize the "pion" detector conceptual design.

7.5.4 Tracking Detectors

As described in Sec. 3.4.3, a tracking system has several critical applications to understand the apparatus and control systematic errors. The GEM technology that is being proposed is part of a significant R&D effort that is important for several other projects after the 12 GeV upgrade at JLab. MOLLER collaborators play a significant role in these initiatives. In addition, a conceptual design for the external GEM detector holders has to be developed, including the capability of remote motion of the tracking planes and a light-weight holder assembly. For a detailed description of design considerations and current R&D activities, see App. F.

7.6 Polarimetry

7.6.1 Compton Polarimetry

The Compton polarimeter upgrade involves physicists from a number of collaborating institutions with prior experience with Compton polarimetry and laser development. One of the largest challenges to operating the JLab Compton polarimeters has been bremsstrahlung photons scattering from narrow beam apertures, which are required by the small electron-laser crossing angle. At 12 GeV, beam emittance growth driven by synchrotron radiation in the arcs of the higher passes might exacerbate this problem.

We will investigate a possible re-design of the electron/photon interaction region to increase the beam apertures. In order to maintain high luminosity at a larger electron-photon crossing angle (required for the larger beam apertures), we propose moving from green to infrared light and upgrading the power build-up cavity gain and injection power. It is essential that the upgraded laser system support a 0.2% measurement of the photon polarization. Recent results from the Hall C Compton polarimeter have demonstrated this level of precision on the laser polarization using back-reflected light to tune the cavity polarization. The Hall A Compton upgrade will implement this technique, and further cross-check the high level of precision claimed for this method.

An alternative concept for a new laser system has also been proposed based on a short-pulse mode-locked laser, either colliding with the beam directly or injected into a low-gain Fabry-Perot cavity. Such a system would significantly simplify the determination of laser polarization while maintaining sufficient statistical power and reducing systematic errors associated with backgrounds. Development of such a laser system could start in parallel with the default design; this alternative would be adopted if studies of the CW system fail to demonstrate sufficient precision in laser polarization measurements.

A separate challenge for 11 GeV operation is the high power of synchrotron light incident on the photon detector from bends in the Compton chicane. Minor changes to the chicane magnets have been implemented to reduce the synchrotron power at 11 GeV to the level observed in 6 GeV operation. These configuration changes will be evaluated when the polarimeter is commissioned following the upgrade. Additional studies of the detector systems for the electron and photon detector systems are also planned, to evaluate their suitability for high precision operation.

7.6.2 Møller Polarimetry

As described in Sec. 4.2.2 and in more detail in App. J, a Møller polarimeter using a pure iron foil target in a 4 T field will be used to cross-check the Compton polarimeter measurement with an accuracy of 0.4%. This is a significant improvement over the PREX-I measurement of beam polarization at 1 GeV in Hall A, which achieved 1.1%, but comparable to the polarimetry accuracy claimed from the Hall C Møller polarimeter. An upgrade of the high-field Møller apparatus in Hall A is underway which will improve its operability and systematic accuracy. It is anticipated that PREX-II (nominally running in 2016) will use this upgraded polarimeter to achieve an accuracy of better than 1%, and further studies will demonstrate the feasibility of 0.4% measurement systematic accuracy.

A separate effort will be made to develop the alternative concept of atomic hydrogen polarimetry for a continuous measurement of the JLab high intensity electron beam. A collaborative effort is in the process of being formed between the institutions interested in this project, led by MOLLER collaborators from the University of Mainz. The Institute for Nuclear Physics there has proposed a new project called MESA. It will produce up to $\sim$10 mA beams with an energy up to 200 MeV and will perform high-precision low-energy parity-violation experiments (e.g. $Q_{\rm W}^p$) as well as dark matter searches. Because of the very low beam energies, the MESA apparatus cannot use a conventional Møller polarimeter or a Compton polarimeter and will need the atomic hydrogen Møller polarimeter for sub-1% measurements. In Fall 2012, the MESA proposal was approved for funding, and the development of the new polarimeter concept has been launched.

It is envisioned that Mainz would become the technical lead on atomic hydrogen polarimetry, though there will be participation also from other US institutions who are part of the MOLLER collaboration. Ultimately, the Jefferson Lab target group would need to play an essential role as well. Researchers have Mainz have acquired a hydrogen cell developed some years ago by the University of Michigan. While this cell is aged and non-functional, it is serving as a model for the construction of a prototype cell. Target cells and the electrodes for sweeping away the ions must be designed. Bench tests will be performed, and beam tests at the Mainz Microtron will be undertaken to prove that the concepts work. This practical experience and testing, along with input from refined simulations, will guide the construction of a polarimeter target for MESA and a modified target cell for JLab (should the decision be made to pursue this option).

The goal of this plan is to produce a working polarimeter based on a storage cell with 100% longitudinally electron spin-polarized hydrogen, with a thickness of at least 6×10^{16} electrons/cm^2, a systematic accuracy of $\leq 0.5\%$, and that can operate in the presence of the 100 μA CEBAF beam. Once the benchmarks have all been established, the apparatus would need to be brought to Jefferson Lab for the MOLLER project. The expensive components are the solenoid and the dilution refrigerator (with its pumps), so it is presently thought that we would share these items between Mainz and Jefferson Lab. The other components of the system are relatively less expensive, and to a degree customized to the laboratory location, so they would be copied locally at each laboratory. We note that the ultimate precision of the polarimetry measurement is only required for the high-statistics Run III. Studies of the iron-foil Møller polarimeter and Compton polarimeter during Runs I and II will either confirm that polarization accuracy of 0.4% is in-hand, or else demonstrate the need for this alternative, continuous polarization measurement.

8 The MOLLER Project

We have taken a first look at all the major MOLLER subsystems to carry out a preliminary costing exercise. Experience from previous experiments, estimates from JLab engineers & designers (albeit quick ones), purchases by other experiments at JLab like Qweak, and quotes from vendors have been used to develop the estimates. While the estimates are very preliminary, attention was paid to apply proper escalation to obtain estimates in actual year dollars, assuming that project engineering and design funding begins in FY16. Table 10 shows the proposed project funding profile after adding 40% contingency. The profile assumes that

Table 10: *Proposed MOLLER project funding profile. Estimates include 40% contingency.*

	Estimated costs in then year $k (escalated)								
	FY12	FY13	FY14	FY15	FY16	FY17	FY18	FY19	Total
Pre-R&D	10	30	50	200					290
R&D									
CDR									
PED					4,678	939			5,617
Construction						9,746	6,099	731	16,576
Pre-ops									
TEC					4,678	10,685	6,099	731	22,193
TPC					4,678	10,685	6,099	731	22,193

CDR = Conceptual Design Report, PED = Project Engineering & Design, TEC = Total Estimated Cost = PED + Construction, TPC = Total Project Cost = TEC + R&D + Construction + Pre-operations.

technical questions requiring prototyping or development have been resolved by the time project engineering & design starts in FY16. With this profile, the experiment could be under assembly in the Hall starting in late 2018, and the first commissioning run could be scheduled in mid-2019. Table 11 shows the Møller project cost highlights, estimated in 2011. A new and more refined cost-estimate which incorporates design studies, prototype tests and cost investigations done over the past couple of years is under way and will be completed by the end of calendar '14.

9 Conclusions

We have described an experimental design to measure parity-violation in electron-electron scattering to unprecedented precision using the 11 GeV electron beam in Hall A at JLab. The project represents a unique opportunity to probe physics beyond the Standard Model. The specific measurement described here would be the most sensitive low energy measurement of a flavor-conserving purely leptonic interaction at low energy and cannot be carried out in any other existing or planned facility anywhere in the world. The project would realize its full potential towards the end of the decade, which is timed well with anticipated results from high luminosity running at the LHC.

A motivated and experienced collaboration is ready to carry out the R&D, design, construction, installation, data collection and analysis. Given the evolution of related projects, the timing of the 12 GeV upgrade, and the compelling physics opportunity, we urge that the MOLLER project be given serious consideration to be reviewed to enter the Critical Decision process as promptly as possible.

Table 11: *Cost highlights of the MOLLER project. Estimates* **do not** *include contingency. The estimates are actual year dollars based on a profile constructed in 2011 escalated for a FY16 project start, as shown in Table 10. Since then, one auxiliary detector has been since eliminated and two more detectors have been added. The estimates shown include JLab overhead.*

Component	Estimate ($k)
Liquid Hydrogen Target	
Engineering & Design (E&D)/Fabrication	1,580
Spectrometer	
Upstream Toroidal Magnet - E&D/Fab.	592
Downstream Toroidal Magnet - E&D/Fab.	1,678
Magnet Collimators - E&D/Fab.	802
Power Supply - 800 kW	326
Main Integrating Detector System - 252 channels	
Quartz, Light-Guides, PMT & HV base	1,283
Pre-Amp & ADC (Triumf)	326
VME Crates, CPUs, cables, connectors, HV supplies	502
Detector Support & Shielding (E&D/Fab.)	797
Testing (including hardware) & installation labor	243
Auxiliary Detectors	
"Shower-Max" Integrating Detectors- E&D/Fab	213
GEM chambers (20 + 4 spares) with electronics	712
Trigger Scintillators	53
Synchronized Rotator with GEM flipping mechanism - E&D/Fab.	191
Pion Detectors (6) (GEMs accounted above)	146
Luminosity Monitors (8) & Shielding/Mech. Support	146
Testing (including hardware), installation labor & integration	300
Hall A Infrastructure	
Beam-line modifications (before target)	788
Add 2 MVA transformer	477
Isolated LCW for magnet cooling - E&D/Fab.	352
300 concrete blocks (stainless-steel rebar)	1,133
Hall cryogenic transfer-line upgrade	1,400
Hall Installation (including labor)	1,112
Miscellaneous	
Computing and Data Acquisition (including CPUs)	415
Project Management	286

A Polarized Beam

A.1 Polarized Electron Source

Laser light illuminates a semiconducting photocathode, the surface of which has been chemically treated to produce a negative work function, referred to as a negative electron affinity (NEA) surface. The laser light wavelength is tuned to promote electrons from a specific valence band to the conduction band of the semi-conductor. The photocathode is held at a negative potential, so as the electrons from the conduction band exit the cathode they are accelerated into the injector beamline.

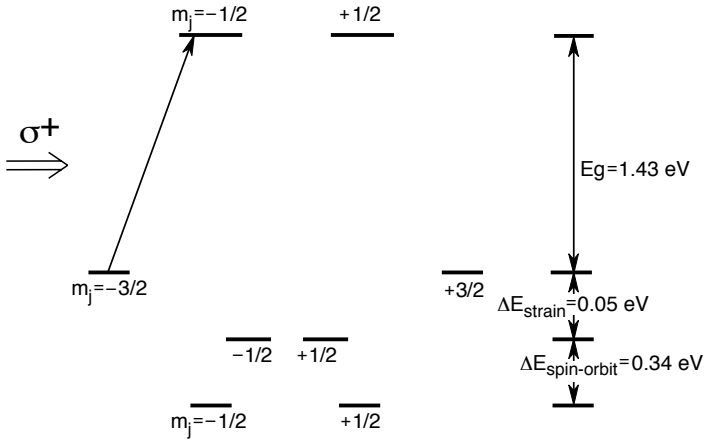

Figure 21: *Band structure of GaAs, showing how circularly polarized laser light produces polarized electrons.*

Through doping or other stress applied to the photocathode, the degeneracy in the spin-orbit states of the specific valence band are split, as shown in Fig. 21. For circularly polarized light, the spin-1 photon is restricted to exclusively promote electrons to a single spin state. This process produces an electron beam polarization of nearly 100%, however, some depolarization occurs in the diffusion of the liberated electrons to the photoconductor surface. The CEBAF polarized source now routinely provides $\sim 85\%$ polarization with up to a few hundred μA beam current.

Since the electron polarization is fully determined by the circular polarization of the incident laser light, it is possible to rapidly flip the helicity of the electron beam by changing the laser polarization. This is accomplished using an electro-optic Pockels cell, acting as a quarter-wave plate to produce circularly polarized light from the initial linear polarization. A reversal of the applied voltage on the Pockels cell reverses the circular polarization of the laser light, and thus the helicity of the electron beam. A schematic diagram of the experimental configuration is shown in Fig. 22.

A.2 Operational Experience

There is significant operational experience in using the polarized electron source for parity-violation experiments at Jefferson Lab [65]. One challenge of these experiments is that changes in the beam properties (intensity, position, profile) will change the detected scattered flux. If the changes in the beam are correlated with the electron helicity, the result can mimic the tiny parity-violating asymmetries. While changes are typically measured and corrections are applied, the corrections are typically made with precision of around 10%. Helicity-correlated beam asymmetries (HCBAs) are therefore a potential systematic error in the mea-

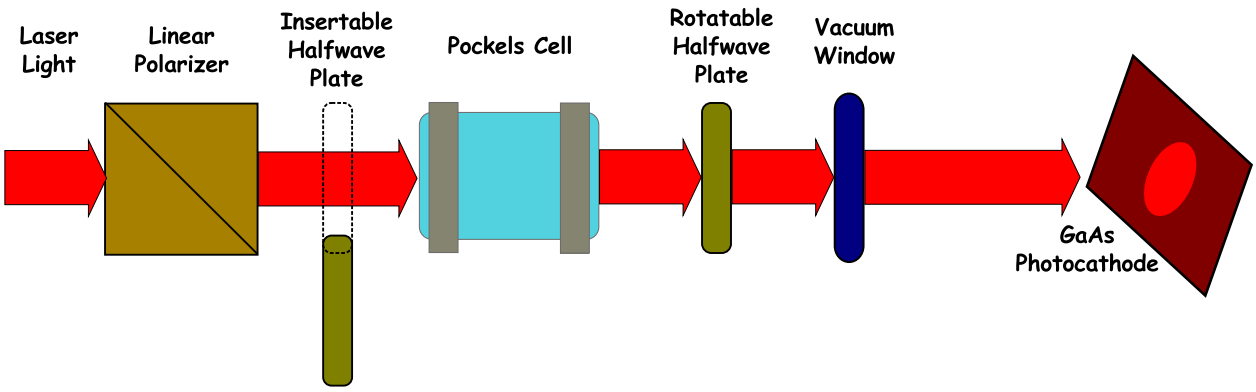

Figure 22: *Schematic of the laser transport line that allows for rapid reversal of the electron beam polarization.*

surement of small asymmetries, and a very high level of control of HCBAs is required for the precision measurement contemplated here.

A sophisticated understanding of the sources of HCBAs at JLab has been achieved. The HAPPEX-II experiment, which ran in Hall A in 2005, made use of this improved understanding to achieve run-averaged helicity-correlated position differences, measured in the experimental hall, which were consistent with zero systematic offset with uncertainties of < 2 nm and 0.2 nanoradian in angle (see Fig. 23).

The PREX experiment, which ran in Hall A in early 2010, and the Qweak experiment, which ran in Hall C during the period October 2010 - May 2012, have statistical-precision goals that are approximately an order of magnitude better than what has been achieved previously at JLab. Regarding systematic effects, the PREX experiment ultimately aims to keep helicity correlated beam motion to < 1 nm (HAPPEX-II achieved < 2 nm) and to bound the beam spot difference to $< 10^{-4}$ of the intrinsic beam size. In the 2010 run, with only eight days of production beam, correlated beam motion was held to < 4 nm with no feedback, a notable achievement in such a short running time when other problems, mostly vacuum related, dominated our efforts. We note finally that the polarized-source setup, fine-tuned to reduce systematics, was probably the best ever achieved. When we are better able to take full advantage of all we have learned about source-related systematics, we are confident that the goal of holding helicity-correlated beam motion to < 0.5 nm for MOLLER is achievable. Between further PREx running (PREx-II is tentatively scheduled to run in 2016), and lessons learned from the completed Qweak experiment, we will gain valuable experience toward meeting the stated MOLLER goals for controlling HCBAs.

A.3 Adiabatic Damping

The impact of helicity-correlated spatial variation in the beam can be greatly reduced in the accelerated beam impinging on the target due to the process of adiabatic damping. A simple consequence of relativistic mechanics is that the available phase space for a beam which has been adiabatically accelerated to a momentum p from a momentum p_0 is reduced by a factor of $\sqrt{p/p_0}$. For the 3 GeV beam energy of the HAPPEX-II experiment, this corresponds to a reduction in beam motion in each dimension by a factor of ~ 95, compared to motion of the 100 keV injector beam.

The benefits of this effect are typically not fully realized; getting close to the theoretical limit requires detailed understanding of accelerator beam optics, tuning and diagnostics. The collaboration typically works closely with accelerator physicists to produce the best results and maintain them over the duration of data

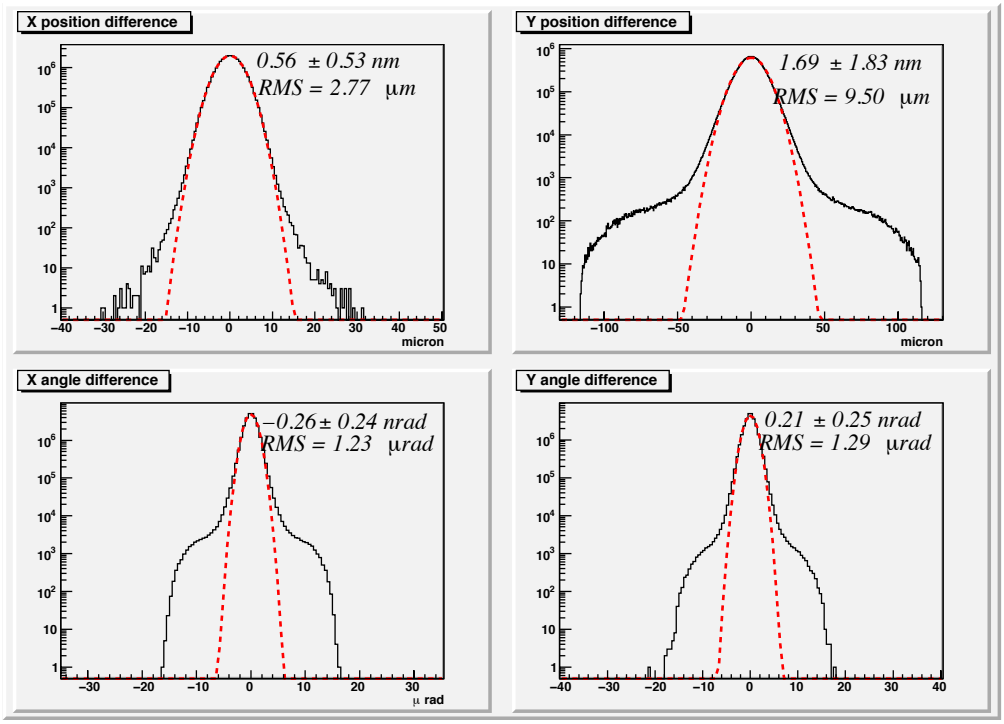

Figure 23: *Beam position and differences, plotted for all* 27×10^6 *pairs of the HAPPEX-II analysis. Arithmetic means, widths, and centroid uncertainty due to random noise are shown. The systematic correlation to helicity was measured to be consistent with zero within the random beam noise. Gaussian fits are included for reference.*

collection. The best performance from the HAPPEX-II experiment suggested that helicity-correlated variations were suppressed by factors up to ~ 30.

The benefits from adiabatic damping have lagged behind the theoretical maximum in part due to difficulties in configuring the 100 keV injector region. Additional diagnostics and optics in that portion of the injector would presumably allow greater benefits to be realized. Such work, in addition to other, already implemented, additions to diagnostics and control, should make it possible to realize a significant fraction of the theoretically maximum suppression factor of 180 for the case of a 11 GeV beam.

Apart from the obvious benefits for helicity-correlated beam fluctuations from adiabatic damping, there are also advantages for random fluctuations in the beam trajectory on target. In order to ensure that one attains the goals for systematic corrections, random fluctuations in beam parameters at 1 kHz must be less than those specified in Table 5. Tests during the running of Qweak have demonstrated that these goals should be straightforward to achieve

A.4 Slow reversals

The technique of "slow helicity reversal" generally refers to the introduction of an additional helicity flip, which changes the sign of the helicity relative to some sources of HCBA. An example would be the introduction of an additional half-cycle $g-2$ rotation, which would reverse the electron beam helicity with respect to the helicity of the beam created in the polarized source. The statistical consistency of data sets taken in different states of the reversal can be used to demonstrate the absence of large, unknown system-

atic errors, and the combination of data sets (appropriately sign-corrected) provides a method for further canceling possible unmeasured or poorly-corrected HCBA effects.

Until quite recently, only one slow-reversal has been commonly employed at CEBAF. A half-wave plate is inserted into the laser path to reverse the sign of laser polarization, relative to the voltage applied to the Pockels cell (see Fig. 22). This slow-reversal is particulary effective for cancelling two types of effects. First, any false asymmetries related to electronic signals, either from the logic or Pockels cell high voltage, will be completely unaffected by the insertion of a half-wave plate. Thus, such false asymmetries will not change sign while the physics asymmetry does change sign. Second, it is well established that when a Pockels cell is pulsed, it can steer or even focus the beam in a fully helicity-correlated fashion that is unrelated to polarization effects. Presumably this is due to the piezoelectric properties of the crystal or simple mechanical stress. Such steering and focussing will be unaffected by the half-wave plate, again insuring the false asymmetries will not change sign when the physics asymmetry does. Many HCBA's, however, are explicitly related to helicity-dependent residual linear polarization. Most of these effects will change sign with the insertion of the half-wave plate just at the physics asymmetry does, and hence are not cancelled. For this reason, other methods of slow-helicity reversal are desirable.

At 11 GeV, the total number of $g-2$ spin rotations will be large, on the order of 120π. It will be possible to change the orientation of spin, while maintaining very similar beam optics properties, by changing the energy of the accelerator by about 100 MeV. This interval is small enough to not require invasive reconfiguration of the experiment: backgrounds, spectrometer optics, etc. should remain very similar. This would be a very effective slow reversal, in that all HCBAs from the source should influence the final measurement with the opposite sign. Since this is disruptive to other halls, this method might be used a few times over the duration of the entire run.

A similarly effective slow reversal that can be used much more often can be created using spin manipulation in the injector. Spin manipulation (using a "Wien rotator") is necessary in the CEBAF source to align the electron polarization into the horizontal plane, and then to set the in-plane launch angle to optimize longitudinal polarization at the experimental target. In principle, it is possible to apply a half-cycle spin rotation without changing the optics of the beam. In practice, this requires a more complicated spin manipulation in the CEBAF injector. The "Double-Wien" filter (shown schematically in Fig. 24) uses a second Wien rotator and a solenoid, which allows a helicity slow reversal using only solenoidal spin manipulation without changes to the Wien rotator setpoints. This system was commissioned prior to the PREX run in 2010, and it was used routinely during both the PREX and the Qweak runs to achieve a slow spin flip with relatively minor changes to the front end beam optics.

A.5 Requirements for 11 GeV

A.5.1 Rapid Helicity Flip

Previous parity-violation experiments at Jefferson Lab have used a rapid helicity reversal frequency of 30 Hz, which had the benefit of largely cancelling beam jitter and electronics noise related to 60 Hz line noise. It will be necessary for future experiments to flip the helicity much more quickly, in large part because it is expected that density flucuations in the high-power cryotarget are limited to frequencies below a few hundred Hz. This proposal is designing around a flip rate of at least 2 kHz, which implies that each helicity state is held for 500 microseconds. In order to avoid excess noise from 60 Hz line variations, a scheme for selecting helicity states will be used which will force complementary pairs at corresponding points in the 60 Hz cycle.

The goal is to flip the Pockels cell within 10 μs, which implies a dead-time of 2%. At present, a settling time of 60 μs is achievable for reversal rates of 960 Hz. However, it has proven difficult to push the transition of the Pockels cell to be shorter than 60 μs while keeping the cell optical properties stable after

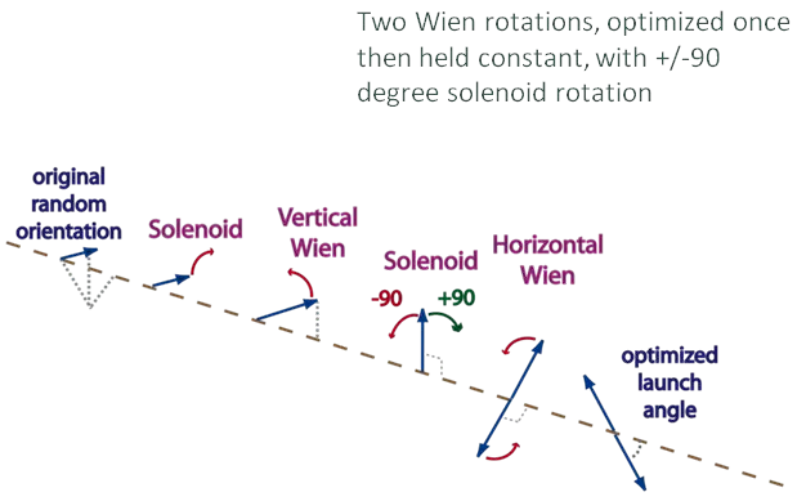

Figure 24: *Schematic of the concept of the "Double-Wien" filter, which allows a full "slow" flip of the electron beam polarization with minimal disruption to the front end electron beam optics. The flip is accomplished by adjusting the second solenoid, without changing the settings of the two Wien rotators.*

the shock of the fast transitions. Additional studies of switching with the Pockels cell will explore possible improvements from both shaping the leading edge of the voltage transition and electrical or mechanical damping of oscillations.

The ringing of the Pockels cell is thought to be related to piezoelectric shock on the voltage transition, and the resistance to completing the transition quickly may be related to other mechanical relaxation effects. A liquid-filled Kerr cell would presumably not suffer from either effect, and is expected to be capable of very fast transitions. Kerr cells are inconvenient compared to Pockels cells, but are none-the-less a very promising route to meeting the needs for MOLLER. R&D on the use of Kerr cells for a polarized source has also been initiated. The studies will make use of characterization techniques developed for Pockels cell studies to evaluate the suitablility of Kerr cells for high-precision measurements.

A.5.2 Measurement and Control of HCBAs

Monte Carlo simulation was used to estimate the sensitivity of the apparatus to beam motion. With the minimum acceptance angle defined by collimators placed 10 meters downstream of the target center, the detected flux in one azimuthal segment is expected to change by approximately 8.5 ppb for a 1 nm shift in the beam centroid. This result is consistent with simple scaling arguments applied to sensitivities measured during HAPPEX-II. This suggests the approximate sensitivity to changes in the beam angle, as well: 85 ppb/nanoradian. The ratio of these sensitivities roughly matches the accelerator which, as a rule of thumb, has a characteristic length of about 10 meters.

A reasonable goal for any measurement of a small asymmetry is to keep the cumulative correction averaged over the entire run due to random or helicity-correlated beam motion to be no larger than the grand statistical error, and to believe the correction to 10% of itself. An important (but not sufficient) step toward achieving this goal is to further insist that beam-related corrections for an individual pulse pair are no larger than the statistical error for that pulse pair, which in our case is 78 ppm for our 1 kHz pairs. The detector for the MOLLER experiment has seven segments and a high degree of azimuthal symmetry. A goal that

greatly facilitates a number of diagnostic techniques is to insist that *the beam-related corrections for each of the detector's segments are no larger than the statistical width of that individual segment, a width that will be around 200 ppm*. It is this goal (together with the caveat that we only assume that we understand our corrections at the 10% level) that guides us in most of our specifications for both beam jitter and monitor resolutions.

It is quite possible to successfully correct for HCBAs on a pulse-to-pulse basis, but still accumulate large HCBAs over the course of the entire run. This could happen, for example, if for whatever reason the corrections were always in a particular direction (with respect to the physics asymmetry). Such a problem might not become apparent until quite late in the run, since the precision of our knowledge of beam parameters during MOLLER will typically only be sufficient to keep corrections small compared to statistics. There are at least two ways out of this conundrum. One is to have significantly improved monitoring of beam parameters, something that would require improved technology beyond what we have demonstrated. The other is to employ feedback. Luckily, we have demonstrated effective feedback for both beam position and intensity at the required level. Of interest here are the sensitivities of the measured asymmetries to the HCBAs, which we will conservatively assume to be ten times better than those quoted above for individual segments.

With all the aforementioned requirements in mind, we find the following specifications for MOLLER:

- The beam centroid must be measured at two locations 10 m apart just upstream of the target with a resolution of a few microns for 1 kHz window pairs.
- The beam centroid and angle jitter must less than ~ 50 microns and ~ 5 microradians respectively at 1 kHz.
- If the beam jitter is significantly larger than quoted above, active position feedback on the electron beam at 1 kHz frequency will be necessary.
- The grand-average helicity-correlated position difference over the duration of the entire run must be less than 1.2 nm and the angle difference should be less than 0.12 nrad.

We elaborate on these issues below. The experience of HAPPEX-II, which found position (angle) differences of around 1 nm (0.2 nrad) suggests that these specifications should be achievable.

A.5.3 Beam jitter and monitor resolution

The most stringent requirement on beam position monitor resolution comes from requiring that the additional random noise contribution from beam jitter (after regression) be no larger than 10% of the counting statistics width for a single azimuthal element of the detector. This leads to a more stringent requirement than applying the same criterion to the average over all detectors. This is important for two reasons. It allows for high precision comparison among selected combinations of the azimuthal detector elements to study the behavior of the linear regression corrections. It also insures the precision necessary to measure the azimuthal dependence of the raw detector asymmetries for the "manual" feedback loop to control transverse polarization described in Sec. 4.3. Applying this criterion leads to a requirement on the beam position monitor measurement resolution of 3 μm for 1 kHz pairs. Qweak has measured the beam position monitor resolution for 480 Hz pairs for the standard "stripline" beam position monitors (BPM). Typical values of ~ 4.5 μm are found (see Fig. 25). Taking the conservative assumption that the monitor noise is dominated by white noise, the scaling from 480 Hz to 1 kHz can be estimated as $4.5\ \mu\text{m} \times \sqrt{2} \sim 6\ \mu$m for the resolution at 1 kHz pair rate. The needed factor of two improvement to achieve the goal should be obtainable from the radiofrequency microwave cavity monitors that are installed in the Hall A beamline. These have not been

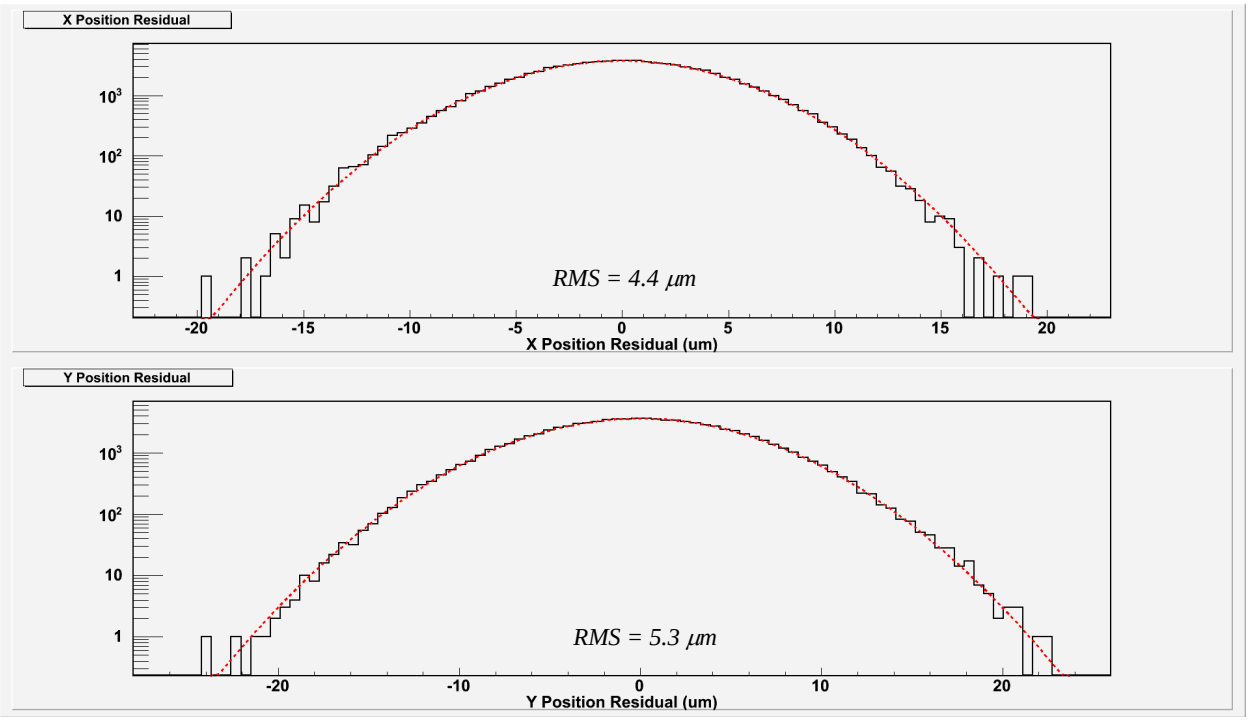

Figure 25: *Typical position measurement resolutions from the Qweak experiment for 480 Hz window pairs for "stripline" beam position monitors. The residuals from a comparison of the measured beam position to the projected position from two upstream monitors are shown.*

used extensively, but initial testing during HAPPEX running in Hall A demonstrated at least a factor of two resolution improvement over the stripline BPMs.

The goal for the accuracy of beam corrections also imposes requirements on the "jitter" (random noise) in the beam properties. Typically, the beam parameter correction sensitivities (the α_j coefficients in Eq. 12) are determined with no better than $\sim 10\%$ precision. For single azimuthal sectors, this implies that the beam property jitter can be no larger than 200 ppm for a single sector (to insure that the resulting random noise contribution after regression is no larger than 10% of the counting statistics width). This leads to these requirements on the maximum allowed jitter (see Table 5): < 47 μm (position), < 4.7 μrad (angle), and $<$ 286 ppm (energy) for 1 kHz window pairs. Typical numbers for the jitter for 480 Hz window pairs from the running Qweak experiment are shown in Figs. 26 and 27. To project to what to expect for 1 kHz pairs, we assume a white noise assumption and multiply by $\sqrt{2}$ to obtain projected jitter values of: ~ 48 μm (position), ~ 1.4 μrad (angle), and ~ 6.5 ppm (energy). Thus, all of the jitter requirements appear achievable, assuming the jitter behavior is similar after the 12 GeV accelerator upgrade.

As with past parity experiments, we will normalize our detector signals to beam intensity on a pulse-to-pulse basis. Here it is critical that the beam charge monitors (BCMs) and detector electronics chain are highly linear, something we expect will be true at the level of 1% or better. In our error budget (Table 4) we have allowed ourselves a 0.3% relative error associated with the BCM linearity, something that corresponds to about 11 ppm for an individual 1 kHz pulse pair when averaged over the entire detector. To be conservative, we have thus set a goal of 10 ppm for the BCM resolution associated with an individual pulse pair. Using this resolution, can can also put a limit on allowable jitter in the beam intensity. With a 10 ppm BCM resolution and 1% linearity we can tolerate beam intensity jitter of 1000 ppm (0.1%) before the jitter itself

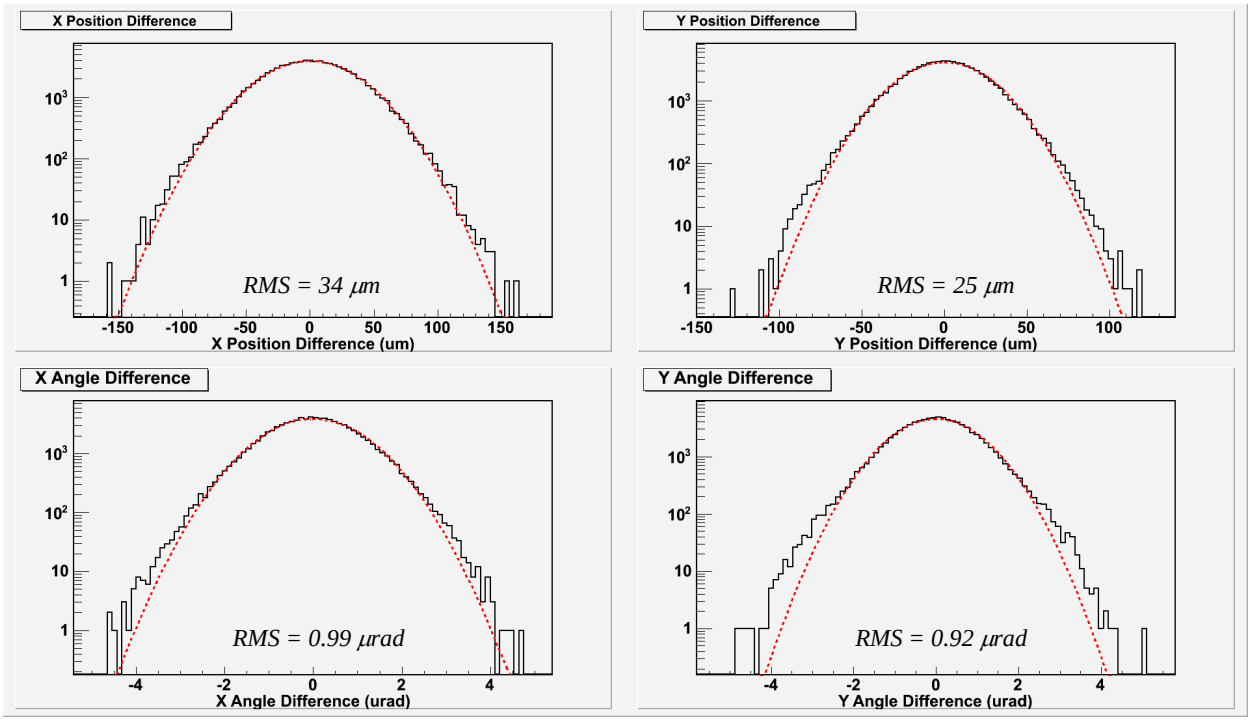

Figure 26: *Typical X and Y position and angle difference distributions for 480 Hz window pairs from the Qweak experiment at 160 μA beam current. The RMS values from the Gaussian fits are the random beam noise ("jitter") in these parameters.*

begins to add to the pulse-to-pulse statistical width. The recent Qweak data on intensity jitter at 480 Hz is shown in Figure 27. Applying the standard $\sqrt{2}$ "white-noise" scaling factor predicts ~ 500 ppm for 1 kHz pairs, so the goal of 1000 ppm seems easily achievable. Finally, we note that random noise at the 10 ppm level from the BCMs, when added in quadrature to the roughly 80 ppm 1 kHz pulse-pair statistical width will result in less than a 1% increase in the statistical width.

A.5.4 Position Feedback

A more significant problem might be the slow convergence of the random beam jitter. Even with no systematic helicity-correlated offset, beam jitter of 5 micron would converge to zero with a 1σ range of 0.8 nm.

A systematic non-zero helicity-correlated position difference could be diagnosed more quickly, and the potential loss of statistical precision could be mitigated, by forcing the random jitter to converge through feedback. This feedback would necessarily be helicity-correlated, and operate with a time-scale between a few minutes and a few hours. The optimized feedback time-scale will depend on the safe dynamic range of the feedback system, the time scale of any slow-reversal or other significant beam disturbance, and the magnitude of the jitter, among other factors.

The goal of any such feedback would be to improve on the statistical rate of convergence for the beam position jitter by a relatively small amount. Under optimal feedback, the centroid would converge to zero as $1/N$, where N is the number of integration periods of the feedback cycle, compared to $1/\sqrt{N}$ for the case without feedback. A balance will need to be found between keeping the average feedback correction small, while still operating on a time scale that drives convergence to zero position difference. Updating feedback

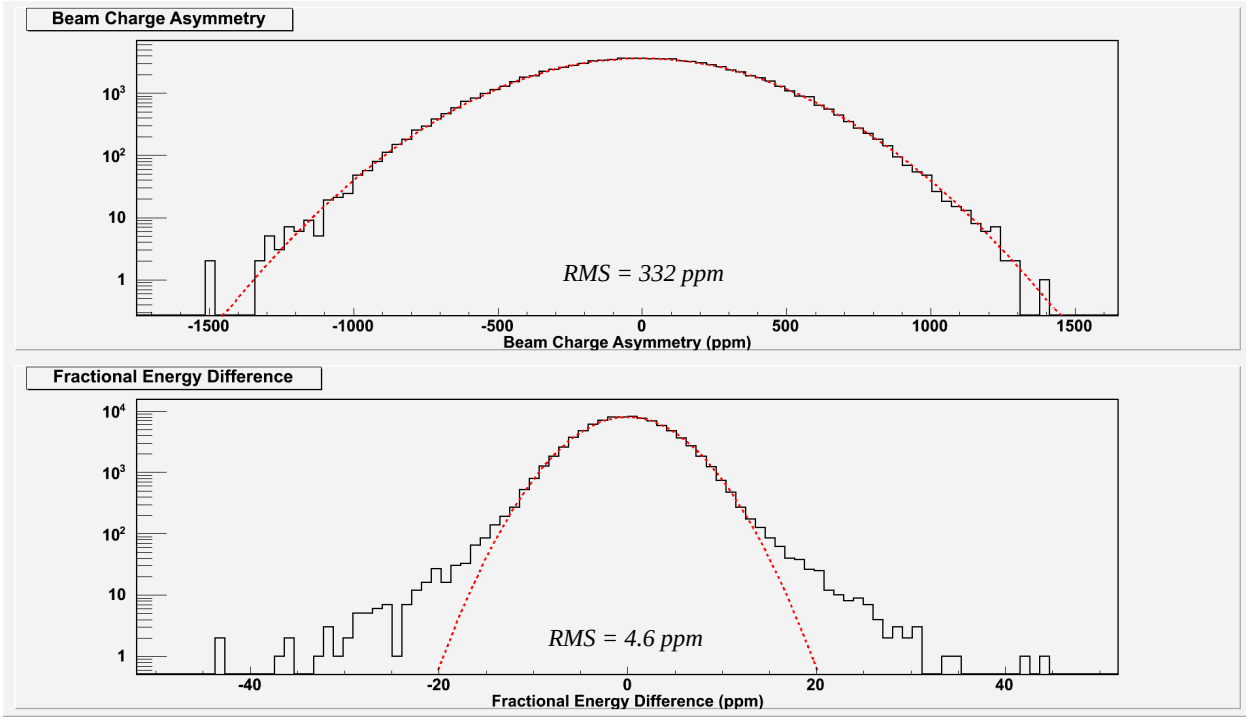

Figure 27: *Typical intensity asymmetry and energy difference distributions for 480 Hz window pairs from the Qweak experiment at 160 μA beam current. The RMS values from the Gaussian fits are the random beam noise ("jitter") in these parameters.*

every hour, for instance would improve convergence by a factor of $\sqrt{8}$ on an ideal shift, while implying that the size of the correction would be around 4×10^{-3} of the beam jitter.

It is important not to mask serious configuration problems in the polarized source with the use of intensity and position feedback systems. For this reason, the average position correction will be monitored for significant non-zero average corrections which indicate the need for re-tuning of the polarized source. It is also crucial that any position dependent feedback does not change intensity asymmetries in a way which reduces the rate of convergence of the crucial intensity feedback.

There are several mechanisms which could be used for position feedback. The commonly employed technique at Jefferson Lab, successfully employed by the G0 collaboration, uses a piezoelectric actuated mirror in the source optics to deflect the laser beam. Similar techniques were employed or tested by the E158 collaboration at SLAC and the SAMPLE collaboration at Bates.

Since the dominant source of position differences is a non-zero first moment in the helicity-dependent residual linear polarization distribution of the laser spot, a superior feedback mechanism might involve a birefringent element with a variable, linear variation of birefringence across the beamspot. Such a device could be conceptually similar to the continuously variable birefringent system, such as the Babinet-Soleil compensator.

There are several disadvantages to position feedback mechanisms which operate on the source laser. The most important is that the photocathode changes significantly on the time-scale of days. Ion back-bombardment damages the photo-cathode, creating a quantum efficiency "hole" at the laser spot and along a path to the electrical center of the cathode. Motion of the beamspot on the cathode can interact significantly with these strong QE gradients, changing the effective slope of the correction and creating significant coupling with electron beam intensity.

These complications can be avoided by using magnetic deflection of the electron beam. A system of 4 air-core magnets has been constructed in the injector, with a fully isolated power and control system. These were constructed by the Electron Gun Group as a potential feedback mechanism. As expected, this system avoids the significant coupling to beam intensity which complicates use of the piezoelectric mirror. Further testing would be required to qualify this system at the required level of precision, and at the 2 kHz reversal frequency.

A.5.5 Beam spot-size asymmetry

Geometric arguments predict that the sensivity to a spot size asymmetry $\delta\sigma/\sigma$ is approximately (12 ppm)$\delta\sigma/\sigma$. An upper bound on the spot size asymmetry should be possible from measurements on the laser table of $\frac{\delta\sigma}{\sigma} < 1 \times 10^{-4}$, which would imply a net false asymmetry of about twice the statistical error bar over the course of the run. Spin precision spin flips, including both the $g-2$ and spin-manipulator slow reversals, will both serve to flip the helicity without changing the spot size asymmetry, and should provide a high degree of cancellation. Assuming roughly equal statistics are collected in each reversal state, the average effect from spot size should be reduced by a factor of 10.

A.6 Strategy for control of HCBA

As described above, modest improvements on the state-of-the-art are necessary to achieve sufficent control on the run-averaged helicity-correlated beam asymmetries. A summary of the strategy is presented here.

The intensity asymmetry requires control at the level of < 10 ppb. As with previous experiments, an automated helicity-correlated feedback on beam intensity will be required to achieve this small value. There does not appear to be any fundamental reason why the conventional asymmetry feedback scheme should not converge to this level. While this is approximately an order of magnitude beyond what will be required for the PREX and Qweak experiments, those runs will provide an opportunity to demonstrate feedback effiency at the required level.

Control of position differences will require careful configuration of the source optics. As is currently done, the optics system will be qualified first with diagnostics on the laser table, and then with measurements of HCBA in the electron beam in the low-energy injector. It is estimated that improvements in the injector measurements are feasible which would enable precision scans of important configuration parameters leading to the verification of injector position differences approaching ~ 20nm. As is required for the PREX experiment, the potential spot size asymmetry will also be bounded in laser table studies at the level of 10^{-4}, which limits the potential effect on the measurement at the level of 1 ppb.

Good optical transport throughout the injector and accelerator is crucial to realizing the benefits of the adiabatic phase space damping. It should be possible to achieve a damping factor approaching 100 (about half of the theoretical maximum) if further improvements in injector diagnostics are made. In combination with a source configuation giving position differences in the injector at the level of 20 nm, the average systematic helicity-correlated offset would lie in the 0.2 nm (0.02 nrad) range, sufficient for this measurement.

If the careful beam preparation succeeds at this level, the dominant source of helicity-correlated beam position difference would be the slow convergence of the random (non-helicity-correlated) beam motion. For this reason, it may be necessary to employ feedback on position differences. The feedback integration period would be long enough to allow small corrections to position differences, which are not likely to interfere with other aspects of beam preparation or delivery. The magnitude of feedback corrections will be monitored for signs of a required reconfiguration of the polarized source.

Several slow reversals will be employed. The insertable halfwave-plate in the source optics will be used frequently, possibly changed at 4-12 hour intervals. A frequent spin-manipulation slow reversal is required to cancel spot size asymmetries, so the injector solenoid slow reversal should be used on a period

of approximately 1 week. The $g-2$ energy change spin flip, should be used at least once, dividing the full data set in two. Although it is potentially more disruptive, it is also expected to be the most effective of the slow reversals, and the experiment would benefit from using it as often as once per month.

B Detailed Discussion of the Hydrogen Target

As mentioned in the discussion of the experimental design, our preliminary assessment using the Computational Fluid Dynamics code `FLUENT` is that the E158 target cell is a good starting point for the design of the high power target required for this experiment. Experience with the Qweak target using JLab's high intensity, CW beam is crucial for benchmarking our simulations so that the performance of the new target can be predicted with confidence. We also examined whether sufficient target cooling power will be available on site in the 12 GeV era. This can be a complex and potentially contentious issue since it depends on things which simply are not known today, such as the ultimate heat load of the new SRF cavities during 12 GeV operations. However, extremely helpful discussions with the Cryo Group have suggested one logical and reasonable path forward which we present below.

The following sections contain a detailed discussion on these issues.

B.1 Comparable Targets

Unpolarized LH_2 targets with internal heat dissipation of up to 1 kW have been successfully and safely run in the SAMPLE, HAPPEX, PVA4, G0 and E158 experiments. The LH_2 target for the Q_{weak} experiment is the first target in the world that has significantly exceeded 1 kW in internal heating. It was recently commissioned and successfully operated at over 2.9 kW, higher than its design power of 2.5 kW.

Although these targets could not be more different in geometry and experimental conditions, they all have as a central part a cryogenic closed re-circulation loop, made of a thin-windowed cell traversed by the beam, a heat exchanger, an in-line pump and a high power heater. The central part of the cryogenic loop is the target cell as it is the region where the interaction between the target fluid and the e^- beam takes place. The rest of the loop is designed around the cell to satisfy the needs for cooling power and fluid flow.

In this respect the MOLLER target will have the same conceptual components as previous LH_2 targets. The design will have to satisfy the detector acceptance requirements, and, more stringently for such a high luminosity and high precision experiment, the target density variations that affect the physics measurement will have to be minimized. In nominal running conditions the MOLLER target is rated for 5 kW.

For the first time for such targets, Computational Fluid Dynamics (CFD) simulations were used to design the Q_{weak} target cell. The CFD software engines used were `FLUENT 6.3` and `FLUENT 12.0` developed by Fluent Inc. (now part of ANSYS). The Qweak target was recently commissioned and its measured performance indicates that its design goals have been met. The target has been successfully operated with 3 kW of cooling power. It has been run routinely now at beam currents between 150 and 180 μA. The target boiling contribution to the asymmetry has been measured using several techniques. At 180 μA, the measured target noise is only 46 ppm with a 4x4 mm^2 raster and 960 Hz helicity reversal frequency. The bulk density changes have also been bounded to less than 0.2% at 150 μA. Further experience with the Q_{weak} target will be used to benchmark the simulations, thus reducing technical risk.

B.2 Target Parameters

The Møller experiment at 11 GeV proposes using a 150 cm long liquid hydrogen target cell. The nominal beam intensity is 85 μA and the nominal beam raster size is 5 mm x 5 mm. The nominal running point for LH_2 in the thermodynamic phase space (p, T) is 35 psia (2.38 atm) and 20 K, although these parameters might change slightly depending on the refrigeration solution for the target. In these conditions the liquid is 3.7 K below the liquid-vapor curve and its density is 71.5 kg/m^3. The target thickness is 10.72 g/cm^2 and its radiation length is 17.5 %. The heating power deposited by the e^- beam in the target cell is given by

$$P = I\rho L\frac{dE}{dx} \tag{14}$$

where ρL is the nominal target thickness in beam, I is the beam intensity and dE/dx is the average energy loss through collisions of one electron in unit target thickness. If $dE/dx = 4.97$ MeV/(g/cm^2) for electrons of 11 GeV in LH_2 then $P = 4533$ W. For an Al target cell made with beam entrance and exit windows of 0.127 mm (0.005") each, the heat deposited by the beam in the windows, calculated with Eq. 14, is 6.4 W per window. The cumulative beam heating in the target cell is then 4546 W. The nominal parameters of the target and beam are in Table 12. In order to minimize target density variations, all high power LH_2

Table 12: *Møller LH_2 target and beam nominal parameters.*

Target Parameters		Beam Parameters	
cell length	150 cm	I, E	85 μA, 11 GeV
cell thickness	10.72 g/cm^2	raster	5 mm x 5 mm
radiation length	17.5 %	beam spot	100 μm
p, T	35 psia, 20 K	detected rate	153 GHz
ϕ acceptance	5 mrad (0.3°)	helicity flip rate	2000 Hz
target power	**5000** W	beam power	**4546** W
ρ fluctuations <26 ppm			

targets run in a closed feedback loop with the high power heater, allowing a constant heat load on the target to be maintained over time. The heater needs to account for beam heating and target power losses to the environment (such as radiative and viscous losses) and maintain a cooling power buffer for the feedback loop. Based on experience with previous such targets, the losses and the buffer account for about 10 % of the beam heating. Taking this into account the Møller target is rated for 5000 W of cooling power in nominal running conditions, which is a factor of 2 higher than the Q_{weak} target rating, and by far the most powerful LH_2 target ever built and with the most stringent requirements on systematic effects.

The measured detector asymmetry width for the Møller detector is given by $\sigma_m^2 = \sigma_A^2 + \sigma_b^2$, where σ_A is the counting statistics width and σ_b accounts for systematic effects independent of counting statistics, which are typically dominated by the target density fluctuation (boiling) on the time scale of the helicity pair. For the current design parameters, the projected counting statistics width for the experiment is about 80 ppm. Target density fluctuations on the level of less than 26 ppm would contribute only a few % to the measured asymmetry width, σ_m.

B.3 Density Variation

The Møller target will use LH_2 as the target material and it thus contributes two important systematic uncertainties on the physics measurement: density reduction and density fluctuation. The equation of state of the target fluid in steady-state isobaric conditions is $\rho(p,T) = \rho(T)$. Density reduction is the effect of the fluid density variation with temperature caused by beam heating over the volume of the target cell illuminated by the beam. A LH_2 temperature increase of 1 K causes a density reduction of $\Delta\rho/\rho \approx 1.5$ %. Whenever the beam is on target, a dynamic equilibrium is established in the interaction region, where the temperature of the fluid increases locally with respect to the beam-off condition and the fluid density decreases, resulting in a net reduction of the target thickness in beam. If the target fluid density reduction is e.g. 5 % then the experiment would have to run 5 % longer to get the same statistics as expected from a fixed target density. Density reduction can be predicted analytically for laminar fluid flow and it is usually mitigated by increasing the fluid turbulence in the interaction region.

For the Møller target a laminar fluid flow of 1 kg/s transverse to the beam axis would result in a temper-

Table 13: *Liquid hydrogen targets for parity violation experiments. The first group represents actual operating targets, while the last one is a target under design.*

	p/T/$\dot{m}$ psia/K/kg/s	L cm	P/I W/μA	E GeV	beam spot mm	$\Delta\rho/\rho$ %	$\delta\rho/\rho$ ppm
SAMPLE	25/20/0.6	40	700/40	0.2	2	1	<1000 @60Hz
					4.8x4.8		<100
HAPPEX	26/19/0.1	25	1000/100	3.481	6x3		@30Hz
PVA4	25/17/0.13	10	250/20	0.854	0.1	0.1	392 @50Hz
E158	21/20/1.8	150	700/11-12	45/48	1	1.5	<65 @120Hz
G0	25/19/0.3	20	500/40-60	3	2x2	1.5	<238 @30Hz
Q_{weak}	35/19/1	35	2500/180	1.165	4x4		<50 @250Hz
Møller	35/20/1	150	5000/85	11	5x5		<26 @2000Hz

ature increase of 0.5 K in nominal running conditions and a relative density decrease of less than 1 %, which would be further decreased by turbulence effects and would be negligible in this experiment. A summary of design parameters and target systematic effects for previous and future LH_2 targets used in parity violation experiments is presented in Table 13. The quoted target systematic effects for targets that have run before are the measured ones, for the Møller targets they are the desired ones. The two highest power LH_2 targets in the world have the most stringent requirements for target density fluctuation compared to the previous targets.

The target density fluctuation effect is usually dominated by the target cell windows region. The heat density deposited by the e^- beam in the thin Al windows is typically one order of magnitude higher than the heat density deposited in LH_2. The heat deposited by the beam in the window material is dissipated through conduction in the window material and convection on only one side of the window, the LH_2 side, as the other side is exposed to vacuum. The target liquid boils at a window with high probability if two partially correlated effects happen simultaneously: surpassing the critical heat flux and a temperature excursion between the window and the bulk liquid greater than some tens of degrees. Typically for these targets the heat flux from the window to LH_2 is much higher than the critical heat flux for boiling. The critical heat flux for LH_2 at a wall is on the order of 10 W/cm^2 [66]. The total heat flux at the windows in nominal conditions is 43 W/cm^2 for the G0, 78 W/cm^2 for the Q_{weak} and 25.6 W/cm^2 for the Møller targets respectively. CFD simulations revealed that over the beam raster area the convective part of the total heat flux is 18 W/cm^2 for the G0 target and 33 W/cm^2 for the Q_{weak} target. The temperature excursions determined with CFD for the G0 and the Q_{weak} targets at the windows are on the order 10-30 K. The G0 and the Q_{weak} targets seem

likely to develop liquid boiling at the windows. Of these three targets the Møller target has the lowest total heat flux at the windows and careful CFD design could drop the convective part of the total heat flux below the boiling threshold.

From experience with previous LH_2 targets, the effect of density fluctuation is mitigated by optimizing both fluid conditions (flow, turbulence etc.) and beam conditions (raster size, intensity). The measurements done with the G0 target [67] at a helicity flip frequency of 30 Hz indicate a drop by a factor of 2.4 in the magnitude of density fluctuations when the raster size was increased from 2 mm to 3 mm at constant pump rotation, and by a factor of 3.5 when the pump pressure drop was doubled at the same raster size.

For the Møller experiment, we plan to run with a helicity flip frequency (2000 Hz) that is nearly two orders of magnitude greater than the 30 Hz that was routinely used for first generation parity experiments. More recently, the Qweak experiment successfully used a flip rate of 960 Hz. As noted above, the counting statistics and target density fluctuation asymmetry widths add in quadrature to give the measured statistical width. The advantage of the higher helicity flip frequency is that it is expected to reduce the relative contribution of the target density fluctuations to the measured asymmetry width. As the helicity flip frequency is increased, the counting statistics width increases, while the expectation is that the target density fluctuation width will decrease (or at worst remain constant) with increasing frequency.

To make an estimate of the target density fluctuation width for the Møller target, we use the measured G0 target properties as a starting point. The G0 target has a longitudinal flow design similar to the E158 target, which we are using for prototyping a Møller target cell. The G0 target was run in the CW JLAB electron beam (as opposed to the pulsed beam used in the E158 experiment at SLAC). An upper limit of 238 ppm was observed for the target density fluctuations in the G0 target at 40 μA beam current. We estimate the density fluctuations in the Møller target by using conservative power laws for each of the parameters known to affect density fluctuations. We expect the target density fluctuations to vary inversely with the raster area and linearly with the beam power; these expectations have been borne out by previous target studies. Data from previous targets on the dependence on mass flow rate have not been completely consistent (which could be due to the fact that different target designs were being compared), but the dependence always rises faster than linear. For this estimate, we assume a linear dependence on mass flow rate, which is the most conservative choice.

Finally, we estimate the dependence on helicity flip frequency from an empirical power law measured in Q_{weak} beam tests done in June 2008. Data were taken at helicity flip frequencies of 30 Hz, 250 Hz, and 1000 Hz on both a carbon and 20 cm hydrogen target at a range of beam currents. The hydrogen target available for the test was not one that was optimally designed for minimization of density fluctuations, but we ran at a variety of beam currents to see if our conclusions were valid over a range of "boiling" conditions. The scattered electron rate was monitored with "luminosity" monitor detectors at small scattering angles. The data from the carbon target were used to determine the parameterization of all sources of random noise other than the target density fluctuation effects in the hydrogen target. The result of the work was the target density fluctuation width as function of helicity flip frequency determined at a variety of beam currents. The results are shown in Figure 28. A simple power law ($\sigma_b \propto f^{-0.4}$) describes the data well as a function of helicity flip frequency f for the beam currents of 40, 60, and 80 μA. Data were also taken at 10 and 20 μA, but contamination from 60 Hz power line noise made it difficult to draw meaningful conclusions; a refined analysis will be pursued to try to extract information at those currents. Explicit measurements with the Qweak target at 960 and 480 Hz helicity reversal frequencies verifiy that target noise scales according to this empirical power law.

In summary, the assumed scaling arguments for estimating the target density fluctuation widths are: linear in beam power, inversely linear in beam raster area, linear in mass flow rate, and $f^{-0.4}$ in helicity flip frequency. The input parameters for the G0 target are an upper limit of 238 ppm target density fluctuations for a 20 cm long target, 40 μA beam current, 2 mm square raster size, 30 Hz helicity reversal rate, and 0.25 kg/s mass flow rate. The corresponding expected parameters for the Møller target are a target length of 150

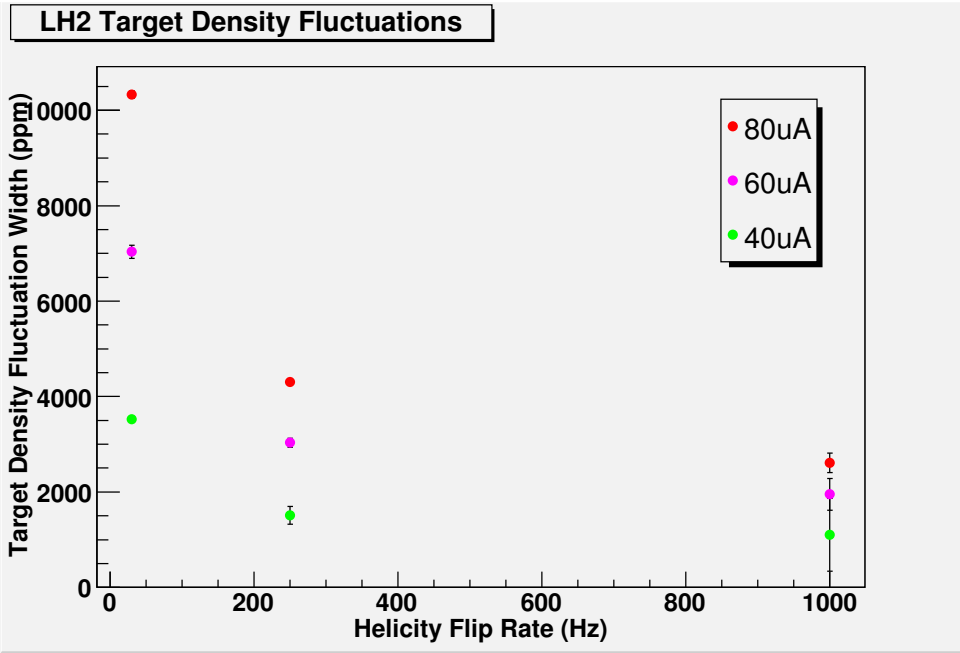

Figure 28: *Target density fluctuation widths versus helicity flip frequency from recent Q_{weak} beam studies.*

cm, 85 μA beam current, 5 mm square raster size, 2000 Hz helicity reversal rate, and 1.0 kg/s mass flow rate. Applying the scaling leads to an estimate that the target density fluctuations for the Møller target could be as large as 26 ppm corresponding to 5% excess random noise.

This will be discussed in more details in section B.6 with the latest Q_{weak} target experience, which shows that the situation is better than the conservative scaling arguments starting from the G0 target information.

B.4 Cell Design

A 150 cm long cell was used in the 55 liter LH_2 target for the E158 Møller scattering experiment at SLAC at 45 GeV and 48 GeV electron beam energies. The E158 target was rated for 700 W beam heating removal and 1000 W cooling power. The E158 target density fluctuations contributed 65 ppm [68] to a Møller detector asymmetry width of 200 ppm at a repetition rate of 120 Hz or about 5 % of the detector asymmetry.

A drawing of the target cell for the E158 experiment is in Fig. 29. The target was designed and built by a group from Caltech led by Cathleen Jones. The cell is made of 3" ID pipe with a 3" inlet and outlet that are connected to the rest of the vertical cryogenic loop. Inside the target cell there are 8 wire mesh rings (see Fig. 29), with a 45^o cut-out and 1.5" diameter clearance in the middle. The rings are to increase fluid turbulence and mixing in the cell. This cell is a natural first candidate for a target cell for the Møller experiment at 11 GeV. For this reason the cell design from Fig. 29 was studied in a steady-state CFD simulation in `FLUENT` under the nominal running conditions from Table 12. The heating from the electron beam was implemented as a uniform power deposition in the volume of the cell illuminated by the rastered beam to yield 4.5 kW in this volume. The cell walls are made of Al and the beam heating in the windows was implemented also as a uniform power deposition to yield 12.5 W. Hydrogen properties are implemented as functions of temperature in isobaric conditions from the freezing point to 300 K. No boiling model was implemented for hydrogen. The mass rate considered was 1.2 kg/s. The cell volume is 7.8 liters. The cell was simulated both with meshes and without. The results from Figs. 30a-30d are for the cell with internal meshes. The global temperature increase of the LH_2 between the inlet and the outlet to the cell is 0.37 K but

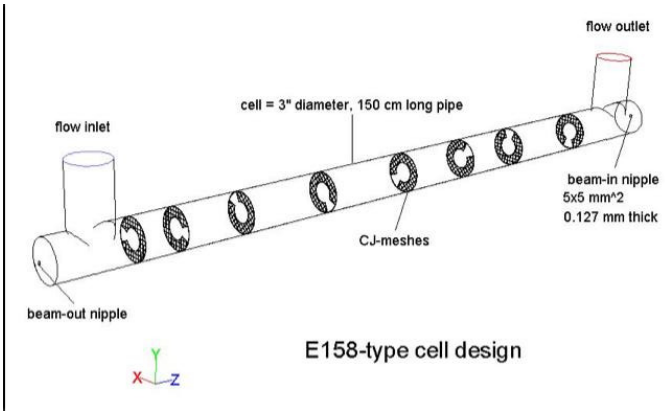

Figure 29: *E158-type target cell design. Note that the fluid flow (left to right) is opposite the electron beam direction (right to left).*

the average over the beam volume is 1.23 K, which yields a LH_2 density reduction of 2 %. The temperature averaged over the cell windows' beam nipples is 30.1 K for the beam-in window and 34.8 K for the beam-out window. The heat flux, predicted by `FLUENT`, from the window nipples to LH_2 is 4 W/cm^2 for beam-in and 8 W/cm^2 for beam-out respectively, which are both less then the critical heat flux for LH_2. *This would indicate that there is a low probability of liquid boiling at the windows.* Although the cell is symmetrical between the inlet and outlet the flow near the end caps of the cell is not. The cap at the inlet (with the beam-out window) experiences a large vortex with very little flow in the middle, where the liquid seems to be boiling. The pressure drop over this cell at this flow rate is 0.49 psid. The cell design would have to be refined to get rid of the bulk liquid boiling, but it looks promising in the windows region.

B.5 Refrigeration

An examination was carried out to ascertain whether sufficient target cooling power will be available on the JLab site in the 12 GeV era. Such an estimate is complex since it depends on things which simply are not known today, such as the ultimate heat load of the new SRF cavities during 12 GeV operations. However, after discussion with the JLab Cryo Group, a logical and reasonable path forward has been established.

If the accelerator delivers electron beams at 12 GeV and all the new SRF cavities continue to show high heat loads, there might be little spare capacity from the new Central Helium Liquefier (CHL). However, the ESR #2 could deliver 4 kW cooling power at 4 K and could be modified to deliver more than 6 kW of cooling power at 15 K and 3 atm. A similarly novel design feature involving the reconfiguration of the existing transfer line has now been validated by Q_{weak}, in order to simultaneously supply both 4 K coolant and 15 K coolant to the target, and in particular, to return both coolant sources on separate lines back to the ESR.

A director's review of JLab cryogenic capacity has been held recently. The final report is available at

`http://www.jlab.org/div_dept/dir_off/ccr/.`

The MOLLER experiment's 5 kW cooling power requirement figures prominently in the report. The report states that the planned ESR #2 by itself has the 5 kW capacity required for the MOLLER experiment. The ESR #2 building is currently under construction, and the refrigerator has been designed (but not yet funded). However, the first of the director's review committee's recommendations is that funding be secured for ESR #2 on a timeline that will make it available for the MOLLER experiment. Finally, the report also

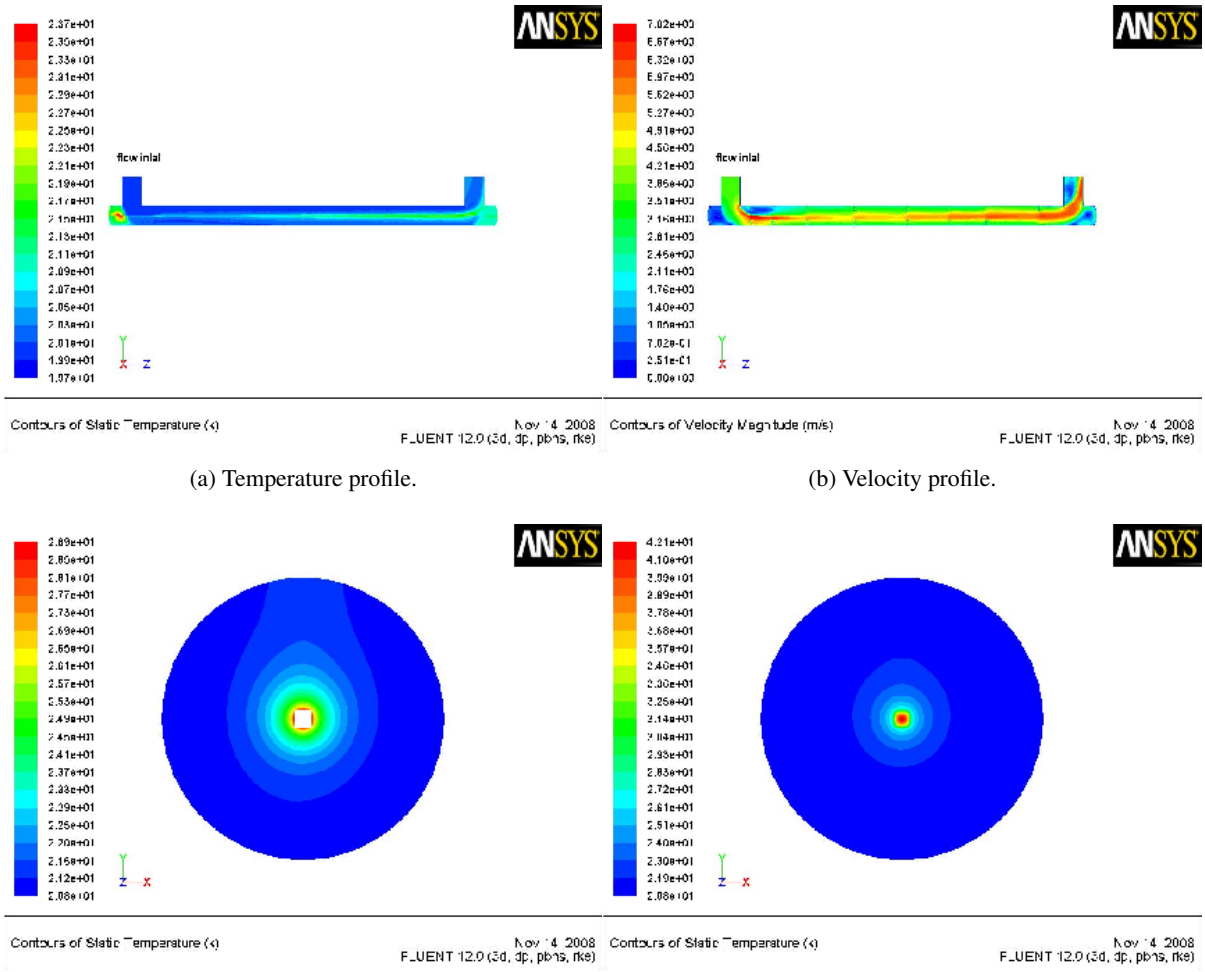

(a) Temperature profile.

(b) Velocity profile.

(c) Beam-out window without nipple.

(d) Beam-out window with nipple.

Figure 30: *CFD simulations of a E158-type cell in nominal conditions.*

recommends that the Hall A 4K transfer lines be re-evaluated and upgraded for the 12 GeV era in part because they have unusually high heat loads associated with them, and in part to better meet the demands of the 12 GeV era (such as the MOLLER experiment).

B.6 Qweak Target Experience and Expected MOLLER Performance

The design of the MOLLER target, as described in the proposal, is predicated on several novel ideas which were to be tested for the first time with the Qweak target. The Qweak target, we argued in the proposal, is really the prototype for the MOLLER target. This section reviews what has been learned from the Qweak experience in order to see whether those Qweak ideas and design aspects crucial to the Moller LH2 target hold any water.

The most crucial aspect of the MOLLER target design which needs to be validated is the novel use of computational fluid dynamics (CFD) as a design tool. Computational fluid dynamics was used in almost all aspects of the design of the Qweak target. It was used to tailor the cell design in order to optimize the flow, temperature and density profiles across the beam axis in the hydrogen volume as well as at the cell windows. These simulations were used to fix the mass flow required of the target, one of the most crucial

design parameters. The pressure head represented by the complicated cell shape was derived by CFD. Analytic calculations for the Qweak target's heater and some aspects of the heat exchanger were checked with CFD simulations. CFD simulations fixed the raster size required for the target and helped us design strategies for various off-normal events. In many respects the novel design which emerged was considered a bit of a gamble, given that CFD was not a proven tool for target design.

The 35 cm long, high power Qweak target has met its ambitious design goals. The target has been successfully operated with 3 kW of cooling power, significantly greater than any target previously built. It has been run routinely now up to 180 μA of 1.165 GeV electrons. The target boiling contribution to the asymmetry widths in the experiment has been measured at a raster size of 3.5x3.5 mm^2 in the beam current range from 50 to 170 μA (Figure 31). The measured performance is in excellent agreement with the expectation estimated from scaling the performance of the G0 target with the CFD model. The bulk density changes have also been bounded to less than 0.2% at 150 μA. This should be compared to the performance of the standard pivot 15 cm machined cells, for which the density variation at 100 μA has been measured to be at the level of 20%. Although the design raster size for the Qweak target was 4x4 mm^2, the target's performance is so good that it is operated routinely at 150 μA with a raster size of only 3.0x3.0 mm^2.

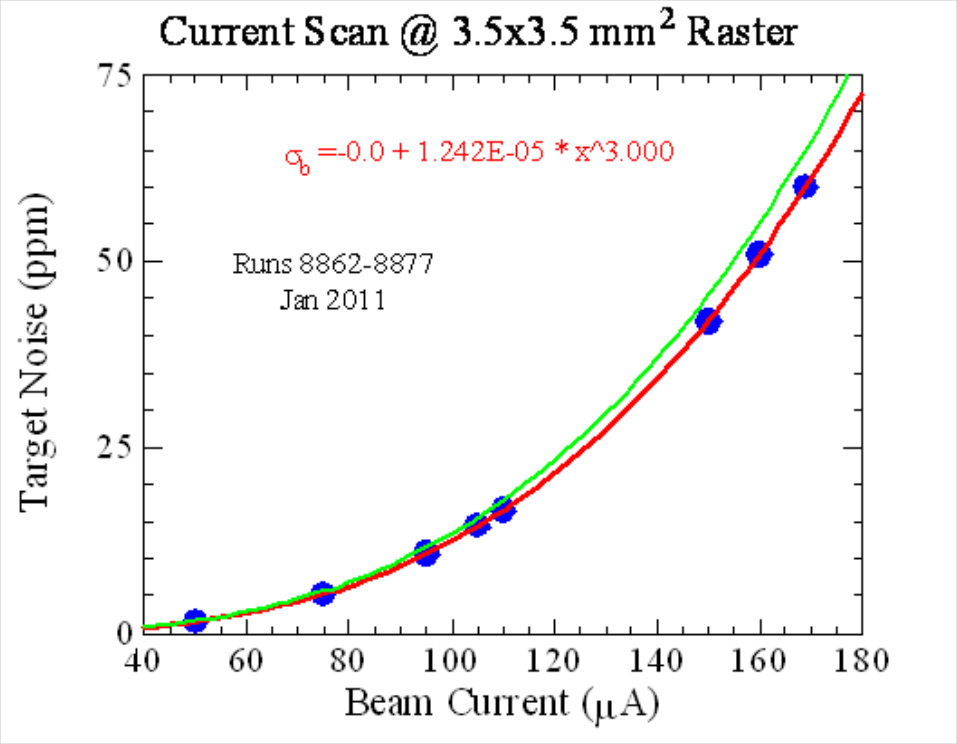

Figure 31: *Qweak target performance: density fluctuation widths versus beam current from recent Q_{weak} measurements. The blue points are measured data. The red curve is a fit to the data. The green curve is another fit, providing a measure of the uncertainties.*

The fact that the Qweak target has achieved all of its design goals validates the use of CFD as a design tool. The expected performance of the MOLLER taregt can now be scaled from the Qweak target performance.The MOLLER target requires the target density fluctuation to be less than 25 ppm at the operation condition of 85 μA with a raster size of 5x5 mm^2 at a helicty flip frequency of 2 KHz. At 85 μA beam current, the measure Qweak target density fluctuation (noise) is about 7 ppm at a raster size of 3.5x3.5 mm^2. At a raster size of 5x5 mm^2, the expected noise is 3.4 ppm. If we scale it with the target length, it will

be 15 ppm. Considering the fact that only the noise due to boiling within LH2 will approximately scale with the target length, while the noise due to the boiling at the aluminum windows will be approximately independent of the target length, the expected noise will be less than 15 ppm. Taking into account the factor that MOLLER plans to have the helicity reversal frequency twice of that for Qweak, the density fluctuation will be further reduced.

Since the density fluctuation due to the film boiling at the aluminum windows is often the dominating factor, a study was carried out with the CFD calculations for the MOLLER in comparison with the two Hall C parity experiments (G0 and Qweak). Figure 32 shows the heat flux for the three experiments, both the convective part, which is responsible for film boiling at the windows, and the total. Also shown is the threshold for film boiling. It is interesting to notice that the MOLLER situation is just below the threshold. A careful design may actually eliminate the film boiling.

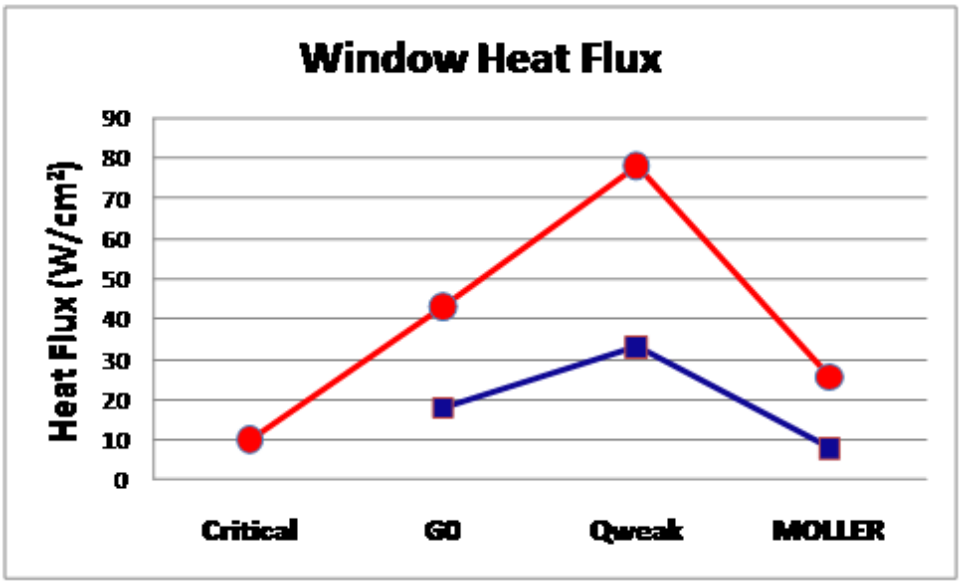

Figure 32: *CFD study of film boiling at the aluminum windows: window heat flux for three experiments (G0, Qweak and MOLLER). The blue points are the convective part of the heat flux, which is mainly responsible for the film boiling. The red points are the total heat flux. The first (red) data point shows the threshold for film boiling.*

We note that the matrix of 24 solid targets that are also part of the Qweak experiment were also designed with CFD. The relationship between temperatures at the center of each target to thermometry scattered around the solid target frame was studied with CFD. Knowing how high these thermometers can safely go, by virtue of the CFD calculations, has made it possible to put more beam current on our solid targets than has ever been done before at JLab.

It also shows that the heat exchanger design process used for Qweak was correct. Note that the Qweak heat exchanger is a completely novel design which combines a 4 K and a 15 K heat exchanger using overlapping heat exchanger coils in the same shell.

It also shows that the high power heater design and fabrication process was correct. The 3 kW heater performance is unmatched. When beam trips occur, or beam is restored to full current, the typical temperature excursions in the target loop thermometers are less than 0.1 K.

The pressure head predicted for the Qweak target at the design mass flow of 1.1 kg/s was 1.2 psi. The head measured with the Qweak target at this massflow is 1.1 psi, in amazingly good agreement with the

prediction considering how very difficult it is to calculate this ahead of time. Note that head and massflow are the two most crucial design parameters for most of the target's components.

The fact that the required massflow and pressure head were achieved for the Qweak target also validates the pump design. Problems have been encountered with the Qweak pump bearings, which have led to some down time. However the basic deliverables of the pump (head and massflow) have been achieved at the required values.

Qweak initiated the use of faster helicity reversal as a tool to mitigate the effects of target noise on the experiment. Fast Fourier transforms acquired under a wide variety of conditions during the Qweak experiment's commissioning phase show that this is an important and effective tool for reaching the goals of the experiment, and its effectiveness for the MOLLER experiment is now also validated.

Qweak also pioneered the use of a recovery heat exchanger at the ESR in order to boost the effectiveness of the ESR by making use of the enthalpy of the returning 4 K coolant. The ESR recovery heat exchanger (designed by Rao Ganni for Qweak) has been used for both the HAPPEX-III/PVDIS experiments in Hall A and for Qweak in Hall C. It has been proven to be enormously successful that it boosted the 15K cooling power the ESR can deliver by about a factor of two.

Another novel design feature now validated by Qweak is the re-configuration of the existing transfer line infrastructure in order to simultaneously supply both 4 K coolant and 15 K coolant to the target, and in particular, to return both coolant sources on separate lines back to the ESR. This required using the LN2 supply shield as a 20 K helium return. A small superconducting polarimeter magnet in the Qweak experiment is also fed and successfully operated with this highly unusual configuration.

To summarize: the Qweak target employed a large number of novel and highly unusual ideas to meet its goals. We now know that every single one of these new ideas has worked. This greatly reduces the risk associated with the extensions needed for the MOLLER target. The expected performance in terms of the density fluctuation should meet the MOLLER requirements. The cooling power needed for the experiment has been carefully considered by the lab and solutions are already under way that will insure the experiment's requirements can be met.

C Simulation Framework

The simulation and analysis software for this experiment was developed internally by the collaboration and is based upon the Geant4 [69, 70] and ROOT framework. The goals of this simulation are to

- Represent the geometries and materials of the target, collimators, magnet coils, and detectors.
- Allow representations of quartz detectors, light guides, and evaluate Cerenkov light generation, interaction, and detection of optical photons.
- Represent magnetic fields and be able to transport particles within them.
- Evaluate rates and asymmetries from, but not limited to, Moller scattering, electron-proton elastic, electron-proton inelastic, low-energy photons, pions, and hyperons.
- Evaluate effects from radiation and multiple scattering.
- Understand the radiation impact on the hall, such as from neutrons.
- Optimize aspects of the experiment such as overall figure-of-merit, systematic errors, collimation, and tracking.

Geant4 provides a dependable and well supported framework for evaluating particle interactions and a variety of common processes, especially those involving low energy electromagnetic processes, hadronic and electromagnetic showering, and optical photons. In addition it provides facilities for tracking particles through detailed magnetic fields, representing geometries, and recording interactions.

C.1 Included Physics

Many commonly studied processes at Jefferson Lab kinematics, such as electron-proton interactions, deep inelastic scattering, and pion electro- and photo-production, are not included or represented sufficiently within Geant4. To study these, we have developed our own event generators, which can provide both rates and asymmetries. Of these, we have implemented

- Moller processes, with parity-violating asymmetries
- Elastic proton, with internal radiative effects and parity-violating asymmetries
- Inelastic proton based on the Christy/Bosted parameterization [71], with a simple Q^2 scaling parity-violating asymmetry
- Charged pion rates based on the Wiser parameterization [64] using the equivalent-photon approximation.

The framework for the generators was done in a general way so that each includes the same multiple-scattering and external radiative effects (where applicable) leading up to the primary interaction vertex. It was also done so that new generators are relatively straightforward to develop. This becomes important for future generators which will be necessary, such as self-analyzing hyperon production and decay.

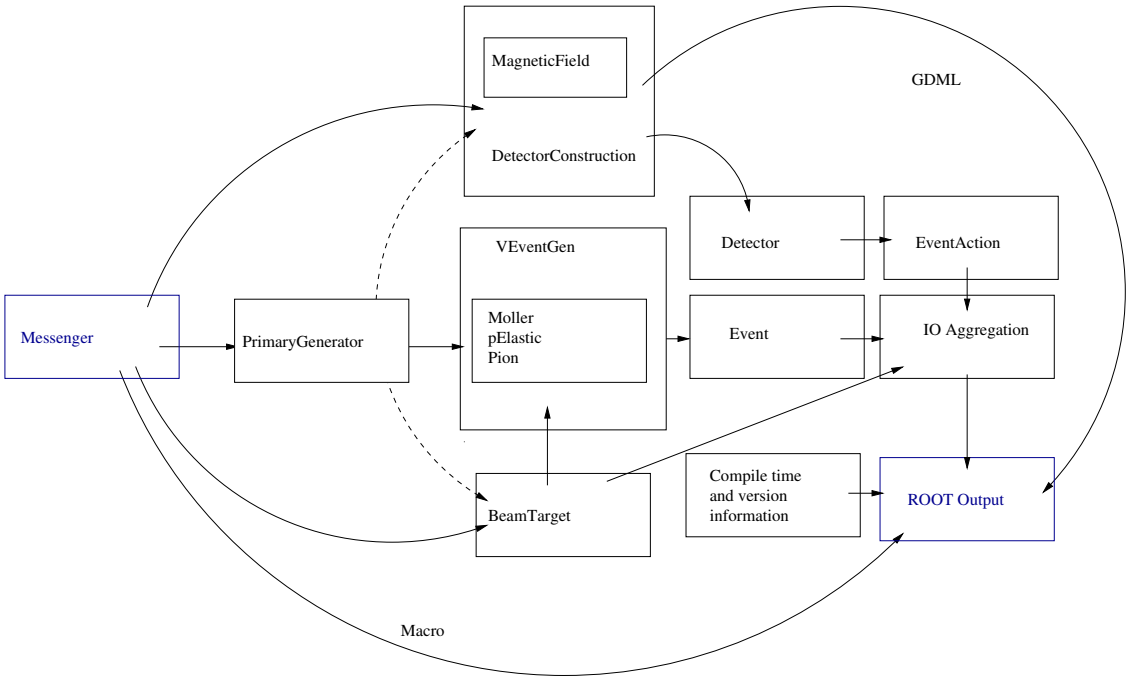

Figure 33: A schematic of the design of the simulation.

C.2 Simulation Design and Infrastructure

In achieving the aforementioned goals, several design philosophies were implemented:

- A modular, object-oriented design, which is natural to such a project
- No "hard-coded" geometries to avoid recompiling while evaluating different configurations.
- No double representation of parameters, such as target position and material, which is required by both the geometry representation and event generators.
- Output directly to ROOT trees.
- Reproducible output, which involves saving run parameters directly with the output.

A schematic of the design can be found in Fig. 33.

All geometries are represented within the GDML framework provided by Geant4. This is an XML-based format which allows for full representations of detectors, materials, optical properties, and facilities for associating auxiliary data such as assigning unique identification for detectors and identifying target components. A 3D representation of this geometry can be seen in Fig. 34. With such a framework, all geometries are then saved as simple text files.

Output is saved in a ROOT tree structure which contains information on the generated events and the particle hits. In the ROOT files containing these trees, a considerable amount of information is stored in a separate object regarding the run conditions. The goal of this to be able to take the output and be able to examine the conditions on how it was produced and reproduce it. This includes the run time and date, compile time and date, Geant4 version, the full input parameters which drive the simulation, the full GDML files with comments, and the git repository information. git provides a method to reference snapshots of the source code and retrieve them later, which would allow one to run with identical source later on (provided it was checked into the repository).

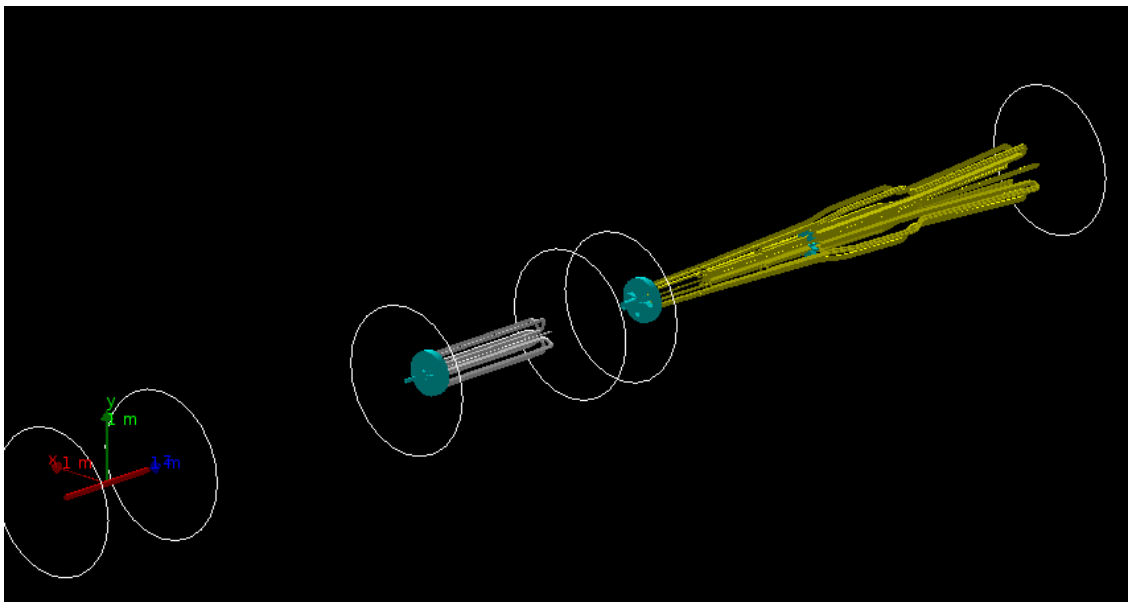

Figure 34: A representation of the spectrometer within the simulation.

D Toroidal Spectrometer

We have already listed the salient features of the spectrometer system in Sec. 3.3. In the following we provide further details of the conceptual design and describe the progression to a buildable coil design with preliminary thermal calculations and force studies.

D.1 Hybrid Toroid Concept

The shape of the hybrid toroid is designed to provide a large range of total $Bd\ell$ correlated to the angle of the track. The conceptual design evolved under the imperative of maintaining a large current in a small volume near the beam line (due to the lowest angle tracks). Idealized currents were found which achieved the desired optical properties, focusing a large range of Møller scattered electron angles and energies, with sufficient separation between the Møller and Mott scattered electron peaks. This original design conformed to the basic requirements of manageable current density and sufficient tolerances for water flow and support structure and was robust under small changes in geometry, but did not take into account the need for a realistic conductor layout.

There were four primary features to the conceptual magnet design:

- In order to maintain sufficient current at realizable density, the magnet fully enclosed the beamline from z=10 meters to z=13 meters.
- The current in the magnet grew from z=10 m to z=13 m, with current returning in 4 different radial paths, spaced along the beamline by about 1 m.
- the back-end of the magnet, with the highest current, juts out to keep the highest-energy Møller-scattered tracks in high field for a longer time, while minimizing the field seen by the Mott-scattered electrons.
- the top of the coil is dropping, over the radial range of accepted flux, so that some tracks receive less $Bd\ell$ by entering the field region comparatively late, or leaving it comparatively early.

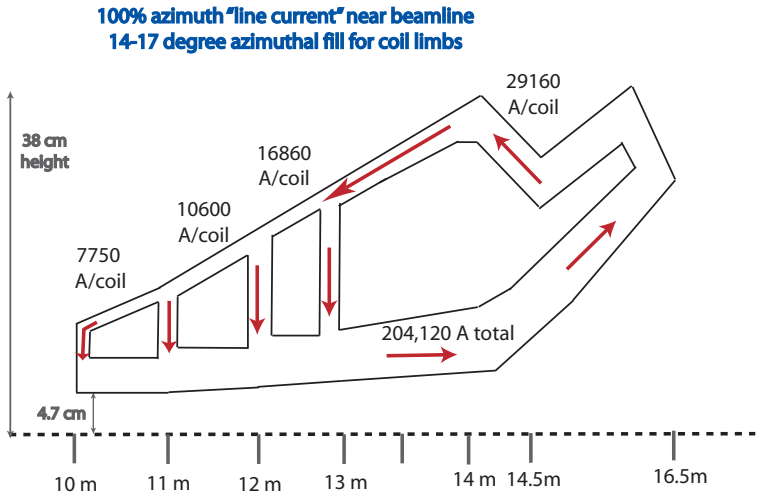

Figure 35: *Schematic of the hybrid toroid design concept.*

Each of the coils in this conceptual design carried around 29 kA, with total power consumption of about 773 kW.

D.2 Detailed Description of Coil Design

In order to achieve a buildable coil design with a realistic conductor layout while achieving the design goals stated in sections 3.3 and above, it was necessary to take into account additional constraints. The most important consideration was to find an actual conductor layout that would not interfere with the scattered electron envelope, but still had a reasonable current density. This was complicated by the need to have multiple current return paths with a minimum bend radius of 5× the radius of the conductor. An additional constraint is that ideally the coils would be wound with a "double-pancake" structure, so that when the conductor is being wound, it can be returned in the second layer by reversing the direction of the winding. The final coil design consists of several individual "double-pancakes" that will fit together, with each pancake designed to be as flat as possible while fitting within the radial and angular acceptances. The segments in z which are formed from the multiple current return paths have values that are as close to the ideal currents as possible.

D.2.1 Conductor Layout

The actual conductor layout was optimized using an iterative procedure, because the scattered electron envelope depends not only on the upstream torus, but also the configuration and current in the upstream parts of the hybrid torus itself. A commercial software program called TOSCA, available from Vector Fields, was used to determine an actual conductor layout by drawing the configuration of individual conductors and then tracking electrons with the correct angle and energy correlations (though lacking radiative effects in the target or other materials) through the fields to check for interferences. The first step was to find a standard conductor size which minimized the current density, if possible. Once a conductor size was chosen, a reasonable layout was designed using a "double-pancake" structure which fit generally into the radial and azimuthal constraints. Tracks were then simulation in TOSCA to check for interferences.

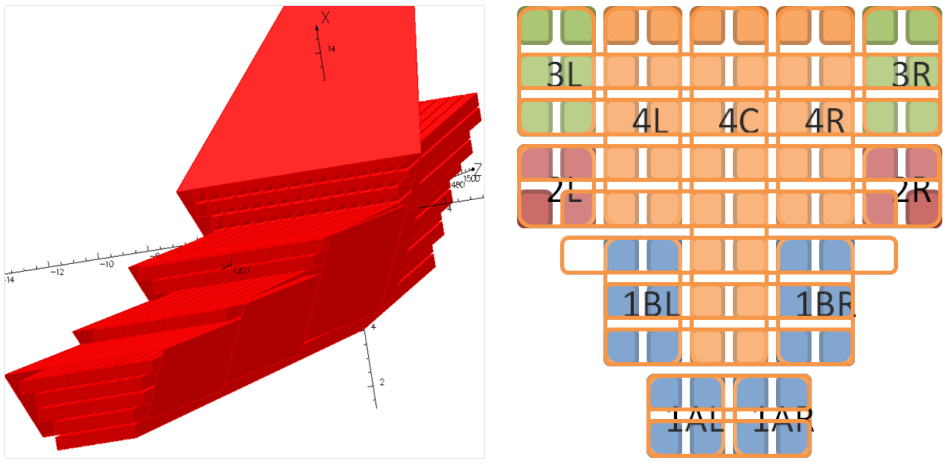

(a) (b)

Figure 36: *Layout of individual conductors within the allowed space at low radius (trapezoidal shapes) in TOSCA for 0.1819 inch OD square conductor (a). Diagram showing the layout for 0.2294 inch OD square conductor, color-coded and labeled by how they are wound in individual "double-pancakes" (b).*

The biggest constraint on the coil cross section comes at the most downstream current return path, at the z location where all of the current returns. In addition to taking into account the water-cooling hole, the space needed for insulation between individual wires was considered. The closest that a coil comes

to the center of the beamline is 5σ of the multiple scattering angle (estimated to be 0.515 mrads) plus 1/2 inch for aluminum supports and tungsten shielding (1/4 inch each). In order to fit the conductor radially (beneath the radius of the lowest angle Møller scattered electrons at that z location) it is necessary to nearly fill the full azimuth in a roughly trapezoidal cross-section. The smaller the conductor, the easier it is to fill the shape of the acceptance, except that more of the area is taken for insulation between the conductors, resulting in a higher current density. With larger conductors, there is unutilized space near the edges of the acceptance, so the choice of the size of the conductor does not impact the current density significantly; in all cases the current density ranged from 1550 to 1600 A/cm^2. However, the smaller the conductor, the easier it is to achieve the idealized currents used in the original field map, leading to the choice of 0.1819 inch OD conductor which was presented to the Magnet Advisory Committee in August 2010.

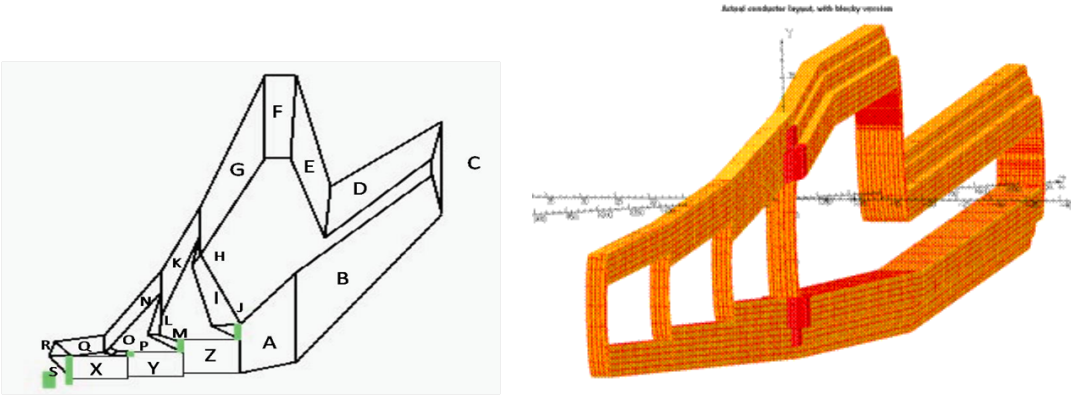

(a) (b)

Figure 37: *Conceptual model of a single hybrid coil, with the segments labeled for reference (a). Model of the actual conductor layout in TOSCA (red) overlayed with the blocky model used for simulation and production of the maps (orange) (b).*

When designing the layout, it was necessary to consider how the coils would be constructed. Figure 36, (b) shows the scheme of how the individual double-pancakes will be put together in a cross-section at z=1300 cm. Currently the simulation design models the conductors as closed loops. Starting at z=1300 cm at the inner radius part of a coil, or segment A in Figure 37, (a), and moving upstream toward segment Z, the conductor in pancakes 1B, 2 and 3 (left and right, or L and R) is bent inward toward the center of the coil, and continues upstream with the conductor in pancakes 1A (L and R). The conductor in pancakes 4 (L, C, and R) bends radially outward to form the current return path of segments J, I, and H. At z=1200 cm, pancakes 3 (L, R) bend radially outward to form the current return path of segments M, and L, and then at z = 1100 cm, pancakes 2 (L, R) form the current return path of segments P and O. Finally, at the upstream nose of the coil, pancakes 1A and B (L, R) bend radially outward to form the current return path of segments S, R and Q. At large radius, the conductor in the pancakes continue downstream and come together again at z=1300 cm and bend outward from the center of the coil so that they have the same cross-section as at the inner radius. The pancakes as labeled in Figure 36, (b) will be wound separately and then put together with the orange ones in the middle, then the green, red and blue ones fitting around them.

D.2.2 Suggestions from the Magnet Advisory Committee

The Magnet Advisory Committee was positive about the design of the magnet, and offered suggestions on how to improve the design and the presentation of the specifications of the magnet. They were not concerned with the size of the current density so much as the size of the water-cooling hole in the chosen conductor

size. It was suggested that chilled water, flowed fast enough, would work for this current density, but that faster water flow rates would also increase the erosion rates. They all agreed that a water cooling hole of at least 0.125 inches ID round would eliminate concerns about back-flows and eddies in the bends in the magnet, which could lead to the build-up of oxides that could cause a plug which would limit the long-term operation of the magnet. The possibility of mounting the coils inside the vacuum pipe was suggested, which would allow for a much simpler vacuum enclosure design, which would reduce the expense of conforming to the ASME standards for the complicated petal-shaped beamline. There was some concern about manufacturing tolerances for the coils which will need to be considered carefully. The magnetic forces on perfectly symmetric coils are very small, but they cautioned that the support structure would need to account for forces on asymmetric coils. They also requested more details about the geometry of the field. Work is ongoing to study the tolerances and the effect of asymmetric coils on the magnetic forces.

D.2.3 Summary of Engineering Work

Some specifics of the design of the coils has been considered in consulation with a group of engineers from MIT-Bates who have since joined the collaboration. A native CAD model of the coils has been created and checked against the TOSCA design. Detailed thermal calculations have been performed for the water-cooling of the hybrid coils taking into account the available power, temperatures and pressures available in the hall. Preliminary work has also been done to develop a conceptual design for the support structure with the coils in vacuum (see Figure 39).

The coils are very long and the water-cooling hole is very small because the outer dimensions of the conductor are small (see Figure 38). The results of the thermal calculations (see Table 14), especially the pressure drop, suggest a slightly larger conductor (#8204) than that which was chosen after the Magnet Advisory Group Meeting (#8339). The outer size of the conductor is only slightly bigger which results in a larger current density (2000 A/cm^2) than originally proposed. However, this new conductor size will minimize the number of water connections, which will be especially important for coils placed inside a vacuum vessel. Preliminary calculations suggested that the magnet, which has a total power of 773kW, could be cooled with a maximum of 4 turns per loop for a total of 19 loops, or 38 water connections per coil. These more detailed calculations suggest it could be made with as few as 14 loops per coil (see Table 15), which would work with 6 turns for some of the pancakes,as desired.

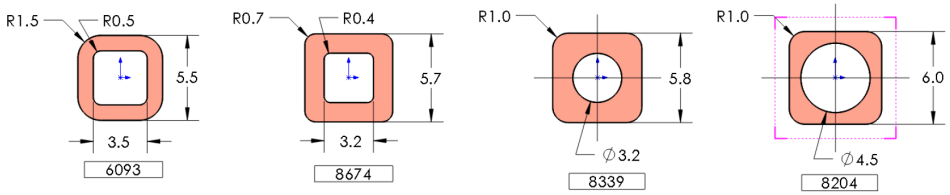

Figure 38: *Standard conductor styles and sizes (mm) available from Luvata considered in the thermal calculations. The recommended conductor (#8204) is circled in magenta.*

Further work is needed to study the manufacturing tolerances and the effect of the magnetic forces on asymmetric coils. A preliminary study of the magnetic forces on the coils indicates a modest centering force of less than 3000 lbs. per coil, with a force along the beamline (z-direction) of 50 lbs. (due to the asymmetric shape). For perfectly placed coils, the force in the azimuthal direction is negligible, but needs to be considered for the case of asymmetrically placed coils. The effect of the placement of the electrical and water connections on the scattered electron envelopes also needs to be studied. Water and electrical connections can be made at the tail (segment B) and at the top (segment F) with some modification from the

Table 14: *Summary of the electrical and flow properties (assuming 4 average-length turns per cooling circuit with ΔT =45°C) for the different standard conductor sizes (see Figure 38).*

Conductor Style and Resulting Power and Voltage for I = 384 A				Flow properties	
Part #	Current Density (A/cm^2)	Voltage Drop (V)	Power (kW)	Velocity (m/s)	Pressure Drop (ave) (atm)
6093	2358	2377	913	3.04	14
8674	1748	1762	677	2.68	13
8339	1553	1566	601	3.03	17
8204	1996	2012	773	1.95	5

Table 15: *Summary of the minimum number of cooling paths per coil for different allowable temperature rises, ΔT (°C) for two different conductor choices.*

T_{max} (°C)	ΔT (°C)	Cooling paths/coil			
		6093	8674	8339	8204
50	35	25	28	25	21
60	45	22	24	24	17
70	55	19	23	22	16
80	65	17	19	19	14

ideal layout for access to the conductor in the inner part of the coil cross section (portions of 4 (L, C and R), see Figure 36).

D.2.4 Summary of Coil Specifications

In order to achieve the necessary field integral while fitting the coils within the sectors behind the collimators, the hybrid toroid is a very long and skinny water-cooled copper resistive magnet (see Fig. 39). The full length of the magnet is ∼7 m and the outer radius of the torus is ∼40 cm, but each coil weighs only 555 lbs. Based on suggestions from the Magnet Advisory Committee, the chosen conductor size is 0.2362 inch OD square with a water-cooling hole of 0.177 inch (round) with 0.08 mm of insulation (0.04 mm half-lapped). All of the bends take into account a minimum bend radius of 5× the conductor OD (for mechanical considerations). With conductor this large, there is more space at the edges that is open in order to avoid interference with adjacent coils, but the current density is still only 1996 A/cm^2.

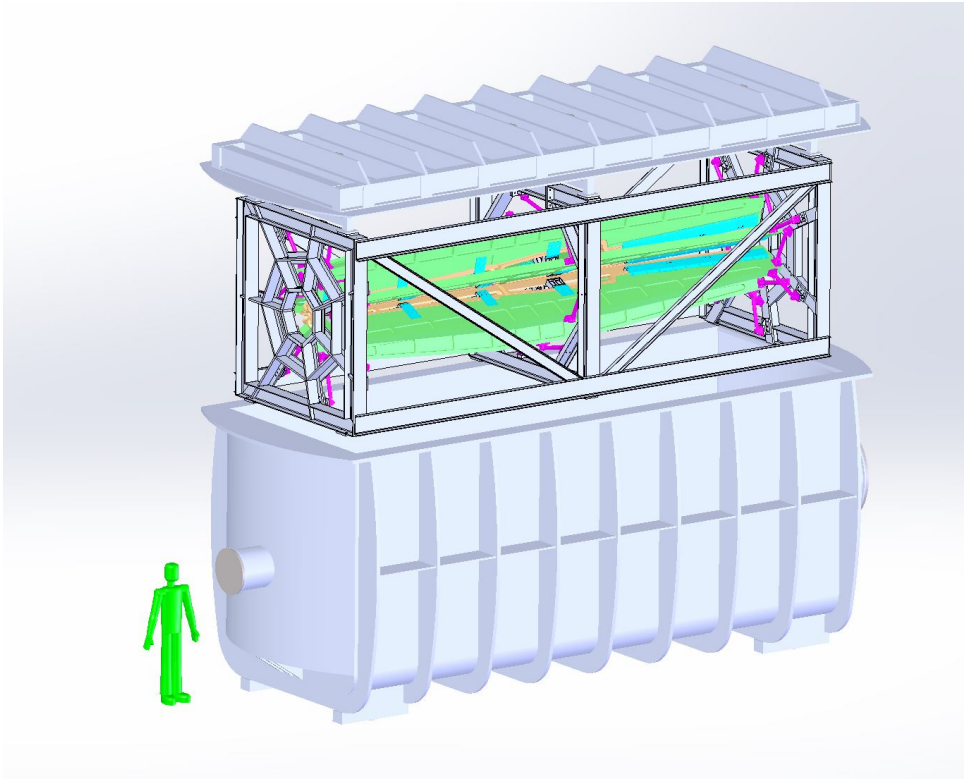

Figure 39: *Conceptual design of hybrid torus supports inside the vacuum vessel. The moller and elastic ep scattered electron envelopes are shown in green for reference.*

D.3 Simulated Properties of the Spectrometer

The simulation of the properties of the MOLLER spectrometer was done using the GEANT4 framework [70]. The simulation was run with three different particle generators which produced Møller electrons, Mott electrons and electrons from inelastic ep scattering, respectively. In each of the generators, electrons are generated with random vertex positions, with z chosen along the length of the target, and the x and y positions chosen within $\pm$2.5 mm in order to simulate the effects of the raster. A scattered electron is produced from the post radiated beam and the appropriate cross section for the process in question, with a random azimuthal angle. The scattered electrons are propagated through the geometry which consists of collimators, magnetic fields for the two toroids, and a detector plane. The detection plane was chosen to be 28.5 m downstream of the center of the target, where the Møller electrons have their tightest radial focus. At this position the ep elastic (Mott) peak and the peak due to Møller electrons are separated by more than 20 cm.

For the conceptual version of the hybrid torus, a code was written to do a Biot-Savart calculation of the fields for the idealized current layout. This field was then read-in to the GEANT4 simulation. TOSCA was used to produce field maps for various versions of the the actual conductor layouts for the upstream and hybrid toroids, as well as for a TOSCA version of the idealized currents for comparison. Using a combination of TOSCA and GEANT4 simulations, the detailed layout of the actual conductor was optimized to achieve similar focusing properties to that of the field map for the idealized currents of the conceptual hybrid torus.

D.3.1 Properties of the Idealized Hybrid Field

The position of the Møller electrons at the z=28.5 m plane in cylindrical coordinates (radius vs. azimuthal angle ϕ) is shown in the left of Figure 40. Here we establish the color convention which will be used in future plots - red for the detector in the center of the open sector, blue for the detector in the center of the closed sector and green for the detector which straddles the open and closed sectors. For quantities that are azimuthally symmetric, the various detectors of the same "color" will have the same distribution, and for the purpose of the following plots, are combined. The plot on the right of Figure 40 shows the distribution of Møller electrons as a function of ϕ_{wrap}, the azimuthal angle from the center of the nearest open segment, plotted in total expected rate (GHz) for all sectors for a beam current of 85 μA.

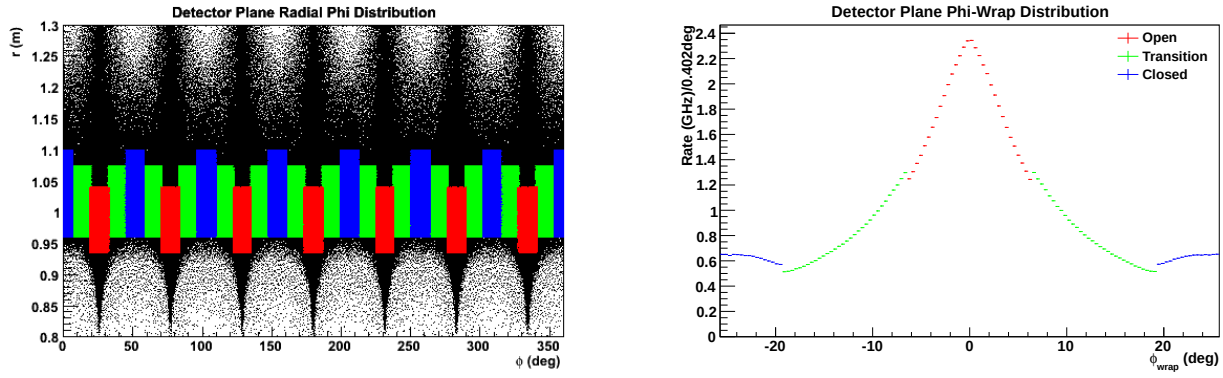

Figure 40: *Møller electrons in the z=28.5 m plane in cylindrical coordinates (radius vs. azimuthal angle ϕ). The detected particles are colored according to which detector they hit, red for the detector in the center of the open sector, blue for the detector in the center of the closed sector and green for the detector which straddles the open and closed sector. On the right is the rate of Møller electrons detected as function of ϕ_{wrap}, the azimuthal angle from the center of the nearest open sector.*

The radial distributions of scattered electrons from Møller, elastic e-p and inelastic e-p scattering have been discussed in Sec. 4.5.1, as shown Figure 20. The primary source of background is the result of initial and final state radiation in the target from Mott scattered electrons. The anticipated position of the Møller electron detector is a ring with inner radius 0.88 m and outer radius 1.00 m, also shown in Fig. 20. The integral of the expected rate within this region is 154 GHz for the Møller electrons and 12.6 GHz for the Mott electrons - a background of 7.6%. If the calorimeter is a "shower max" detector, then the background would be 8.3% due to the slightly higher average energy of the background electrons. Figure 41 shows the Q^2 distribution of the background from elastic e-p scattering that is accepted by the detector; this distribution is relevant for estimating the size of the background correction.

Figure 42 shows the E′ and θ_{lab} distributions for Møller electrons that hit the main detectors. One can see that the "red" detector contains mostly the higher energy, forward Møllers, the "blue" detector is mostly the lower energy, backward Møllers and green has a mixture of both. The numbers relevant for estimating detector rates and predictions for asymmetries are listed in Table 1.

D.3.2 Properties of the Actual Conductor Layout

The field calculation for the conceptual hybrid design was verified by directly comparing the actual field values and by comparing the results of GEANT4 simulations using the different field maps. The comparison of the fields (T) for a radius of 15 cm shown in Figure 43 is of the primarily azimuthally (de-)focusing

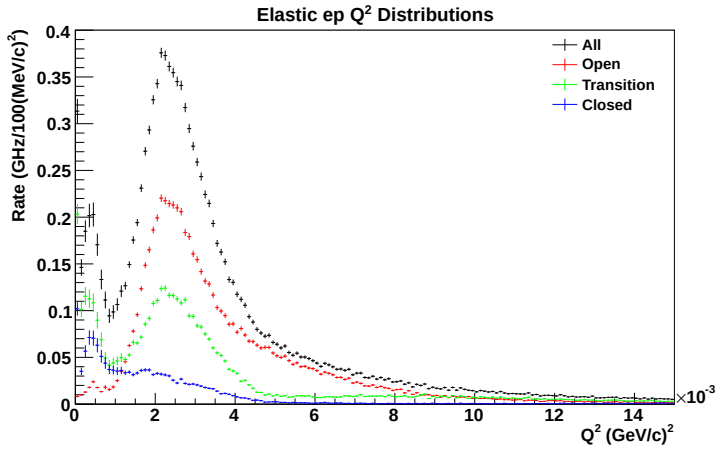

Figure 41: *Rate of Mott electrons detected as function of Q^2, the square of the four momentum transfered in the scattering. Color convention from Fig. 40.*

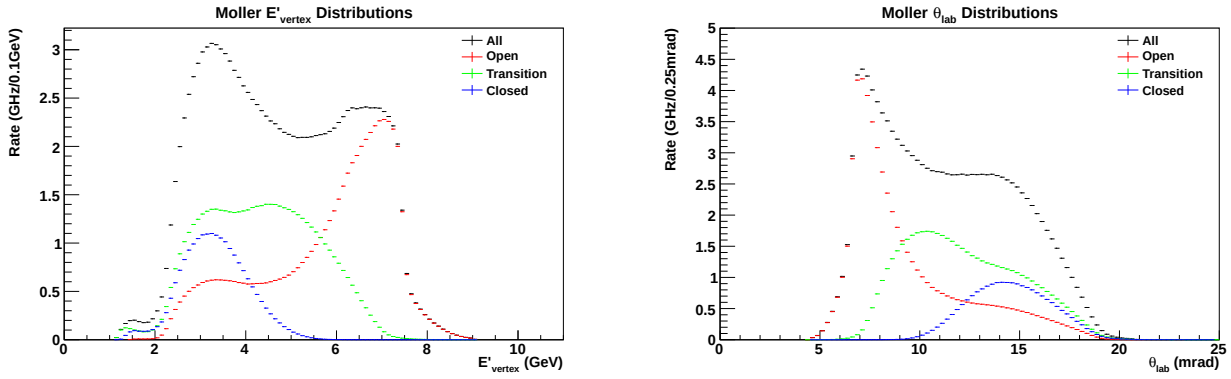

Figure 42: *Rate of Møller electrons as a function of E'_{vert}, the energy of the scattered electron immediately after the interaction (left), and θ_{lab}, the scattering angle in the laboratory frame (right). Color convention from Fig. 40.*

component (B_x in this sector) vs. z. At each z location there are 5 points in ϕ. The top plot is for $-25 \leq \phi \leq 20$, the next is for $-20 \leq \phi \leq 15$, etc., with the bottom plot for $-5 \leq \phi \leq 0$. The field of the conceptual hybrid is shown in red, and the TOSCA version is shown in black. The black points are not visible for the most part because they are directly beneath the red points. The top plot shows some extra scatter in the red points because this is actually within the location of conductor in the model. TOSCA seems to handle the calculation of the fields at these points in a relatively smooth manner. The results of the comparison using the GEANT4 simulations are also very similar, with small differences due to the fact that the geometries of the TOSCA version did not exactly reproduce the idealized current distribution.

A default actual conductor layout has been designed which yields similar simulated properties as that of the idealized currents in the conceptual hybrid design. The magnet which was presented to the Magnet Advisory Committee yielded properties that were remarkably similar to those of the conceptual hybrid. When the suggestions from the committee were taken into account, it was necessary to perform some optimization of the resulting coil geometry in order to get back to similar focusing properties. Much of the optimization was

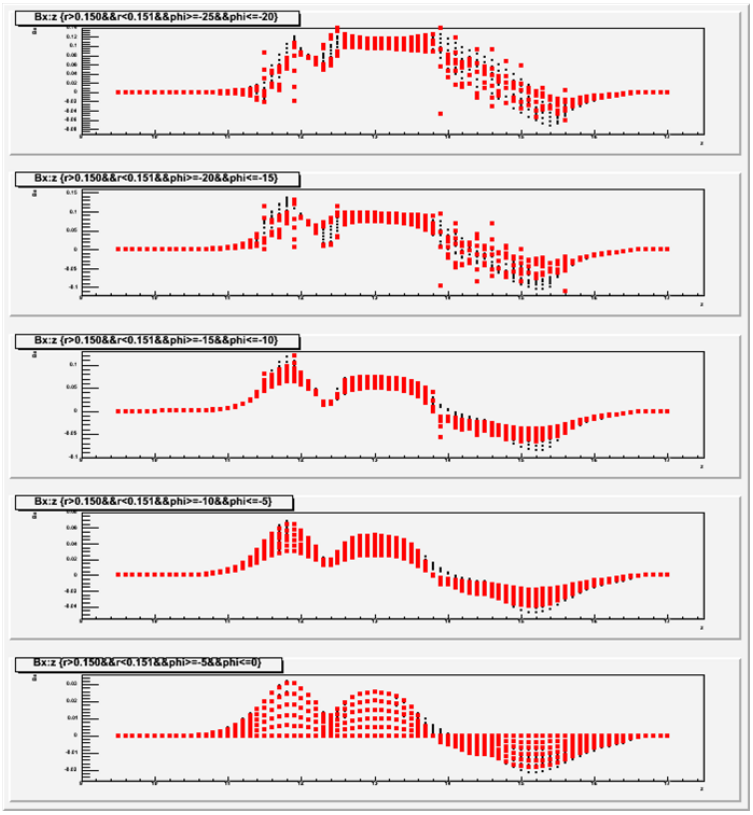

Figure 43: *Plot comparing the B_x component of the magnetic field (T) vs. z (cm) of the conceptual hybrid (red) and the TOSCA version (black) of the conceptual hybrid for a radius of 15 cm for different bins in ϕ.*

done using TOSCA simulations of the Møller and Mott electrons, with the proper scattering angle/energy correlations. The final comparison requires GEANT4 simulations to account for radiative effects. Figure 44 shows some of the progression of the ϕ_{wrap} and θ_{lab} distributions from the conceptual hybrid to the default actual conductor layout which is being used in the simulation for other studies.

The conceptual field map had a ϕ_{wrap} distribution which was relatively flat. This distribution becomes more rounded in the actual conductor layout versions due to additional azimuthal pre-focusing when the electrons pass close to adjacent coils at the inner radial part of the coil, especially in the upstream toroid. Thus the actual conductor layouts seem to have more low angle electrons in the "red" or open segment. The rates for the default field are 155 GHz, 14 GHz and 0.5 GHz for the Møller, Mott and inelastic ep electrons respectively, for a background rate of 8%. In the bottom plot of Figure 44 there is an additional bump in the θ_{lab} distribution at high angles because the collimators have not yet been optimized for this field map. Figure 45 shows a comparison of the radial and θ_{cm} distribution of the conceptual field map and that of the default actual conductor layout. The radial distribution of the default map is slightly wider and is centered at a slightly larger radius than for the conceptual field, while the θ_{cm} distribution is slightly more unbalanced in favor of the larger angles. It is desired that the forward and backward acceptance be very similar, both because we want full azimuthal acceptance for the accepted range of scattering angles (see Section 3.3) and because the transverse asymmetry will cancel more fully (see Section 4.3). Further optimization of the coil geometry and optimization of the collimator is needed to improve these properties.

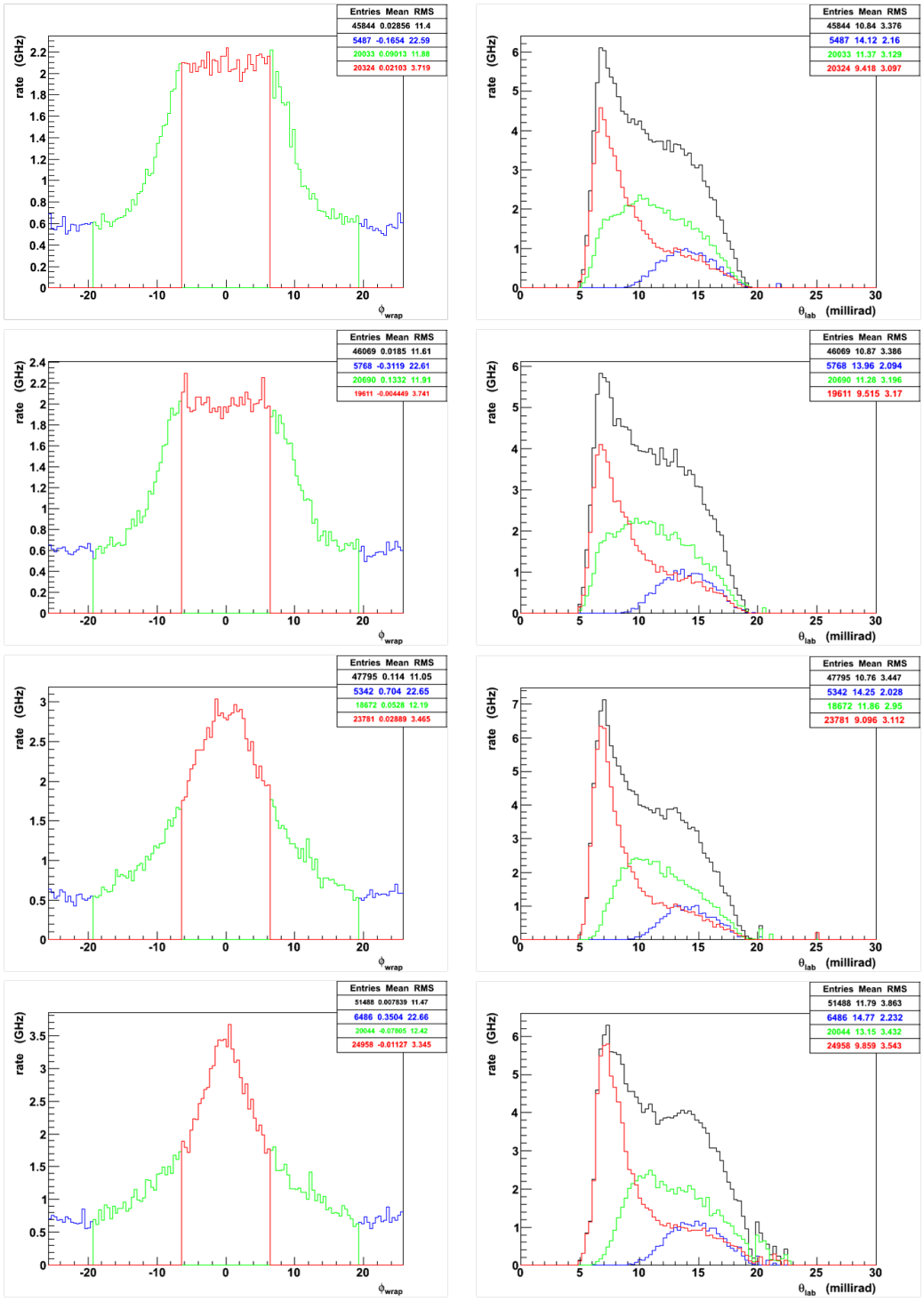

Figure 44: *Plots showing the progression of changes in the ϕ_{wrap} (left) and θ_{lab} (right) distributions from the conceptual field (top). The conceptual field was first verified using TOSCA (second row) and then the actual conductor layout which was presented at the Magnet Advisory Committee was developed (third row). The default field (bottom) is the result of optimization of the conductor layout which takes into account the suggestions from the Magnet Advisory Committee. Color convention from Figure 40.*

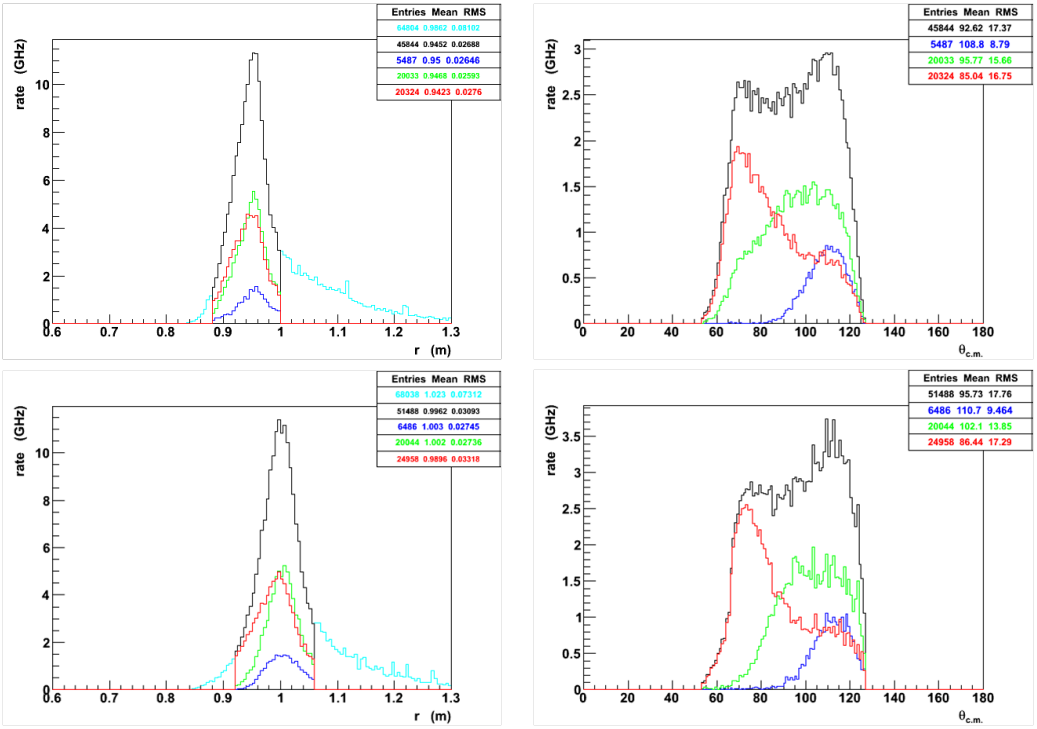

Figure 45: *Plots comparing the radial (left) and θ_{cm} (right) distributions of the conceptual field (top) and the field for the actual conductor layout (bottom). Color convention from Figure 40.*

E Integrating Detector

The general requirements of the main integrating detectors were discussed in Sec. 3.4.1. In brief, the primary measurement of the relative flux is carried out in integrating (or current) mode; this drives various design and material choices for the detectors to confront the high signal magnitude, corresponding noise suppression, the requisite detailed understanding of the scattered flux profile, and sufficient suppression and identification of background. The latter requirements leads to the definition of auxiliary detector and the conditions and frequency of calibration runs.

The integrating detectors will consist of three major parts: the active detection volume, made from quartz, the light guide (currently envisioned to consist of an air-core light guide with walls made from a high reflectivity material), and a quartz window photomultiplier tube. In a current mode measurement, a dominant component of the detector noise behavior (electronics excluded) is determined by the single event signal level i.e. the number of photo-electrons created at the PMT photocathode per incident electron. This quantity is a strong function of the choice of detector material and geometry, and is thus the primary focus of this section.

E.1 Design Considerations

Since the primary detector response to the very high rate of scattered electrons of interest is integrated over the duration of each helciity window, the ideal detector material is artificial fused silica (henceforth ”quartz”), since it is radiation-hard, and has negligible scintillation response. When operating detectors in integrating mode, there is no way to make event mode cuts, based on pulse shape, and true counting statistics is not achievable. Therefore the two primary concerns for the detector design are to reduce background sensitivity as much as possible and to reduce excess noise to a level that allows the detectors to operate as close to counting statistics as possible. Both of these issues are intimately connected to the detector geometry. In particular, aside from electronic noise, the level of excess noise in the detectors is primarily a result of two competing effects as a function of increasing quartz thickness: shower activity inside the active detector material, which increases fluctuations in the detector response, and increasing single event light yield, which decreases the width of the average detector response. Both of these depend on the detector geometry, as further explained below.

In addition, the detectors must measure the relative flux in the nominal acceptance, be insensitive to soft backgrounds, and be radiation-hard. Because the tail of all radiative electron-proton elastic and inelastic processes results in an important systematic correction, the detector must be able to measure these background electrons in *several* bins, so trends in yield and asymmetry can be compared to simulations. The detector must also minimize cross-talk between adjacent radial bins, with widely differing asymmetries, and minimize electron hit location and electron incident angle dependent biases. The latter point, again, primarily places restrictions on the individual detector active material geometry. Additionally, event-mode acquisition at much lower beam currents for systematic studies is also required, for the purpose of background determination and momentum transfer determination. Having chosen the optimal detector material, the most important task is the optimization of the detector geometry, as further discussed below.

the quartz active volume of each detector is connected to a PMT by an air-core light guide. This is done to remove all PMTs from the envelope of scattered electrons and backgrounds as much as possible while, at the same time, reducing sensitivity to background (the latter resulting in the choice for the air-core, rather than a solid material). The integrated response of the PMT to the collected light yield is then the experiment’s measure of the scattered electron flux [55]. Photoelectrons (defined as electrons created at the PMT cathode, due to incident light) represent the actually collected signal, as a result of the light created by each event in the active material (quartz) and *all* noise properties of the detectors are determined by the average and root-mean-square (RMS) of the photoelectron count distribution for single detector events!

The total number of photoelectrons depends on the amount of light, due to a single electron event in the quartz, that is actually incident on the cathode, and the quantum efficiency of the cathode. After emission of the Ĉerenkov light from the quartz, the amount of light hitting the cathode is a strong function of the diffractive and reflective properties of the interface between the quartz and the light guide and the light guide surfaces, as well as the length of the light guide. The orientation of the light guide with respect to the quartz and the shape of the light guide largely determine the number of reflections the Ĉerenkov light undergoes, before hitting the PMT cathode. Each reflection reduces the probability for detection at the cathode. The careful orientation of the entire detector assembly (quartz, light guide, and PMT) with respect to the envelope of scattered electrons has the potential to reduce the accidental detection of events from the light guide and reduce backgrounds.

The production of showers inside the quartz, suboptimal geometry, and poor light collection efficiency typically lead to an increase in excess noise (because they produce additional variation in photoelectron count), while a higher average number of photoelectrons, per event, leads to a decrease in excess noise.

E.2 Current-Mode Signal Magnitude

As discussed in section 3.4 and shown in figures 16 and 17, the detector array is envisioned to be segmented into 28 azimuthal bins, in general, and 84 azimuthal bins for the main Møller peak ring, in particular. At the proposed maximum beam current, the rate will vary by about an order of magnitude around the azimuth, within a given ring and by about two orders of magnitude from highest to lowest, among all of the integrating mode detectors. The highest flux in a single quartz detector will be about 6 GHz, while the lowest rate will be a few hundred MHz.

Based on the test results discussed above, the Cherenkov light from each detector will be collected by a single 3" PMT with quartz windows and will conservatively register 15 photoelectrons per track.

With the PMT gain adjusted to 675, the resulting signal amplitude will be

8.1 μA

$$I_{anode} = 5.0 \text{ GHz} \times 15 \text{ pe/track} \times 675 \times 1.6 \times 10^{-19} e/C = 8.9 \ \mu A.$$

This is a large signal, and still below the nominal 10 μA maximum usually recommended by PMT manufacturers for good long-term stability.

12 nA

Another consideration for the PMT operational envelope is the *cathode* current of 11 nA. This is far too much current to draw from a standard semiconducting bi-alkali cathode without collapsing the voltage in the center of the cathode, causing defocusing and loss of gain. Hence we will either use a conducting S20 ("multi-alkali") cathode as used in Qweak, or a cathode with thin conducting grid laid across a bi-alkali cathode. The trade-offs are a higher thermionic emission noise in the case of the S20 cathode (which is only an issue at the low rate of the event mode studies), versus reduced quantum efficiency in the case of the cathode overlaid with the conducting grid. The choice will require detailed study. The current-mode PMT parameters are summarized in Table 16.

E.3 Event-Mode Signal Magnitude

Event mode operation is helpful for verifying the magnetic optics and essential for detailed background studies. JLab's CW beam and the flexibility of PMTs allows the detectors to be reconfigured for event-mode operation simply by reducing the beam current, increasing the PMT high voltage, and routing the signal from the parity ADCs (which integrate in 1 msec bins) to flash ADCs (which integrate in bins of a few nsec). At a gain of 1×10^7, the average voltage pulse across a 50 Ω termination is

$$V_{signal} = I_{signal} \times R = (15pe \times 10^7 \times 1.6 \cdot 10^{-19} C/e/10^{-8} sec) \times \ 50\Omega = 120 \text{ mV}$$

which is a robust signal. Even a single photoelectron signal of 8 mV, produced for example by Compton scattering of a few MeV gamma-ray background in the radiator, could be easily observed.

A modest rate of only 100K tracks/second would require the beam current be reduced to 2.25 nA. By employing a combination of laser attenuator and narrow chopper slit, the JLab injector group has provided stable beam to Hall C well below 1 nA for Qweak calibration studies. The beam position is checked at regular intervals by wire scanners. The event-mode PMT parameters are also summarized in Table 16.

Table 16: *Parameters for the PMT signals from the quartz detector with the largest flux.*

Parameter	**Value**
Total PMTs	252 (6×28 and 1×84)
current mode:	
$I_{cathode}$	11 nA
gain	675
I_{anode}	8.9 μA
non-linearity (goal)	$5{\times}10^{-3}$
pulsed mode:	
$I_{cathode}$	0.24 pA at 100 KHz
gain	$1{\times}10^{7}$
I_{anode}	2.4 μA
V_{signal} (no amp.)	8 mV for 1 pe; 120 mV for 15 pe
non-linearity (goal)	$< 10^{-2}$

E.4 Detector Design Status

Over the past year, significant progress has been made in the design of the integrating detectors. The first step was to develop a small set viable detector configurations (geometry and material combinations between quartz and light guide), using detailed simulations. These were then implemented as prototype detectors and tested with minimum ionizing cosmic rays and beam electrons. In October 2013, the detector working group carried out a number of tests with prototype detectors at the MAMI facility in Mainz, using 855 MeV electrons. Measurements were carried out to determine the single event photoelectron yield for a the simulated quartz and light guide geometries as well as for a variety of light guide reflective materials and two PMT sizes. In addition, several tests were carried out to determine the signal magnitude from events going through the light guide, to study the signal relative signal dilution when events from traverse the light guides, as opposed to the quartz. This is further discussed below. The results of these tests were compared to those obtained from previous cosmic ray studies and are now being used to benchmark the simulations.

E.4.1 Simulations

A complete detector design has been implemented in the full MOLLER simulation and many single detector simulation studies were performed to optimize geometry material and background rejection. An example of a single detector simulation study is shown in Figures. 46 and 47. A complete angle study was carried out, to study the effects of the quartz orientation with respect to the incident electrons and to study the effects of the light guide orientation with respect to the quartz. Simulations also included variations of quartz geometry, including trapezoidal and rectangular chapes, thickness and flat or 45 degree angle cuts along the edge that interfaces with the light guides (see Figs 46 and 51). Light guide geometry (length, flare, size)

were also studied using simulations. The primary results that were obtained for each configuration include photoelectron yield and signal RMS width. The simulations were checked agains cosmic ray data, however, to get a definitive value for the number of photoelectrons, to benchmark the simulations against, and to carry out a realistic study of light yield variation as a function of reflective material properties in the light guide (which is very difficult to simulate accurately), dedicated prototype test needed to be performed with minimum ionizing beam electrons.

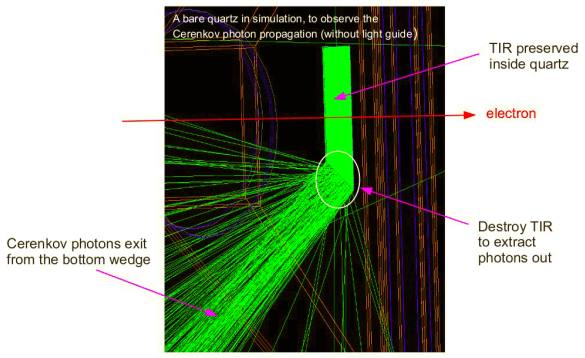

Figure 46: *Simulated event in a single MOLLER main detector.*

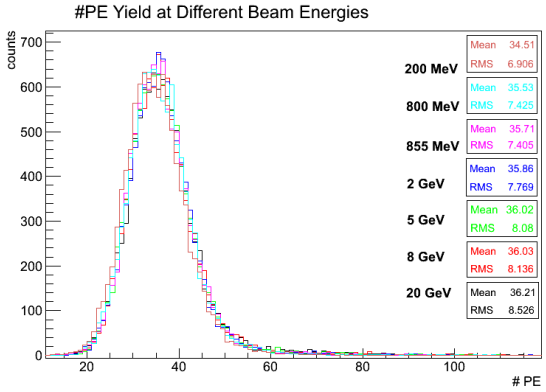

Figure 47: *Simulated photoelectron yield for a variety of energies, for a 35 cm long light guide coupled to a 1.5 cm thick quartz with a single 45 degree cut (Q1, as shown in Fig. 51) and a 3 inch PMT, arranged as seen in Fig. 52. The beam was at normal incidence to the quartz, as shown in Fig 46.*

E.4.2 The MAMI Prototype Beam Tests

Figures 48 and 49 show the setup for the prototype beam tests at MAMI facility. The overall configuration of the test setup is shown schematically in Fig. 50. An 855 MeV electron beam was directed through the prototype detectors, which were mounted on a vertical and horizontal translation stage. Using the translation stage, the beam transverse position of the detectors could be adjusted remotely. This was used to carry out several scans, to determine the sensitivity of photoelectron yield with respect to electron hit location on the quartz and on the light guides. The beam pipe exit flange included a thin (0.5 mm) aluminum window, to reduce background and beam divergence due to passage through excess material. Two scintillator detectors were used as a trigger for the gate input to a charge integrating ADC.

Overall, three different light guide lengths were tested (60 cm, 35 cm, and 25 cm), together with three different reflective materials for each length, except the 35 cm length, for a total of 8 light guide assemblies. The guides were coupled to three different quartz geometries that were hand polished (some grey, some scratch) with a thickness of 1 inch (see Fig 51) and to one 1 cm thick, highly polished (no grey, no scratch) quartz piece with a single 45 degree cut (same as Q1 in Fig 51 that was borrowed from PREX. The lateral dimensions for the 1 inch thick quartz pieces were 8×6 cm^2, while the lateral dimensions of the 1 cm thick PREX detector were 4×18 cm^2. The beam tests were done with 3 inch photomultipliers with quartz windows and bialkali cathodes, manufactured by Electron Tubes Inc. Table 17 summarizes the main tests that were done and the general results obtained. A discussion of the implications is presented below.

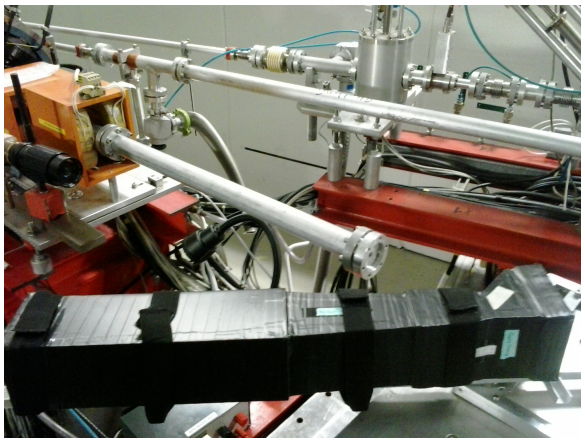

Figure 48: *Upstream view of the beam test setup at the MAMI facility.*

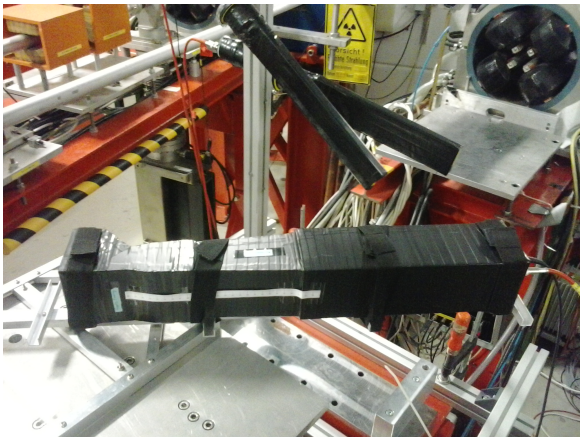

Figure 49: *Downstream view of the beam test setup at the MAMI facility. The trigger scintillator detectors are visible.*

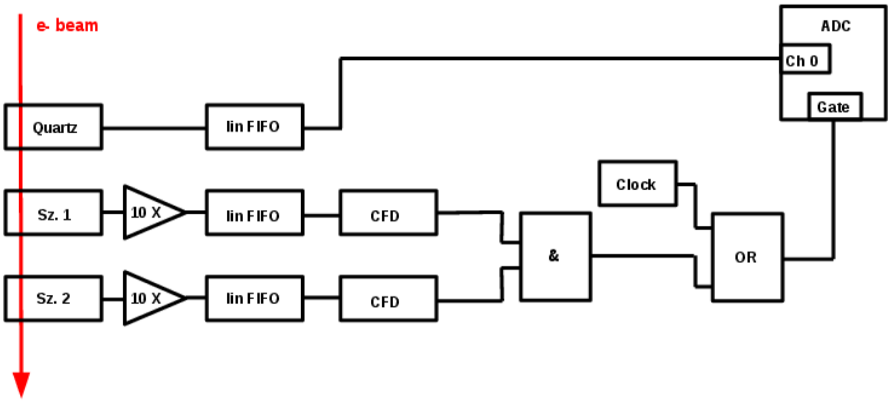

Figure 50: *A schematic of the basic MAMI prototype test setup.*

E.4.3 Implications of Beam Test Results

The beam tests performed at the MAMI facility in Mainz, prove that the current detector design is viable. As listed in Table 17, test results (1) through (4) show that the light yield is high enough and the excess noise low enough to perform the measurement with the proposed detector design. The largest difference in the light yield occurs for different quartz wrapping materials, as noted in result (5) and shown in Fig. 53. Test result (6) notes that no significant variations in light yield due to varying electron hot locations was observed. This is largely expected for small detectors like these. For most of these tests, beam was normally incident on the quartz, and the light guide was tilted 45 degrees with respect to the beam, with the PMT located upstream of the quartz. The results quoted here were taken from plots with the pedestals removed and the ADC channels converted into number of photoelectrons, using single photoelectron calibrations.

The focus of the next round of tests will be to quantitatively examine the dilution and the additional noise introduced into the integrated detector response from events traversing the light guide. For example, Fig. 15 and Fig. 17 in Sec. 3 show that the $e - p$ ring will have a significant Møller rate in its light guides.

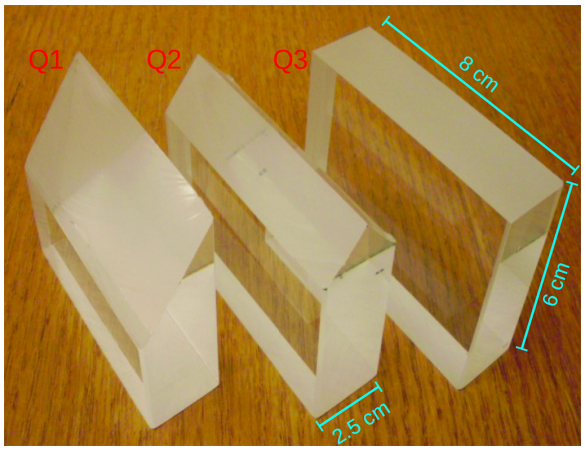

Figure 51: *Three of the quartz geometries with a thickness of 1 inch, used during cosmic ray tests and during the beam tests at MAMI.*

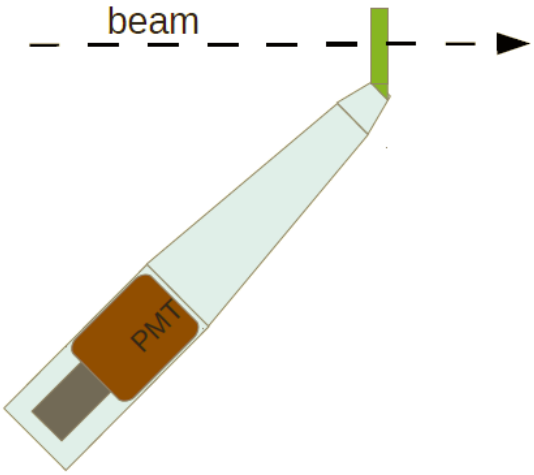

Figure 52: *Prototype detector setup schematic of one of the setups tested with an 855 MeV electron beam, at MAMI.*

We must therefore carefully determine how much of a dilution this will produce. Since the Møller ring is one of the first rings, this effect is much reduced and this has been analyzed in simulations (by weighting the measured light yield from the guides with the simulated rates) to contribute a dilution of about 1%. A way to increase the relative yield from the quartz versus the light guides, is to increase the thickness of the quartz. This is especially an option for the rings at smaller radius, measuring the *e-p* events. Test number (2) in table 17 shows that this can be done without much increase in excess noise from shower activity. Tests performed with the 1 cm thick quartz geometry (item (1)) form the benchmark tests for the current design.

E.5 Radiation Hardness

Radiation damage is in principle a concern, since Cerenkov light production occurs predominantly in the UV, which is exactly where loss in light transmission first shows up. For example, the familiar "yellowing" of lead-glass is due to the loss of transmitted light at the blue end of the spectrum. The dose to the artificial, fused-silica radiator material from the $e + e \rightarrow e + e$ events will be only 15 MRad by the end of the experiment. Given the average path length in the radiators of only a few cm, and our non-agressive short wavelength cutoff of 250 nm set by the UV glass of the PMT windows, no measurable loss is transmission is expected. This is ideal since it means that the photoelectron yield and any detector biases (e.g., with respect to Q^2) will be stable throughout the experiment.

All other detector construction materials in the beam envelope (such as radiator supports) must be vetted for susceptibility to damage under 15 MRad dose. Degradation by potentially elevated ozone and nitric acid levels may also be a factor in the choice of detector materials.

Table 17: *Most Important Prototype Tests Performed at MAMI*

	Description	**General Results**
1	Light yield from 1.0 cm thick highly polished quartz, 25 cm Miro-Silver guide (Fig. 52 setup)	A minimum of 25 photoelectrons per event, with 4% excess noise.
2	Light yield from 2.5 cm thick hand polished quartz, 25 cm Miro-Silver guide (Fig. 52 setup)	A minimum of 55 photoelectrons per event, with 5% excess noise
3	Comparison of various common Light guide reflective materials (with Fig. 52 setup), including UVS, Miro-Silver, Alanod, and mylar.	Data with Kapton blacked-out guide shows that a small portion of the light is from direct shine and most of it is reflected into the PMTs from the guide walls. Relative light yields for the tested materials are all within 90% of each other.
4	Light guide length comparison for 2.5 cm thick quartz between 60 cm and 25 cm Miro-Silver guide (Fig. 52 setup)	60 cm, corresponding to longest guide in current design, looses 32% of the light relative to the 25 cm guide.
5	Comparison of different quartz wrapping materials: No wrapping, mylar, and white paper (e.g. millipore) (with Fig. 52 setup and 2.5 cm thick)	White paper produced by far the best result increasing the yield by a factor of 3 with respect to no wrapping. Mylar increased the yield by a factor of 2 with respect to no wrapping (see Fig. 53).
6	Electron event hit location position scans: Lateral position scan away from the light guide and transverse to the light guide.	Only small amounts light yield variations were were observed for either direction ($\sim 8\%$) (see Figs 54 and 55.)

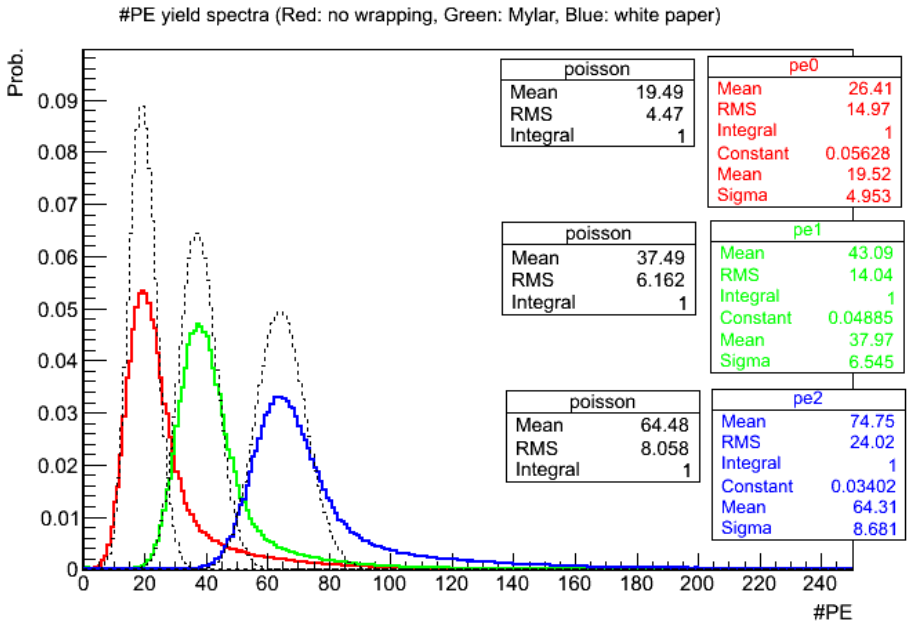

Figure 53: *Results obtained from wrapping the 2.5 cm thick quartz geometry Q1 in mylar, or white paper (e.g. millpore), or leaving it unwrapped.* The black dotted lines correspond to the expected Poisson distribution without excess noise and centered on the fitted means. The starting point and raising edge of the Poissonian distributions fit the corresponding spectrum very well, but the falling edges are not in agreement with the spectrum due to shower tails. The mean and RMS of the whole spectrum, as well the Gaussian-fit parameters of the spectrum are also shown. The Gaussian-fit parameters are very close to the Poissonian parameters. Evidentally, white paper is the best wrapping material.

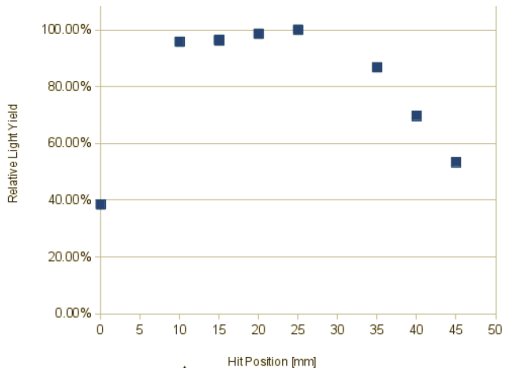

Figure 54: *Normalized light yield from a vertical position scan of an 8 cm wide, 2.5 cm thick quartz piece (geometry Q1).*

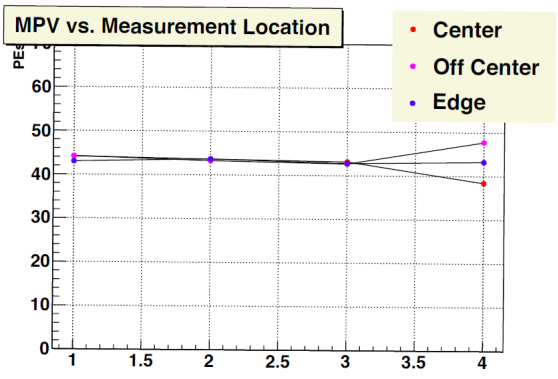

Figure 55: *Prototype detector setup schematic of one of the setups tested with an 855 MeV electron beam, at MAMI.*

F Tracking Detectors

F.1 Introduction

Precision tracking systems are important for several auxiliary measurements within the MOLLER experiment. These include verifying the acceptance of the quartz detectors, understanding the optical properties of the magnetic field configuration, and position dependent responses of the quartz detectors. The tracking requirements for this experiment are full azimuthal coverage (though not necessarily in a single configuration), moderate position and angle resolution, and reasonably uniform efficiency.

The challenge of measuring the acceptance and quantifying its uncertainty is non-trivial, but important as the relative contributions of Møller-scattered events over the full range of acceptance, with proper weighting, is required to relate the measured parity-violating asymmetry A_{PV} to the underlying theoretical prediction. This is the kinematic-dependent term defining the "kinematic factor" or analyzing power, $\mathcal{A} \equiv A_{PV}/Q_W^e$ from Eqn. 3 in Sec. 1.2, dependent on the beam energy E and the center-of-mass scattering angle θ

$$\mathcal{A} \equiv \frac{mG_F}{\sqrt{2}\pi\alpha} \frac{4E\sin^2\theta}{(3+\cos^2\theta)^2}. \tag{15}$$

Because of the very broad momentum acceptance of the spectrometer and the possibility for accurate placement of acceptance-defining collimators, the problem simplifies greatly. If the momentum acceptance is uniform as a function of accepted angle, sufficiently accurate construction and placement of the acceptance-defining collimators is all that is required. The purpose of the magnetic optics reconstruction in this context is to validate the underlying assumptions.

The proposed tracking system would consist of several GEM layers after the magnetic elements and immediately before the quartz. Multiple layers spaced along the beam axis provides a lever arm to reconstruct not only the positions, which we will denote with cylindrical coordinates r and ϕ, but also the directions, which we will call $r' = dr/dz$ and $\phi' = d\phi/dz$, shown in Fig. 56. These four independent variables map from the independent variables which describe the scattered particle, the lab scattering angle $\theta_{\rm lab}$, the electron momentum p, the lab azimuthal angle $\phi_{\rm lab}$ and the reaction vertex position v_z (we neglect the v_x and v_y coordinates as these are known event-by-event from the raster current and represent small perturbations in the map).

F.2 Calibration Requirements

To measure the acceptance of the apparatus, a model of the magnetic transport optics must first be obtained. Calibration of the optics over a relatively broad range can be performed by mapping out specific and identifiable points with defined polar and azimuthal angles, momentum, and target position. Using a nuclear elastic or Møller interaction with a well defined beam energy correlates the momentum and polar angle.

With the use of foil target and a removable sieve before the magnetic elements, the remaining variables can be constrained. The sieve must be at least $\sim 40\ X_0$ to be able to sufficiently stop the highest energy electrons. As this sieve must be tied to the acceptance-defining collimator, absolute positioning can be done both by survey and cross-checked by measuring and then minimizing the azimuthal modulation of rates resulting from a small transverse displacement of the acceptance defining collimator.

Figure 57 shows the amplitude of the rate modulation as a function of the collimator displacement. An array of scintillator pairs immediately behind the quartz will allow for counting mode operation with well-defined relative azimuthal efficiency. Assuming a modulation amplitude measurement to an accuracy of 2% of the average rate per sector, the positioning of the collimator can be determined to an accuracy ~ 1 mm. The impact of the residual uncertainty of 1 mm on the transverse position of the acceptance-defining collimator will be less than 1% on the average analyzing power variable $\langle\mathcal{A}\rangle$, and thus negligible.

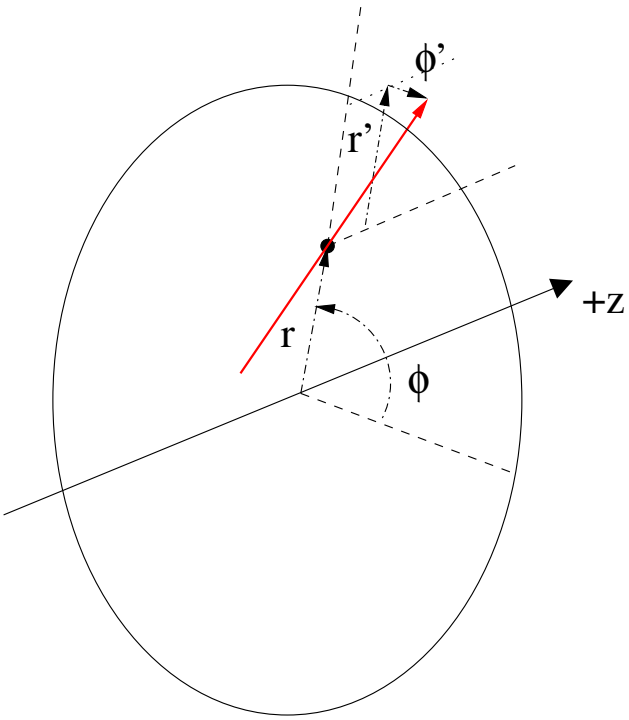

Figure 56: Tracking coordinates system. Note that r' and ϕ' must be taken with infintesimal change in z.

Nevertheless, knowing the value of this shift is important for constraining other systematics, such as parity conserving asymmetries and helicity-correlated beam trajectory differences which which could produce their own azimuthal modulations in the observed detector asymmetries.

By having a map of $(\theta_{\rm lab}, p, \phi_{\rm lab}, v_z) \rightarrow (r, \phi, r', \phi')$ at specific points and if this map is one-to-one, the problem of optics reduces to interpolating between these points. The propagated uncertainty on $\langle \mathcal{A} \rangle$ is then dependent on the number of calibration points and the functional form of the acceptance used. The form of the acceptance must rely upon simulations and perturbations on various positioning and magnetic fields which can then be used for a maximum likelihood fit. This is also critical to take into account higher order effects such as beam raster, multiple scattering, and radiative effects.

While direct measurement of the Møller acceptance over the full region of phase space is possible, this may prove to be unnecessary. There is a natural kinematic relation between the Møller-scattered, and elastic $e-p$ scattered events; see Fig. 58. By comparing the form of the $e-p$ elastic events to various simulation position and field scenarios, in addition to directly measured acceptance points and the Møller optics, additional confidence can be built in the acceptance function. Based on Monte Carlo simulations using simple models of the acceptance, such as splines which contain no actual physics or geometrical information, differences between the average analyzing power variable through various methods and the "true" value were found to be $\lesssim 0.5\%$.

To obtain the relative Møller acceptance at individual points in $\theta_{\rm lab}$, which is directly related to the free variable θ in Eqn. 15, the first step is to measure judiciously chosen narrow angle bites of Møller-scattered events at the 11 GeV beam energy. A fixed sieve where each of six sectors samples a pair of different angles is proposed, which relies on the symmetry of the magnetic field sectors. One sector will be covered by the sum of all 12 slits as a check of the symmetry. To maximize ϕ coverage (which is desirable to see edge effects of the phi acceptance), fixed ϕ coordinates can be obtained by blocking small sections through constant θ "slots".

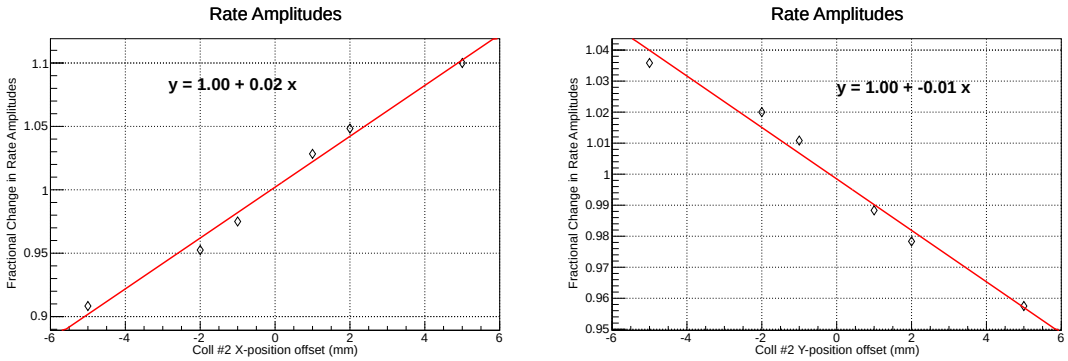

Figure 57: A misplacement of the acceptance-defining collimator transverse to the beam produces a small azimuthal modulation in rate of about 2-3%/mm.

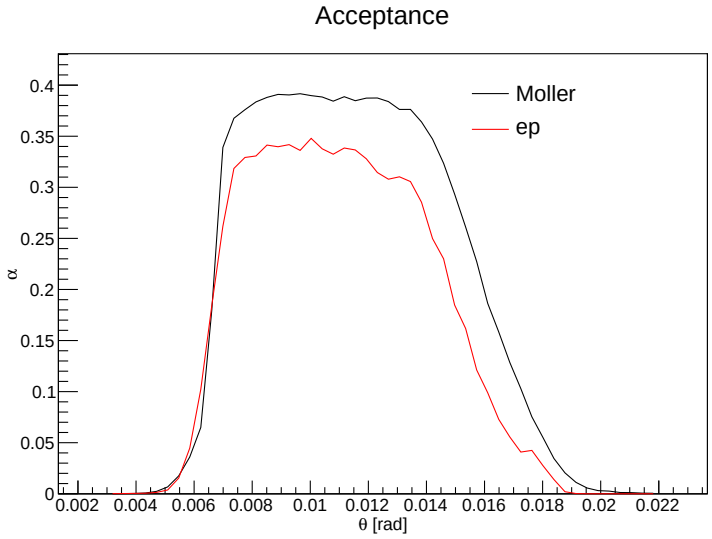

Figure 58: Acceptance of Møller and elastic events, scaled arbitrarily, and ignoring radiative effects.

Calibration runs at special incident beam energies of 4.4, 6.6 and 8.8 GeV will help to map out variations in the momentum acceptance which must be folded in to account for radiative effects. To make relative relationships between different energies, the angles must be placed where 11 GeV Møller-scattered momenta would coincide with nuclear-elastically scattered (equivalently, the incident beam) momenta i.e. $\theta \sim 12$ and 8 mrad respectively for 4.4 and 6.6 GeV.

A separation between the top row points in Fig 59 is all that is required by the GEMs for this task, meaning a few mm resolution in position with a GEM spacing of a few meters (to guarantee a resolution of $r' \sim 10^{-3}$). Kinematically at these angles, elastic scattering from even light nuclear targets do not have large recoil energies, providing scattered electrons which are practically mono-energetic. This is fortunate, because as Z increases, the nuclear cross section increases as Z^2, whereas the Møller cross section increases as Z (the bound number of electrons). A set of light target foils, such as ^{12}C, will be used for the calibration runs.

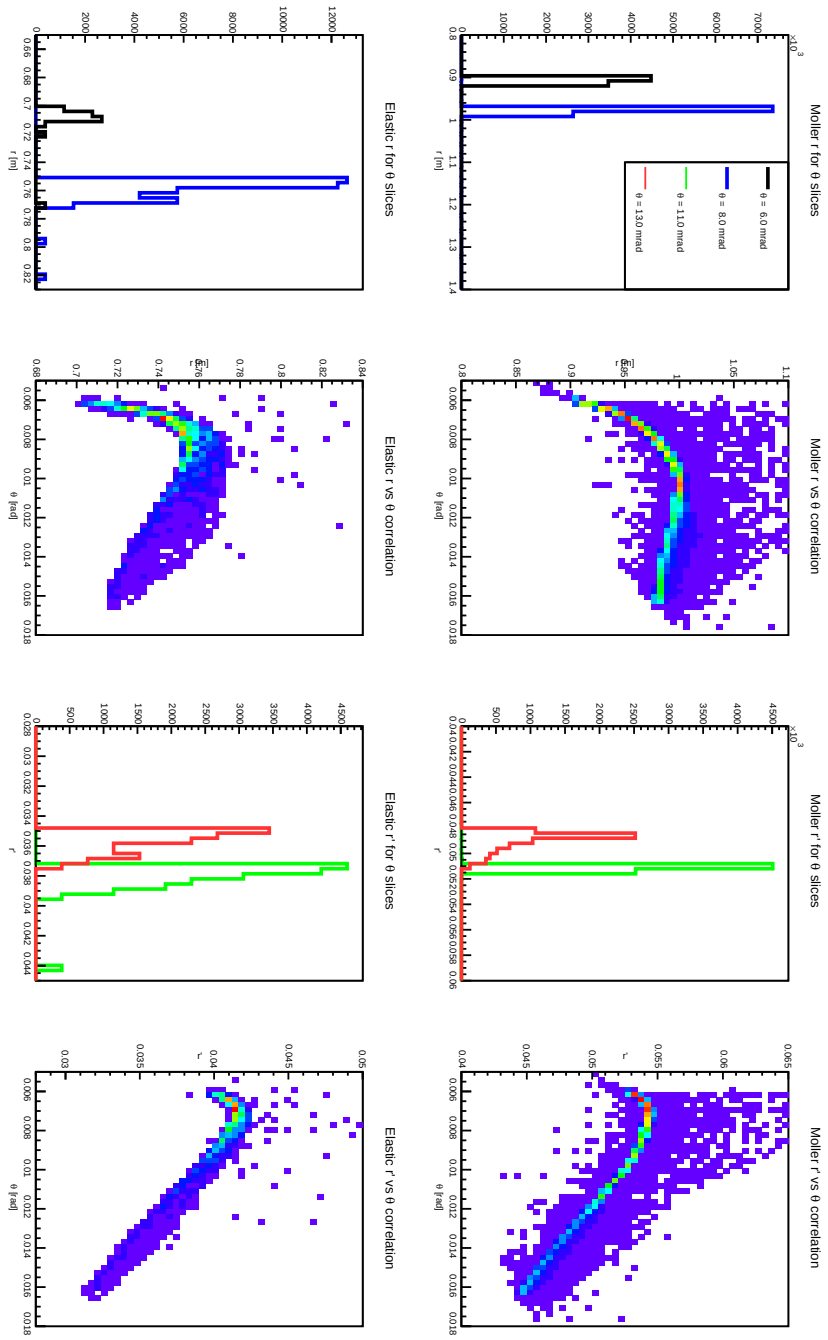

Figure 59: The general properties of the optics reconstruction. Shown in the 1D histograms are the radius r and tangent $r' = dr/dz$ for Moller (top row) and elastic (bottom row) events for two 0.2 mrad slices in θ each. Raster effects are suppressed and only thin foil target is considered. The separation between Moller events, as well as the elastic events, is clear at the mrad level. Small angles ($\theta_{\mathrm{lab}} < 10$ mrad) may be reconstructed with the variable r while for larger angles, r' can be used and is practically linear. There is a small ϕ dependence and a sector dependence which has been averaged over for simplicity.

F.3 Tracking Detector Requirements

As discussed above, our tracking system is designed to verify the spectrometer optics, to measure the appropriately weighted mean of the kinematic factor $\mathcal{A}$ that multiplies A_{PV}, and to determine backgrounds. To this end, the tracking system will consist of 4 GEM planes, located downstream of the two magnets, and upstream of the main integrating quartz detectors. The primary requirement for the acceptance is to be able to separate between events from different sieve holes when we use a staggered-hole configuration. Based on Fig. 59, this can be fulfilled with $1\ \mathrm{mm}$ spatial and $1\ \mathrm{mrad}$ angular resolution.

As discussed above, the GEM planes will be placed in two sets of pairs in rotatable wheel assemblies, as shown in Fig. 19. The GEM planes must be insertable to intercept the charge particle flux after they exit the vacuum window, but must be out of the way during the collection of production data. In order to reduce costs, we propose to cover four septants and have them attached to a remotely controlled "wheel" with the ability to rotate in the azimuth up to one septant, providing full and redundant coverage.

The present design of a GEM chamber presented roughly a 0.5% radiation length for electrons incident normal to the plane. Using the standard multiple scattering formula for the central 98% of the scattered distribution of ultra-relativistic particles , for the lowest momentum electrons of interest ($\sim$ 2 GeV), and $x/X_0 = 2 \times 0.5\%$ for the two upstream foils, this corresponds to $\delta\theta$ of about $0.4\ \mathrm{mrad}$. This is the limiting factor on the angular resolution in the GEMs, but is still sufficient to separate the staggered peaks in the acceptance calibration.

F.3.1 GEM Detectors in Simulation

Within the simulation, placeholder GEM detectors, each composed entirely of vacuum but capable of recording hits, is currently implemented in the simulation package developed for this experiment presented in App. C. A total of 4 GEM detectors are represented within the simulation. The GEM detectors are located along the beam propagation axis in two sets of pairs. Each pair consists of GEM detectors separated by 1 m. The two pairs are separated by 4 m. Their nominal locations in simulation are 22.6, 23.6, 27.6 and 28.6 m respectively from the center of the target. (The quartz detectors are located at 28.7 m). The Monte Carlo hits recorded by the GEM detectors, r_{MC}, ϕ_{MC}, r'_{MC} and ϕ'_{MC}, are used to generate "reconstructed" track variables, r_{rec}, ϕ_{rec}, r'_{rec} and ϕ'_{rec}. This is done via χ^2-minimization of the straight line fit through coordinates defined by r_{MC}, ϕ_{MC}, r'_{MC} and ϕ'_{MC} for each track.

F.3.2 GEM Detector Sizes

The GEM detector sizes depend on their location along the beam propagation axis, with the detectors located further downstream requiring larger area in order to inercept the electrons in acceptance. Simulation is used to determied the GEM detector sizes. The GEM sizes necessary to intercept electrons in a given septant are determined by observing electrons that Møller scatter inside the target, and arrive at the quartz detectors. The 4 GEM detectors are located at their nominal positions of 22.6, 23.6, 27.6 and 28.6 m. The quartz detectors are located at 28.7 m.

Because strong ϕ-defocusing results in electrons being swept across the septant boundaries by the time they arrive at the quartz detectors, the electrons that arrive at a particular septant at the nominal location of the quartz detectors are selected and tracked upstream through each of the GEM planes in order to determine the sizes of individual GEM planes. The GEM detector shapes determined from this study are trapezoidal, but with its parallel sides replaced by arcs of two different radii of a concentric center.

The GEM detector sizes determined via such analysis, and incremented by 5% in r and 10% is ϕ is presented in Table 18. These are the sizes required to intercept electrons from any one particular septant. The proposed 4-septant GEM configuration is shown in Fig. 60 which would allow for the full azimuthal range to be covered through only one rotation to the neighboring septant. Precise placement around the

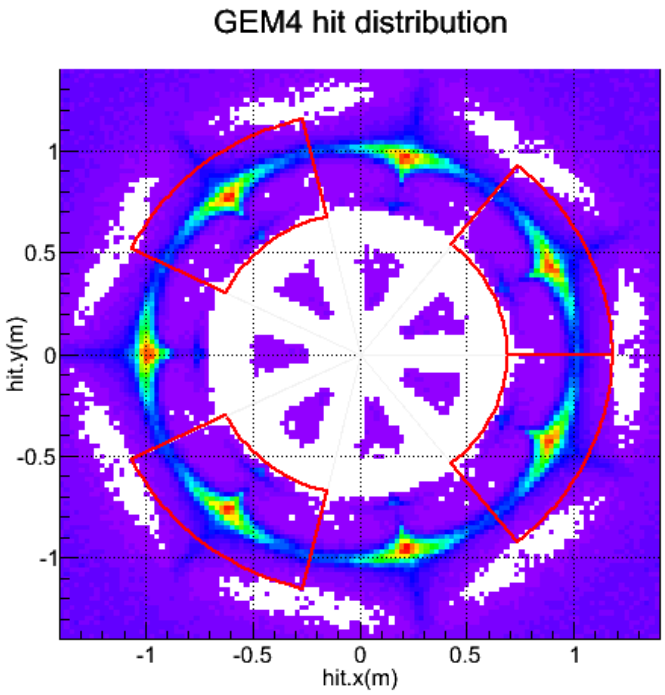

Figure 60: The proposed GEM configuration that covers four septants. Such a configuration allows full azimuthal coverage through only one septant rotation.

azimuth at fixed septants, shown, and also half septants would be useful to test GEM efficiency across the face. Allowing a set of GEMs to have a range of motion that it can be placed across three adjacent septants would allow full cross referencing distributions in each septant by at least two GEM sets.

	z(m)	Inner rad(m)	Outer rad(m)	$\pm\phi$(deg)	Area (m^2)
GEM #1	22.64	0.45	0.88	31.0	0.31
GEM #2	23.64	0.49	0.93	30.5	0.33
GEM #3	27.64	0.65	1.14	28.8	0.44
GEM #4	28.64	0.68	1.19	28.8	0.48

Table 18: GEM detector sizes needed to intercept electrons incident on the quartz detector of a given septant.

F.3.3 GEM chamber R&D program

The University of Virginia group is currently leading an aggressive R&D program to develop large area GEM chambers for the Hall A Super Bigbite apparatus (SBS). The active area of large tracking chambers of SBS will be 60×200 cm^2. These large GEM trackers will be assembled by combining 60×50 cm^2 "chamber modules" with narrow edges. The UVa group has already constructed several 60×50 cm^2 and GEM chamber modules and is currently setting up for the production of 40 such modules for SBS. The expertise gained with these GEM modules will be applied to the design of GEM modules for SoLID.

The UVa group operates a well-equipped GEM R&D facility that includes the following:

- **UVa Detector development lab:** This 10×10 m^2, well-equipped nuclear physics detector lab has been used for the development, construction and testing of many large detector systems. The detector lab consists of two 3×3 m^2 level 1,000 clean rooms located within a 4×10 m^2 semi-clean area. So far ten large area GEM chambers have been sucessfully constructed in this clean room. The specialized GEM construction equipment in the lab includes large area GEM foil stretchers, GEM foil testing high-voltage boxes, a large volume ultra-sonic cleaner for GEM frame cleaning, a Keithley 6485 picoammeter for GEM foil testing, and a GEM foil storage dry N_2 box.
- **GEM readout systems based on APV25-S1 electronics:** The UVa group has two APV25 based readout systems: a 10,000 channel SRS system from CERN and a 3,500 channel system developed by the INFN group. Both systems are fully operational and are used for testing prototype GEM chambers.
- **Wiener-Iseg multi-channel high voltage system** The UVa detector group owns a brand new Wiener-Iseg multi-channel high voltage system that is especially suited to provide high voltage to sensitive tracking chambers. This system currently has 24 channels and can be expanded to 160 channels.

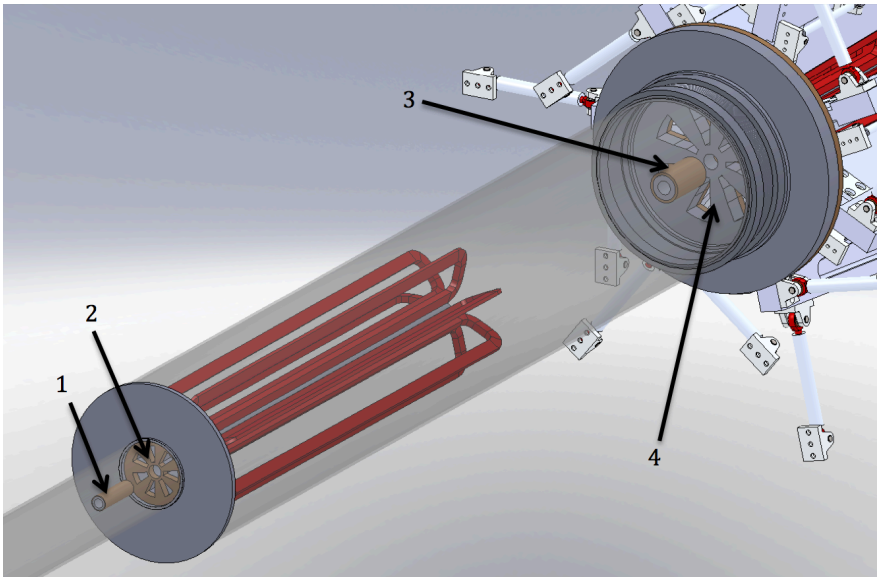

Figure 61: Overview of the collimators.

G Acceptance Sensitivity

In this section we present a summary of the positioning tolerances and estimate their contributions to the acceptance systematic uncertainty in the asymmetry. The contributions from positioning uncertainties by the target, collimator, or magnetic field are all negligible compared to the upstream collimator inner radius, which is defined by a machining tolerance. Given a tolerance of $200\ \mu\mathrm{m}$ on machining and an $1\ \mathrm{mm}$ tolerance on uncorrelated positioning between systems, this gives a systematic uncertainty of $0.03\ \mathrm{ppb}$, or 0.1% in the measured asymmetry. In the subsequent subsections, discussion of how each contribution is calculated is presented.

G.1 Target Alignment

The sensitivity of misalignments in the position of the target in z is studied via varying the target position along the nominal beam trajectory. The effect on the asymmetry was found to be less than 0.05% per cm.

G.2 Collimator Tolerance

As the collimating system is used to define the geometric acceptance of the electrons, positioning and machining tolerances must be defined. We consider the transverse positioning of the collimators as well as changes in the inner and outer radius of their apertures. The schematic and numbering of the collimators are given in Fig. 61 and we adopt the standard Hall A right-handed coordinate system where the z direction is nominally the beam direction and y is against gravity. Collimator 2 is of particular importance as it is designed to be the acceptance-defininig collimator.

The tolerances in the transverse alignment of collimators 2 and 4 are studied by adding small positional offsets relative to their nominal positions. The offsets are introduced independently along the transverse direction to the beam propagation direction. In all cases the dependence was found to be quadratic and the linear component to be negligably small for changes on the order of $1\ \mathrm{mm}$, Table 19.

	a (ppb)	b (ppb/mm)	c (ppb/mm^2)
Coll # 2, x-scan	2.99e+1	7.34e-4	3.66e-3
Coll # 2, y-scan	2.99e+1	4.88e-4	3.98e-3
Coll # 4, x-scan	2.70e+1	-5.78e-5	3.84e-3
Coll # 4, x-scan	2.70e+1	1.49e-4	3.53e-3

Table 19: Parameters of the fit equation of the form $y = a + bx + cx^2$ of asymmetry vs collimator position offset.

Asymmetry		
	a (ppb)	b (ppb/mm)
Inner-rad	29.95	0.14
Outer-rad	29.94	-0.06
Fractional change in asymmetry		
	a	b (1/mm)
Inner-rad	-4.19e-4	-4.74e-3
Outer-rad	-4.35e-5	2.12e-3

Table 20: Parameters of the fit equation of the form $y = a + bx$ of asymmetry and fractional change in asymmetry vs inner/outer radius change of collimator 2.

G.2.1 Collimator Apertures

The inner and outer radii of collimators 2 and 4 were varied independently within the simulation. The effects on the measured asymmetry for collimator 2 are shown in Table 20 and Fig 62. These define the machining tolerances and in particular for collimator 2, the inner radius must be machined within 200 μm for a systematic uncertainty of 0.03 ppb on the asymmetry, or 0.1%. This is the dominant systematic.

G.3 Magnetic Field

Changes in the magnetic field can cause changes to particle trajectory and therefore the acceptance of the quartz. A study was done by modifying a single coil position and angle and then generating a modified field map and then studying the change in measured asymmetry. Variations were done for position along the beam line, radial position, and azimuthal position. In addition rotations of a single coil about its center of mass was done about three independent axes. In all cases, the change in asymmetry was less than 0.4 ppb per cm for the position dependent cases and 0.2 ppb per degree for the rotation cases.

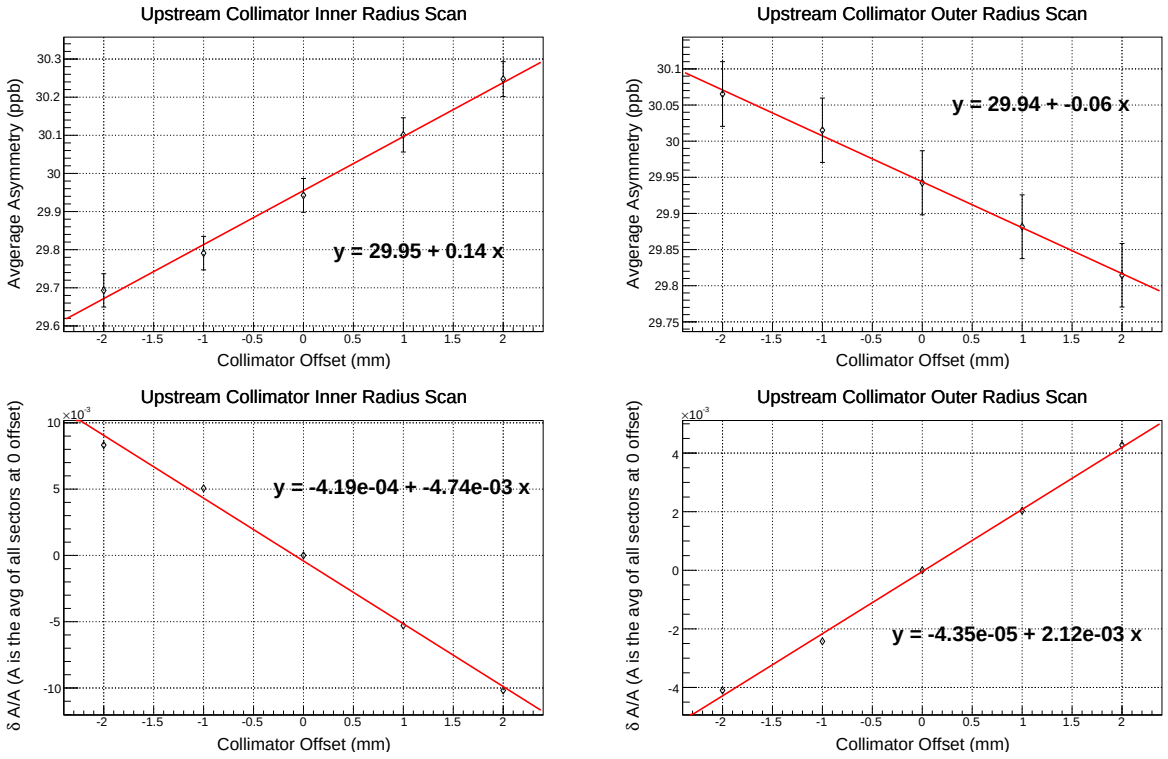

Figure 62: Coll #2, inner/outer radii-scan

H DAQ and Electronics

H.1 Overview

Similarly to the Qweak experiment and other parity-violating experiments, two DAQ systems will be required: 1) An integrating DAQ for the production data, and 2) A counting-mode DAQ for low-current calibrations, e.g. measurement of Q^2.

An overview of the integating DAQ is shown in figure 63. The DAQ runs in the framework of CODA, the Jefferson Lab DAQ toolkit in which multiple VME or other types of crates are synchronized by a custom Trigger Supervisor board; the event fragments are gathered via a standard TCP/IP network to a workstation where whole events are built and written to local disk and subsequently stored in the Mass Storage Tape Silo (MSS). The same diagram describes the concept of both DAQ systems, but the differences are in the trigger source and the types of frontend boards that digitize the data. The trigger source goes to the Trigger Supervisor, as well as to the frontend boards. For the main integrating DAQ, the trigger source is a Master Pulse from the helicity electronics, while for the counting-mode DAQ the source of triggers will be scintillators positioned to intercept tracks through the GEM detectors. The integrating DAQ will run deadtime-free at the anticipated ~ 2 kHz helicity flip rate and integrate signals over the helicity period (0.5 msec). The signals consist of PMTs from the detectors or few-volt voltage levels from various devices such as beam position monitors (BPM) or beam current monitors (BCM). When the ADCs integrate over the helicity pulse, the first fraction (~ 0.1 msec) of the pulse is blanked-off to remove instabilities due to the switching of HV on the Pockels cell which controls the beam polarization. The counting-mode DAQ will run at low current and the triggers can be prescaled to ensure a low deadtime; this DAQ will use standard digitization devices to record the information from the GEMs and scintillators, much of which will have already been developed for the SBS spectrometer.

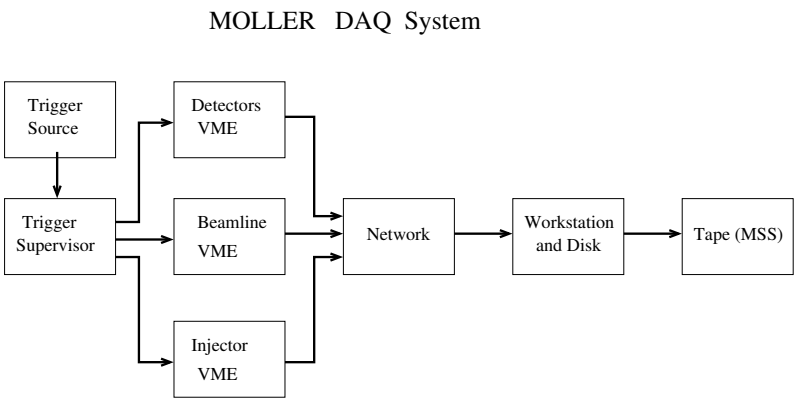

Figure 63: *Overview of the DAQ system for the MOLLER Experiment based on the standard JLab CODA system. For the integrating-mode DAQ, the trigger source is the master pulse from the helicity electronics. For the counting-mode DAQ, the triggers come from a scintillator-based tracking trigger.*

H.2 The TRIUMF Electronics

The heart of the integrating-mode DAQ will be the low-noise electronics developed for the Qweak experiment by TRIUMF should be suitable with little or no modification for the 11 GeV Møller measurement. Signals handled by the front end electronics are shown schematically in Figure 64 for the quarz detector with the largest flux of about 5 GHz. The gain of the photomultiplier will be adjusted to yield an anode current of 6 μA, depending on the measured flux in each detector. The current signal is converted to a voltage by a transimpedance preamplifier located close to the detectors. The voltage signal goes to electronics outside the Hall where it is sampled at 500 KHz with an 18-bit ADC. These digitized samples are then integrated over each spin state in an internal FPGA. The signal levels anticipated will be similar to those of the Qweak experiment, so the same, or very similar, electronics will be appropriate.

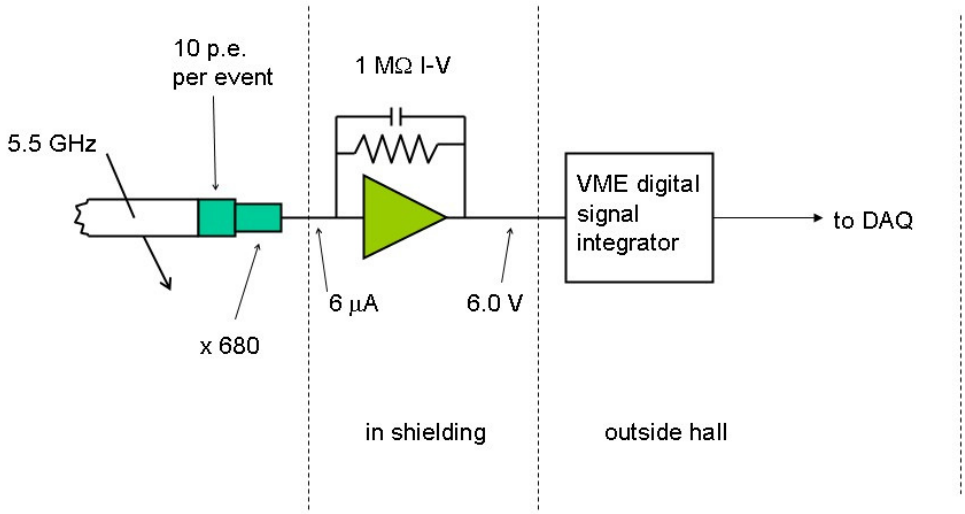

Figure 64: *Possible front-end signals assuming a 5.5 GHz event rate and 10 photoelectrons per event. The photomultiplier gain is set to deliver 6 μA to the 1 MΩ current to voltage preamplifier.*

Preamplifiers Figure 65 shows one of the preamplifiers built for the main detectors of the Qweak experiment. The main features are:

- Gain: V_{out}/I_{in} = 0.5, 1, 2, or 4 $M\Omega$, switch selectable.
- Output: ± 10 volts. Adjustable ± 2 V offset. Drives 130 m RG-213 cable.
- Input: current limit set by gain and 10 volt output limit.
- Power: +5 VDC on Lemo connector.
- Bandwidth: $f_{3db} = 26$ kHz.
- Noise: 0.5 $\mu V/\sqrt{\text{Hz}}$ referred to output with 1 MΩ gain setting. (Amplifier noise specification assumes the input capacitance of 5 m of RG-62.)
- Packaging: two channels per 80 mm x 70 mm x 28 mm box.

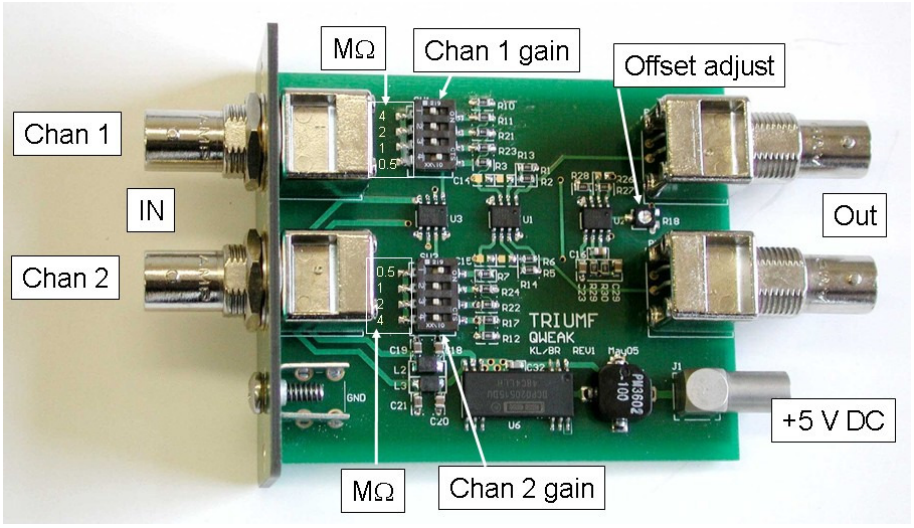

Figure 65: *TRIUMF current-to-voltage preamplifier for the Qweak experiment.*

Digital Integrators Figure 66 shows a TRIUMF digital integrator built for the Qweak experiment. The module has 8 channels in a single width VME module. The main features are:

- Trigger: external NIM signal or internal trigger selectable.
- Integration time: selected as a number of samples, up to 1/30 second.
- Sample rate: selectable up to 500 ksps. 18-bit ADCs.
- Clock: internal 20 MHz or external NIM selectable.
- Input: ± 10 volts. High impedance quasi-differential.
- Output: 32 bit sum. The integration period may be sub-divided into up to four blocks. No dead time between blocks.
- Anti-aliasing: 5-pole filter with 50 kHz cutoff.

H.3 Performance

Table 21 shows that based on reasonable assumptions about the main detector signals on the Møller experiment, the Qweak electronics seem suitable. Noise in the table is referred to the preamp output. The total electronic noise is negligible compared to counting statistics. A null-asymmetry test with a battery-driven current source could be made in one shift at the part per billion level, or 0.1 ppb in 30 days.

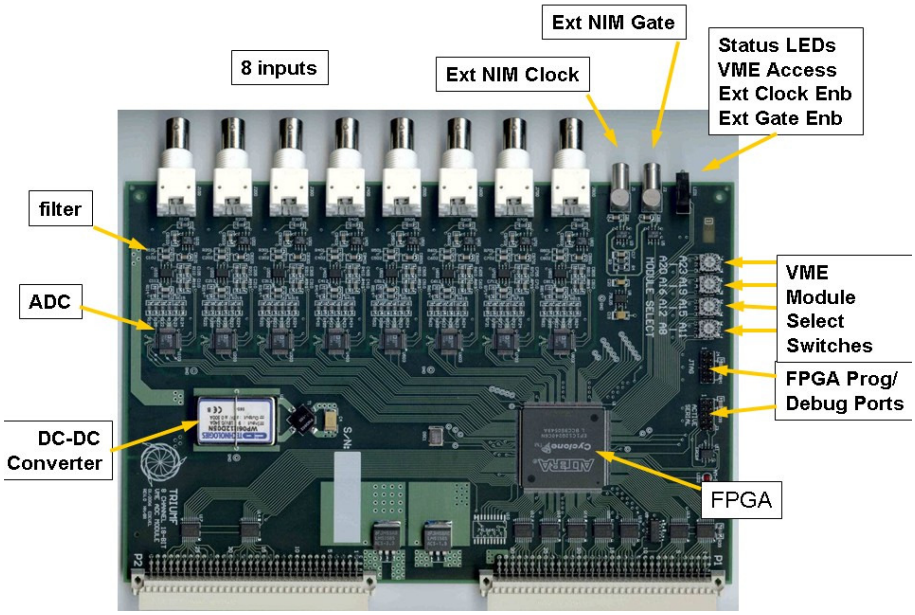

Figure 66: *TRIUMF VME-based digital integrator for the Qweak experiment.*

Table 21: *Comparison of various sources of noise assuming the signals of Figure 64. "Beam on" shot noise is equivalent to counting statistics. The electronic noise is based on tests with TRIUMF electronics built for the Qweak experiment. The electronic noise alone is negligible compared to counting statistics. A null test with a noiseless battery could be made to* $\leq 10^{-9}$ *(one ppb) in a day.*

Type of Noise	charge quantization (e)	Spectral density $\mu V/\sqrt{Hz}$	RMS Noise in 500 Hz BW (1 ms integral)	RMS Noise in 50 KHz BW (VME input)
"beam on" shot	6800	114	2560 μV	25,600 μV
LED test shot	680	36	800 μV	8,000 μV
battery test shot	1	1.4	31 μV	310 μV
preamp		0.5	11 μV	110 μV
digital integrator		1.3	29 μV	290 μV

I Compton Polarimetry

Compton polarimetry is a very promising technique for high precision polarimetry at beam energies above a few GeV. Beam interactions with a photon target are non-disruptive, so Compton polarimetry can be employed at high currents as a continuous polarization monitor. The photon target polarization can be measured and monitored with a very high precision, and the scattering between a real photon and free electron has negligible theoretical uncertainty, without the atomic or nuclear effects which can complicate other measurements. Radiative corrections to the scattering process are at the level of 0.3% and are very precisely known. While the SLD collaboration result, with a precision of 0.5%, demonstrates the feasibility of very high accuracy Compton polarimetry, that measurement was ultimately limited by the inability to detect individual scattered particles (due to the pulsed beam) and the high Bremstralung background in the photon detector due to the proximity to the interaction region. Conditions at JLab are favorable for both of these concerns. The existing apparatus and plans for future improvements are described below.

I.1 The Hall A Compton Polarimeter Baseline Upgrade

As pictured in Fig. 67, the Hall A Compton polarimeter [72] is located in a chicane, about 15 meters long, just below the beamline. After modification of the bend angle to accommodate 11 GeV running with the existing chicane magnets, the electron-photon interaction point will be 21 cm below the primary (straight-through) beamline. After passing the electron-photon interaction point, the electron beam is bent about 3.5 degrees by the third chicane magnet and then restored to the main beamline. The scattered electrons are separated from the primary beam and detected using silicon microstrips, just before the fourth chicane magnet. Scattered photons pass through the bore of the third chicane magnet to be detected in a calorimeter.

The photon target is a 0.85 cm long Fabry-Perot cavity crossing the electron beam at an angle of 1.4°. The laser system can be configured for infrared (1064 nm) or green (532 nm) light, and has achieved power levels of 10 kW of green light for polarimetry measurements. The laser light is polarized using a quarter-wave plate, and can be toggled between opposite polarizations of highly circularly polarized light. The feedback loop which locks the laser to the cavity resonance can be disabled to enable backgrounds from all non-Compton-scattering processes. To reduce overhead from the time required to re-lock the cavity, the transition between laser states is typically performed with a period of 1-2 minutes. The polarization of the transmitted light from the locked cavity and the reflected light from the unlocked cavity are each monitored and can be used to characterize the laser polarization at the interaction point.

The vacuum in the interaction region is at the level of few $\times 10^{-8}$ torr, implying a photon background rate due to Bremsstrahlung scattering from residual gas of around 5 Hz/μA. The dominant source of background in the photon detector is thought to be tails of the beam halo distribution interacting with the apertures in the interaction region. In contrast, for the electron detector the dominant background is thought to be dominated by energy tail or position halo of the primary beam since electrons from aperture scattering would presumably not cleanly transit the third dipole. When well-tuned, the background rates in the photon and electron detectors have been seen to be roughly similar: around $<$100 Hz/μA in recent use. At 11 GeV, with a 10 kW IR cavity, the Compton-scattered rates would be approximately 20 kHz/μA and the asymmetry will range from 17.8% to -4% over the energy spectrum. If backgrounds remain comparable to recent operation, statistical precision of 0.4% would be possible in less than 5 minutes, depending on the specific detection and analysis approach which is considered.

Electrons are detected in a set of 4 planes of silicon microstrips located just before the 4th dipole. Each microstrip instruments 192 strips with a pitch of 240 μm. Custom readout electronics pre-amplify and discriminate signals from the microstrips, implement a simple tracking algorithm to reduce non-directional backgrounds, and count hits in each strip over specified integration gates corresponding to the helicity pattern of the electron beam. Presently, this system is operating at low efficiency with poor signal size for a

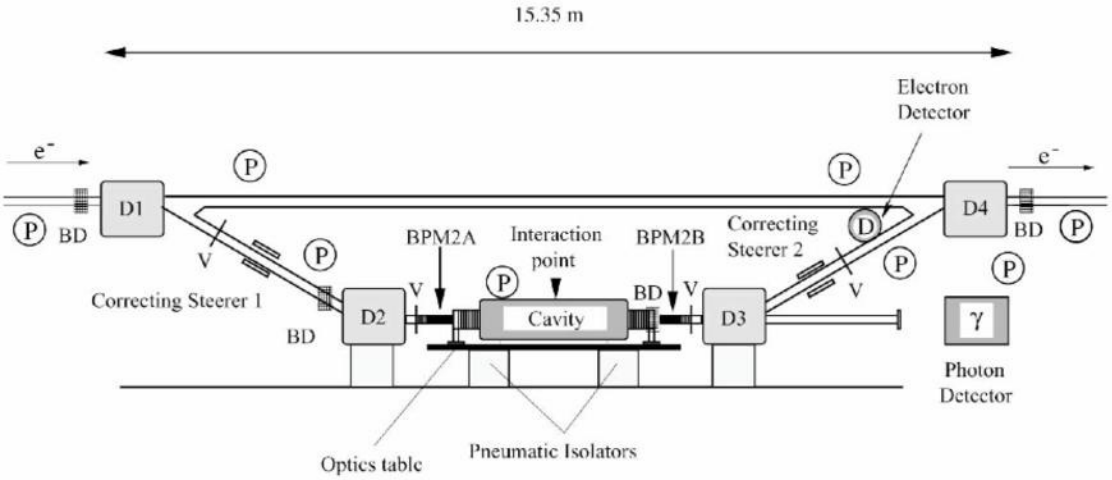

Figure 67: *Schematic of the Hall A Compton polarimeter. Figure from [72].*

minimum ionizing track compared to environmental noise on individual strips. The baseline upgrade would include an improvement in this system to achieve high efficiency and high signal-over-noise for the microstrip readout. The use of diamond microstrips, such as were recently successfully used for the Hall C Compton polarimeter [73], is under consideration. Such diamond microstrips are more difficult to procure and in principle are more challenging to instrument than silicon strips, however, they are more radiation hard and less susceptible to low-energy photon backgrounds.

The calorimeter for detecting scattered photons lies about 7 meters downstream of the interaction point. The strong forward boost of scattered photons leads to a tightly collimated photon beam ($<$1 mrad), so the calorimeter size determined by consideration of energy resolution through shower loss. The photon calorimeter is a GSO crystal scintillator of 6 cm diameter and 15 cm length, with a single photomultiplier tube. The PMT signal is split between two parallel data acquisitions: one with a fast-counting, buffered ADC self-triggered on pulses from the photon detector, and the other utilizing a 250MHz flash ADC (fADC) to integrate the total signal over periods corresponding to the helicity pattern of the electron beam. The fADC system can also record a very low rate of individual pulses for calibration. Each of these dual readouts can be analyzed independently. The fast counting ADC readout and the sample pulses in the fADC system can both be triggered using the electron detector, providing an electron-photon coincidence spectrum for calibration.

I.2 Upgrades Beyond the Baseline

There are several issues which must be addressed, related either to operation at the higher beam energy or to the very high level of precision which is proposed.

- The electron beam halo - a term meant to describe a long tail on the momentum or position distribution of the beam - is expected to be larger at 11 GeV compared to 6 GeV operation, due to synchrotron light emission in the recirculation arcs which will increase the momentum-normalized beam emittance. For Compton polarimetry, a tail on the beam energy distribution is directly responsible for the dominant backgrounds in electron detection, while scattering of beam halo from narrow apertures in the interaction region is thought to dominate backgrounds in photon detection.

- The measurement of the laser polarization must be performed with very high precision.
- The total power of synchrotron radiation emitted by the beam in the chicane arcs will be more than an order of magnitude higher compared to Compton measurements in the 6 GeV era, and this radiation spectrum will be significantly stiffer. Dilution from this radiation would complicate photon and electron detection.
- Photon detection must provide a well-characterized and linear response for photons in an energy range from about 3 GeV to low energies and over a large variation in signal rate, while being radiation hard and also insensitive or shielded from the synchrotron radiation power.

These issues are addressed by several modifications which go beyond the baseline 11 GeV upgrade, listed below and described in the following sections. These improvements are expected to allow us to achieve the precision goals listed in Table 22.

- **Laser system** A larger crossing angle for the photon and electron beams would allow larger electron beam apertures, and reduce backgrounds in the photon detector. This increase in crossing angle comes at the expense of lower luminosity, leading to a tradeoff in signal rate and background rate. With the high cavity power that has been achieved with this laser system, we do not expect to be limited by laser power even at increased crossing angle. The decision on crossing angle can be made when more is known about beam conditions at 11 GeV. The beamline through the chicane magnets is one inch inner diameter, which is about a factor of three larger than the aperture required by the present laser crossing angle. The luminosity would drop roughly linearly with crossing angle, and even with a factor of 1/3 the statistical power of the signal rate for a 10 kW cavity would still be sufficient assuming a reduced background fraction.

  In addition to the option to increase this crossing angle, a system for measuring laser polarization inside the resonant optical cavity (although not while locked to resonance) must be developed and used, along with a thorough study of all optical components, to improve knowledge of the photon polarization.
- **Chicane Modification** The synchrotron light power on the photon detector will be significantly reduced by installing shims to increase the fringe fields of the chicane dipole magnets in the interaction region. This would also soften the synchrotron energy spectrum, making shielding more effective. The effect of synchrotron light on the electron detector is being investigated, with the possibility to add some baffling to limit reflection into the detector.
- **Photon Detector** The photon detection system used for recent running will be replaced with a detector better matched to the Compton photon energy spectrum for 11 GeV operation.

These upgrades are described in more detail below.

I.2.1 Laser System and Luminosity

As described above, in the current configuration of the Hall A Compton, the electron beam interacts with green (532 nm) light in a resonant optical cavity at a crossing angle of about 1.4°. After accounting for the length of the optical cavity (about 85 cm) and the finite size of the cavity mirror, it is necessary to enforce an aperture on the electron beam of ± 5 mm. It is thought that this narrow aperture is the dominant source of background for 6 GeV running. At higher energies, synchrotron light emission in the accelerator recirculation arcs will increase the beam emittance and presumably lead to significantly larger backgrounds from this aperture scattering. In present use of the Compton polarimeter, frequent beam tuning is required to

Relative error (%)	electron	photon
Position asymmetries*	-	-
E_{Beam} and λ_{Laser}*	0.03	0.03
Radiative Corrections*	0.05	0.05
Laser polarization*	0.20	0.20
Background / Deadtime / Pileup	0.20	0.20
Analyzing power Calibration / Detector Linearity	0.25	0.35
Total:	0.38	0.45

Table 22: *Goals for systematic errors for the Hall A Compton polarimeter at 11 GeV. Topics marked * are a common systematic error between the photon and electron analyses, while the other are largely independent between the detector systems.*

maintain operation with the signal-over-background >10. A large background signal is often associated with large fluctuations over the period of time in the laser on/off cycle used to measure backgrounds. This reduces the measurement precision, and potentially introduces a significant systematic error through instability in the phototube under large variations in rate. For this reason, it is desirable to keep the signal-over-background ratio large.

The aperture can be widened only by increasing the laser crossing angle which would also lower the luminosity. Although the baseline upgrade plans do not make provision for changing this crossing angle, operability at 11 GeV may require larger apertures. At a finite crossing angle α, the luminosity for a continuous-wave electron and photon beam, with intersecting electron and photon waists sizes σ_e and σ_γ, is given by:

$$\mathcal{L} \approx \frac{1+\cos\alpha}{\sqrt{2\pi}} \frac{I_e P_\gamma}{e k_0 c} \frac{1}{\sqrt{\sigma_e^2+\sigma_\gamma^2}} \frac{1}{\sin\alpha} \tag{16}$$

Here P_γ is the power of the photon beam, I_e is the current in the electron beam, and k_0 is the photon energy scattered at the kinematic maximum limit of collinear backscattering. As an example: at 10000 W stored power at 532 nm, the Compton scattering rate would be about 12 kHz/μA at 1.4° crossing angle and about 4.8 Hz/μA at 3.5°. At the expense of approximately a factor of 2.5 in luminosity, that larger crossing angle would allow a ± 0.5 inch aperture, comparable to the maximum aperture allowed by the 1" beam pipe diameter in the bore of the existing dipole magnets in the chicane.

With an available laser power of 10 kW, the polarimeter is not expected to be limited by low signal rates even at the larger crossing angles. However, the drop in luminosity with increasing crossing angle suggests that any change must be optimized from the point of view of signal-over-background. Until beam tests at higher beam energies are preformed to form reliable estimates of background levels, it is prudent to design for both large crossing angle and large luminosity.

We propose the use of an infrared cavity storing 10 kW of optical power at 1064 nm The primary disadvantages to the longer photon wavelength are the reductions in analyzing power and softening of the energy spectrum (17% analyzing power and 1.8 GeV maximum photon energy for IR at 11 GeV, compared to 32% and 3 GeV for 532 nm). The advantages for the IR system would be a greater available luminosity and system reliability. While the cross-section is very similar between the two photon energies, at 1064 nm there are twice as many photons per unit energy. At 10 kW, an IR cavity would provide a rate of 9 kHz/μA at the increased crossing angle to allow the full ± 0.5" electron beam aperture, or 23 kHz/μA at the original design 1.4° crossing angle. The 532 nm system requires an additional stage to frequency-double the original

1064 laser light. Without this doubling stage, the IR system can inject higher power to the cavity, enabling higher cavity power or the same cavity power with reduced cavity gain. A lower gain cavity will typically be more robust, and and less sensitive to radiation damage of the cavity optics.

Precision electron beam polarimetry also requires precise determination of the polarization of the photon target. This has proved to be the dominant systematic error contribution in recent Hall A Compton polarimeter measurements, in part because the use of a high-gain resonant cavity significantly complicates this determination. In a resonant cavity, the polarization state of the stored light can not be directly measured without destroying the resonance. For the present Hall A polarimeter, the laser polarization is inferred from measurements of the light that transmits through the cavity. A transfer function, relating the polarization of light in the Compton Interaction Region (CIP) to the polarization measured in the transmitted beam outside the vacuum vessel, is determined from measurements with an un-locked cavity. The highly-reflective cavity mirrors must be removed for these measurement, and the cavity must be open to air, which implies a relaxation of stress-induced birefringence of the vacuum entrance and exit windows. Contributions from birefringence in the cavity mirror substrate and stress on the vacuum windows can be characterized separately, but as a practical matter these corrections are difficult to determine with high precision. For the Hall A polarimeter, previous studies have quoted the uncertainty in beam polarization to be 0.35%, but in recent operation the uncertainty could not be bounded to better than 0.7%.

An improved technique has been used in Hall C to control the laser polarization uncertainty. The polarization of light arriving at the cavity entrance can be inferred from light reflected back from the cavity and analyzed with the same apparatus used to create the initial polarization state, measuring a single power level [74]. This technique was employed in Hall C to maximize the circular polarization of light injected in the cavity and to monitor the polarization during the run. It was verified to work by two methods. In the first, with the cavity under vacuum in running conditions, a scan over a broad range of initial polarization states was performed, and the recorded analyzed reflected power was shown to be well described by the simple hypothesis of optical reversibility. A more direct verification was made with the cavity opened, directly measuring the polarization of the injected light in the cavity and correlating this with the analysis of the reflected light. The correlation is shown over the full range of the scan, and zoomed in for measurements at maximum circular polarization, in Fig. 68. In operation, the Hall C Compton polarimeter ran with the reflected light very near minimum, with an implied uncertainty on the circular polarization within the cavity of 0.1%.

These studies demonstrate that this technique may provide knowledge and monitoring of the circular polarization in the cavity to the level of 0.1%. An *in situ* measure of the polarization would be a valuable confirmation of this procedure. Modifications to the interaction region will be made to allow an insertable, vacuum-compatible analysis assembly for measurements of the beam in the CIP. The power level for such measurements will necessarily be very low, as the highly reflective mirrors of the cavity will attenuate incident light, but such a direct measurement would include all effects of birefringence and depolarization in the injection of optical power into the cavity.

I.2.2 Alternative Laser System

An alternative laser system has also been considered, based on the use of a short-pulse RF laser synchronized to the electron bunch frequency. Such a system would concentrate laser power on the electron bunches, in effect creating an electron-photon collider. For a laser with narrow pulse structure (≈ 10 ps) and repetition frequency sub-harmonic to the electron beam ($f_{laser} = 499$ MHz / n with integer n), the the ratio of luminosity for the same average power goes as:

$$\frac{\mathcal{L}_{pulsed}}{\mathcal{L}_{CW}} \approx \frac{c}{f_{beam}\sqrt{2\pi}} \frac{1}{\sqrt{\sigma_{e,z}^2 + \sigma_{\gamma,z}^2 + \frac{1}{\sin^2\alpha/2}\left(\sigma_e^2 + \sigma_\gamma^2\right)}}. \tag{17}$$

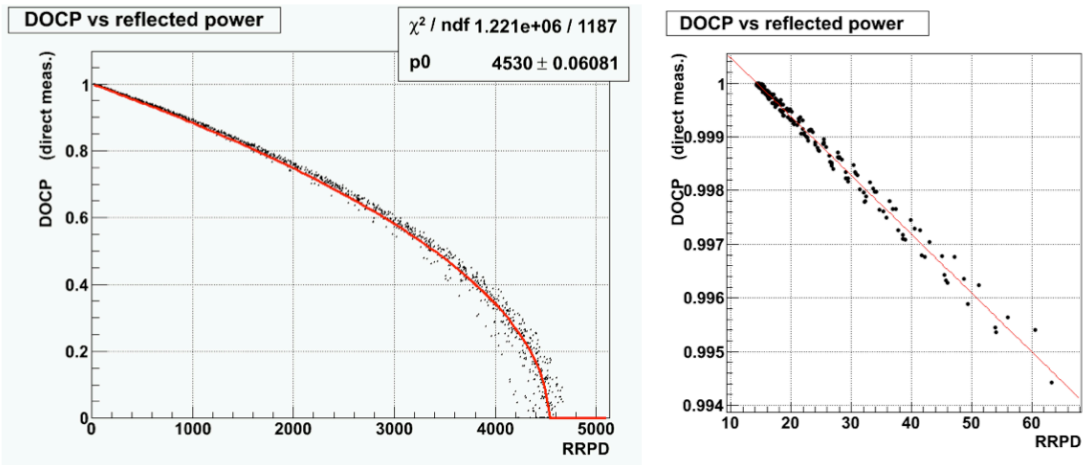

Figure 68: *Measured degree of circular polarization in the Hall C Compton laser cavity vs. the polarization-analyzed reflected light, measured over a broad scan of initial polarization states. The figure on the right is zoomed in the region of maximum circular polarization.*

Here f_{beam} is the electron repetition rate and $\sigma_{e,z}$ ($\sigma_{\gamma,z}$) is the longitudinal size of the electron (laser) pulse. For the parameters relevant to the proposed system, this corresponds to an enhancement of luminosity per unit power of between 20-50. Commercially available mode-locked laser systems has been identified providing 45 W at 1064 nm, with 100 MHz repetition rates and 10 ps pulse widths. Assuming an average injected power of 30 W at the 3.6° crossing angle, such a pulsed laser would provide 330 Hz/μA with a single-pass beam, that is, without the resonant optical cavity.

Although the relatively low rates would be expected to be a disadvantage, it may turn out to be operable depending on the characteristics of the 11 GeV electron beam. The statistical precision (0.4% in about 3 hours) would be sufficient for a high precision measurement. The primary advantage of such a system would be a more straightforward determination of the laser polarization, relative to a high-gain optical cavity. There are other advantages as well. Locking and unlocking a cavity takes time, so to maintain a high duty factor for a cavity system the locked and un-locked periods used to determine backgrounds are long ($\approx$ 1 minute) relative to the fluctuations in the background. On the other hand, a laser can be turned off or deflected to a dump quickly, so background measurements for such a single pass system could take place quickly, potentially providing superior control of background fluctuations even if the signal-over-background ratio is smaller. Similarly, without the requirement to maintain the delicate balance of signal levels necessary to robustly lock a high-gain cavity, systematic studies varying laser power or position would be simplified.

Should the rate from such a system be unmanageably small relative to backgrounds, it could be roughly doubled using a "butterfly" cavity to recirculate the exit beam through the interaction point. A more powerful option would be a hybrid system in which the RF pulses are stored in a resonant optical cavity. A moderate cavity gain $\approx$ 20 would double the Compton signal rate compared to the 10 kW, gain $\approx$ 3000 CW default design. At such a low gain, the cavity lock would be relatively easy to acquire, potentially enabling more rapid background measurements than the high-gain system. The polarization measurement would also likely be simpler than for a high-gain cavity system, as the injection beam in the interaction region would still be similar to the beam stored through relatively few resonant reflections.

Such a cavity would require the dual resonance condition of being both an integral number of optical and RF wavelengths. This is not a particularly difficult condition to maintain. The injection laser must be mode-locked to ensure coherence between pulses. Locking mode-locked lasers to Fabry-Perot cavities has been

actively pursued over the last decade in development studies for Compton-based X-ray sources [75, 76] and for a polarized positron source for the ILC [77, 78], with significant technical success beyond the requirements for this proposed system.

The above discussion demonstrates the utility and technical feasibility of the alternative proposal for a 10 ps pulse length, 100 MHz, 1064 nm laser system operating either as an injection laser for a gain ≈ 20 resonant cavity or as a 30 W single-pass system. This alternative proposal would require new investment for acquisition of the injection laser and high-power optics. In addition, the possibility of time-dependent polarization in the short RF laser pulse may additionally complicate the laser polarization determination. The alternative system remains as a backup should complications in determining the laser polarization inside the high-gain laser cavity prove to be insurmountable.

I.2.3 Chicane Magnet Modification

At 11 GeV, significant synchrotron radiation is emitted when the electron beam is bent in a magnetic field. The total radiated power rises as β^4 for the same bend radius. At 11 GeV, this radiation load will be a significant background in the photon detector and may overwhelm the signal from Compton scattering. Figure 69 shows the energy spectrum of synchrotron light attenuated by lead shielding between 1–5 mm thick, depending on the beam energy. On the left, the spectrum for 11 GeV with unmodified magnets is compared to calculations for the recent runs of HAPPEX-III (3 GeV) and PV-DIS (6 GeV). On the right, the energy spectrum ("Fringe 2") is shown when iron extensions, 15 cm in length, are added to the dipole magnets in order to provide an extended region of reduced field. This reduced magnetic field produces synchrotron light with lower energy range and with reduced intensity, for the portion of the electron beam trajectory that projects to the photon detector. With this modification, the bending strength of the magnet remains the same but the synchrotron light radiated into the detector is reduced by a factor of 10^4, to a level comparable to HAPPEX-III. The magnetic field extensions were modeled using TOSCA, and have been constructed. Field measurements have been taken to verify the magnetic model for both the integral Bdl and the shape of the fringe field with and without the field extensions. These field extension pieces have been built and will be ready for installation at the start of 11 GeV operations.

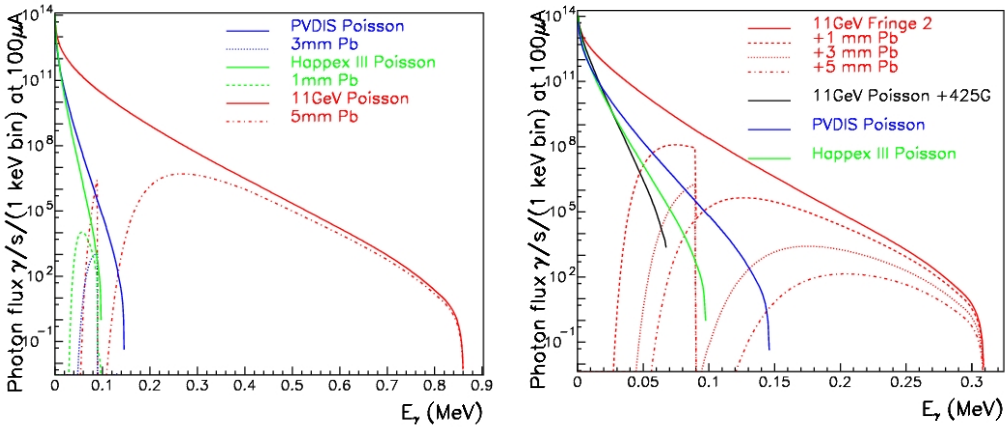

Figure 69: *Energy spectrum of synchrotron radiation penetrating lead shielding of thickness listed. Plot on left shows unmodified chicane magnets, plot on right shows energy spectrum for proposed magnetic shims which reduce the field for the bend radiating into the Compton photon detector acceptance. Note the different horizontal scales between the plots.*

I.2.4 Photon Detection

The specific calorimeter to be employed is not yet determined. The present calorimeter is a GSO crystal scintillator, which has excellent light yield suitable for measurements at low energies. The crystal is too small to contain most showers at higher energies, and a new calorimeter will be required for precision measurements at 11 GeV. In the past, Hall A has used an undoped lead tungstate ($PbWO_4$) array. This may be suitable for 11 GeV operation; the relatively low light yield for $PbWO_4$ is not an issue for higher photon energies of the proposed measurements or for the integrating measurements, and the high speed of this material reduces pile-up issues in counting measurements. Designs for multi-layer sampling calorimeters, using either scintillation or Cherenkov light, will also be considered.

I.3 Systematic Uncertainties

While the proposed system should assure operability and sufficient statistical precision at 11 GeV, the challenge will be achieving an absolute measurement of beam polarization with a precision of 0.4%. Table 22 summarizes the goals for various contributions to systematic uncertainty. The first four rows list sources of uncertainty which are highly or completely correlated between the electron and photon analyses. Other potential systematic errors arise in detector readout or calibration and are mostly or entirely decorrelated between the analyses. Each of these separate categories of potential systematic uncertainty: correlated, electron-only, and photon-only, will be discussed in the following sections.

I.3.1 Sources of Correlated Error

Any error associated with the Compton scattering process will be a common source of systematic error between the electron- and photon-detector analyses. One example lies in the energy normalization of the scattering process. The analyzing power is a function of both electron energy and photon energy, so these must be precisely determined. The photon wavelength will be determined to better than 0.1 nm and the electron energy to 0.05%, which leads to an uncertainty at the level of 0.03%. A similarly small uncertainty will come from radiative corrections, which are calculable [79] with high precision and will contribute at the level of 10^{-3}.

Helicity-correlated changes in luminosity of the laser/electron interaction point can introduce a false asymmetry. Various causes of luminosity variation must be considered, such as electron beam intensity, beam motion or spot-size variation. The control of helicity-correlated beam asymmetries is now a standard technology at Jefferson Lab, and typically achievable results (few part per million intensity, 10's of nanometers beam motion, $<10^{-3}$ spot size changes) will suitably constrain the electron-photon crossing luminosity variations. Another possible source of false asymmetry would be electronics pickup of the helicity signal, which could potentially impact an integrating photon analysis. However, the demands of the primary experiment for isolation of the helicity signal exceed those for polarimetry by several orders of magnitude. In addition, the laser polarization reversal provides an additional cancellation for asymmetries correlated to the electron beam helicity. For these reasons, beam asymmetries are expected to be a negligible source of uncertainty in this measurement.

A more significant potential source of error comes from the uncertainty in the photon polarization. As described above, the determination of photon polarization will be improved with the analysis of light reflected from the cavity input mirror, which will allow precise control and measurement of the polarization state injected into the cavity. This will be suplemented by an insertable stage to measure the polarization in the interaction region directly. The circular polarization of the laser will be determined and cross-checked with a precision of 0.2%. If studies do not demonstrate that this can be achieved within the high-gain cavity, the alternative laser system will need to be developed.

I.3.2 Systematic Errors for the Electron Detector

The electron detector is composed of 4 planes of silicon microstrips normal to the electron beam trajectory and positioned on the low-energy side of the beam trajectory in the dispersive chicane. Electrons which have given up energy to a scattering process are separated from the primary beam by the third chicane dipole, and the energy of a detected electron is implied by the distance of the track from the primary beam with a dispersion of about 0.45% of the beam energy per millimeter. Models of the chicane magnets are used to calculate the electron energy as a function of position in the detector. The effects of electronics noise and non-directional backgrounds are reduced by triggering on tracks which are restricted to very small angles relative to the beam. The trigger can be adjusted for the range of track angles and number of planes used in the track, including a single plane trigger. The efficiency of individual strips can also be measured using data from the multiple planes.

The silicon detector may also be sensitive to synchrotron light, and while the detector is not in line-of-sight to synchrotron emission in dipole 3, synchrotron photons rescattered in the beam pipe may be a problem. The 11 GeV upgrade includes a gate valve installed on the straight-through beam pipe, to block synchrotron light from the first dipole of the chicane during operation of the polarimeter.

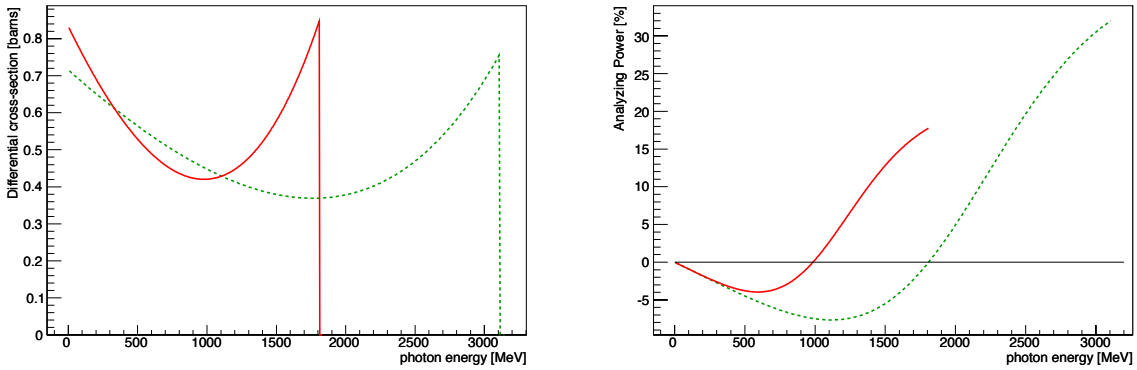

Figure 70: *The cross-section and asymmetry plotted versus Compton scattered photon energy for the Hall A polarimeter at 11 GeV for 532 nm (green dotted line) and 1064 nm (red solid line) laser options.*

The cross-section and asymmetry as a function of Compton scattered photon energy is plotted in Figure 70 for 11 GeV electron beam. The Compton edge (the kinematic endpoint of the Compton energy spectrum) is observed in the electron detector and used to calibrate the distance of the detector from the primary beam. In addition, the asymmetry as a function of photon energy k exhibits a zero crossing. Determining the location of this asymmetry zero crossing (0xing) provides a second absolute energy calibration point, so together the Compton edge and 0xing can be used to calibrate two parameters: the detector location relative to the beam and the strength of the magnetic field in dipole 3. In this way, survey results and magnetic field maps serve as a cross-check to a beam-based self-calibration of the Compton energy spectrum. The precision of this calibration is limited by delta-ray production in the microstrips, which distorts the measured spectrum, and efficiency variations between the microstrips.

In operation at low beam energies, the 0xing is close to the primary beam: for HAPPEX-II, the separation was approximately 5 mm. At this proximity, background rates were extremely sensitive to beam tuning in the injector and RF phase corrections in the linacs, presumably due to energy tails. At 11 GeV with the IR laser, the 0xing will be around 16mm from the primary beam, which should allow for robust operation. The analyzing power for the measured electron distribution can be very accurately determined with use of this self-calibration, with the systematic error dependent upon the specifics of the analysis approach.

For an example of a specific analysis technique, consider an asymmetry measured from the Compton edge to some selected cut-off in the electron spectrum. This would need to be compared to the theoretically expected average asymmetry, which would be sensitive the the energy cut-off threshold. In an analysis that computed a single count-rate asymmetry from the integrated rate from the 0xing to Compton edge, an error in determining the 0xing would act approximately as a dilution effect (as the asymmetry is small in the neighborhood of the 0xing). While there may be statistical variation in determining the 0xing, this would be merely a source of statistical noise. If the systematic bias in determining the 0xing is estimated to be within 1/10 μstrip width (about 25 μm), this would imply a systematic bias in the analyzing power of about 0.15%. While this is a useful estimate of the error due to energy calibration, this analysis relies on integrating the rate-weighted average asymmetry over the accepted energy range, and so would likely suffer a larger contribution of systematic error due to efficiency variations in the μstrips.

Other analysis techniques which would be less sensitive to efficiency variations would rely on averaging asymmetries over a range of strips, rather than averaging the count rate. In this case, both energy calibration points are needed to determine the expected asymmetry at each μstrip. Because the Compton edge will be extracted from the rate spectrum, efficiency variation between the silicon strips must be minimized and well-known to avoid biasing this determination. In addition, careful study of the contribution of delta-ray production, which distorts the asymmetry spectrum at the 0xing and the rate spectrum at the Compton edge, will also be important. Here also, a high strip efficiency will be helpful, by providing a high-efficiency for vetoing events with multiple tracks. Strip-by-strip efficiencies can be calculated by comparing track-hit efficiency between the multiple planes of the μstrip detector, and comparisons between planes can also help benchmark corrections for delta-ray production. A uniform and high-efficiency detector will be an important component of this system.

It is worth noting a measurement using only the last, single silicon strip at the Compton edge will be capable of 0.4% statistical precision on time-scales of around one hour. The rate of change of the asymmetry in this region is only 0.5% / mm. Locating this strip, relative to Compton edge, to a little better than half its own width should provide a robust accuracy on the analyzing power better than 0.4%. This technique would be sensitive to determination of the location of the Compton edge, but otherwise very insensitive to other calibration parameters.

Similarly, if the electron detector can be moved close to the primary beam (about 9 mm from the primary beam for the IR laser at 11 GeV) the asymmetry minimum could be detected. The statistical power is much lower in this region, with a single strip requiring 20 hours to achieve 0.4% statistical precision on the polarization (assuming signal-noise ratio of 10:1). However, here the asymmetry is not changing with position, so there is minimal calibration error in selecting a strip in this minimum. Beam position and angle may vary the asymmetry minimum over hundreds of microns during this time span, but such changes can be tracked using beam position monitors or the Compton edge, and the analyzing power varies by only about 0.4% of itself over a range of ± 300 μm, suggesting minimal corrections will be necessary .

Cross-checks between calibrations and techniques should provide convincing evidence that the system is well understood. Given these considerations, it seems likely that the calibration of the electron detector will be understood at the level of 0.3% or better.

Regardless of the analysis, contributions from deadtime and pileup will need to be understood. The fast-counting DAQ can take very high rates with low deadtime, and deterministic deadtime intervals are enforced in readout and acquisition electronics stages. While the total Compton-scattered data rates may as high as 1 MHz, rates in individual strips will be reduced by segmentation to $<$15 kHz, which will allow dead-time and pile-up systematic errors to be controlled at the level of 0.2%. The high statistical power of the measurement is of significant use here; high precision studies can be performed to benchmark models of the readout system against changes the laser power or the parameters of the triggering (preamp levels, logical gate lengths, coincidence levels, etc).

Backgrounds are also a potential but small source of systematic uncertainty. Backgrounds are studied

with the laser cavity unlocked, allowing both the background level and asymmetry to be well determined. However, high backgrounds could impact the systematic error due to deadtime or pile-up corrections. There is also the possibility of backgrounds from Compton-scattered electrons, which can produce delta rays when scattering in the detector or in its shielding. These tracks can themselves be sufficiently forward-going to pass the trigger, thus changing the analyzing power as a function of energy. Simulation will be used to avoid such problems, and studies of track distribution and electron-tagged photon energy spectra can be used to identify such effects in the data.

Finally, it is perhaps obvious, but worth stating, that beam properties at 11 GeV will be important for the precision of the electron detector analysis. If simulations reveal that halo backgrounds for the electron detector are likely to be large in the region $\sim$15 mm from the primary beam, then the green laser option would be required for high precision polarimetry. Using 532 nm light in a cavity would put the zero-crossing about 33 mm from the primary beam. It is also worth noting that the single-strip analyses would be also improved with the higher resolution and larger asymmetries (and larger distances from the primary beam) available from a green laser.

I.3.3 Systematic Errors for the Photon Detector

The precise determination of the analyzing power as a function of energy is more difficult for the photon calorimeter than for the electron detector due to the width and shape of the detector response function. In order to fit the asymmetry as a function of detected photon energy, the analyzing power must be calculated as a convolution of the response function with the theoretical analyzing power curve. The response function shape and energy calibration can be simulated, and studied using the photon tagging through coincidence triggers with the electron detector.

In general, determining the effect of a low-energy threshold on the analyzing power depends sensitively on the shape of the response function; at low energies this is a major source of uncertainty. At high energies, the improved resolution and consistency of the response function shape over the range of interest should significantly reduce this problem. As noted above, the photon calorimeter will be upgraded to better contain showers from high energy photons, with the primary objective to provide a response function which scales linearly over a broad range of energy.

The pulse-counting analysis in the photon detector is also sensitive to pile-up, which distorts the asymmetry distribution. Background and rate distributions will serve as inputs to simulation for corrections to the analyzing power. In the current Hall A analysis, pile-up corrections are estimated at the level of 1%, and the effect can be controlled at a level better than 10% of itself. Deadtime corrections, which can vary significantly with background conditions, will also represent a potential systematic uncertainty.

Uncertainties related to the threshold, response function shape, absolute energy calibration, deadtime and pile-up can also be eliminated by integrating the photon calorimeter signal, without threshold [80]. These previous problems are then replaced with a requirement on the linearity of the average response to the photon energy. Because the analyzing power integral is energy-weighted, the statistical figure-of-merit in not badly degraded by the negative asymmetry region at low photon energies.

The PREX experiment, with a beam energy near 1 GeV, relied on the integrating photon method for polarimetry at the level of 1% precision. Simulations of the photon response function were sufficient to control the analyzing power uncertainties for those measurements. The dominant uncertainty in the asymmetry measurement arises from variation in the photomultiplier response with changes in average rate which introduces a systematic error through background subtraction.

At high energies, with the ability to study response function with the electron-detector-tagged photon beam over a large fraction of the energy range, the photon detector analyzing power normalization uncertainty in the range of 0.3% should be achievable. Characterization of the phototube response as a function of rate and pulse-size will also be important. As described above, Bremsstrahlung scattering from apertures

in the interaction region, coupled with the characteristics of the 11 GeV electron beam, present a possible source of background.

I.4 Summary of Compton Polarimetry

The prospects for 0.4% Compton polarimetry are excellent. This ambitious goal will require vigorous and dedicated efforts to reduce sources of systematic uncertainty. It is expected that some significant fraction of data production time wil be used for studies of the Compton polarimeter system which are not disruptive to the experiment, for example, scans of detector positions, laser power and polarization, and data acquisition parameters. The scattering asymmetry at 11 GeV is relatively large which, for some analysis approaches, will provide statistical precision at the level of $\sim$0.5% in a few minutes of data collection. Given this high statistical power, these studies will be an effective method for constraining many of the possible experimental systematic uncertainties.

The future use of the Hall A polarimeter at 11 GeV will be a very different situation from the recent operation. The dominant systematic errors in recent operation lay in the determination of the analyzing power and laser polarization. Operating at lower energies the asymmetries were significantly lower and therefore the statistical power was worse. In addition, the limits of systematic uncertainty had not been pushed by demands of the experiment precision.

The 0-Xing "self-calibration" of the electron detector was attempted for the first time for the HAPPEX-II and HAPPEX-He measurements. The situation was complicated due to the low beam energy of around 3 GeV, which not only reduced the average asymmetry but also reduced the ratio of Compton-scattered photon energies and the electron energies. At 3 GeV, the zero-crossing was about 5 mm from the primary beam, which was as close as the electron detector could get to the beam. Geometric efficiency at the edge were a significant complication in this approach. In addition, the microstrip detector was damaged and displayed low and uneven efficiency, which complicated the analysis. The estimated systematic errors for that analysis which were not associated with these efficiency issues are consistent with Table 22. A similar technique has been successfully employed in the Hall C Compton polarimeter at 1 GeV, where a larger chicane and green laser were used to optimize for the low beam energy during the Qweak experiment. While analysis is ongoing, the current status indicates that the ultimate precision will be significantly better than 1%.

For the photon detector, the integration readout method has been successfully used in the HAPPEX-3 and PREX experiments, with the primary limitations being the characterization of the phototube response over the range of signal levels. The rapid access to high statistical power expected for 11 GeV operation, which is so powerful for cross-checking potential sources of systematic uncertainty, has never before been available to the Hall A Compton. Coincidence measurements between the photon and electron detectors will also provide a significant cross-check to the response function and energy calibrations. As described above, recent improvements in available laser power, analysis techniques, laser polarization measurements, and the favorable kinematics of the higher electron beam energy have opened the door to 0.4% precision Compton polarimetry for the MOLLER program.

J Møller Polarimetry

This appendix describes our plans for precision Møller polarimetry in Hall A. Møller polarimetry will provide a useful cross check on beam polarization measurements performed with Compton scattering, gathering high statistics in a short amount of time and with different attendant systematic error. The principal challenge is to achieve high precision ($\sim$0.5% on the beam polarization) through careful control of the systematic effects.

Electron-electron scattering, with arbitrary spin orientation for the beam and target, has been calculated in lowest order QED by many authors [81, 82, 83, 84], and the basic formulas for (non parity-violating) polarized Møller scattering are given in many places. For example, following [85], the cross section at high energies in the center of mass frame can be written as

$$\frac{d\sigma}{d\Omega_{\rm cm}} = \frac{\alpha^2}{s}\frac{(3+\cos^2\theta)^2}{\sin^4\theta}\left[1 - P^{\rm B}_{\rm long}P^{\rm T}_{\rm long}A_{\rm long}(\theta) - P^{\rm B}_{\rm tran}P^{\rm T}_{\rm tran}A_{\rm tran}(\theta)\cos(2\phi-\phi_B-\phi_T)\right] \qquad (18)$$

Here, $s = (2E)^2$ for electron energy E, θ is the scattering angle, $P^{\rm B,T}_{\rm long,tran}$ are the longitudinal and transverse polarizations of the beam and target electrons, ϕ is the azimuthal scattering angle, and $\phi_{\rm B,T}$ are the azimuthal angles of the beam and target polarizations. The analyzing powers are

$$A_{\rm long}(\theta) = \frac{(7+\cos^2\theta)\sin^2\theta}{(3+\cos^2\theta)^2} \qquad \text{and} \qquad A_{\rm tran}(\theta) = \frac{\sin^4\theta}{(3+\cos^2\theta)^2} \qquad (19)$$

which are maximized at $\theta = 90^\circ$ with $A_{\rm long}(90^\circ) = 7/9$ and $A_{\rm tran}(90^\circ) = 1/9$. The electron laboratory scattering angle for $\theta = 90^\circ$ is $(2m/E)^{1/2}$, rather small for GeV electron beams.

A Møller polarimeter makes use of Eq. 18 to measure the beam polarization vector $\vec{P}^{\rm B} = (P^{\rm B}_{\rm long}, P^{\rm B}_{\rm tran})$ by incorporating a target with a known electron polarization vector $\vec{P}^{\rm T} = (P^{\rm T}_{\rm long}, P^{\rm T}_{\rm tran})$ into a spectrometer to detect one or both of the scattered electrons. By reversing the beam polarization vector $\vec{P}^{\rm B} \to -\vec{P}^{\rm B}$, one can deduce its magnitude, and perhaps its direction, through the analyzing powers (19). The ideal Møller polarimeter, for determining longitudinal beam polarization $P^{\rm B}_{\rm long}$, is set at $\theta = 90^\circ$ with maximal (minimal) target longitudinal (transverse) polarization $P^{\rm T}_{\rm long(tran)}$.

We describe two techniques for getting as close as possible to the ideal Møller polarimeter. One is based on iron foil targets, in which the outer atomic electrons are polarized, and the other is based on an atomic hydrogen target. In the case of the iron foil target design, polarimeters at Jefferson Lab have already described control of systematic errors near the 0.5% level. We describe upgrades already in progress in Hall A in preparation the general 12 GeV program at Jefferson Lab which will enable that level of performance. While potentially very precise, such a polarimeter requires calibration from a body of magnetization studies with iron, and this normalization has never been cross-checked to the required precision. In addition, iron foil polarimeters require dedicated measurements at low current, and so measured polarization must be interpolated between spot measurements and extrapolated to the high currents used for production. Møller polarimetry with an atomic hydrogen target, in contrast, would be able to provide a continuous, non-invasive polarization measurement and would not require external calibration for accuracy at the few 10^{-3} level, but would be a new technology requiring significant technical R&D.

The strategy for Møller polarimetry, therefore, is to complete the upgrade of the Hall A iron foil polarimeter and seek to maximize the accuracy of this device. A cross-calibration with the upgraded Compton polarimeter should demonstrate that normalization of the target foil polarization is under control. The atomic hydrogen polarimeter option will be pursued if it is needed to confirm results of those studies.

J.1 The Hall A Upgrade: "High Field" Iron Foil Targets

Nearly all high energy Møller polarimeters operated to date [62, 86, 87, 88, 89, 90, 91, 92] make use of tilted ferromagnetic foil targets. High permeability alloys coupled with ∼few hundred Gauss magnetic fields preferentially polarize in the plane of the foil, so tilting the foil at a moderate angle gives a substantial longitudinal target polarization. Calculating the effective polarization, however, is typically the limiting systematic error, and such devices cannot ultimately do better than several percent precision.

A different approach [60], implemented in Hall C at Jefferson Lab, using a high magnetic field perpendicular to the foil plane [57, 61], has reported 1% precision on the beam polarization. It is this target design that we are adopting for MOLLER, and indeed are already preparing to implement in Hall A.

Below we describe the principles of "high field" iron foil targets, the plans for redesign of the scattering chamber, and modifications to the existing spectrometer including simulations for operation at high energy.

J.1.1 Ferromagnetic Foil Targets

Materials respond to external magnetic fields because atomic electrons, with spin and orbital angular momentum, align themselves to an applied field. However, with a Bohr magneton equal to 5.8×10^{-5} eV/Tesla, the magnetic energy at several Tesla is still much smaller than the thermal energy at room temperature, so the effects of magnetic fields in most materials ("diamagnetism" and "paramagnetism") are quite small.

Ferromagnetism, on the other hand, is a quantum mechanical phenomenon in which a subset of atomic electrons in some elements and alloys spontaneously align. These alignments happen in localized domains, which themselves are randomly oriented. However, the application of relatively small magnetic fields cause the domains themselves to line up, leading to large induced magnetic fields.

Magnetostatics (in CGS units) is governed by the equations $\vec{\nabla} \cdot \vec{B} = 0$ and $\vec{\nabla} \times \vec{H} = 4\pi\vec{j}/c$ where $\vec{B}$ is the magnetic field, $\vec{j}$ is the free current density, and $\vec{H}$ absorbs the magnetic response of the medium. To be precise, $\vec{H} \equiv \vec{B} - 4\pi\vec{M}$ where the magnetization $\vec{M}$ is the magnetic dipole moment per unit volume. It is the magnetization $\vec{M}$ that we interpret, ultimately, as the polarization of target electrons.

For *linear* materials (which *do not* include ferromagnets), we define the magnetic permeability μ through $\vec{B} = \mu\vec{H}$. It is nevertheless a habit to speak of μ for ferromagnetic materials in terms of vector magnitudes, that is $B = \mu H$. For most materials, μ is a constant slightly larger than unity. In ferromagnets, however, μ is a strong function of H and can be very large.

Figure 71 shows magnetization data for pure iron. At several tens of Gauss of "applied" field H, the magnetic field B saturates at ~ 1.5 Tesla because the domains are aligned. The resulting magnetization corresponds to ~ 2 Bohr magnetons per iron atom, that is, roughly two electrons worth of magnetic dipole moment in *each* iron atom. As H reaches and exceeds several Tesla, the magnetization field simply adds directly to the applied field. The value of μ rises to several thousand for a few Gauss, and then decreases to unity for fields much greater than saturation.

Møller polarimeters using "low field tilted" foil targets operate in the region where $\mu \gg 1$. In fact, they generally make use of special alloys that have exceptionally high values of μ, that is, saturate at relatively low values of H. In this case $\vec{B} = 4\pi\vec{M}$ to a very good approximation. Since $\vec{\nabla} \cdot \vec{B} = 0$ implies that perpendicular components of $\vec{B}$ are continuous across the foil surface, and since $B = H$ outside the foil is hundreds of times smaller than the magnetization, the only way to meet the boundary condition is for $\vec{M}$ to point in the plane of the foil. (Of course, this argument breaks down if the foil is at right angles to the applied field.) Thus a target tilted at some angle, say $\sim 20^\circ$ provides a dominantly longitudinally polarized target for an incident electron beam in the same direction as the applied field.

The limiting precision of polarimeters using such targets, however, is extracting the target electron spin polarization from the magnetization. The ratio of "spin" magnetization M_s to the total can be written as [93]

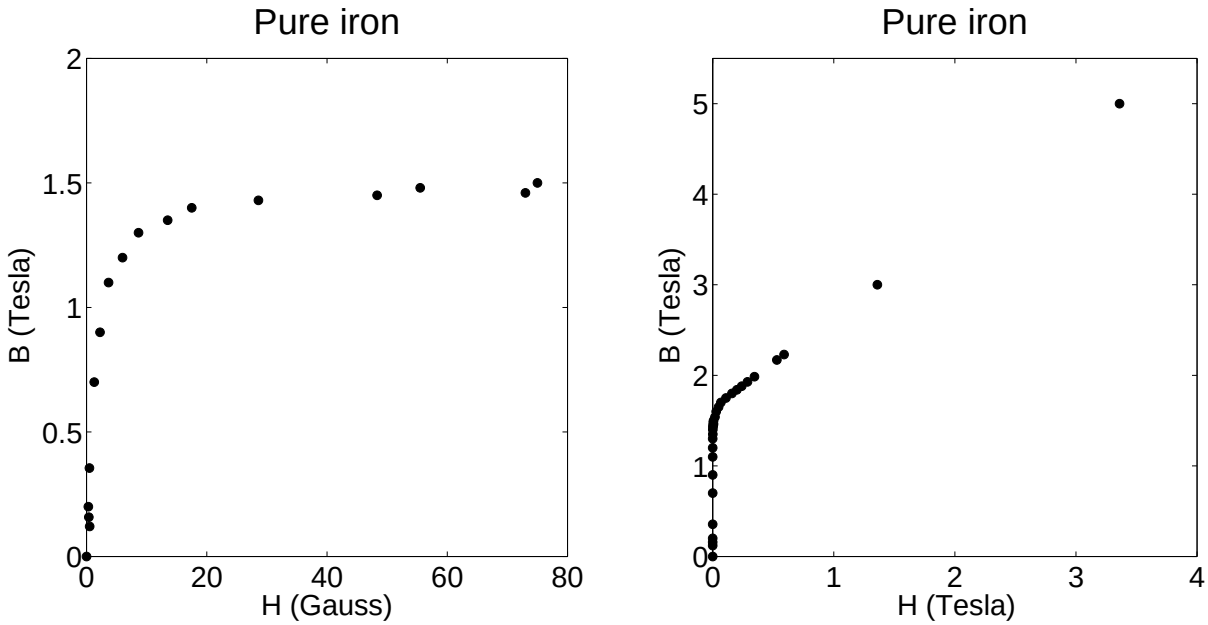

Figure 71: Magnetization curves for pure iron, from http://www.fieldp.com/magneticproperties.html. We use CGS units, so both B and H are properly measured in Gauss, but 1 Tesla$= 10^4$ Gauss. Both plots are of the same data set, but the horizontal scale is much expanded on the right.

$M_s/M = 2(g' - 1)/g'$, with g' close to, but somewhat less than 2. The attendant uncertainties in g' for the alloys used in tilted target applications, limit one's knowledge of the target polarization to several percent.

Measurements in *pure* iron or nickel, however, point to very precise knowledge of their magnetization parameters [94, 95]. The approach used by the Basel/Hall C group [57, 60, 61] is to not only use pure iron foil targets, but to polarize them with a very high (several Tesla) field, provided by superconducting coils. This overcomes limitations of a not-so-large value of μ for pure iron.

It is important to note that the magnetization of the foils in the strong longitudinal field has not been measured, but is taken from published data on the properties of bulk iron, which claims an accuracy of $\sim 0.1\%$. The orbital contributions to the magnetization of about 5% can be evaluated and subtracted using the magneto-mechanical factor, measured by other dedicated experiments [96]. With strong external fields of 3-4 T several additional corrections summing to about 0.5% have to be made. These corrections are temperature dependent. It will be important to carefully evaluate the literature on these measurements and their interpretation to verify that the uncertainty is not larger than a few 10^{-3}. For example, it is apparent that the anomolous magnetic moment of the electron has not been accounted for in recent publications, amounting to a correction of more than 0.2% to the target electron spin polarization.

Calculations of the longitudinal magnetization of a foil placed pependicularly (or nearly so) to an applied field, are quite difficult. Figure 72, taken from [57, 61], shows the magnetization (relative to its maximum value) of a pure iron foil as a function of applied magnetic field, for different angles between the field and the normal to the foil. To be sure, this calculation is in fact of a model of non-interacting prolate ellipsoidal domains [97], and the extent to which it applies to a pure iron foil is not clear.

A polarimeter based on this "high field" target was constructed in Hall C at Jefferson Lab [60]. The device has performed well, with experimenters claiming accuracy of 1% or better on the longitudinal beam polarization. Much of the updated design of the Hall A Møller polarimeter is based on the Hall C experience.

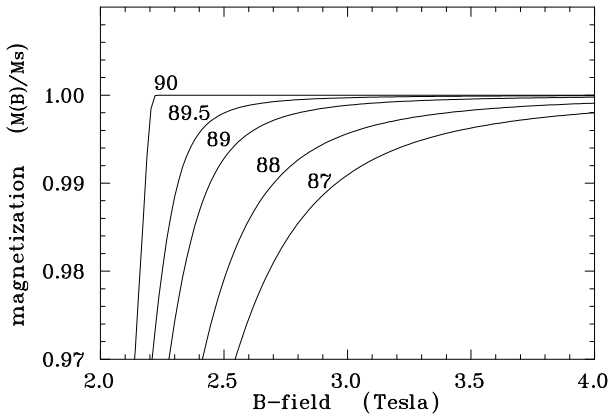

Figure 72: *Simulations of foil magnetization for angles between the foil plane and the B-field direction close to 90 degrees. Errors due to imperfect alignment or a slight warp of the foil could produce such a result. Taken from [57, 61], which uses a calculation [97] of magnetization curves for uniformly magnetized prolate ellipsoidal domans.*

J.1.2 Simplified Møller Scattering Target Assembly

Quite a number of small, systematic effects need to be considered in order to achieve 0.5% uncertainty on the longitudinal beam polarization. For example, Figure 72 gives an idea of the tolerance needed on iron target alignment. In order to be assured of at least 99.8% of the maximum target polarization for a field of ~ 3 T, the tolerance on the foil angle misalignment is $\sim 1^\circ$.

Figue 73 includes a photograph of the high-field foil target chamber previously in place in Hall A, and some details of our current plans for the upgrade. Our plan is to retain the cryogenic magnet system and the target chamber and overall adjustment mechanism, but to replace the target actuator assembly. Originally designed to provide adjustments in many degrees of freedom, the existing actuator assembly proved unwieldy for regular use. It was also very heavy, and required stabilization through a connection to the dewar for the cryogens. The redesign relies on precision construction with fewer adjustable degrees of freedom, and will be much lighter.

In order to interpret the target polarization to high precision, it is imperative that the foil be saturated. This can be confirmed by studying the Møller scattering asymmetry as a function of applied magnetic field. The cryogenic magnet is limited to fields less than 4 T, so according to Fig. 72 we need to have the target angle precise to about 1°. It would be useful to in fact confirm the behavior suggested by the figure, by making these measurements with the target arm rotated by various angles close to 90°.

J.1.3 Møller Spectrometer Operation at 11 GeV

The Møller scattering spectrometer needs to have a well defined acceptance in the neighborhood of $\theta = 90^\circ$, so the average analyzing power can be determined to sufficient precision. One also needs to understand uncertainties due to the Levchuk effect [98, 99], which results from the most deeply bound (and unpolarized) atomic electrons having a very different momentum distribution. When the accepted scattering angle is closely tied to the electron momentum, the Levchuk effect can be quite large, as the momentum p_e of K-shell electrons in iron is ~ 100 keV/c and the effect goes like p_e/m.

The Hall C spectrometer design [60] is based on a simple two-quadrupole approach, where Q1 focusses in the horizontal plane and Q2 defocusses. Between these two elements is a straightforward collimator system. This approach has worked well, but affords little ability thoroughly analyze the final state electrons, and the size of the Levchuk effect is calculated to be $\approx 3\%$. Furthermore, limitation in the magnetic field strength would require significant reworking to operate at beam energies 11 GeV.

We will continue to use the existing Hall A Møller spectrometer system [62, 86], in which the Levchuk corrections are somewhat smaller, estimated to be $\sim 2\%$ [62]. Originally a QQQD magnetic array, a fourth quadrupole has been added to optimize operation up to 11 GeV. The dipole magnet will remain as is, but the

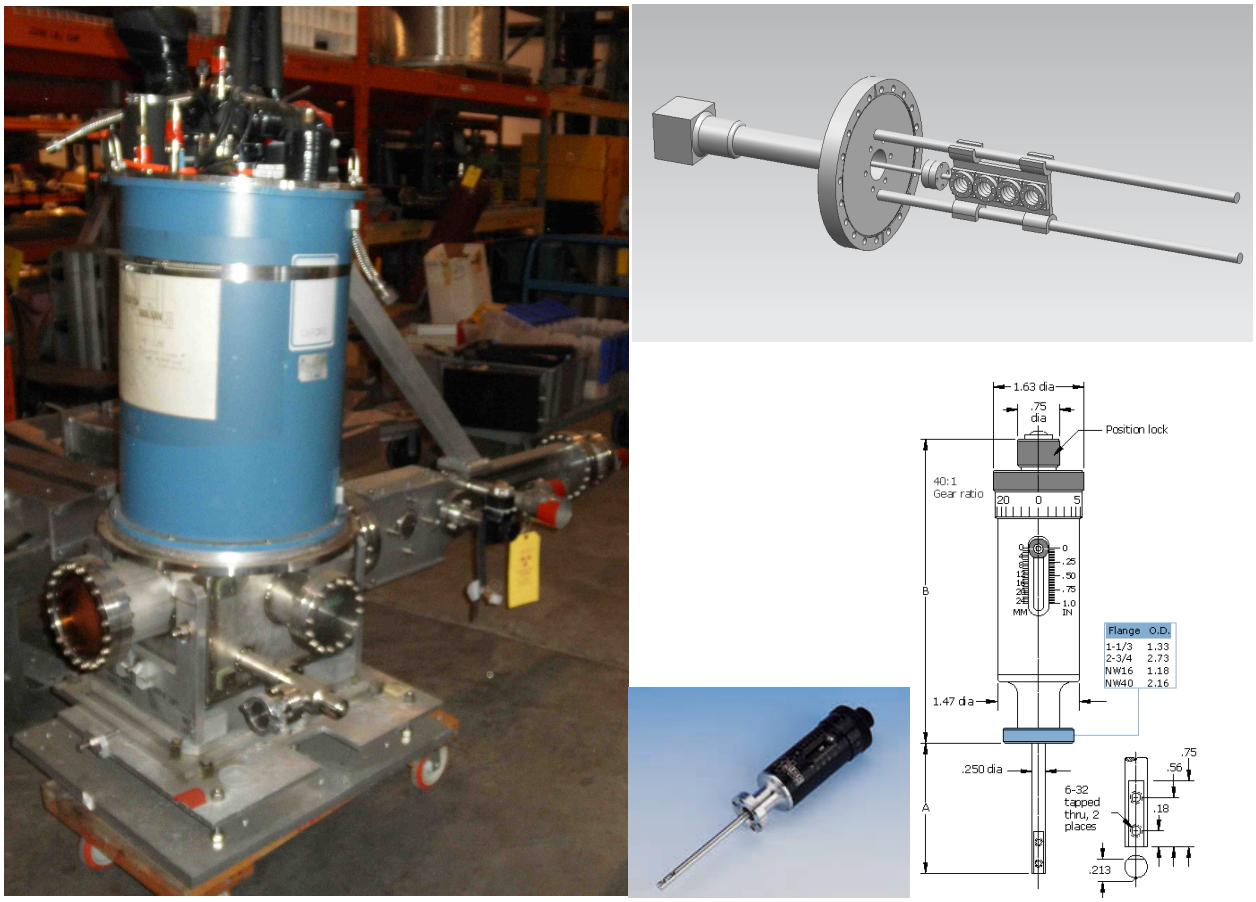

Figure 73: *Left*: Existing Hall A target chamber with ladder actuator extending off to the right. The magnet cryogenic system sits on top of the chamber. Our plan is to replace the actuator assembly, here shown supported by a boom attached to the cryo system. *Right*: Design concept for a new ladder actuator system, based on the Hall C design, along with a photo and schematic of the MDC660034 linear motion feedthrough.

detector position will be adjusted for higher energy operation. The detectors are segmented to better identify the correlations with scattering angle and energy, and an upgraded data acquisition system has been put in place for high rate operation.

Simulations of the spectrometer are underway, with some results shown in Fig. 74. For these tests, all four quadrupoles are energized, using settings determined at some time in the past. We are investigating optimal settings for these elements at different beam energies, but the results are already quite promising at 11 GeV, with the acceptance maximized at the peak of the analyzing power, and a well defined region for angles not quite at 90°. For coincidence detection of both electrons, we find an acceptance region approximately $85^\circ < \theta < 95^\circ$ in center of mass scattering angle, and $-25^\circ < \phi < 25^\circ$ in azimuthal angle, relative to the horizontal plane.

Upgrades are underway to the segmented detector package and data acquisition electronics. These will lead to studies of the event distributions in energy and angle, including measurements as a function of rate. From this we will determine backgrounds and dead time corrections with precisions indicated in Table 8.

The counting rate for a 1 μm iron foil and a 10 μA beam current is $\approx 5 \times 10^4$ events per second. For a nominal target polarization of 8% and beam polarization of 80%, the raw asymmetry would be $\approx 5 \times 10^{-2}$. To measure this asymmetry to 0.25% statistical precision would therefore require about half an hour of

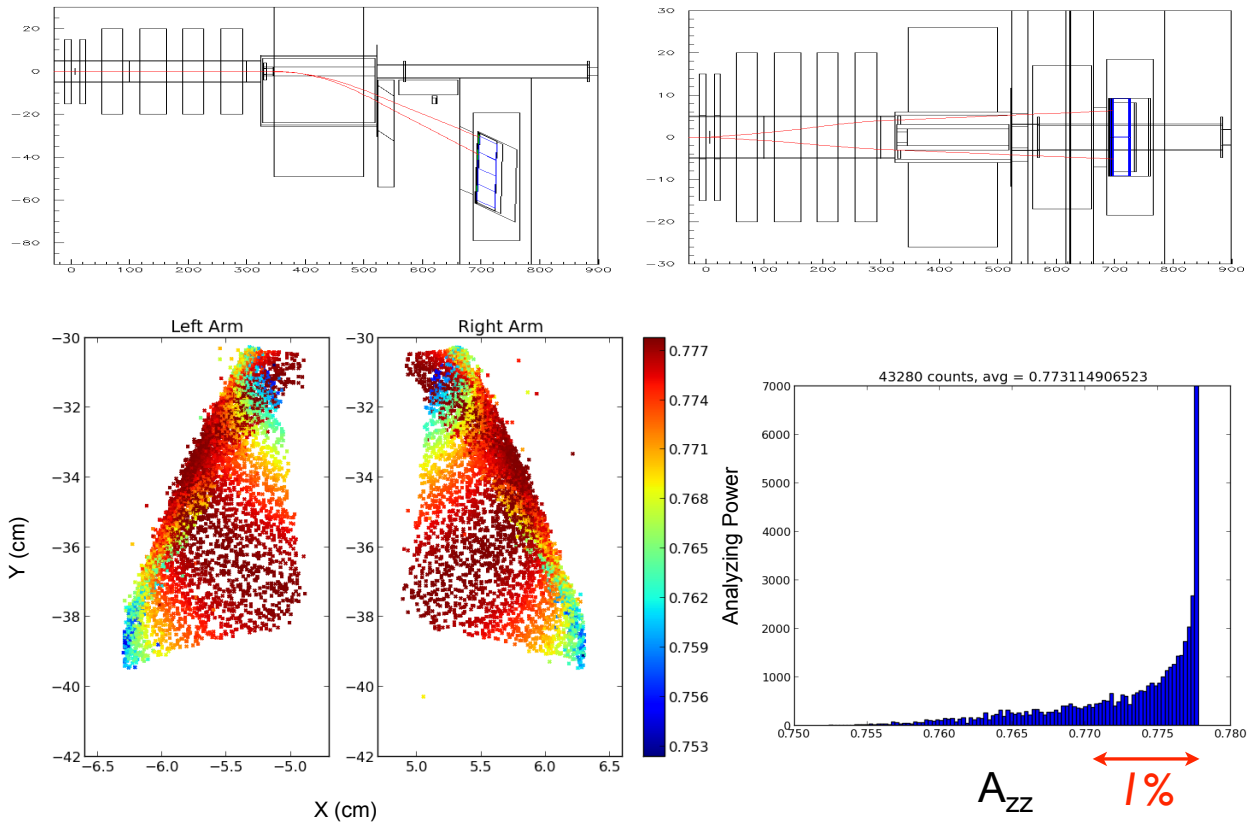

Figure 74: Simulation of the Hall A Møller polarimeter spectrometer at 11 GeV. In this QQQD design, the first two quadrupoles defocus in the horizontal plane and the second two focus before both electrons enter the dipole magnet. Two separate detector arms each detect electron. The spectrometer is optimized for center of mass scattering angle $\theta = 90°$, and the determining the effective analyzing power $\langle A_{zz} \rangle$ to a precision much smaller than 1% should be straightforward.

beam time. Careful run planning will be needed to meet the statistical precision required for 0.5% beam polarization monitoring.

J.1.4 Target Heating Effects

Target heating is important consideration for precision Møller polarimetry using polarized iron foils. Saturation magnetization on iron is a function of temperature, and in fact all alloys lose their ferromagnetic ability completely above some critical temperature. At high currents, the heating cannot be tolerated, so polarimeter measurements must be made at much lower currents than used for parity violation running.

These effects have been studied using the Hall C target and polarimeter. Figure 75 displays the relative magnetization of a pure iron foil, measured using the Kerr effect in laser light reflected from the foil, as the foil is heated. The desire is to operate at room temperature and keep beam heating excursions to a minimum. Although the direct foil measurements show several percent decrease in the magnetization for temperatures of hundreds Celsius, the beam measurements are encouraging. No clear decrease with high beam current is observed, albeit not yet at a level consistent with our precision goals.

One can attempt to mitigate foil heating effects and allow operation at higher beam current by using a fast beam kicker system combined with a thin strip or wire target. In this system, the electron beam is kicked at some low duty cycle onto or across a pure iron target. The beam is only impinging on the target

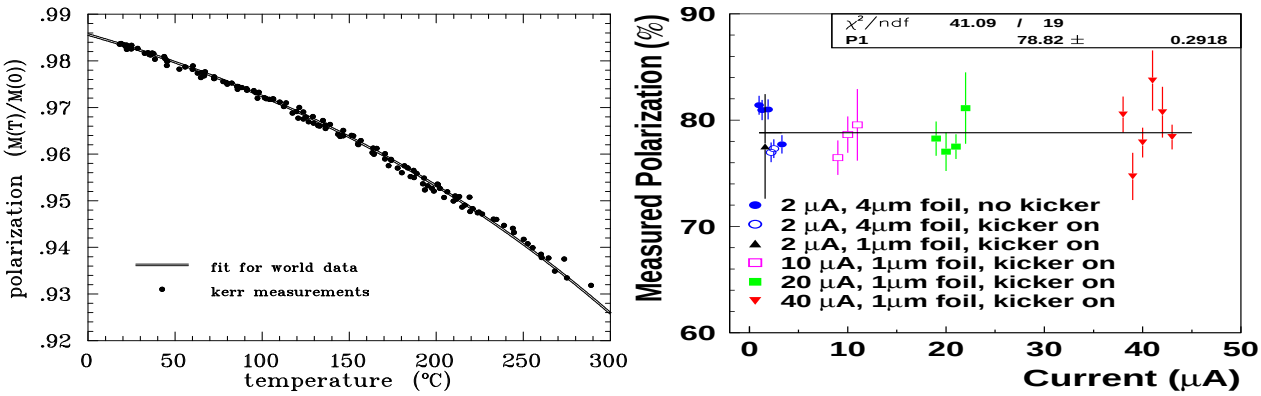

Figure 75: Measurements related to target foil heating from the Hall C/Basel group. *Left*: Relative magnetization versus temperature for a pure iron foil driven to saturation [57, 61]. The plan is to run at room temperature. *Right*: Measurements of the beam polarization at different beam currents, with and without a beam kicker to raster the beam on the foil target.

for timescales on the order of μs such that the target does not have much opportunity to heat up, while the relatively long time between kicks allows the target to cool.

A series of tests have been performed in Hall C with two prototype kicker magnets and two different target configurations [100]. Initial tests were performed with 25 μm diameter iron wires replacing the iron foil at the Møller target. While these tests were moderately successful, it was found that the high instantaneous current combined with the relatively thick profile of the target lead to a high rate of random coincidences. The second generation prototype target replaced the iron wires with a 1 μm strip target, reducingthe instantaneous rate.

Results from the second generation tests are also shown in Fig. 75. In this case, the duration of the beam "kick" was about 10 μs at a repetition rate between 5 and 10 kHz. Data were taken using the kicker and iron strip target up to 40 μA. In general, the results were consistent with there being no effect from target heating, albeit with relatively low precision. Problems with beam transport precluded the use of higher beam currents. Finally, it should be noted that apparent instabilities with either the source or Hall C Møller polarimeter itself (found by taking "calibration" data at 2 μA from a normal iron foil) made it difficult to conclude that target heating effects were completely avoided.

The extent to which the beam polarization at high current varies from that at lower currents is not well known. The rastered data in Fig. 75 addresses this to some extent, and no effect is evident. Another option that one can use to at least partially overcome the low current constraint imposed by the use of saturated pure iron foils is to operate the electron beam in a lower duty-cycle mode, such that the average current impinging on the target is relatively small, while the instantaneous current of a particular electron beam pulse is much larger. In particular, one can operate the polarized electron source in a so-called "beat-frequency" mode in which the source laser frequency is slightly different from that of the RF (chopper) system used to clean-up, and potentially adjust the intensity of the electron beam pulses for each hall independently. When an appropriate laser frequency is chosen, the majority of the electron pulses are out of phase with the opening of the acceptance defining slit in the chopper, and only the Nth pulse, where $N = f_{cavity}/(f_{cavity} - f_{laser})$, is accepted.

This technique was first tested in 2006, when it was used in a variety of applications in Halls A and C [101]. A test using the Hall C Møller polarimeter was performed with the laser frequency set to 467.8125 MHz (RF cavity frequency 499 MHz) such that the nominal current of the electron beam reaching Hall C was reduced by a factor of 16 due to the loss of bunches on the aperture defining slits.

The results of the Hall C test are shown in Figure 76, where three scenarios are illustrated. The bottom

plot shows the electron beam polarization as measured with the beam current being reduced using the photocathode laser power. In this case, the current from the photocathode is the same as the current arriving in Hall C. In the middle plot, high current ($\approx$ 60 μA) is generated from the photocathode, but the electron beam current is reduced to a few μ A using the chopper slit. In this case, the edges of the electron beam pulse are thrown away, so one is potentially sensitive to any changes of polarization across the electron beam pulse duration. The top plot shows the polarization as measured using the beat-frequency technique. In this case, the current from the photocathode was reduced by a factor of 16, such that measurements made at an average current of $\approx$ 3 μA in Hall C corresponded to a current of about 48 μA at the source. In this particular test, all measurements agreed very well, regardless of beam current, or technique used to reduce current sent to the hall.

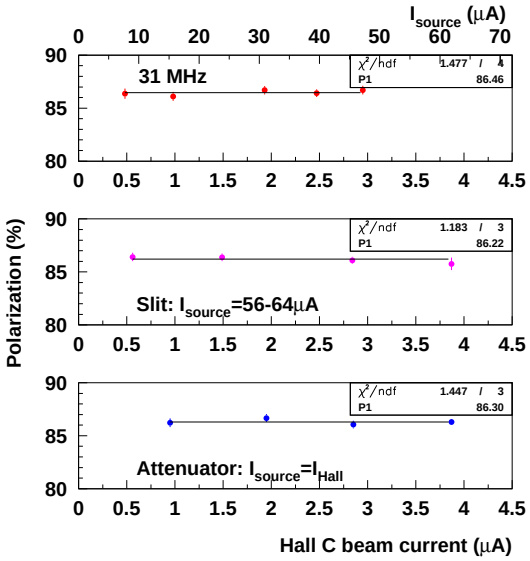

Figure 76: Results of 2006 electron source beat-frequency mode tests. The bottom plot shows the polarization measurements with the beam current controlled using the laser power directly; in the middle plot, the current was reduced using the chopper slit (high current from the photocathode); the top plot shows the current reduced using the beat-frequency technique described in the text.

Use of this beat-frequency mode allows measurements of the beam polarization in a mode that mimics high current running at the source, without any modification of the electron beam pulse itself. Use of this technique could be easily implemented for the MOLLER experiment at 11 GeV.

J.2 Potential and Prospects for a Polarized Atomic Hydrogen Target

This project has been described in detail in [102]. A summary is presented here. While this section describes a novel polarimeter scattering target which has yet to be demonstrated, R&D has started for a similar system

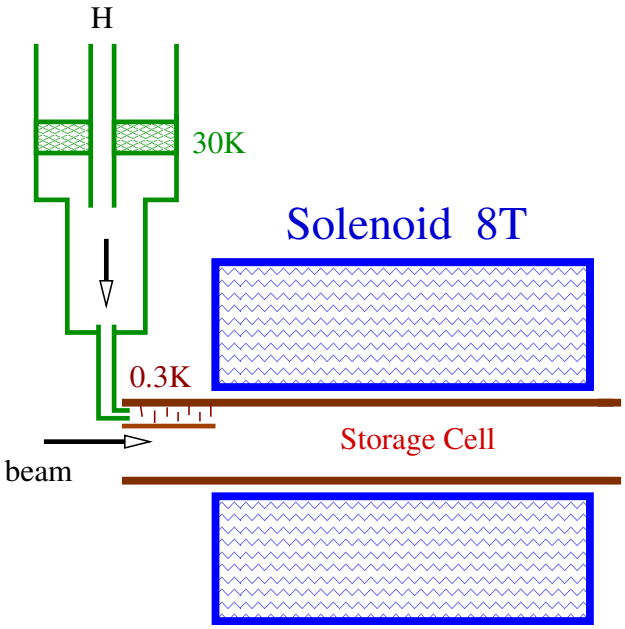

Figure 77: *A sketch of the polarized hydrogen gas storage cell, along with the holding field magnet.*

in Mainz. That system would be used for polarimetry for high precision parity-violation experiments using an extracted beam on fixed targets at the MESA facility. The MESA facility is presently under construction, with a goal of starting the parity-violation measurements in 2017, suggesting that this development project is compatible with the schedule for the MOLLER experiment.

J.2.1 Hydrogen Atom in Magnetic Field

The magnetic field B_S and the hyperfine interaction split the ground state of hydrogen into four states with different energies. The low energy states are $|a\rangle$ = $|\downarrow\uparrow\rangle \cdot \cos\theta - |\uparrow\downarrow\rangle \cdot \sin\theta$ and $|b\rangle$=$|\downarrow\downarrow\rangle$, where the first and second (crossed) arrows in the brackets indicate the electron and proton spin projections on the magnetic field direction. As far as the electron spin is concerned, state $|b\rangle$ is pure, while state $|a\rangle$ is a superposition. The mixing angle θ depends on the magnetic field B_S and temperature T: $tan\ 2\theta \approx 0.05\ \mathrm{T}/B_S$. At B_S =8 T and $T = 0.3$ K the mixing factor is small: $\sin\theta \approx 0.003$. State $|b\rangle$ is 100% polarized. State $|a\rangle$ is polarized in the same direction as $|b\rangle$ and its polarization differs from unity by $\sim 10^{-5}$. In addition, there are high-energy states $|c\rangle$and $|d\rangle$which have the wrong polarization, but which get rapidly rejected from the field region (explained more below).

J.2.2 Storage Cell

In a magnetic field gradient, a force $-\nabla(\vec{\mu_H} \cdot \vec{B})$, where μ_H is the atom's magnetic moment, separates the lower and the higher energy states. The lower energy states are pulled into the stronger field, while the higher energy states are repelled from the stronger field. The 0.3 K cylindrical storage cell, made usually of pure copper, is located in the bore of a superconducting ∼8 T solenoid. The polarized hydrogen, consisting of the low energy states, is confined along the cell axis by the magnetic field gradient, and laterally by the wall of the cell, as shown in Fig 77.

At the point of statistical equilibrium, the state population, p follows the Boltzmann distribution:

$$p \propto \exp(\mu_e B/kT), \tag{20}$$

where μ_e is the electron's magnetic moment ($\mu_H \approx \mu_e$) and $k = k_B$ is the Boltzmann constant. The cell is mainly populated with states $|a\rangle$ and $|b\rangle$, with an admixture of states $|c\rangle$ and $|d\rangle$ of $\exp(-2\mu_e B/kT) \approx 3 \cdot 10^{-16}$. In the absence of other processes, states $|a\rangle$ and $|b\rangle$ are populated nearly equally. The gas is practically 100% polarized, a small ($\sim 10^{-5}$) oppositely polarized contribution comes from the $|\uparrow\downarrow\rangle$ component of state $|a\rangle$.

The atomic hydrogen density is limited mainly by the process of recombination into H_2 molecules (releasing ~4.5 eV). The recombination rate is higher at lower temperatures. In gas, recombination by collisions of two atoms is kinematically forbidden but it is allowed in collisions of three atoms. On the walls, which play the role of a third body, there is no kinematic limitation for two atom recombination. At moderate gas densities only the surface recombination matters. In case of polarized atoms, the cross section for recombination is strongly suppressed, because two hydrogen atoms in the triplet electron spin state have no bound states. This fact leads to the possibility of reaching relatively high gas densities for polarized atoms in the traps.

A way to reduce the surface recombination on the walls of the storage cell is coating them with a thin film (~50 nm) of superfluid ^{4}He. The helium film has a very small sticking coefficient[4] for hydrogen atoms.In contrast, hydrogen molecules in thermal equilibrium with the film are absorbed after a few collisions and are frozen in clusters on the metal surface of the trap [103].

The higher energy states are repelled from the storage cell by the magnetic field gradient and leave the cell. Outside of the helium-covered cell, the atoms promptly recombine on surfaces into hydrogen molecules which are either pumped away or are frozen on the walls. Some of the higher energy states recombine within the cell and the molecules eventually are either frozen on the helium-coated wall, or leave the cell by diffusion.

The cell is filled with atomic hydrogen from an RF dissociator. Hydrogen, at 80 K, passes through a Teflon[5] pipe to a nozzle, which is kept at ~30 K. From the nozzle hydrogen enters into a system of helium-coated baffles, where it is cooled down to ~0.3 K. At 30 K and above, the recombination is suppressed because of the high temperature, while at 0.3 K it is suppressed by helium coating. In the input flow, the atoms and molecules are mixed in comparable amounts, but most of the molecules are frozen out in the baffles and do not enter the cell.

The gas arrives at the region of a strong field gradient, which separates very efficiently the lower and higher atomic energy states, therefore a constant feeding of the cell does not affect the average electron polarization. This technique was first successfully applied in 1980 [104], and later a density[6] as high as $3 \cdot 10^{17}$ atoms/cm^3 was achieved [105] in a small volume. So far, the storage cell itself has not been put in a high-intensity particle beam.

For the project being discussed a normal storage cell design can be used, with the beam passing along the solenoid axis (Fig. 77). The double walls of the cylindrical copper cell form a dilution refrigerator mixing chamber. The cell is connected to the beam pipe with no separating windows. The tentative cell parameters are (similar to a working cell [106]): solenoid maximum field of $B_S = 8$ T , solenoid length of $L_S = 30$ cm, cell internal radius of $r_\circ = 2$ cm, cell length of $L_C = 35$ cm and temperature of $T = 0.3$ K. The effective length of such a target is about 20 cm. For the guideline, we will consider a gas density of $3 \cdot 10^{15}$ cm^{-3}, obtained experimentally [107], for a similar design.

J.2.3 Gas Properties

Important parameters of the target gas are the diffusion speed. At 300 mK the RMS speed of the atoms is ~80 m/s. For these studies we used a calculated value [108] of the hydrogen atoms cross section $\sigma =$

[4] The sticking coefficient defines the atom's adsorption probability per a collision with a surface.

[5] Teflon has a relatively small sticking coefficient for hydrogen atoms.

[6] This parameter is called concentration, but we will use the word density in the text; mass of the gas is not important here.

$42.3 \cdot 10^{-16}$ cm^2, ignoring the difference between the spin triplet and singlet cross sections. This provided the mean free path $\ell = 0.57$ mm at density of $3 \cdot 10^{15}$ cm^{-3}.

The average time, τ_d for a "low field seeking" atom to travel to the edge of the cell, assuming its starting point is distributed according to the gas density, is[7]: $\tau_d \approx 0.7$ s. This is the cleaning time for an atom with opposite electron spin, should it emerge in the cell and if it does not recombine before. The escape time depends on the initial position of the atom, going from ~ 1 s at $z = 0$ to 0.1 s at $z = 8$ cm. The average wall collision time is about 0.5 ms.

J.2.4 Gas Lifetime in the Cell

For the moment we consider the gas behavior with no beam passing through it. Several processes lead to losses of hydrogen atoms from the cell: thermal escape through the magnetic field gradient, recombination in the volume of gas and recombination on the surface of the cell. The volume recombination can be neglected up to densities of $\sim 10^{17}$ cm^{-3} [105].

The dominant process, limiting the gas density, is the surface recombination. In order to keep the gas density constant the losses have to be compensated by constantly feeding the cell with atomic hydrogen. Our calculations, based on the theory of such cells [105], show, that a very moderate feed rate of $\Phi \sim 1 \cdot 10^{15}$ atoms/s would provide a gas density of $7 \cdot 10^{15}$ cm^{-3}.

This can be compared with the measurement [107] of $3 \cdot 10^{15}$ cm^{-3}. The average lifetime of a "high field seeking" atom in the cell is $\sim$1 h.

J.2.5 Unpolarized Contamination

The most important sources of unpolarized contamination in the target gas in absence of beam are:

1) hydrogen molecules: $\sim 10^{-5}$;

2) high energy atomic states $|c\rangle$ and $|d\rangle$: $\sim 10^{-5}$;

3) excited atomic states $< 10^{-10}$;

4) other gasses, like helium and the residual gas in the cell: $\sim 10^{-3}$

The contributions 1)-3) are present when the cell is filled with hydrogen. They are difficult to measure directly and we have to rely on calculations. Nevertheless, the behavior of such storage cells has been extensively studied and is well understood [105]. The general parameters, like the gas lifetime, or the gas density are predicted with an accuracy better than a factor of 3. The estimates 1)-3) are about 100 times below the level of contamination of about 0.1% which may become important for polarimetry. In contrast, the contribution 4) can be easily measured with beam by taking an empty target measurement. Atomic hydrogen can be completely removed from the cell by heating a small bolometer inside the cell, which would remove the helium coating on this element, and catalyze a fast recombination of hydrogen on its surface. However, it is important to keep this contamination below several percent in order to reduce the systematic error associated with the background subtraction.

J.2.6 Beam Impact on Storage Cell

We have considered various impacts the $\mathcal{I}_b = 100$ μA CEBAF beam can inflict on the storage cell [102]. The beam consists of short bunches with $\tau = \sigma_T \approx 0.5$ ps at a $\mathcal{F} = 499$ MHz repetition rate. The beam spot has a size of about $\sigma_X \approx \sigma_Y \sim 0.1$ mm. The most important depolarization effects we found are:

[7] This time was estimated using simulation, taking into account the gas density distribution along z and the repelling force in the magnetic field gradient.

A) gas depolarization by the RF electromagnetic radiation of the beam: $\sim 3 \cdot 10^{-5}$;

B) contamination from free electrons and ions: $\sim 10^{-5}$;

C) gas excitation and depolarization by the ionization losses: $\sim 10^{-5}$;

D) gas heating by ionization losses: $\sim 10^{-10}$ depolarization and a $\sim$30% density reduction.

The effects A) and B) are described below.

J.2.7 Beam RF Generated Depolarization

The electromagnetic field of the beam has a circular magnetic field component, which couples to the $|a\rangle \rightarrow |d\rangle$ and $|b\rangle \rightarrow |c\rangle$ transitions. The transition frequency depends on the value of the local magnetic field in the solenoid and for the bulk of the gas ranges from 215 to 225 GHz. The spectral density function of the magnetic field can be presented in the form of Fourier series with the characteristic frequency of $\omega_\circ = 2\pi\mathcal{F}$. The Fourier coefficients are basically the Fourier transforms of the magnetic field created by a single bunch. The bunch length is short in comparison with the typical transition frequency ($\omega_{trans}\tau \sim 0.1$). The resonance lines of the spectrum (a reflection of the 499 MHz repetition rate) populate densely the transition range (see Fig. 78). The induced transition rate depends on the gas density at a given transition frequency. This rate was calculated taking into account the beam parameters and the field map of a realistic solenoid. Provided that the field of the solenoid is fine tuned to avoid the transition resonances for the bulk of the gas in the cell (see Fig. 78), the depolarization described has the following features:

– the transition rate is proportional to $\mathcal{I}_b^2$;

– the average rate of each of the two transitions is about $0.5 \cdot 10^{-4}$ of the target density per second;

– at the center around the beam the full transition rate is about 6% of the density per second.

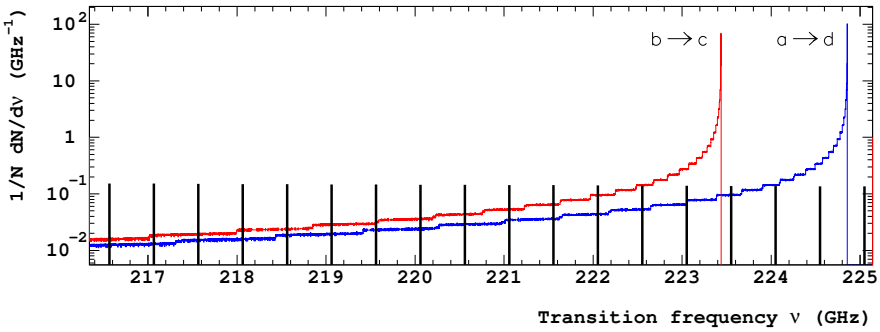

Figure 78: *Simulated spectra of the transitions on the axis of the hydrogen trap with the maximum field of 8.0 T. The density of atoms depends on the field as $exp(-\mu_e B/kT)$. The two curves show $\frac{1}{N}dN/d\nu_{ad}$ and $\frac{1}{N}dN/d\nu_{bc}$ - the relative number of atoms which can undergo $|a\rangle \rightarrow |d\rangle$ and $|b\rangle \rightarrow |c\rangle$ transitions at the given frequency, per one GHz. The resonant structure of the spectral function of the beam-induced electromagnetic field is shown as a set of vertical bars, 499 MHz apart.*

In order to estimate the average contamination we take into account that each resonance line presented in Fig. 78 corresponds to a certain value of the solenoid field and, therefore, affects the gas at a certain z. Using a realistic field map of the solenoid we obtained that the average depolarization in the beam area will be reduced to about $\sim 0.3 \cdot 10^{-4}$ by the lateral gas diffusion and by the escape of the "low field seeking" atoms from the storage cell.

In order to study experimentally the depolarization effect discussed, one can tune the solenoid magnetic field to overlap a resonance line with the transition frequency of the gas at the cell center. This would increase the transition rate by a factor of $\sim$70.

J.2.8 Contamination by Free Electrons and Ions

The beam would ionize per second about 20% of the atoms in the cylinder around the beam spot. The charged particles would not escape the beam area due to diffusion, as the neutral atoms would do, but will follow the magnetic field lines, parallel to the beam. An elegant way to remove them is to apply a relatively weak $\sim$1 V/cm electric field perpendicular to the beam. The charged particles will drift at a speed of $v = \vec{E} \times \vec{B}/B^2 \sim 12$ m/s perpendicular to the beam and leave the beam area in about 20 μs. This will reduce the average contamination to a 10^{-5} level.

J.2.9 Application of the Atomic Target to Møller Polarimetry

This feasibility study was done for the possible application of the target discussed to the existing Møller polarimeter in Hall A at JLab.

The beam polarization at JLab is normally about 80%, at beam currents below 100 μA. Scaling the results of the existing polarimeter to the hydrogen target discussed we estimated that at 30 μA a 1% statistical accuracy will be achieved in about 30 min. This is an acceptable time, in particular if the measurements are done in parallel with the main experiment.

There is no obvious way to measure directly the polarization of the hydrogen atoms in the beam area. The contamination from the residual gas is measurable. The rest relies on calculations. All calculations show that the polarization is nearly 100%, with a possible contamination of $<$0.01%, coming from several contributions. The impact of the most important of these contributions can be studied, at least their upper limits, by deliberately increasing the effect. For example, the beam RF induced transitions can be increased by a factor of $\sim$70, by fine tuning of the solenoid magnetic field. The contribution from the charged particles in the beam area can be varied by a factor up to $\sim 10^4$, by changing the cleaning electric field.

The systematic errors, associated with the present Hall A polarimeter, when added in quadrature give a total systematic error of about 3%. Scaling these errors to the design with the hydrogen target reduces the total error to about 0.3%. If we scale the accuracy of the Hall C polarimeter (see Table 8), the projected total error would be better than 0.2%. There is no doubt that achieving such an accuracy is a major challenge and will require re-evaluation of the error budget for including smaller effects, so far neglected. However, the technique described has a potential to deliver an accuracy of 0.4% required for the experiment proposed.

References

[1] P. L. Anthony *et al.* [SLAC E158 Collaboration], Phys. Rev. Lett. **95**, 081601 (2005) [arXiv:hep-ex/0504049].

[2] K. Abe *et al.* [SLD Collaboration], Phys. Rev. Lett. **84**, 5945 (2000) [hep-ex/0004026].

[3] Nuclear Science Advisory Committee Long Range Planning Document (2007):

`http://hallaweb.jlab.org/12GeV/Moller/downloads/mie/nuclear_science_low_res.pdf`

[4] Report of the Director's Review (January 2010):

`http://hallaweb.jlab.org/12GeV/Moller/downloads/mie/Final_Draft_MOLLER_Review_Report.pdf`

[5] Report to NSAC on Implementing the 2007 Long Range Plan (2013):

`http://hallaweb.jlab.org/12GeV/Moller/downloads/mie/2013_NSAC_Implementing_the_2007_Long_Range_Plan.pdf`

[6] Ya.B. Zel'dovich, Sov. Phys. JETP **94**, 262 (1959).

[7] E. Derman and W. J. Marciano, Annals Phys. **121**, 147 (1979).

[8] A. Czarnecki and W. J. Marciano, Phys. Rev. D **53**, 1066 (1996) [arXiv:hep-ph/9507420].

[9] A. Czarnecki and W. J. Marciano, Int. J. Mod. Phys. A **15**, 2365 (2000) [arXiv:hep-ph/0003049].

[10] J. Erler and M. J. Ramsey-Musolf, Phys. Rev. D **72**, 073003 (2005) [arXiv:hep-ph/0409169].

[11] K. S. Kumar, S. Mantry, W. J. Marciano and P. A. Souder, Ann. Rev. Nucl. Part. Sci. **63**, 237 (2013) [arXiv:1302.6263 [hep-ex]].

[12] V. Cirigliano and M. J. Ramsey-Musolf, Prog. Part. Nucl. Phys. **71**, 2 (2013) [arXiv:1304.0017 [hep-ph]].

[13] J. Erler and S. Su, Prog. Part. Nucl. Phys. **71**, 119 (2013) [arXiv:1303.5522 [hep-ph]].

[14] A. Aleksejevs, S. Barkanova, A. Ilyichev and V. Zykunov, Phys. Rev. D **82**, 093013 (2010) [arXiv:1008.3355 [hep-ph]].

[15] A. Aleksejevs, S. Barkanova, A. Ilyichev, Y. Kolomensky and V. Zykunov, Phys. Part. Nucl. **44**, 161 (2013) [arXiv:1010.4185 [hep-ph]].

[16] A. Aleksejevs, S. Barkanova, Y. Kolomensky, E. Kuraev and V. Zykunov, Phys. Rev. D **85**, 013007 (2012) [arXiv:1110.1750 [hep-ph]].

[17] A. G. Aleksejevs, S. G. Barkanova, Y. M. Bystritskiy, A. N. Ilyichev, E. A. Kuraev and V. A. Zykunov, Eur. Phys. J. C **72**, 2249 (2012).

[18] A. G. Aleksejevs, S. G. Barkanova, V. A. Zykunov and E. A. Kuraev, Phys. Atom. Nucl. **76**, 888 (2013) [Yad. Fiz. **76**, 942 (2013)].

[19] S. C. Bennett and C. E. Wieman, Phys. Rev. Lett. **82**, 2484 (1999) [Erratum-ibid. **83**, 889 (1999)] [hep-ex/9903022].

[20] V. A. Dzuba, J. C. Berengut, V. V. Flambaum and B. Roberts, Phys. Rev. Lett. **109**, 203003 (2012) [arXiv:1207.5864 [hep-ph]].

[21] D. Androic *et al.* [Qweak Collaboration], Phys. Rev. Lett. **111**, 141803 (2013) [arXiv:1307.5275 [nucl-ex]].

[22] C. Amsler *et al.* [Particle Data Group], Phys. Lett. B **667**, 1 (2008).

[23] G. P. Zeller *et al.* [NuTeV Collaboration], Phys. Rev. Lett. **88**, 091802 (2002) [Erratum-ibid. **90**, 239902 (2003)] [arXiv:hep-ex/0110059].

[24] [ALEPH Collaboration and DELPHI Collaboration and L3 Collaboration and OPAL Collaboration and SLD Collaboration and LEP Electroweak Working Group and SLD Electroweak Group and SLD Heavy Flavour Group], Phys. Rept. **427**, 257 (2006) [arXiv:hep-ex/0509008].

[25] W. J. Marciano, AIP Conf. Proc. **870**, 236 (2006).

[26] M. E. Peskin and T. Takeuchi, Phys. Rev. Lett. **65**, 964 (1990).

[27] W. J. Marciano and J. L. Rosner, Phys. Rev. Lett. **65**, 2963 (1990) [Erratum-ibid. **68**, 898 (1992)].

[28] W. J. Marciano and A. Sirlin, Phys. Rev. D **29**, 945 (1984) [Erratum-ibid. D **31**, 213 (1985)].

[29] D. London and J. L. Rosner, Phys. Rev. D **34**, 1530 (1986).

[30] I. Maksymyk, C. P. Burgess and D. London, Phys. Rev. D **50**, 529 (1994) [hep-ph/9306267].

[31] A. Kurylov, M. J. Ramsey-Musolf and S. Su, Phys. Rev. D **68**, 035008 (2003) [arXiv:hep-ph/0303026].

[32] H. Davoudiasl, H. -S. Lee and W. J. Marciano, Phys. Rev. D **85**, 115019 (2012) [arXiv:1203.2947 [hep-ph]].

[33] H. Davoudiasl, H. -S. Lee and W. J. Marciano, Phys. Rev. Lett. **109**, 031802 (2012) [arXiv:1205.2709 [hep-ph]].

[34] P. G. Blunden, W. Melnitchouk and A. W. Thomas, Phys. Rev. Lett. **109**, 262301 (2012) [arXiv:1208.4310 [hep-ph]].

[35] B. Holdom, Phys. Lett. B **166**, 196 (1986).

[36] P. Fayet, Phys. Rev. D **70**, 023514 (2004) [hep-ph/0403226].

[37] C. Bouchiat and P. Fayet, Phys. Lett. B **608**, 87 (2005) [hep-ph/0410260].

[38] M. Pospelov, Phys. Rev. D **80**, 095002 (2009) [arXiv:0811.1030 [hep-ph]].

[39] G. W. Bennett *et al.* [Muon G-2 Collaboration], Phys. Rev. D **73**, 072003 (2006) [hep-ex/0602035].

[40] H. Davoudiasl, H. -S. Lee and W. J. Marciano, arXiv:1402.3620 [hep-ph].

[41] E. Eichten, K. D. Lane and M. E. Peskin, Phys. Rev. Lett. **50**, 811 (1983).

[42] M. J. Ramsey-Musolf, Phys. Rev. C **60**, 015501 (1999) [arXiv:hep-ph/9903264].

[43] W. F. Chang, J. N. Ng and J. M. S. Wu, Phys. Rev. D **79**, 055016 (2009) [arXiv:0901.0613 [hep-ph]].

[44] V. Cirigliano, A. Kurylov, M. J. Ramsey-Musolf and P. Vogel, Phys. Rev. D **70**, 075007 (2004) [arXiv:hep-ph/0404233].

[45] F. Petriello and S. Quackenbush, Phys. Rev. D **77**, 115004 (2008) [arXiv:0801.4389 [hep-ph]].

[46] J. Erler, P. Langacker, S. Munir and E. Rojas, arXiv:1108.0685v1 [hep-ph].

[47] Y. Li, F. Petriello and S. Quackenbush, Phys. Rev. D **80**, 055018 (2009) [arXiv:0906.4132 [hep-ph]].

[48] M. J. Ramsey-Musolf and S. Su, Phys. Rept. **456**, 1 (2008) [arXiv:hep-ph/0612057].

[49] P. A. Souder *et al.*, Phys. Rev. Lett. **65**, 694 (1990).

[50] D. T. Spayde *et al.* [SAMPLE Collaboration], Phys. Lett. B **583**, 79 (2004) [arXiv:nucl-ex/0312016].

[51] A. Acha *et al.* [HAPPEX collaboration], Phys. Rev. Lett. **98**, 032301 (2007) [arXiv:nucl-ex/0609002].

[52] The Lead Radius Experiment PREX, E06002, K. Kumar, R. Michaels, P. Souder, G. Urciuoli spokespersons, http://hallaweb.jlab.org/parity/prex/ .

[53] The Qweak Experiment, http://www.jlab.org/Hall-C/Qweak/index.html, , R. Carlini Principal Investigator.

[54] C. Y. Prescott *et al.*, Phys. Lett. B **77**, 347 (1978).

[55] R.S. Hicks *et al.*, "Flux Profile Scanners for Scattered High-Energy Electrons", NIM **A553** (2005), pp 470-482.

[56] M. Gericke, "Excess Noise as a Function of Detector Thickness", September 1, 2005, a Qweak technical note available at http://qweak.jlab.org/doc-public/ShowDocument?docid=532 .

[57] L. V. de Bever, J. Jourdan, M. Loppacher, S. Robinson, I. Sick and J. Zhao, "A target for precise Mller polarimetry," *Nucl. Instrum. Meth.*, vol. A400, pp. 379–386, 1997.

[58] E. Chudakov and V. Luppov, "Møller polarimetry with atomic hydrogen targets," *IEEE Trans. Nucl. Sci.*, vol. 51, pp. 1533–1540, 2004.

[59] E. Chudakov and V. Luppov, "Moeller polarimetry with atomic hydrogen targets," *Eur. Phys. J.*, vol. A24S2, pp. 123–126, 2005.

[60] M. Hauger *et al.*, "A high-precision polarimeter," *Nucl. Instrum. Meth.*, vol. A462, pp. 382–392, 2001, nucl-ex/9910013.

[61] M Loppacher, "Møller Polarimetry for CEBAF Hall C," PhD thesis, Universität Basel, April 1996.

[62] A. V. Glamazdin *et al.*, "Electron beam Moeller polarimeter at JLAB Hall A," *Fizika*, vol. B8, pp. 91–95, 1999, hep-ex/9912063.

[63] N. L. Hall, P. G. Blunden, W. Melnitchouk, A. W. Thomas and R. D. Young, Phys. Lett. B **731**, no. issue, 287 (2014) [Erratum-ibid. B **733**, 380 (2014)] [arXiv:1311.3389 [nucl-th]].

[64] D.E. Wiser, PhD thesis, University of Wisconsin-Madison, 1977.

[65] K. D. Paschke, Eur. Phys. J. A **32**, 549 (2007).

[66] E. G. Brentari et al., 1965, *Boiling Heat Transfer for Oxygen, Nitrogen, Hidrogen, and Helium*, National Bureau of Standards, TN 317

[67] S. D. Covrig et al., 2005, *The cryogenic target for the G0 experiment at Jefferson Lab*, Nucl. Instr. and Meth. **A 551**, 218-235

[68] J. Gao et al., 2003, *A liquid hydrogen target for the precision measurement of the weak mixing angle in Møller scattering at SLAC*, Nucl. Instr. and Meth. **A 498**, 90-100

[69] Geant4. `http://geant4.cern.ch/`.

[70] S. Agostinelli *et al.* [GEANT4 Collaboration], Nucl. Instrum. Meth. A **506**, 250 (2003).

[71] Christy, M.E. *et al.* Phys.Rev. **C81** (2010) 055213
arXiv:0712.3731

[72] N. Falletto *et al*, "Compton scattering off polarized electrons with a high finesse Fabry-Perot cavity at JLab,", *"Nucl. Instrum. Meth."*, A459, 212-425, 2001.

[73] A. Narayan, D. Dutta, V. Tvaskis and J. W. Martin, Nuovo Cim. C **035N04**, 134 (2012).

[74] N. Vansteenkise, P. Vignolo, and A. Aspect, "Optical Reversibility Theorems for Polarization: Application to Remote Control of Polarization", J. Opt. Soc. Am. A, Vol. 10, No. 10, (1993) 2240.

[75] R.J. Loewen, "A compact light source: Design and technical feasibility study of a laser-electron storage ring X-ray source," SLAC-R-0632 (2003).

[76] S. Miyoshi *et al*., Photon generation by laser-Compton scattering at the KEK-ATF, NIM A623 (2010) 576.

[77] A. Variola *et al*., The LAL Compton Program,, NIM A608 (2009) S83.

[78] V. Brisson *et al*., High finesse Fabry-Perot cavities in the picosecond regime, NIM A608 (2009) S75.

[79] A. Denner and S. Dittmaier, "Complete o() QED cor- rections to polarized Compton scattering", Nucl. Phys. B **540** 58 (1999).

[80] M. Friend *et al*, "Upgraded photon calorimeter with integrating readout for Hall A Compton Polarimeter at Jefferson Lab", Nucl. Instrum. Methods A676, 96-105, 2012. [arXiv:1108.3116].

[81] G. W. Ford and C. J. Mullin, "Scattering of Polarized Dirac Particles on Electrons," Phys. Rev. **108**, 477 (1957); Erratum, Phys. Rev. **110**, 1485(E) (1958).

[82] A. M. Bincer, "Scattering of Longitudinally Polarized Fermions," Phys. Rev. **107**, 1434 (1957).

[83] P. Stehle, "Calculation of Electron-Electron Scattering," Phys. Rev. **110**, 1458 (1958).

[84] A. Raçzka and R. Raçzka, "Møller Scattering of Arbitrarily Polarized Electrons," Erratum, Phys. Rev. **110**, 1469 (1958).

[85] G. Alexander and I. Cohen, "Møller scattering polarimetry for high-energy e^+e^- linear colliders," Nucl. Instrum. Meth. A **486**, 552 (2002) [hep-ex/0006007]. This paper contains the basic formulas for Møller polarimetry, as well as references to calculations of higher order QED corrections.

[86] E. A. Chudakov, A. V. Glamazdin, V. G. Gorbenko, L. G. Levchuk, R. I. Pomatsalyuk, P. V. Sorokin, "Electron beam Møller polarimeter at Hall A, JLab", Prob.Atom.Sci.Tech. **40**, 43 (2002)

[87] P. S. Cooper, M. J. Alguard, R. D. Ehrlich, V. W. Hughes, H. Kobayakawa, J. S. Ladish, M. S. Lubell and N. Sasao *et al.*, "Polarized electron Electron Scattering at GeV Energies," Phys. Rev. Lett. **34**, 1589 (1975).

[88] B. Wagner, H. G. Andresen, K. H. Steffens, W. Hartmann, W. Heil and E. Reichert, "A Møller polarimeter for CW and pulsed intermediate-energy electron beams," Nucl. Instrum. Meth. A **294**, 541 (1990).

[89] J. Arrington, E. J. Beise, B. W. Filippone, T. G. O'Neill, W. R. Dodge, G. W. Dodson, K. A. Dow and J. D. Zumbro, "A Variable energy Møller polarimeter at the MIT Bates Linear Accelerator Center," Nucl. Instrum. Meth. A **311**, 39 (1992).

[90] K. B. Beard, R. Madey, W. M. Zhang, D. M. Manley, B. D. Anderson, A. R. Baldwin, J. M. Cameron and C. C. Chang *et al.*, "Measurement of the polarization of a pulsed electron beam with a Møller polarimeter in the coincidence mode," Nucl. Instrum. Meth. A **361**, 46 (1995).

[91] H. R. Band, G. Mitchell, R. Prepost and T. Wright, "A Møller polarimeter for high-energy electron beams," Nucl. Instrum. Meth. A **400**, 24 (1997).

[92] P. Steiner, A. Feltham, I. Sick, M. Zeier and B. Zihlmann, "A high-rate coincidence Moller polarimeter," Nucl. Instrum. Meth. A **419**, 105 (1998).

[93] G. G. Scott and H. W. Sturner, "Magnetomechanical Ratios for Fe-Co Alloys," Phys. Rev. **184**, 490 (1969).

[94] J. Crangle and G. M. Goodman, "The Magnetization of Pure Iron and Nickel," Proceedings of the Royal Society of London, Series A, **321**, 477 (1971).

[95] C. D. Graham, Jr., "Iron and Nickel as Magnetization Standards," J. Appl. Phys. **53**, 2032 (1982).

[96] G. G. Scott, "Review of gyromagnetic ratio experiments," *Rev. Mod. Phys.*, vol. 34, pp. 102–109, Jan 1962.

[97] E. C. Stoner and E. P. Wohlfarth, "A Mechanism of Magnetic Hystersis in Heterogeneous Alloys," Phil. Trans. Royal Soc. London, Series A **240**, 599 (1948).

[98] L. G. Levchuk, "The Intraatomic motion of bound electrons as a possible source of a systematic error in electron beam polarization measurements by means of a Møller polarimeter," *Nucl. Instrum. Meth.*, vol. A345, pp. 496–499, 1994.

[99] M. Swartz, H. R. Band, F. J. Decker, P. Emma, M. J. Fero, R. Frey, R. King and A. Lath *et al.*, "Observation of target electron momentum effects in single arm Møoller polarimetry," Nucl. Instrum. Meth. A **363**, 526 (1995) [hep-ex/9412006].

[100] D. Gaskell, D. G. Meekins, and C. Yan, "New methods for precision Møller polarimetry," *Eur. Phys. J.*, vol. A32, pp. 561–564, 2007.

[101] M. Poelker, J. Grames, J. Hansknecht, R. Kazimi, J. Musson, Phys. Rev. ST Accel. Beams **10**, 053502 (2007).

[102] E. Chudakov and V. Luppov, "Møller polarimetry with atomic hydrogen targets," tech. rep., JLab, 2005. `http://www.jlab.org/~gen/hyd/loi_3.pdf`.

[103] I. F. Silvera, "Ultimate fate of a gas of atomic hydrogen in a liquid-helium chamber: Recombination and burial," *Phys. Rev. B*, vol. 29, pp. 3899–3904, Apr 1984.

[104] I. F. Silvera and J. T. M. Walraven, "Stabilization of atomic hydrogen at low temperature," *Phys. Rev. Lett.*, vol. 44, pp. 164–168, Jan 1980.

[105] I. F. Silvera and J. T. M. Walraven, "Spin polarized atomic hydrogen," *Progress in Low Temperature Physics, vol. X*, pp. 139–370, 1986.

[106] T. Roser *et al.*, "Microwave driven extraction of stabilized spin polarized atomic hydrogen," *Nucl. Instrum. Meth.*, vol. A301, pp. 42–46, 1991.

[107] M. Mertig, V. G. Luppov, T. Roser, and B. Vuaridel, "Continuous density measurement of atomic hydrogen by means of a bolometer," *Rev. Sci. Instrum.*, vol. 62, pp. 251–252, 1991.

[108] M. D. Miller and L. H. Nosanow, "Possible "new" quantum systems. ii. properties of the isotopes of spin-aligned hydrogen," *Phys. Rev. B*, vol. 15, pp. 4376–4385, May 1977.